Unpolarized Neutral Current
$e^{\pm}p$ Cross Section Measurements
at the H1 Experiment, HERA

Dissertation

zur Erlangung des Doktorgrades
des Department Physik
der Universität Hamburg

vorgelegt von

Shiraz Z Habib

aus Trinidad and Tobago

Hamburg

2009

Gutachter der Dissertation: Prof. Dr. Robert Klanner
PD Dr. Alexandre Glazov

Gutachter der Disputation: Prof. Dr. Robert Klanner
JProf. Dr. Johannes Haller

Datum der Disputation: 10. September 2009

Vorsitzender des Prüfungsausschusses: Prof. Dr. Guenter Huber

Vorsitzender des Promotionsausschusses: Prof. Dr. Robert Klanner

Dekan der MIN Fakultät: Prof. Dr. Heinrich Graener

Leiter des Department Physik: Prof. Dr. Joachim Bartels

Abstract

Measurements of the unpolarized inclusive neutral current reduced cross section in $e^{\pm}p$ scattering at a center of mass energy of $\sqrt{s} \simeq 319$ GeV are presented. The data was collected by the H1 detector during the HERA II running phase, after the 2000 luminosity upgrade, and corresponds to an integrated luminosity of 145 pb^{-1} and 167 pb^{-1} for the $e^{-}p$ and $e^{+}p$ periods respectively. The cross section measurements were made for the negative four-momentum transfer squared range $65 \leqslant Q^2 \leqslant 30000$ GeV^2 and Bjorken-x range $0.00085 \leqslant x \leqslant 0.65$. Dedicated measurements at inelasticity $y = 0.75$ and $Q^2 \leqslant 800$ GeV^2 are also made. The details of the analysis are presented here.

The cross section measurements presented here are found to agree with previously published data as well as predictions determined from various NLO QCD fits. Scaling violation of the $\tilde{F}_2$ structure function as well differences between the e^- and e^+ cross sections at high Q^2 due to the $x\tilde{F}_3$ structure function have been observed. The cross sections in the range $Q^2 \leqslant 800$ GeV^2 at inelasticity $y = 0.75$ suggest non-zero values of the longitudinal structure function F_L.

Kurzfassung

Diese Arbeit stellt eine Messung des Wirkungsquerschnitts des reduzierten, unpolarisierten neutralen Stroms der $e^{\pm}p$ Streuung bei Schwerpunktsenergien von $\sqrt{s} \simeq 319\,\text{GeV}$ vor. Der dazu verwendete Datensatz wurde mit dem H1 Detektor in der HERA II Phase aufgenommen, nachdem im Jahre 2000 die HERA Luminosität erhöht worden war. Insgesamt entsprechen die Daten einer integrierten Luminosität von 145 pb für Elektron-Proton Wechselwirkungen ($e^{-}p$), beziehungsweise 167 pb für Positron-Proton Wechselwirkungen ($e^{+}p$). Die Messung wurde für negative quadratische-Vierimpuls-Überträge im Bereich $65 \leqslant Q^2 \leqslant 30000$ GeV^2 und einem Bjorken-x Bereich von $0.00085 \leqslant x \leqslant 0.65$ vorgenommen. Zusätzlich werden spezielle Messungen bei inelastischen $y = 0.75$ und $Q^2 \leqslant 800$ GeV^2 präsentiert.

Die Ergebnisse der hier diskutierten Messungen stimmen sowohl mit Ergebnissen vorangegangener Veröffentlichungen als auch mit NLO QCD Fits überein. Zusätzlich wurden Skalenverletzungen der $\tilde{F}_2$ Strukturfunktion und Unterschiede zwischen den e^- und e^+ Wirkungsquerschnitten aufgrund der $x\tilde{F}_3$ Strukturfunktion beobachtet. Die gemessenen Wirkungsquerschnitte bei inelastischen $y = 0.75$ im Bereich $Q^2 \leqslant 800$ GeV^2 deuten auf eine nicht verschwindende longitudinale Strukturfunktion F_L hin.

Contents

Introduction

Scattering is an established tool used by particle physicists to probe the structure of matter. When Rutherford scattered α-particles onto a gold target, he was astounded to find a significant number of particles deflected through very large angles. This was inconsistent with the idea held at the time that the charge of the atom was uniformly distributed over its volume. The observation could be explained if one assumed the charge to be tightly packed into what is now called the nucleus, and so the atomic model acquired structure.

In the late sixties Bjorken predicted that at high energies the inelastic structure functions were independent of the relevant scale Q^2. This *scaling* was verified at SLAC in the late sixties. Callan and Gross proposed the relationship between the Bjorken's scaling functions which was also experimentally confirmed. Scaling and the Callan-Gross relation were consequences of the fact that the proton consisted of pointlike spin-$\frac{1}{2}$ constituents, now identified as quarks. The model of the *proton* had now acquired structure, and became known as the Quark Parton Model(QPM). In the QPM, the sum of the momentum distributions of the quarks is directly related to the F_2 structure function. Experimentally, F_2 is derived from the double differential *ep* cross section. This sets the stage as an experimental test of a theory of proton structure.

Quantum Chromodynamics (QCD) is presently accepted as the field theory of the strong interaction, the force which holds the quarks together in the proton. As it turns out, the strong mediators, *gluons* carry about half of the proton's momentum. The increase of F_2 with Q^2 at low x and decrease at high x – scaling violation – is predicted by QCD, the observation of which was a triumph of the theory. QCD is not yet able to *predict* the quark and gluon densities however but can evolve the density at one value of the given scale to another. This forms the basis for QCD fits which parametrize the parton densities at an initial scale, evolve them to the scale of the measurement and then fit them to the data.

HERA continues the tradition of deep inelastic scattering by colliding electrons[1] with protons at a centre of mass energy of $\simeq 319$ GeV. The collisions at HERA therefore provide

---

[1] Throughout the thesis, the term "electron" refers generically to both electrons and positrons, unless otherwise stated.

a laboratory to study structure functions at Bjorken-$x \gtrsim 10^{-6}$ for Q^2 values $\gtrsim 0.2$ GeV^2. At the highest values of Q^2 the weak interactions of the Standard Model (SM) may also be tested. In the very last phase of its operation, collisions at the centre of mass energies of 460 and 575 GeV aimed at producing a measurement of the longitudinal structure function were achieved.

This thesis explores the ***high*** Q^2 regime of the kinematic region accessible at HERA. Measurements of the unpolarized neutral current $e^{\pm}p$ reduced cross sections are presented in the kinematic range $65 \leqslant Q^2 \leqslant 30000$ GeV^2 and $0.00085 \leqslant x \leqslant 0.65$. Dedicated measurements at inelasticity $y = 0.75$ and $Q^2 \leqslant 800$ GeV^2 are also made. The data used was collected by the H1 detector during operation of the HERA collider in its HERA II phase of running, that is, after the 2000 luminosity upgrade and corresponds to a centre of mass energy of $\simeq 319$ GeV. The data sets correspond to an integrated luminosity of 145 pb^{-1} and 167 pb^{-1} for the e^-p and e^+p periods respectively.

This report takes the reader along the following path. Chapter 1 summarizes the theory relevant to the analysis. As it is difficult to have an appreciation for any measurement without some knowledge of the instruments used, chapter 2 introduces the HERA collider and the H1 detector giving basic information on aspects of the detector most relevant to the analysis. Simulation is used extensively throughout, therefore chapter 3 gives a short introduction into Monte Carlo programs as a tool in high energy physics. Chapter 4 explains why a neutral current cross section measurement needs to be performed as two distinct analyses termed the “nominal analysis” and the “high y analysis.” No measurement is useful without first calibrating and aligning the scientific instrument, chapter 5. The selection used to produce the final samples from which the cross section is measured is detailed in chapters 6 and 7. The measurement begins – first reconstructing and binning the kinematic variables (chapter 8) then extracting the cross section (chapter 9). Results are then summarized and conclusions drawn.

Chapter 1

Theoretical Framework

This chapter provides a short summary of the theoretical background which both motivates the cross section measurement as well as provides a basis for its interpretation. After defining the various kinematic variables, the cross section dependence on the various structure functions is introduced. The Quark Parton Model interpretation of these structure functions is then laid out. Basic aspects of Quantum Chromodynamics are stated, then applied to electron-proton scattering; the implications are then discussed with their relevance to the present measurement.

1.1 Deep Inelastic Scattering (DIS) Kinematics

In deep inelastic scattering (DIS) ep collisions, two types of interactions are distinguished: the neutral current (NC) process $ep \rightarrow eX$ and the charged current (CC) process $ep \rightarrow \nu_e X$. Both processes are measured at HERA. In the Standard Model (SM), the interactions are mediated by the exchange of a photon/Z boson (γ/Z) for NC interactions, and a W boson for CC, as shown in their Feynman diagram representation, figure 1.1. The 4-momenta of the particles involved are:

- l for the incoming electron
- l' for the outgoing lepton
- p for the incoming proton
- p' for the system of particles X in the outgoing hadronic final state.
- $q \equiv l - l'$ for the exchanged boson.

The kinematics of a given scattering process is uniquely defined by two variables for a given centre-of-mass energy $\sqrt{s}$. Variables used in this thesis are the negative four-

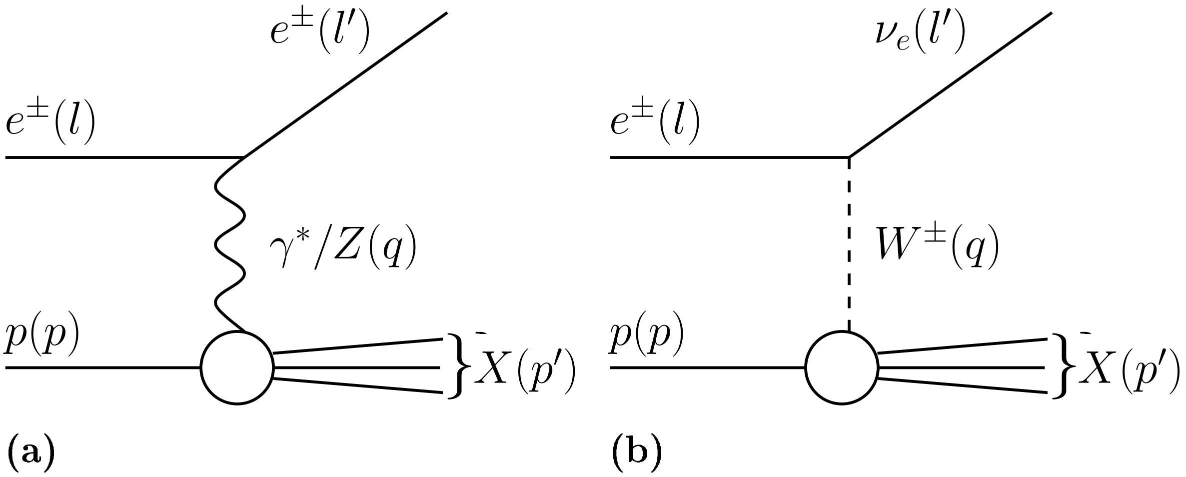

Figure 1.1: *Feynman diagram representations of the (a) neutral current and (b) charged current processes. Particle types and associated 4-momenta are indicated.*

momentum transfer squared (Q^2), Bjorken-x and the inelasticity y defined by:

$$Q^2 \equiv -q^2 = -(l-l')^2, \qquad x = \frac{Q^2}{2p \cdot q}, \qquad y = \frac{p \cdot q}{p \cdot l}. \tag{1.1}$$

Since $s \equiv (l+p)^2$ it follows that $Q^2 = sxy$.

Q^2 determines the spatial resolution Δ of the virtual boson probe as derived from the Heisenberg Uncertainty Principle:

$$\Delta = \frac{\hbar c}{\sqrt{Q^2}} \tag{1.2}$$

which for the centre-of-mass energy at HERA of $\simeq$ 319 GeV, corresponds to a maximum resolution of $\Delta = 10^{-18}$ m. The inelasticity y is the fraction of energy of the incident electron transferred to the proton target in the frame where the proton is at rest. In the Quark Parton Model (QPM) the inelastic ep collision is interpreted as an *elastic* collision between the incoming lepton and a quasifree point-like constituent of the proton – the parton – figure 1.2(a). The variable x then equals the fraction of the momentum of the proton carried by the struck parton in the infinite momentum frame where the proton momentum is so much more than its mass, that the partons can be regarded as massless. In the QPM these partons are held to be quarks.

1.2 Inclusive NC Cross Sections and the Structure Functions

NC cross sections for ep scattering $e^{\pm}p \rightarrow e^{\pm}X$ can be expressed by a propagator term and the structure function term ϕ_{NC}. The Born cross section is given by [1]:

$$\frac{d^2\sigma_{NC}^{e^{\pm}p}}{dxdQ^2} = \frac{2\pi\alpha^2}{xQ^4}\phi_{NC}^{\pm}(x,Q^2) \tag{1.3}$$

with

$$\phi_{NC}^{\pm} = Y_+\tilde{F}_2^{\pm}(x,Q^2) \mp Y_-x\tilde{F}_3^{\pm}(x,Q^2) - y^2\tilde{F}_L^{\pm}(x,Q^2) \tag{1.4}$$

and

$$Y_{\pm} = 1 \pm (1-y)^2. \tag{1.5}$$

α is the electromagnetic coupling constant ($= e^2/4\pi$). $\tilde{F}_L$ is known as the longitudinal structure function. The generalized $\tilde{F}_2$, $x\tilde{F}_3$ and $\tilde{F}_L$ structure functions can be separated into contributions arising from pure γ exchange, γZ interference and pure Z exchange. For unpolarised leptons:

$$\tilde{F}_2 \equiv F_2 \quad - v_e\frac{\kappa Q^2}{Q^2+M_Z^2}F_2^{\gamma Z} \quad + (v_e^2+a_e^2)(\frac{\kappa Q^2}{Q^2+M_Z^2})^2F_2^Z, \tag{1.6}$$

$$x\tilde{F}_3 \equiv \quad - a_e\frac{\kappa Q^2}{Q^2+M_Z^2}xF_3^{\gamma Z} \quad + (2v_ea_e)(\frac{\kappa Q^2}{Q^2+M_Z^2})^2xF_3^Z. \tag{1.7}$$

Here $\kappa = 1/(4\sin^2\theta_W\cos^2\theta_W)$ where θ_W is the Weinberg angle and M_Z is the mass of the Z boson. v_e and a_e are the the vector and axial-vector weak couplings respectively of the electron to the Z. The structure function F_2 originates from pure γ exchange, F_2^Z and xF_3^Z from pure Z exchange and $F_2^{\gamma Z}$ and $xF_3^{\gamma Z}$ from γZ interference. Over most of the kinematic range at HERA, the largest contribution to the cross section comes from pure γ exchange via F_2. The contributions from γZ and Z exchange become significant at large $Q^2 \gtrsim M_Z^2$. The $x\tilde{F}_3$ structure function contributes positively to the e^-p cross section and negatively to the e^+p cross section.

The probability density of quark type q is denoted by $q(x,Q^2)$ defined such that $q(x,Q^2)dx$ is the number of quarks with momentum fraction between x and $x+dx$ at the momentum transfer Q^2. The probability densities are also known as *parton distribution functions* (PDFs). In the QPM the structure functions F_2, $F_2^{\gamma Z}$ and F_2^Z are related to the sum of the various quark and anti-quark ($q(x,Q^2)$ and $\bar{q}(x,Q^2)$) PDFs by:

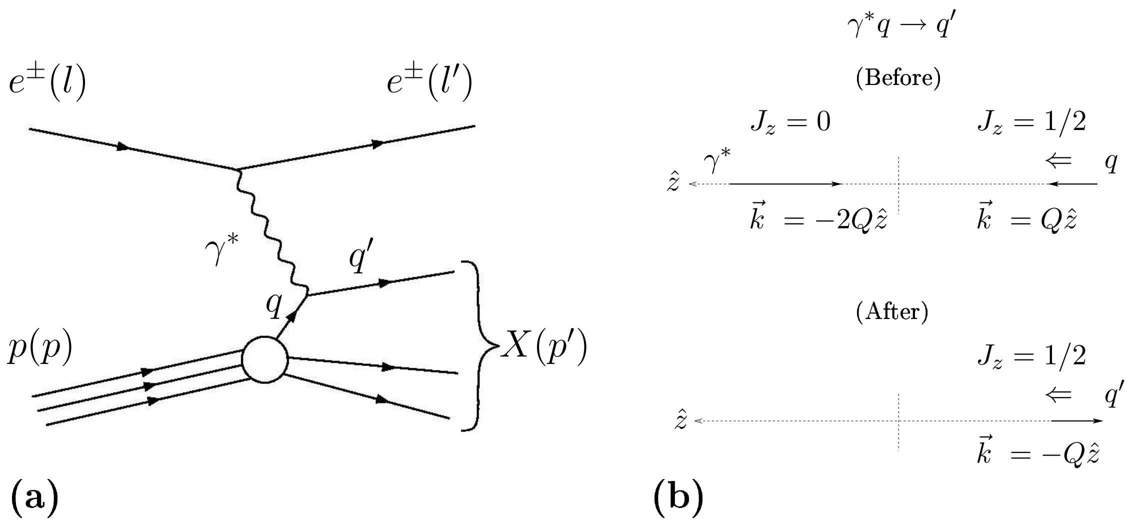

Figure 1.2: *(a) ep scattering as seen from the Quark Parton Model (only electromagnetic interaction shown) – the virtual photon γ^* collides elastically with a quark constituent q from the proton. (b) The $\gamma^* q \rightarrow q'$ interaction where the photon is longitudinally polarized as seen from the Breit frame. The momentum $\vec{k}$ and spin component J_z of each particle is given; the $\hat{z}$ direction is defined as the direction of propagation of the incoming quark.*

$$F_2 = x \sum_q e_q^2 \{q + \bar{q}\} \tag{1.8}$$

$$F_2^{\gamma Z} = x \sum_q 2 e_q v_q \{q + \bar{q}\} \tag{1.9}$$

$$F_2^{Z} = x \sum_q (v_q^2 + a_q^2) \{q + \bar{q}\} \tag{1.10}$$

while $xF_3^{\gamma Z}$ and xF_3^{Z} are related to the difference, which determine the valence quark distributions $xq_v(x, Q^2)$,

$$xF_3^{\gamma Z} = 2x \sum_q e_q a_q \{q - \bar{q}\} = 2x \sum_{q=u,d} e_q a_q q_v \tag{1.11}$$

$$xF_3^{Z} = 2x \sum_q v_q a_q \{q - \bar{q}\} = 2x \sum_{q=u,d} v_q a_q q_v . \tag{1.12}$$

In equations 1.8 and 1.11, e_q is the charge of quark q, while v_q and a_q are the vector and axial-vector weak coupling of the quarks to the Z^0 respectively.

The Longitudinal Structure Function $\tilde{F}_L$

The longitudinal structure function $\tilde{F}_L$ can be decomposed into a purely electromagnetic term F_L, a purely weak term F_L^Z and an interference term $F_L^{\gamma Z}$, similar to $\tilde{F}_2$. Neglecting the weak interaction, it is possible to consider ep scattering as $\gamma^* p$ scattering where a flux of virtual photons interacts with the proton[2]. The double differential cross section is then:

$$\frac{d^2\sigma}{dxdQ^2} = \Gamma(y)(\sigma_T + \epsilon(y)\sigma_L) \tag{1.13}$$

where $\Gamma(y) = \alpha Y_+/(2\pi Q^2 x)$ is the flux factor, $\epsilon(y) = 2(1-y)/Y_+$ defines the photon polarization, and σ_T and σ_L are the cross sections for transversely and longitudinally polarized photons respectively. The F_2 and F_L structure functions are then related to the cross sections by:

$$F_2 = \frac{Q^2}{4\pi^2\alpha}(\sigma_T + \sigma_L) \tag{1.14}$$

$$F_L = \frac{Q^2}{4\pi^2\alpha}(\sigma_L) \tag{1.15}$$

where F_2, F_L, σ_T and σ_L are all functions of x and Q^2. Since the cross sections σ_T and σ_L must be positive, it follows that $0 \leqslant F_L \leqslant F_2$. It is evident from equation 1.4 that F_L contributes at higher values of inelasticity y due to its y^2 coefficient.

Figure 1.2(b) shows the elastic collision between the quark q from the proton and a longitudinally polarized virtual photon γ^* as seen in the Breit frame[1]. Choosing the $\hat{z}$ direction as that of the incoming quark, the momentum of the virtual photon is $-2Q\hat{z}$ and of the incoming and outgoing quarks are $Q\hat{z}$ and $-Q\hat{z}$ respectively. This process is suppressed as it violates helicity conservation, therefore $\sigma_L = 0$. Thus in the QPM, $F_L = 0$, equation 1.15.

The Reduced Cross Section

In this thesis the cross section measurements are quoted as reduced cross sections $\tilde{\sigma}_{NC}$ defined by:

$$\tilde{\sigma}_{NC} \equiv \frac{xQ^4}{2\pi\alpha^2}\frac{1}{Y_+}\frac{d^2\sigma}{dxdQ^2} = \tilde{F}_2 \mp \frac{Y_-}{Y_+}x\tilde{F}_3 - \frac{y^2}{Y_+}\tilde{F}_L. \tag{1.16}$$

In most of the kinematic range, $\tilde{F}_2$ gives the largest contribution and so $\tilde{\sigma}_{NC} \approx \tilde{F}_2$.

---

[1] The Breit frame is defined as that in which $2x\vec{p} + \vec{q} = 0$ where $\vec{p}$ and $\vec{q}$ are the 3-momenta of the proton and virtual photon respectively. The quark "rebounds" with an equal but opposite 3-momentum – thus the alternate name "Brick Wall" frame.

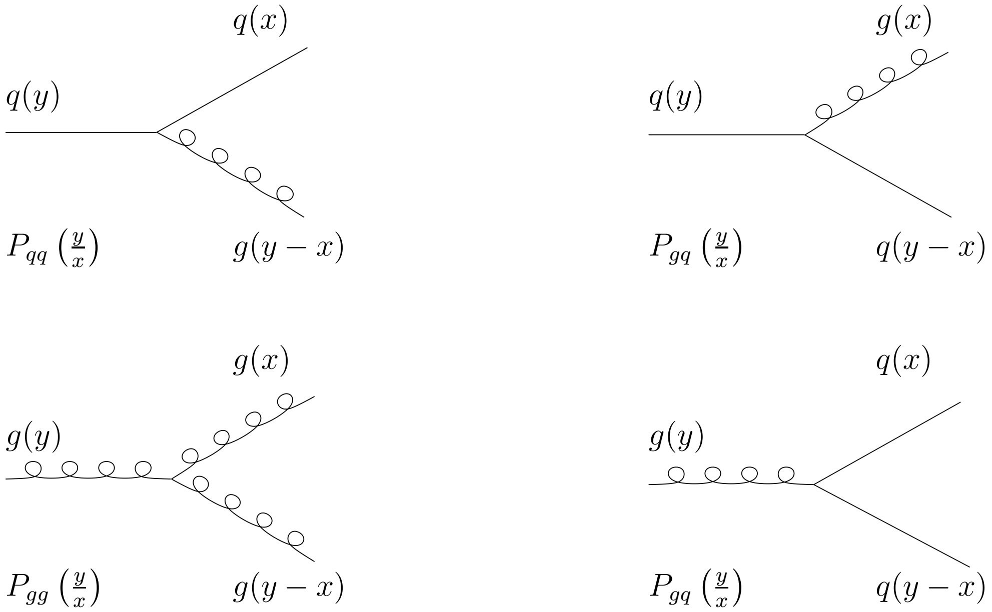

Figure 1.3: *Feynman diagrams for the four splitting functions in the DGLAP evolution equation.*

1.3 Quantum Chromodynamics (QCD)

The interaction between the quarks within the proton can be described by the theory of the strong interaction, Quantum Chromodynamics (QCD). QCD is a non-abelian gauge theory. The “charge” of QCD is colour which can take the values red, green and blue as well as anti-red, anti-green and anti-blue. Each quark carries a colour charge. The gauge boson of QCD is the massless gluon and unlike its electromagnetic counterpart – the photon which carries no electric charge – does carry colour, and hence can couple to itself.

QCD is characterised by the strong coupling constant α_s which has a strong dependence on the scale (for example Q^2). At small distances (high Q^2) the coupling becomes small; this is known as *asymptotic freedom.* At large distances the coupling increases which leads to *confinement* – the observation of quarks and gluons in bound states (the hadrons), not as free particles. In leading order (LO) α_s is given by

$$\alpha_s = \frac{12\pi}{(33 - 2n_f)ln(Q^2/\Lambda^2_{QCD})} \tag{1.17}$$

At high Q^2 QCD can be treated as a pertubative theory (pQCD). Though pQCD cannot calculate the PDFs from first principles, it can evolve a given PDF at some starting scale to different values of Q^2 and x. Several evolution schemes exist, the most popular being DGLAP[3, 4, 5, 6] and BFKL[7, 8] each with a different kinematic region of applicability.

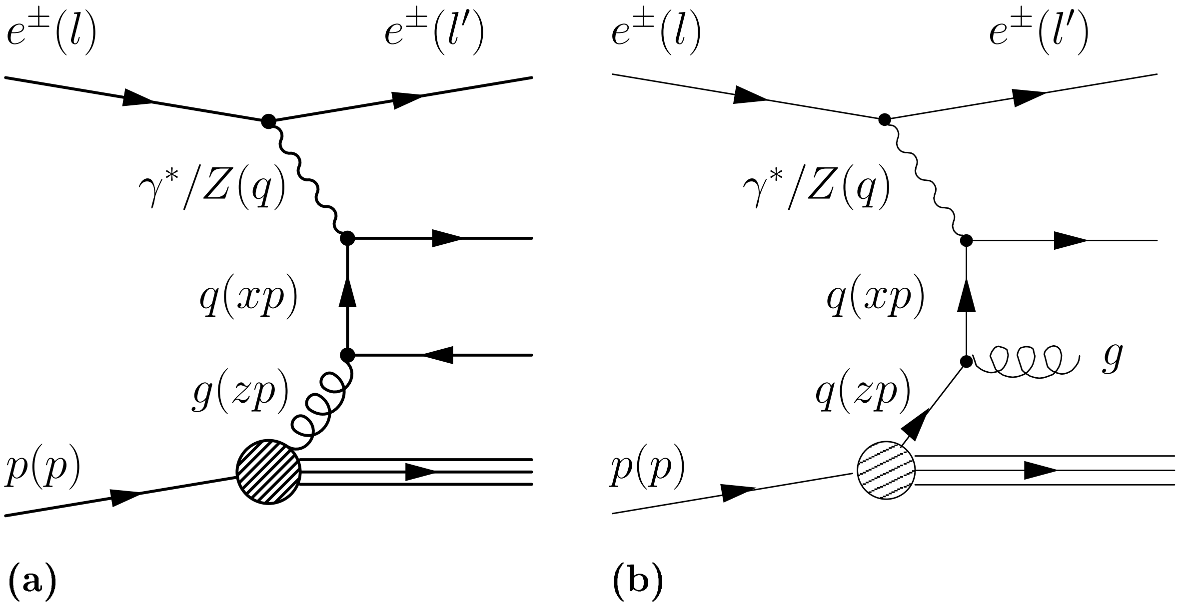

Figure 1.4: *ep scattering in leading order pQCD – $\mathcal{O}(\alpha_s)$. (a) Boson-Gluon Fusion (BGF) where the virtual photon interacts with a gluon via a quark. The momentum fractions are x and z as indicated. (b) The quark radiates a gluon before interacting with the virtual photon.*

The DGLAP evolution equations describe the evolution of the PDFs in $ln(Q^2)$ while BFKL evolves the PDFs in $ln(1/x)$.

The DGLAP evolution equations are:

$$\frac{\partial q(x,t)}{\partial t} = \frac{\alpha_s(t)}{2\pi}\int_x^1 \frac{dy}{y}\left[q(y,t)P_{qq}\left(\frac{x}{y}\right) + g(y,t)P_{qg}\left(\frac{x}{y}\right)\right] \tag{1.18}$$

$$\frac{\partial g(x,t)}{\partial t} = \frac{\alpha_s(t)}{2\pi}\int_x^1 \frac{dy}{y}\left[q(y,t)P_{gq}\left(\frac{x}{y}\right) + g(y,t)P_{gg}\left(\frac{x}{y}\right)\right] \tag{1.19}$$

where $t = ln(Q^2/\Lambda_{QCD})$ and P_{ab} are the splitting functions. The splitting functions give the probability of parton b with momentum fraction y producing parton a with momentum fraction x. The Feynman diagrams corresponding to the four splitting function are shown in figure 1.3.

Incorporating QCD into the QPM

The sum of the average momentum carried by all quark types in the proton

$$\sum_i \int_0^1 x f_i(x) dx \qquad\qquad i = u, \bar{u}, d, \bar{d}... \tag{1.20}$$

is experimentally 0.5[9]. The “missing” half is carried by the gluons which do not couple to the photon, W or Z. Incorporating the strong force into the QPM leads to diagrams shown in figure 1.4. In 1.4(a) a gluon is radiated from a quark within the proton which in turn produces a quark-antiquark pair; the quark then interacts with the virtual photon as shown – a process known as Boson-Gluon fusion. In 1.4(b) the quark radiates a gluon before it is struck by the virtual photon. Both processes depicted in figure 1.4 are in leading order (LO), $\mathcal{O}(\alpha_s)$.

Scaling Violation

One consequence of contributions such as those depicted in figure 1.4 is that F_2 depends not only on x but on Q^2 as well – known as scaling violation. The experimental verification of scaling violation as predicted by QCD is one of the triumphs of the theory of the strong force.

Non-zero F_L

Since gluons carry spin 1, diagrams such as those in figure 1.4 allow helicity to be conserved for interactions mediated by longitudinally polarized virtual photons[10]. Thus within the framework of QCD, non-zero F_L values are allowed. In NLO F_L is given by:

$$F_L(x,Q^2) = \frac{\alpha_s}{4\pi}x^2\int_x^1 \frac{dz}{z^3}\left[\frac{16}{3}\sum_q(q+\bar{q}) + 8\sum_q e_q^2\left(1-\frac{x}{z}\right)\cdot zg\right] \tag{1.21}$$

where the first sum in the integral corresponds to figure 1.4(b) and the second sum corresponds to the contribution coming from diagram 1.4(a).

In this way F_L is sensitive to the gluon distribution $g(x,Q^2)$. For this reason high y cross section measurements – the main subject of this thesis – where F_L becomes appreciable play an important role in verifying the understanding of the gluon distribution.

1.4 QCD Fits

As mentioned previously, pQCD can evolve the PDFs, however their shapes as a function of x are not determined. The PDFs have to be determined experimentally by first parameterizing their shape at a starting scale Q_0^2 using smooth functions of x with a limited number of parameters, then evolving to the Q^2 of the data using next-to-leading order (NLO) pQCD. The parameters are then determined by a χ^2 fit to the data.

In this thesis several QCD fits are used. The **H1 PDF 2000** fit is based on cross sections measured by the H1 experiment corresponding to the HERA I period of running. Details are found here[1]. The **H1 PDF 2009** fit[11] relies on more accurate new H1 data and differs in the treatment of heavy quarks. Also used are the global fits **CTEQ 6m**[12] and **MRSH**[13] which rely not only on deep inelastic scattering data, but also Drell-Yan pair production in fixed target and collider experiments, and Tevatron cross sections.

The PDFs from the H1PDF2000 fit at the initial scale $Q_0^2 = 4$ GeV^2 is shown in figure 1.5.

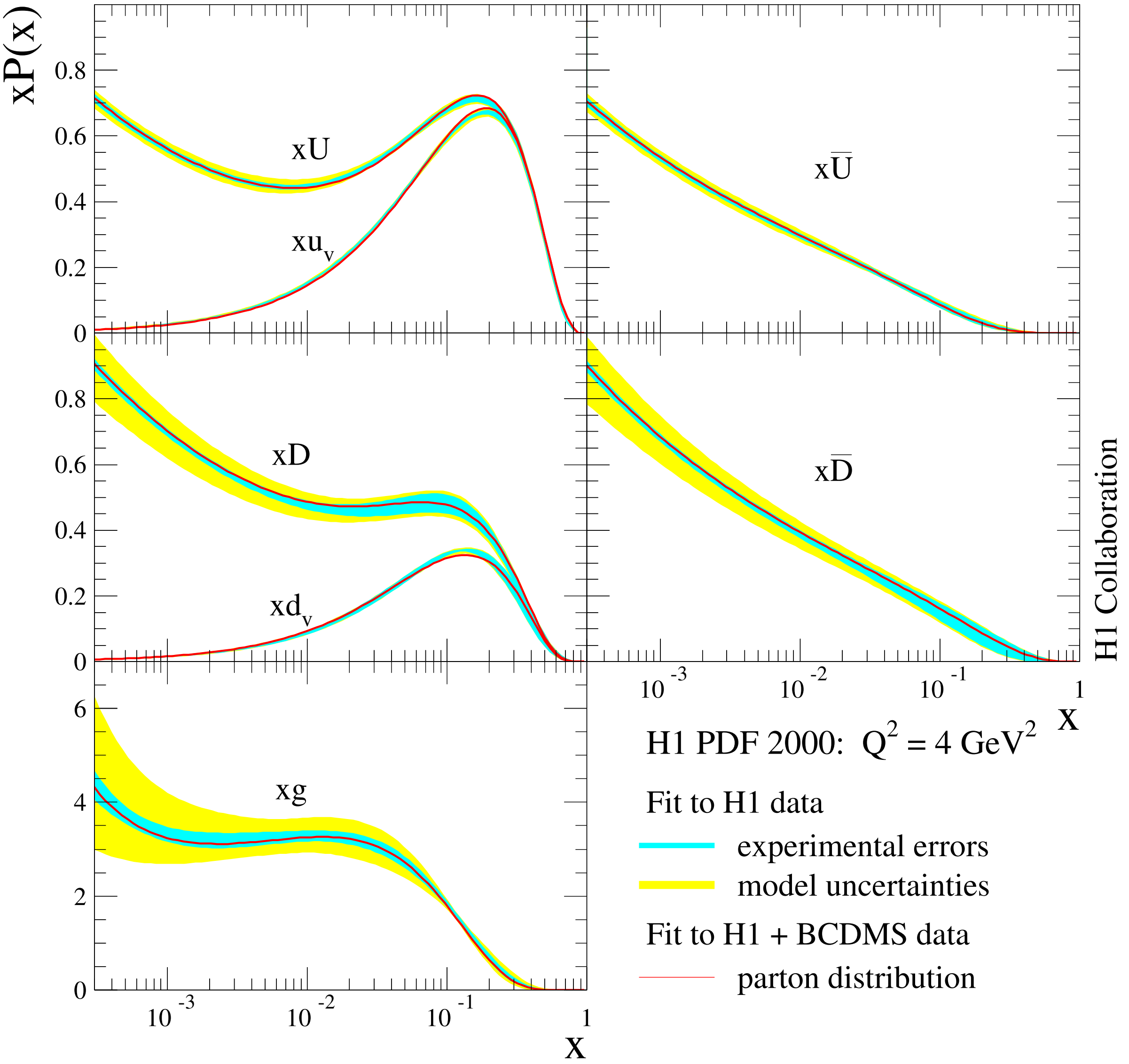

Figure 1.5: Parton distributions (a)xU, (b)$x\bar{U}$, (c)xD, (d)$x\bar{D}$ and (e) xg as determined from the H1PDF 2000 Fit to H1 data only. The distributions are shown at the initial scale $Q_0^2 = 4$ GeV^2. The inner error band represents the experimental uncertainty as determined from the fit. The outer error band shows the total uncertainty by adding in quadrature the experimental and model uncertainties. The valence quark distributions (a)xu_v and (c)xd_v are also shown. For comparison, the parton distributions from the fit to H1 and BCDMS muon scattering data[14] are shown as the full curves.

Chapter 2

The Experiment

To investigate the structure of the proton as described in Chapter 1 requires a device which produces ep collisions and one which is capable of observing the resulting particles produced and measuring their four-momenta. This chapter introduces the HERA collider and H1 detector. The detector section focuses on the most relevant subdetectors for this analysis. A general description of the H1 trigger system then follows, after which the trigger information used in selecting events in this analysis are explained.

2.1 The HERA Collider

The HERA particle accelerator (*Hadron-Elektron-Ring-Anlage*) located at DESY (*Deutsches Elektronen-Synchrotron*), Hamburg, collides electrons at 27.6 GeV with protons at 920 GeV corresponding to a centre of mass energy $\sqrt{s} \simeq 319$ GeV. The electron beam serves as an ideal probe into the structure of the proton since the electroweak interactions of electrons are well understood. Figure 2.1(a) shows a schematic view of the HERA storage ring with the four experiments H1 and ZEUS (colliding-beam), HERMES (lepton beam on gas target) and HERA-B (proton beam on nuclei).

August 2000 marked the end of the first phase of operation (HERA I) of HERA, with a total integrated luminosity of approximately 130 pb^{-1} having been delivered to H1, figure 2.1(b). In September 2000 the collider underwent a shutdown, the aim of which was to embark on a major luminosity upgrade program designed to increase the instantaneous luminosity by a factor 4 compared to HERA I [15]. This task involved the installation of almost 80 new magnets, and was a major engineering challenge. The increased luminosity however was accompanied by an unforeseen increase in background. After much effort, the problem was reduced to a satisfactory level as H1 demonstrated in February 2004 tolerable levels of background up to the highest beam intensties. Figure 2.1(b) shows the final result of such efforts – a total of approximately 400 pb^{-1} of integrated luminosity –

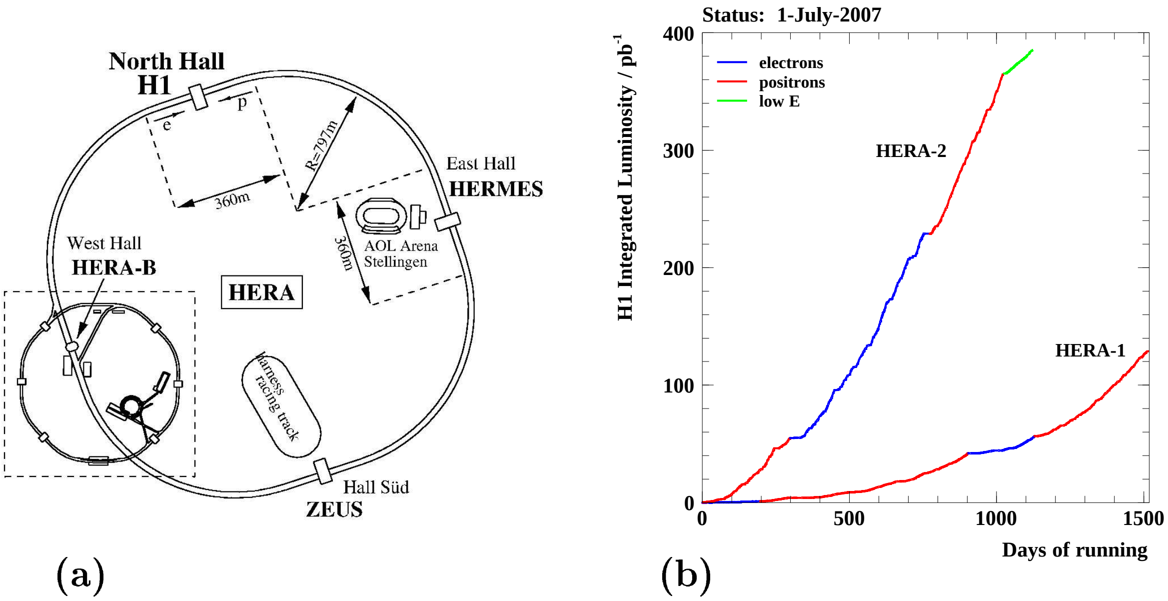

Figure 2.1: *(a)The HERA storage ring with the colliding-beam experiments H1 and ZEUS and the fixed target experiments HERMES and HERA-B. (b) Integrated luminosity collected by H1 during the running periods HERAI and HERAII.*

which includes both e^-p and e^+p collisions allowing the study of electroweak effects in both charged current and neutral current processes. In the very final phase of its operation, the collider made two special low proton energy runs of 460 and 575 GeV which allowed the measurement of the longitudinal structure function, F_L[16].

Another objective of the upgrade program was to produce longitudinally polarized electron beams for the two colliding-beam experiments. This was achieved by the installation of special magnets called *spin rotators* before and after the interaction points, figure 2.2(a). By February 2003, HERA successfully delivered high longitudinal spin polarization, and in so doing became the world's first to achieve longitudinally polarized positron and high energy proton collisions [17]. Figure 2.2(b) shows the dependence of the total charged current e^+p cross section on the polarization of the positron beam measured at H1[18].

The H1 experiment stopped data taking at the end of June, 2007.

2.2 The H1 Detector

The purpose of the H1 detector is to identify particles produced in ep interactions and to reconstruct their four-momenta. This is done by surrounding the interaction point with several *subdetectors*, each sensitive to energy deposited by the particles traversing it. The

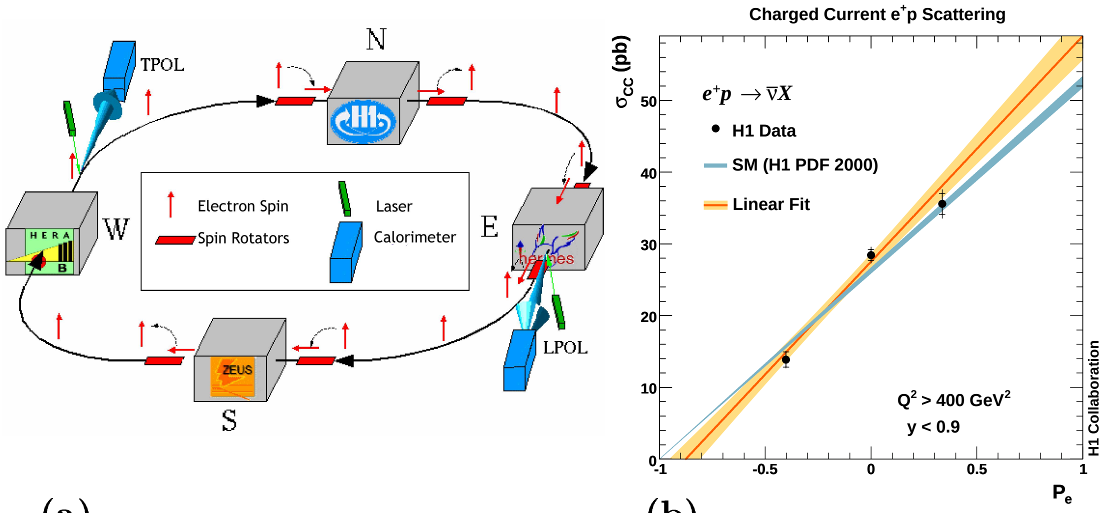

(a) (b)

Figure 2.2: *(a) Spin rotators used to achieve longitudinally spin polarized lepton beams. (b) Total charged current cross section as a function of polarization.*

energy lost by a particle is converted into electrical signals which are then read out and interpreted as a physics quantity (energy or position for example). By combining the measurements of the various subdetectors (using track reconstruction and particle finder algorithms for example), a single *ep* collision can be reconstructed as an *event*.

Figure 2.3 shows a 3-dimensional view of the H1 detector. The *ep* collisions occur near the *nominal interaction point*, defined as the origin of the H1 frame of reference. The x-axis points in the horizontal direction towards the center of the HERA ring, the y-axis points upwards and the z-axis points in the flight direction of the proton. Three regions of the detector can be distinguished with respect to polar angle coverage: the *forward* region corresponding to $\theta \lesssim 25°$, the *central* region corresponding to $25° \lesssim \theta \lesssim 155°$ and the *backward* region corresponding to $155° \lesssim \theta$. As the proton's momentum is much higher than the electron's, most of the particles produced are scattered into the forward region of the detector.

Particles produced in *ep* interactions first traverse the trackers (Central Track Detector and Forward Track Detector) followed by the calorimeters (Liquid Argon (LAr) calorimeter in the central and forward regions and the Lead-Fiber Spaghetti (SPACAL) calorimeter in the backward region). A superconducting solenoid surrounding the calorimeters produce a homogeneous magnetic field of 1.15T. The Instrumented Iron Return Yoke (Tail Catcher) detects particles that penetrate beyond the calorimeters – important in identifying muons

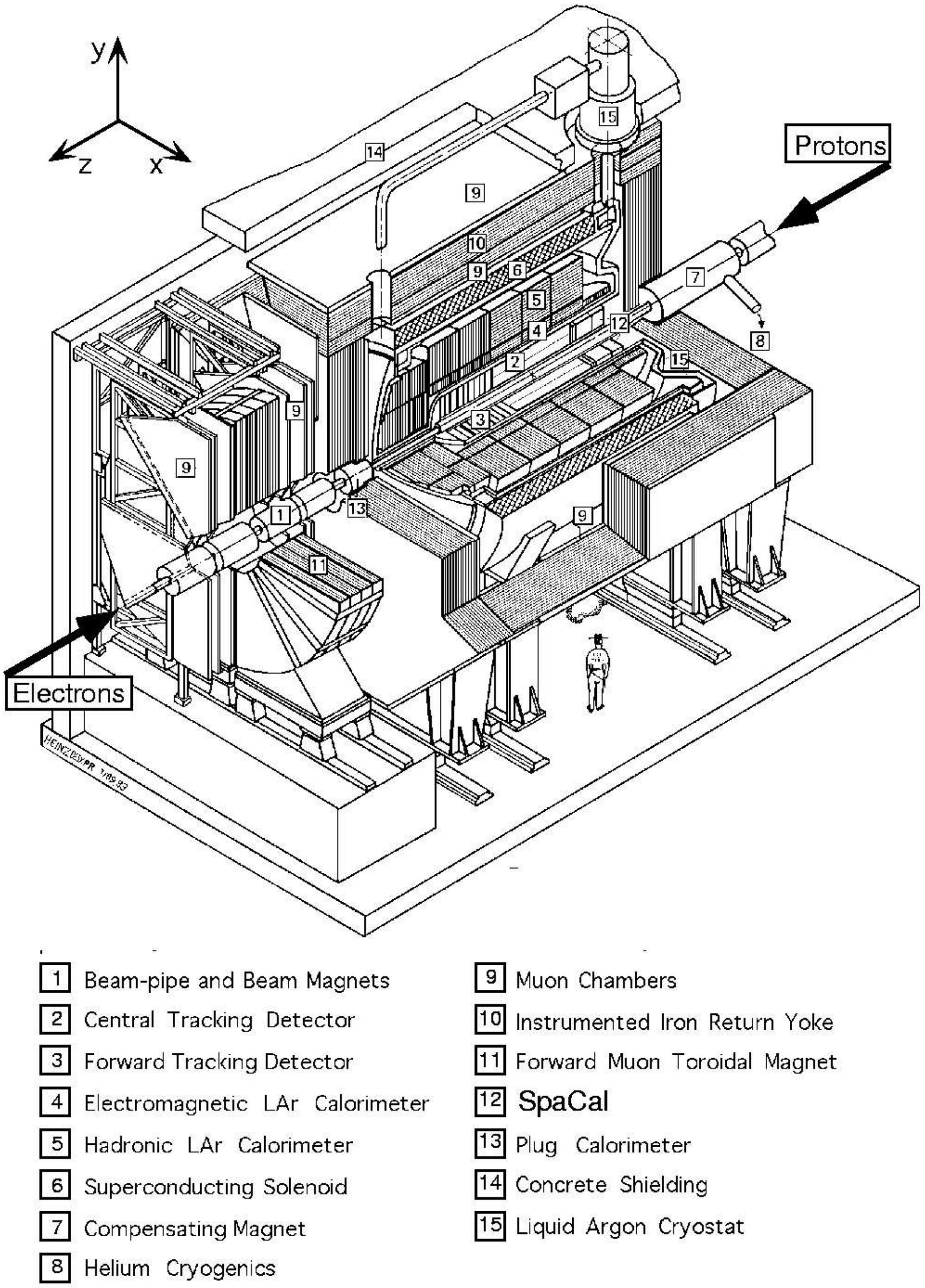

Figure 2.3: *3-Dimensional view of the H1 detector.*

as well as reconstructing the hadronic shower tails. Beyond the iron in the forward region is the Forward Muon Detector (FMD): drift chambers in a toroidal magnetic field which are used to identify muons and measure their trajectories.

The most relevant subdetectors used in this analysis are presented in the following pages.

2.3 H1 Calorimeters

The main calorimeters of the H1 detector are the Liquid Argon (LAr) calorimeter which covers the polar angle range $4° \lesssim \theta \lesssim 153°$ and the Spaghetti (SPACAL) calorimeter covering $153° \lesssim \theta \lesssim 174°$. For the kinematic range covered in this analysis, the electron is scattered into the central part of the detector. Thus the LAr calorimeter is the most important subdetector of the analysis, from the trigger level where the electron signature is tagged to the analysis level where the electron particle candidate is fully reconstructed and kinematics are calculated.

Liquid Argon Calorimeter

The physical structure of the LAr calorimeter is shown in figure 2.4(a) in the rz-view. It is made of 8 wheels: Backward Barrel Electromagnetic (BBE), Central Barrel (CB1, CB2, CB3), Forward Barrel (FB1, FB2), Outer Forward (OF) and Inner Forward (IF) as shown. All wheels apart from the BBE consists of an electromagnetic section (EM) and a hadronic section (HAD). The BBE has one section which is EM, the OF has two HAD sections. All wheels are housed in a single cryostat. Each wheel is divided into 8 octants in the ϕ direction. Figure 2.4(b) shows the $r\phi$-view of the CB2 wheel. The $r\phi$-view of a BBE octant is shown in figure 2.5; it has a 16-fold symmetry. The region of dead material between the wheels and octants are known as the z- and ϕ-cracks respectively.

The sensitive region of the calorimeter is made of layers of absorber material interleaved with layers of sampling material (liquid argon). A particle entering the calorimeter interacts electromagnetically or hadronically with the absorber material producing a shower of particles. The charged particles produced in the shower ionize atoms in the sampling layers producing free electrons which are used to produce a signal. The signal, integrated over all layers, is proportional to the energy of the initial particle. The absorber material in the EM section is lead having a depth of 22 and 30 radiation lengths (X_0) in the central and forward regions respectively. The HAD section is made of stainless steel plates of about 5 to 8 interaction lengths (λ). The LAr calorimeter's response to hadronic showers is ≈30% less than for electromagnetic showers due to energy lost in nuclear excitation and break up. This is corrected for in the software [19].

The smallest unit of the LAr calorimeter is a "cell" of which there are ≈45 000. The EM sections consists of 3 layers of cells for the BBE, CB and FB1 wheels, 4 layers for the FB2 wheel and 7 layers for the IF. The high granularity afforded by the 45 000 cells ensure a good spatial resolution of the deposited energies. This in turn allows the design of reliable electromagnetic shower identification algorithms (by which the electron is identified) as well as the precise determination of cluster centres (by which the electron polar angle is calculated).

Test beam measurements [20, 21, 22] of the LAr modules yielded the following energy resolutions for electrons (σ_{em}) and charged pions (σ_{had}):

$$\begin{aligned}\frac{\sigma_{em}(E)}{E} &= \frac{12\%}{\sqrt{E[GeV]}} \oplus 1\% \\ \frac{\sigma_{had}(E)}{E} &= \frac{50\%}{\sqrt{E[GeV]}} \oplus 2\%.\end{aligned}$$

The absolute energy scale uncertainty is determined *insitu* using NC events and presented in chapter 5.

A more detailed description of the LAr calorimeter is given here [23].

"Spaghetti" Calorimeter

The "Spaghetti" calorimeter (SPACAL) is used to identify electrons in the backward part of the detector allowing NC cross section measurements down to $Q^2 = 0.4$ GeV^2. It consists of electromagnetic (EM) and hadronic (HAD) sections like its LAr counterpart. The absorber material is lead. Shower particles enter the scintillating fibres aligned parallel to the z-axis. Molecules excited by these charged shower particles emit scintillations which are collected by photomultiplier tubes which in turn convert the light energy into electrical signals. These electrical signals which are then read out and used to determine the incident particle energy. The EM and HAD sections both have active material equivalent to one nuclear interaction length [10]; the active EM and HAD section corresponds to 27.8 and 29.4 radiation lengths respectively[24]. The electron energy resolution (σ_{em}) and hadronic energy resolution (σ_{had}) are:

$$\begin{aligned}\frac{\sigma_{em}(E)}{E} &= \frac{7\%}{\sqrt{E[GeV]}} \oplus 1\% \\ \frac{\sigma_{had}(E)}{E} &= \frac{56\%}{\sqrt{E[GeV]}} \oplus 7\%\end{aligned}$$

In this analysis the SPACAL is used in the reconstruction of the hadronic final state.

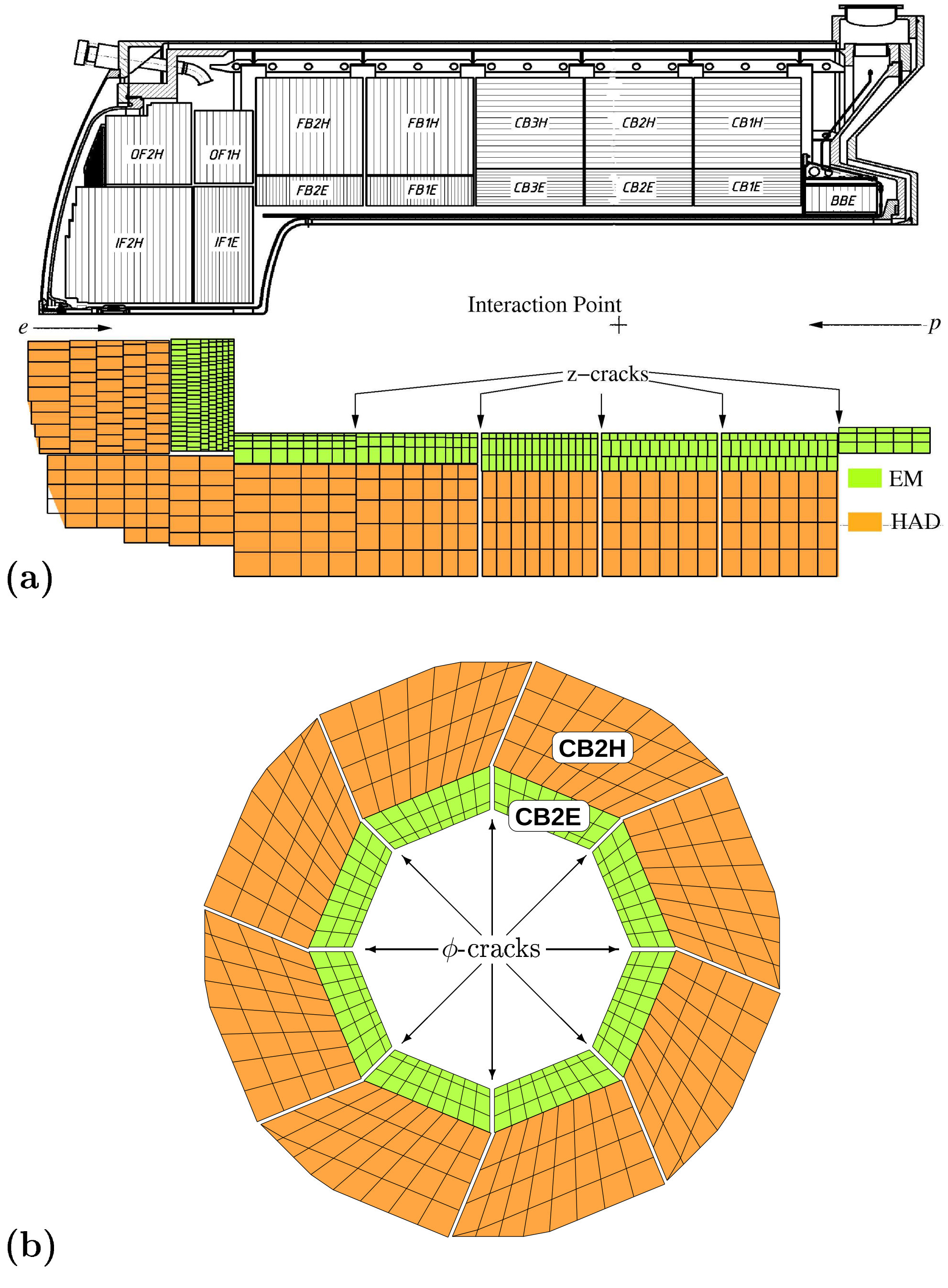

Figure 2.4: *(a) Schematic view of the wheel and cell structure of the LAr calorimeter. Shown are the Backward Barrel Electromagnetic (BBE), Central Barrel (CB1, CB2, CB3), Forward Barrel (FB1, FB2), Inner Forward (IF) and Outer Forward (OF) wheels, with the electromagnetic (EM) and hadronic (HAD) sections indicated. The z-cracks are also shown. (b) Schematic view of the octant structure of the CB2 wheel with ϕ-cracks indicated.*

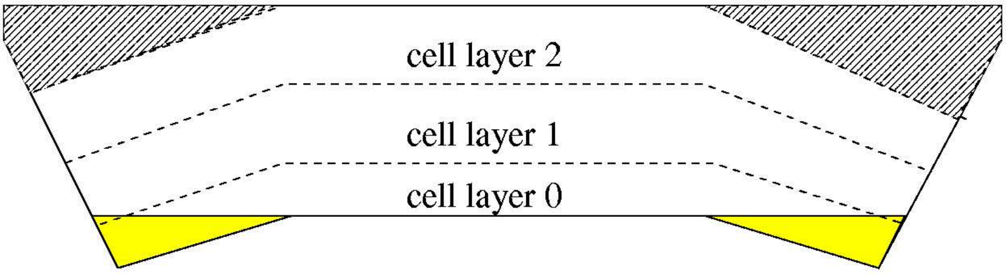

Figure 2.5: *Schematic view of a BBE octant showing the 16-fold symmetry. The grey areas indicate the regions where there is no overlap with the CB1 wheels.*

2.4 H1 Tracker

The aim of the H1 Tracker is the reconstruction and identification of charged particles and their trajectories as well as the reconstruction of the event vertex, the position at which the interaction took place. The tracker comprises the Central Track Detector (CTD) and Forward Track Detector (FTD) shown in figure 2.6(a).

The CTD is composed of various subdetectors arranged concentrically as shown in figure 2.6(b). These are described below.

The Drift Chambers (CJC1,CJC2)

The inner (CJC1) and outer (CJC2) drift chambers are the most important subdetectors of the tracker. They are placed in the presence of a 1.15T magnetic field running parallel to the z-axis. Charged particles therefore follow a helix trajectory through the CJCs. The trajectory projected unto the $r\phi$-plane is a circle with radius inversely proportional to the transverse momentum of the particle.

The sensor wires of the CJCs run parallel to the z-axis. CJC1 contains 720 sensor wires distributed in 30 azimuthal cells with 24 radial layers each. CJC2 contains 1920 sensor wires (60 azimuthal cells × 32 radial layers). The sensor wire signal induced by a charged particle allows the reconstruction of a *hit*. The hit resolution in the $r\phi$-plane is $\approx$170 μm. The z-position of the hit is determined by charge division – the charges collected at both ends of the wire are compared – and leads to a resolution of $\approx$2-3 cm.

The Central Inner Proportional Chamber (CIP)

The CIP[25] is a Multiwire Proportional Chamber (MWPC) located between the Central Silicon Tracker (CST) and CJC1. The CIP consists of 5 separate layers, each of which

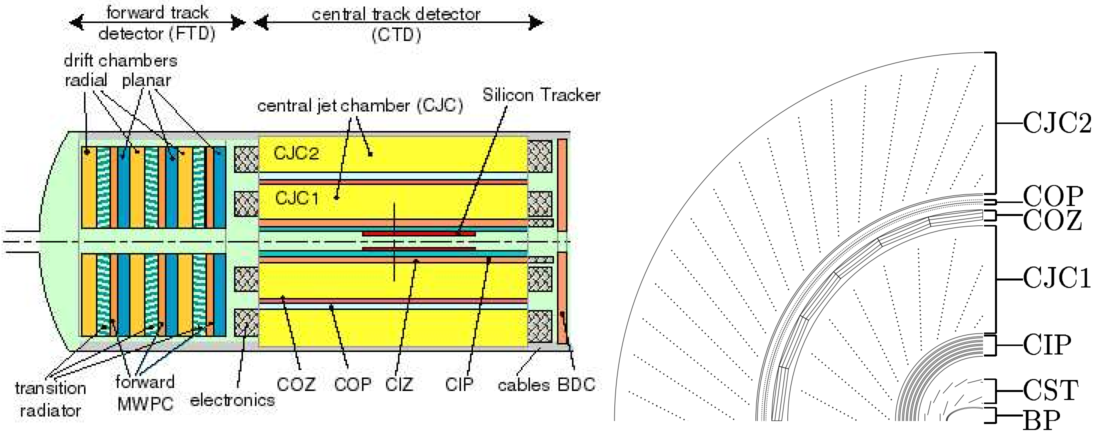

(a) **(b)**

Figure 2.6: *(a) A side view of the H1 Tracker distinguishing the Forward Track Detector (FTD) and Central Track Detector (CTD). The Central Inner z-Chamber (CIZ) was removed to make way for the Central Inner Proportional Chamber (CIP) used in the HERAII period of running. (b) The $r\phi$-view of the Central Track Detector (CTD) showing its subdetectors – Central Silicon Tracker (CST), Central Inner Proportional Chamber (CIP), Central Jet Chambers (CJC1, CJC2), Central Outer z Chamber (COZ) and Central Outer Proportional Chamber (COP). The beam pipe (BP) is also indicated.*

can be regarded as a separate MWPC. MWPCs are characterized by very fast responses to charged particles, typically having time resolutions of 10 ns. The CIP is used primarily to provide trigger signals (section 2.6).

The Central Outer z-Chamber (COZ)

The COZ is located between CJC1 and CJC2. With sensor wires perpendicular to the z-axis a hit resolution of $\approx$350 μm in z results. The COZ provides precise measurements in z for the track fitting procedure described below.

The Central Silicon Tracker (CST)

The innermost subdetector of H1 is the CST[26] which immediately surrounds the beam pipe of elliptical cross section as indicated in figure 2.6(b). The detector is designed to be very thin so that particles see only 0.40 g cm^{-1} of material while passsing through. It is a silicon tracker having sensor strips running parallel to the z-axis on the p-side and normal to the z-axis on the n-side. The CST is made of two layers, the inner layer with 12 ladders and outer layer with 20 ladders as arranged as shown in figure 2.7. The ladders are oriented such that straight tracks approach normally onto their sensor pads thereby optimizing the resolution. The hit resolution in $r\phi$ and z are 12 μm and 22 μm respectively.

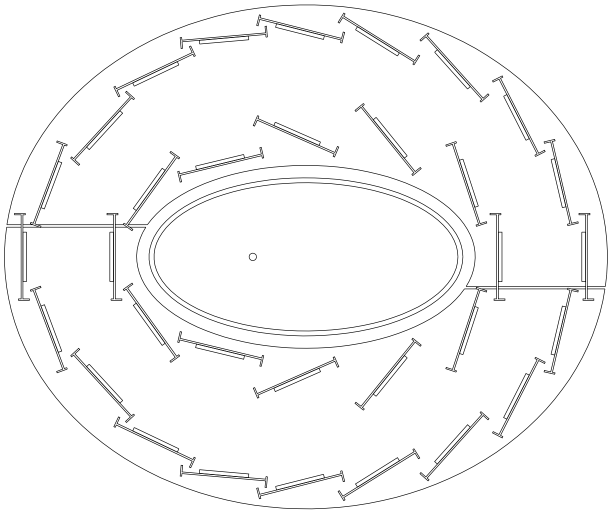

Figure 2.7: *The layout of the 12 inner ladders and 20 outer ladders of the Central Silicon Tracker (CST). The small circle in the centre denotes the interaction point.*

The FTD is a set of drift chambers located in the forward part of the main detector. With a polar angle coverage of $5^\circ \lesssim \theta \lesssim 25^\circ$, the FTD extends the reach of the H1 Tracker into the forward region.

The hits collected by the various tracker subdetectors are used as input into the track-fitting procedure. Firstly, track segments are built from hits in the CJC and FTD. The track segments are then constrained to an interaction vertex. Some tracks may not be successfully fitted to the vertex. The COZ and CST hits are then linked to the tracks which can lead to improvements in the z and $r\phi$ resolutions. The linking of hits and fitting is done iteratively. At the end of the procedure tracks which are fitted to the vertex are termed "DTRA" tracks; those not fitted are termed "DTNV."

In this analysis the track belonging to the scattered electron is used to reduce background (section 6.3). The hadronic final state is also composed from track-based particle candidates (section 5.4). The requirement of an event vertex not only rejects non-ep background but also allows the calculation of event kinematics to a greater precision. The tracker also provides trigger signals (section 2.6).

2.5 H1 Luminosity System

The H1 Luminosity System [27] provides the measurement of the luminosity as seen by the main detector. It uses the Bethe-Heitler $ep \longrightarrow ep\gamma$ process whose cross section σ_{bh} has an uncertainty of 0.5% [1].

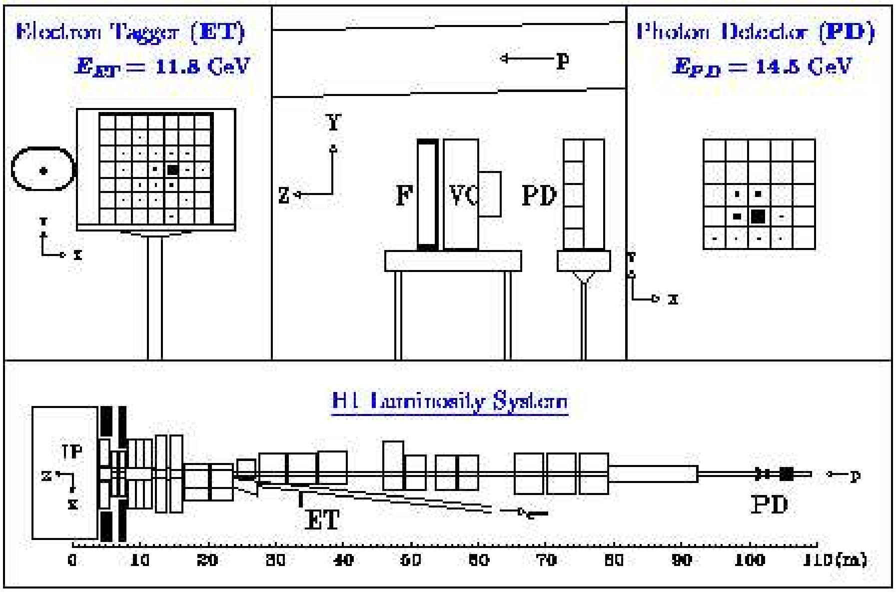

Figure 2.8: *The detectors of the H1 Luminosity System: electron tagger (ET), photon detector (PD) and Čerenkov counter (VC).*

The detectors used to measure the rate of Bethe-Heitler events are the electron tagger (ET), photon detector (PD) and Čerenkov counter (VC), figure 2.8. The electron detected by ET and photon detected by PD scatter at very small angles (0-5 mrad for the electron and 0-0.45 mrad for the photon) so that these components are placed near the beam pipe and distant from the main detector. VC is used to provide a veto condition. The main source of background is bremsstrahlung from beam electrons interacting with gas molecules in the beam pipe. The event rate corrected for background R' is then used to determine the luminosity L:

$$L = \frac{R'}{\sigma_{bh}^{vis}} \tag{2.1}$$

where σ_{bh}^{vis} is the visible part of σ_{bh} taking into account trigger efficiency and acceptance corrections.

The electron tagger is also used to detect the scattered electron in photoproduction processes ($Q^2 \lesssim 0.01$ GeV^2) which is used in analyses where photoproduction is the process under study or where it contributes as a source of background.

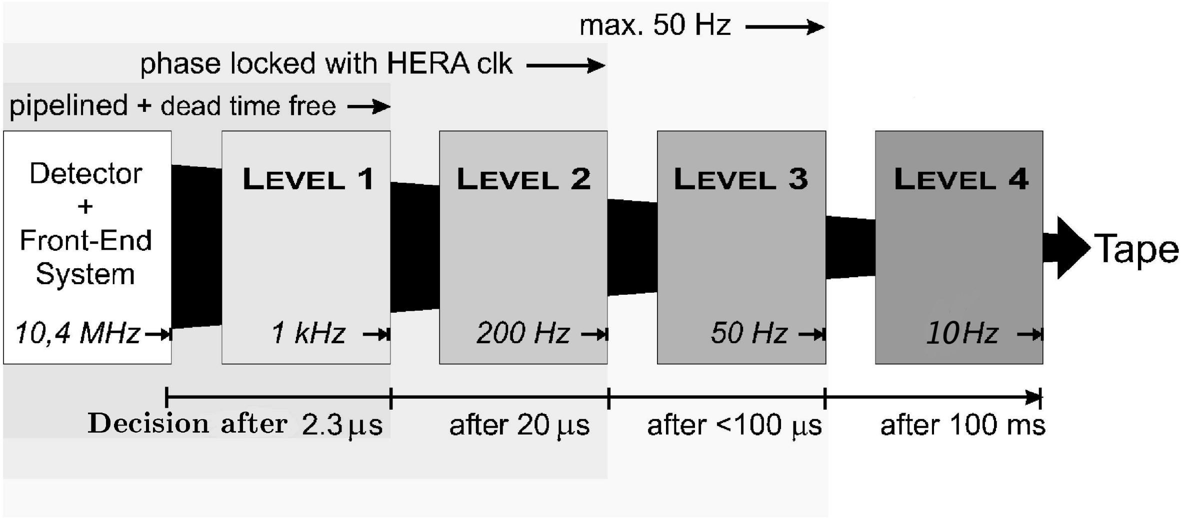

Figure 2.9: *A schematic view of the trigger levels. The input and output rates as well as the time limit of every trigger level are illustrated. The first level trigger must come to a trigger decision within 2.3 μs. It reduces the input rate of 10.4 MHz to $\approx$ 1 kHz. Clear non-ep events are rejected in an early stage of the trigger.*

2.6 H1 Trigger System

The majority of the events seen by the H1 detector are non-*ep* interactions which outnumber *ep* interactions by a factor 10^4 depending on beam conditions[28]. The rate at which events can be written to tape and stored is limited to 10 Hz and so a decision making process is necessary to reduce the input rate of 10.4 MHz which corresponds to the bunch crossing (BC) rate. A complete readout of the detector necessarily involves dead-time – the time for which the detector is effectively “blind.” The goal of the H1 trigger system therefore is to separate out interesting *ep* physics events while keeping dead-time to a minimum.

The trigger system is divided sequentially into four trigger levels (L1-L4) which form the "pipeline“ as shown schematically in figure 2.9. As an event progresses down the pipeline, more time is allocated to make a decision as the algorithms become more complex combining more precise detector information. Events that make it through the pipeline get written to tape for permanent storage.

The First Level Trigger (L1)

Many subdetectors provide L1 trigger information to the central trigger control (CTC) in the form of trigger element bits (TE). A subtrigger (ST) is a logical combination of the TEs from various subdetectors which characterize a particular *ep* event signature. There are 128 STs which reflect the physics interest of the experiment. The CTC evaluates each of the STs and registers an L1KEEP decision (“true” or “false”) based on the outcome. As the CTC must register an L1KEEP decision every bunch crossing, each subdetector stores its data in a pipeline buffer. The length of the buffer limits the length of processing time for an event to 2.3 μs. A positive L1KEEP decision stops the buffer; dead-time begins. L1 reduces the event rate from 10.4 MHz to 1 kHz.

The Second Level Trigger (L2)

The L2 trigger system gathers information from the different subdetectors and processes the event in greater detail. The tracker reconstructs rough tracks (L2FTT) and the LAr and SPACAL calorimeters produce L2 TEs based on pre-programmed topologies (L2TT). Neural networks (L2NN)[29] trained with samples of *ep* physics and background events are also used to produce L2 TEs. The L2 trigger system must decide within 20 μs whether or not to reject the event. If the event is to be rejected, the central trigger restarts the pipelines. In the case of the event being kept, readout of the $\approx$270 000 channels of the H1 detector begins. The event rate is reduced to 200 Hz at the end of L2.

The Third Level Trigger (L3)

The L3 trigger system uses the Fast Track Trigger (FTT, section 2.7) tracks and information from other subsystems to search for exclusive final states and to verify the L1 and L2 trigger decisions. In the case of an L3REJECT, the detector read out is immediately aborted. L3 makes a decision within 100 μs and realizes an output rate of 50 Hz. The third level trigger became active in the beginning of 2006.

The Fourth Level Trigger (L4)

This final trigger level performs the full reconstruction and classification of the event. Once all raw information from the subdetectors are gathered, the pipelines are restared thus terminating the dead-time, and full reconstruction begins using the software H1REC. Events not allocated to an *ep* physics class are rejected apart from 1% for monitoring purposes. Events are written to tape at a rate between 5-10 Hz on POT files (Physics Output Tape – raw and reconstructed information @ 150 kB/event) and DST files (Data Summary Tape – reconstructed information @ 20 kB/event). The DST files serve as the starting point for physics analyses.

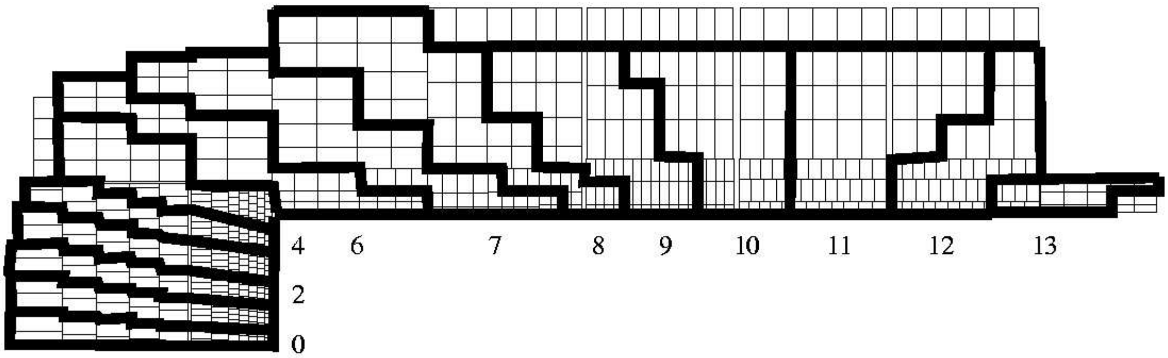

Figure 2.10: *Definition of the Big Towers (BTs) in the Liquid Argon Calorimeter.*

2.7 Neutral Current Triggers

In this section, the trigger elements and subtriggers relevant to this analysis are described.

Liquid Argon Calorimeter

The signature of a high Q^2 NC event is a deposition of energy in the EM part of the LAr calorimeter due to an energetic electron at large scattering angles. Such a signature is detected at the trigger level and is used as a positive condition for keeping the event. The signals from the 45000 cells of the calorimeter are summed up[30] into 256 big towers (BTs). The big towers are geometrically oriented to match the features of a genuine ep event where particles originate from the vertex at the nominal interaction point and deposit their energies in the calorimeter.

For the purpose of triggering, 16 neighbouring cells of the LAr calorimeter are grouped together into Trigger Cells (TCs). These TCs are further grouped into Trigger Towers (TTs). The analog signal of the trigger towers are summed and then digitized using FADCs (flash analog to digital converter). These FADCs are then summed into Big Towers (BTs). The BTs are grouped into 14 BT sectors in θ, figure 2.10. Each sector has either 8, 16 or 32 BTs in ϕ depending on the sector. Thresholds are introduced to suppress electronic noise and background.

The two L1 LAr TEs used in this analysis are `LAr_electron_1` and `LAr_electron_2` which corresponds to two sets of thresholds, table 2.1. The threshold values depend on the sector of the big tower in question. Each big tower sector corresponds to a range in the z-coordinate of the impact position of the electron on the surface of the LAr calorimeter, z_{im}, and this is also indicated. The `LAr_electron_2` thresholds are less than the

BT Sector	z_{im} range [cm]	`LAr_electron_2` [FADC count]	`LAr_electron_1` [FADC count]
0	$z_{im} = 294.4$	248	256
1	$z_{im} = 294.4$	248	256
2	$z_{im} = 294.4$	248	216
3	$z_{im} = 294.4$	248	144
4	$z_{im} = 294.4$	48	96
5	$287.55 \leqslant z_{im} \leqslant 294.4$	32	72
6	$199.4 \leqslant z_{im} < 287.55$	32	62
7	$135.15 \leqslant z_{im} < 199.4$	28	48
8	$88.45 \leqslant z_{im} < 135.15$	35	48
9	$45.95 \leqslant z_{im} < 88.45$	35	48
10	$-3.35 \leqslant z_{im} < 45.95$	35	48
11	$-64.1 \leqslant z_{im} < -3.35$	35	48
12	$-119.35 \leqslant z_{im} < -64.1$	35	48
13	$z_{im} < -119.35$	50	48

Table 2.1: *The* `LAr_electron_2` *(s75) and* `LAr_electron_1` *(s67) thresholds for the 14 Big Tower Sectors. The range in the z-coordinate of the impact position of the electron on the surface of the LAr calorimeter z_{im} for the various BT Sectors are also indicated. The energy thresholds are given in FADC counts where 10 FADC Counts ≡ 1 GeV.*

`LAr_electron_1` threshholds, apart from the very forward regions and sector 13 where it is 0.2 GeV less. A maximum threshold of ≈ 25 GeV is found in the very forward regions where noise levels are high. The `LAr_electron_n` (n=1,2) TE is set if one of the big towers records an electromagnetic energy deposit beyond its respective threshold.

The LAr calorimeter also provides the L2 `LAr_electron` TE which is a topological trigger.

Central Jet Chamber (CJC)

The dcrϕ trigger utilizes signals from the CJCs to reconstruct track candidates using seven layers of wires from CJC1 and three layers from CJC2[28]. In this analysis the `DCRPh_THig` TE is used which fires if at least one track with transverse momentum greater than 800 MeV is found.

To cope with the increased background which accompanied the 2000 luminosity upgrade as well as increase the trigger efficiency, the Fast Track Trigger (FTT)[31] was developed and implemented in January 2005 replacing the dcrϕ trigger. Using the signals from selected wires from both the inner and outer CJCs that form “trigger groups”, track segments are built and later linked into tracks. The trigger decision is based on the track multiplicity and transverse momenta of the individual tracks. The FTT trigger element relevant to this

	$r \leqslant 1$	$r > 1$	$r > 2$	$r > 4$
`CIP_sig`	0	1	2	3

Table 2.2: *The CIP significance* `CIP_sig` *as a function of the ratio* r *of central to background tracks.*

analysis is the level I `FTT_mul_Td>0` which fires if at least one track with transverse momentum greater than 900 MeV is found. The FTT has a much more precise track counting and better pt-resolution than the dcrϕ trigger.

Central Inner Proportional (CIP) Chamber

In this analysis, the CIP is used in providing the following level I TEs:

- **Significance of tracks from the central region,** `CIP_sig` : `CIP_sig` can take integer values between 0 and 3 depending on the ratio r of the number of central tracks (N_{cen}) to the number of background tracks (backward N_{bwd} + forward N_{fwd}) detected by CIP:

  $$r = N_{cen}/(N_{bwd} + N_{fwd})$$

  The values assumed by `CIP_sig` depending on r are given in table 2.2.

- **Multiplicity information,** `CIP_mul`: The CIP multiplicity `CIP_mul` takes integer values between 0 and 7 for run numbers $R < 372641$ and between 0 and 15 for later runs. It is determined by comparing the total number of tracks N_{cip} in all regions ($= N_{cen}+N_{bwd}+N_{fwd}$) to 8 or 16 thresholds, depending on the run number. `CIP_mul` is ascribed a value depending on the largest threshold exceeded.

  Beam associated background has usually small significances and large multiplicities. This can be exploited as a veto condition in the subtrigger definitions.

- **T0 information,** `CIP_T0`, `CIP_T0_nextbc`: The CIP detector is well suited to determine in which bunch crossing an event occurred. The `CIP_T0` TE is set to 1 if at least one track is identified in the central region and so provides information as to which bunch crossing the event came from. The value of this TE is given to the previous bunch crossing as the `CIP_T0_nextbc` TE.

Time-of-Flight System (ToF)

The Time-of-Flight system [32, 33] uses several subdetectors placed at various locations along the beam line relative to the main detector to detect particles originating from the proton beam, electron beam and *ep* interactions. The distinction between particles originating from background processes such as beam-wall interactions of the proton beam or synchrotron radiation from the electron beam, and particles originating from *ep* processes is made by using the time the particle was detected relative to the *ep* bunch crossing time. A time window of 96 ns, the time between two bunch crossings, is first defined. In the case of the Backward ToF detector (BToF), a scintillator located at $z \approx -3.3$ m, particles produced from proton beam induced background events arrive first, after which particles from the *ep* interaction and electron beam are detected. The 96ns time window is divided into a background (BG), interaction (IA) and global (Gl) window from which corresponding trigger bits are defined: BToF_BG, BToF_Gl and BToF_IA. These bits form level I trigger elements and are used to *veto* events in the context of part of a physics subtrigger definition. Apart from the BToF, other ToF subdetectors used in this analysis are the SPACAL ToF (SToF), Vetowall and Forward Interaction Timing (FIT).

Neutral Current Subtriggers

The subtriggers used in this analysis are s67 and s75. The definition of each subtrigger changes with time as more efficient TEs become available or as more efficient combinations of existing TEs are discovered. One subtrigger definition valid at a particular period of data taking is provided for s67 and s75 below.

s67 Definition – Run : 372718 Date : 21/02/04

L1:
(LAr_electron_1) && (CIP_T0||(LAr_T0&&!CIP_T0_nextbc)) &&
(!VETO_BG&&!BToF_BG&&!SToF_BG) && (FIT_IA||!FIT_BG) &&
(!(CIP_mul>7&&CIP_sig==0))

s75 Definition – Run : 492559 Date : 01/01/07

L1:
(LAr_electron_2) && (CIP_T0&&(CIP_sig>0)) && (FTT_mul_Td>0) && (!VETO_BG)
&& ((!(BToF_BG&&BToF_Gl&&(!BToF_IA))) && (!SToF_BG)) && (FIT_IA||(!FIT_BG))
&& (!((CIP_mul>7)&&(CIP_sig==0)))

L2:
(LAr_electron)

The composition of each subtrigger is explained in some detail in sections 6.2 and 7.1

where efficiency studies are presented.

Chapter 3

Simulations and Corrections

To correct for effects resulting from geometrical acceptance, inefficiency and resolution requires a firm understanding of the detector. To correct for radiative effects requires a firm understanding of physics. This knowledge is expressed in the form of a Monte Carlo (MC) simulation, an indispensable tool used in high energy physics.

3.1 Monte Carlo Simulations

It is difficult to claim to have a thorough understanding of a detector without first using a detector simulation. For example, the energy resolution of the scattered electron cannot be known using only data, since the *true* energy is never known. Instead of comparing to the true energy then, one can use an independent reference which is insensitive to the electromagnetic calorimeter response (section 5.3). In this way it is possible to check the agreement between the reconstructed energies in the data and the simulation to this reference. If this agreement is good, the energy resolution in data may be regarded as corresponding to that of the simulation.

If it can be shown that the distributions of the simulation are in good agreement to those in the data by means of *control plots*, then the real power of simulations can be exploited – the power to *correct*. Because the behavior of the simulation well mimics those in the data, effects due to acceptances, efficiencies, resolution as well as radiative effects can be corrected for in producing the measurement.

Event generators are ambitious computer programs that use our best knowledge of physics to produce events with the final state completely defined. This by itself is no easy task, for in the ideal case, an ensemble of MC generated events would reproduce what would be found in nature. At the end of the MC generating process is a set of known particles with their four-momenta completely specified.

Just as detector simulation can correct for detector effects, so too can MC generators correct for *physics* effects. For example, in data, it may be impossible to know if a particular event has initial state radiation and in what amount, even given a perfect detector. However, if the simulation has radiative effects built in, then the simulation can be used to make radiative corrections. Detector simulations if handled properly are indeed powerful.

Finally, a correction is just that – a correction. It is the physicist's assertion that *both* physics and simulation are understood well enough to make the correction to the data. The correction need not be perfect but is usually given with an estimated uncertainty; this uncertainty is then propagated as an error to the measurement.

3.2 Generators

Signal Generator

DIS events are generated using the DJANGO Monte Carlo simulation program[34] which is based on LEPTO[35] for the hard interaction and HERACLES[36] for single photon emission off the lepton line and virtual EW corrections. LEPTO combines $\mathcal{O}(\alpha_s)$ matrix elements with higher order QCD effects using the color dipole model as implemented in ARIADNE[37]. the JETSET program[38] is used to simulate the hadronisation process.

The input PDFs used to generate the events are taken from the H1 PDF 2000 fit.

Background Generators

The main sources of *ep* background relevant to this analysis are described in section 6.4; they are summarized below together with their respective MC generators:

- **Photoproduction** (γp): PYTHIA event generator[39] – Lund typed MC program simulating direct and resolved processes. Initial and final state QCD radiation is included; hadronization by JETSET. The partonic "hard" scattering cross sections are calculated in LO.

- **Low Q^2 DIS events**: No simulation used as the expected contribution is expected to be negligible compared to photoproduction.

- **Elastic QED Compton**: WABGEN event generator[40].

- **Lepton pair production** (l^+l^-): GRAPE event generator[41] – Includes contributions from the full set of LO electro-weak processes and approximates NLO effects by simulating initial and final state radiation. Includes electron, muon and tau production.

3.3 Detector Simulation

The response of the detector to the generated particles is simulated by the H1SIM-package[42] which is based on the GEANT-program [43]. The parameters used by this program were determined in test beam measurements and optimized during *ep* data taking. For energy response of the calorimeters, a fast parametrization for the development of electromagnetic showers and the electromagnetic part of hadronic showers is used – for the hadronic part of shower development the full simulation is used. Both data and simulated events are then subject to the same reconstruction program H1REC.

Chapter 4

The Nominal And High y Analyses

The sensitivity of the neutral current cross section to the longitudinal and $x\tilde{F}_3$ *structure functions at higher values of inelasticity* y *makes the* y *dependence of the cross section interesting to study. As high* y *kinematics are associated to low energies of the scattered electron, the detection of which forms the basis of any neutral current analysis, the detector response also becomes a function of* y*. As a result two dedicated analyses are defined. One analysis, the nominal analysis, corresponds to the high electron energy regime at low* y *or at very high* Q^2 *and is used to estimate the* $\tilde{F}_2$ *contribution to the high* y *cross section. The other analysis, the high* y *analysis, corresponds to the low electron energy regime, where energies can get to a few GeV.*

This chapter defines the nominal and high y *analyses and lays out in very broad terms the basic features that distinguish the two. This provides an overview for what follows in subsequent chapters where the individual analyses are presented in some detail.*

For a given Q^2, the energy of the scattered electron E_e' decreases linearly with the inelasticity y according to:

$$E_e'(y) = \left(\frac{Q^2}{4E_e} + E_e\right) - (yE_e) \tag{4.1}$$

where $E_e = 27.6$ GeV, the electron beam energy. This y dependence is shown in figure 4.1 for Q^2 values of 56, 133 and 891 GeV^2. At very high y the electron energy can reach to a few GeV. The signature of a neutral current event is a compact electromagnetic energy deposition by the scattered electron. Lower electron energies are associated to increased levels of background contamination as the signature becomes easier for hadrons to fake. For $y > 0.9$ uncertainties of background corrections can become too large to produce cross section measurements of useful precision.

The high background at high y does not only have implications at the analysis level where the event is reconstructed at its best precision, but also at the trigger level. As

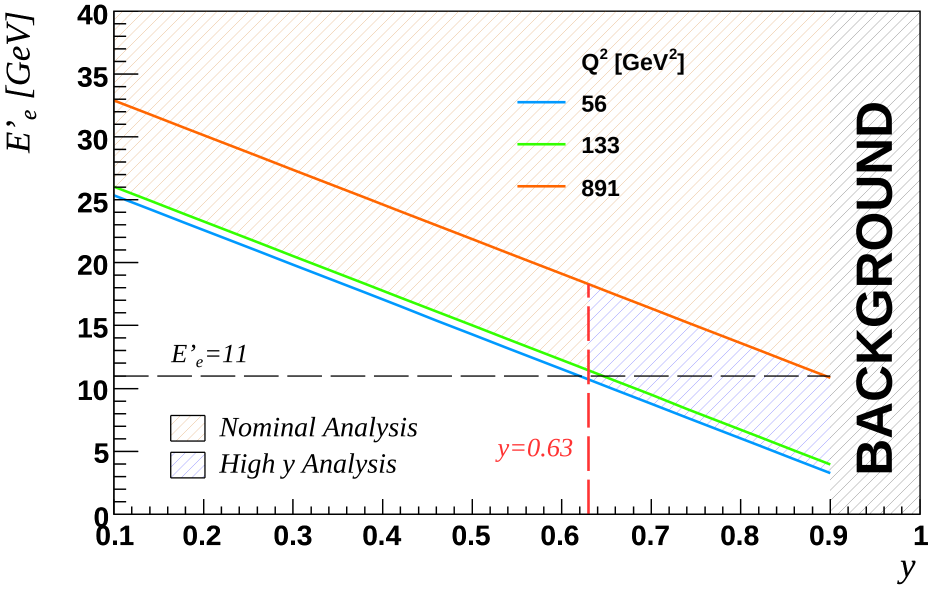

Figure 4.1: *The energy of the scattered electron* E'_e *as a function of* y *for fixed values of* Q^2*: 56, 133 and 891* GeV^2*. Also shown are the kinematic ranges that correspond to the nominal and high* y *analyses.*

high background causes increased trigger rates, two separate triggers are implemented - one designed for high electron energy events and the other designed for low electron energy events in the high y regime. The high energy trigger becomes close to 100% efficient for $E'_e \gtrsim 11$ GeV. The low energy trigger is accomplished by lowering the trigger energy threshold but also including added restrictions to cope with the anticipated increase in trigger rate. From figure 4.1(a) it can be seen that energies below 11 GeV are contained in the region $Q^2 \lesssim 891$ GeV^2. Therefore two analyses are performed in distinct parts of phase space:

- **Nominal Analysis** defined by the kinematics: $y < 0.63$ for $133 < Q^2 < 891$ GeV^2 and $y < 0.9$ for $Q^2 > 891$ GeV^2.
- **High y Analysis** defined by the kinematics: $0.63 < y < 0.9$, $56 < Q^2 < 891$ GeV^2.

The kinematic ranges corresponding to the two analyses are shown in figure 4.1.

In the chapters - “Event Selection I - The Nominal Analysis Event Selection” and “Event Selection II - The High y Analysis Event Selection” - treatment of the data from the two analyses are described.

Chapter 5

Alignment & Calibration of the LAr Calorimeter

As with any scientific instrument, the LAr calorimeter which measures both position and energy needs to be properly aligned and calibrated before any meaningful observation can be recorded. In this chapter the procedure used to align/calibrate the calorimeter is introduced. Resulting from this procedure is a set of alignment/calibration constants. Though the determination of these constants is not actually performed as part of this analysis, the uncertainties introduced by these constants into the electron polar angle, electron energy and hadron energy measurements are discussed. Also explained are the finders and algorithms which are used to reconstruct the electron particle candidate and hadronic final state.

5.1 LAr Electron Finder Algorithm

Particles entering the calorimeters deposit their energy in the cells which are grouped together into clusters. Electrons and photons deposit their energy in the form of characteristic electromagnetic showers. An algorithm which uses the cell's energy and position as input and which is sensitive to the properties of an electromagnetic shower is used to identify electron candidates. The LAr electron finder algorithm used to identify electrons in the LAr calorimeter[44], based on the work of Bruel[45], is now briefly described.

Clusters are preselected if more than 90% of their energy comes from the LAr calorimeter of which more than half must be in the EM part. The cluster energy is required to be > 2 GeV. Such clusters are *seeds* for electron candidates. From such a seed, a cone is then defined whose axis is the line joining the vertex to the center of the cluster. The cone begins at a point 1 m from the cluster center, opens at 7.5° and ends at the first HAD layer. Clusters with more than half of their energy within this cone are merged to the seed. At the end of the procedure the merged clusters form an electron candidate.

At this point cuts are applied to the candidates based on estimators which are characteristic of electromagnetic showers. These cuts limit:

- the transverse radius of the cluster
- the amount of energy in the cluster outside the EM sections
- the amount of energy in the cluster outside the hot core (most energetic neighbouring cells).

The actual limits depend on the polar angle of the electron candidate. In order to test for isolation of the cluster to prevent energy deposition from jets being misidentified as electrons, the energy of all clusters whose distance to the electron is less than 0.25 in $\eta\phi$ are summed into the quantity E_{iso}. Here η is the pseudo-rapidity defined as $-ln(tan(\theta/2))$ and ϕ the azimuthal angle. The candidate is then considered isolated if:

- more than 98% of E_{iso} is due to the electron candidate OR
- more than 95% of E_{iso} is due to the electron candidate providing the amount of hadronic energy in the cone not due to the candidate is less than 0.3 GeV.

Candidates that are isolated which have a $p_t > 1$ GeV and comprises > 3 calorimeter cells are then flagged as electrons. If there are many electrons in an event, the one with the highest p_t is flagged as the scattered electron.

5.2 Electron Polar Angle

The laboratory frame of reference of the H1 Detector is defined by the tracking system. The LAr Calorimeter is designed to be installed at a set position relative to the tracker called its *nominal* position. After the installation process, the calorimeter will not be exactly in its nominal position and so cell and cluster positions need to be corrected. The procedure of extracting the correction is termed *alignment*[10] and is explained briefly here.

By considering the calorimeter as a whole entity, it may be “off” its nominal position by a rotation around the x, y and z axes together with a translation along the x, y and z axes. Let the rotation be characterized by the angles α, β and γ around the x, y and z axes respectively, and the translation characterized by the displacements ΔX, ΔY and ΔZ along the x, y and z directions. The new position of the calorimeter may be regarded as the effect of a transformation $\mathcal{T}$ characterized by the 3 given angles and 3 given displacements. A nominal position on the calorimeter (x,y,z) will be mapped to its

Alignment Constant	Value
α	0.0 mrad
β	-0.9 mrad
γ	0.0 mrad
ΔX	+0.14 cm
ΔY	-0.40 cm
ΔZ	0.00 cm

Table 5.1: *The alignment constants of the LAr calorimeter[10].*

aligned position (x',y',z') by $\mathcal{T}$ according to:

$$x' = x'(x, y, z, \Delta X, \beta, \gamma) \tag{5.1}$$

$$y' = y'(x, y, z, \alpha, \Delta Y, \gamma) \tag{5.2}$$

$$z' = z'(x, y, z, \alpha, \beta, \Delta Z) \tag{5.3}$$

where the functions $x'(x, y, z, \Delta X, \beta, \gamma)$, $y'(x, y, z, \alpha, \Delta Y, \gamma)$, and $z'(x, y, z, \alpha, \beta, \Delta Z)$ define the transformation $\mathcal{T}$. See [10] for the functional form of x', y' and z'.

The extraction of these 6 parameters (α, β, γ, ΔX, ΔY, ΔZ) is performed by utilizing the difference between the scattered electron position as measured using the calorimeter (subscript "cl") and its position as measured using the tracker (subscript "tr"). By considering the difference of the azimuthal angle ($\Delta\phi = \phi_{cl} - \phi_{tr}$) and polar angle ($\Delta\theta = \theta_{cl} - \theta_{tr}$) of the electron as a function of ϕ_{tr} for fixed ranges in z, the 6 parameters are determined. These 6 parameters are the alignment constants. As an indication of the size of these constants, a particular set of constants is given in table 5.1 applicable for a given period of running.

The poor hit resolution of the CJCs in the z direction results in a poor resolution of the electron polar angle when estimated using the electron track (θ_{tr}). Therefore in this analysis, the electron polar angle θ_e is taken from its cluster in the LAr calorimeter:

$$\theta_e = \theta_{cl}$$

In order to assign a systematic uncertainty on θ_e, θ_{cl} is compared to θ_{tr} in different geometrical regions of the detector using events from the nominal analysis. A systematic uncertainty of $\Delta\theta_e = 3$ mrad is assigned based on the agreement between data and signal MC distributions.

$\theta_{cl} - \theta_{tr}$ distributions for events from the high y analysis are shown in figure 5.1(a) for the e^- period. Distributions shown are for the data and signal MC (central value of θ_e as well as ±3 mrad shifts). The MC describes the data within the given uncertainty.

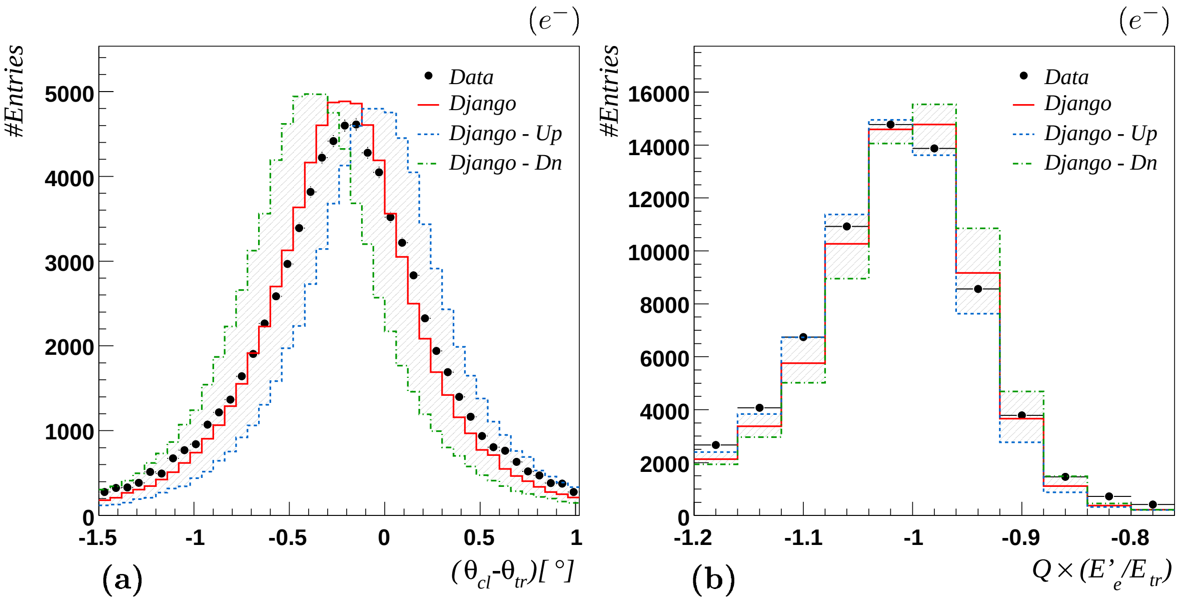

Figure 5.1: *(a) The difference between the electron polar angle as measured from the calorimeter (θ_{cl}) to its value as measured from the associated track (θ_{tr}). (b) The ratio of the electron energy as measured from the calorimeter (E_{cl}) to its value as measured from the tracker (E_{tr}) times the charge of the electron beam (Q). Both plots are for the high y analysis, shown for the e$^-$ period. Included are the distributions in data and signal MC (central value of the calorimeter (a) energy and (b) polar angle as well as $+1\sigma$ ("Up") and -1σ ("Dn") shifts on the energy and polar angle).*

5.3 Electron Energy

The energy of the scattered electron can be expressed in terms of its electron polar angle θ_e and the inclusive hadron angle γ_h(section 5.4):

$$E_{da} = \frac{2E_e \sin\gamma_h}{\sin\gamma_h + \sin\theta_e - \sin(\gamma_h + \theta_e)} \tag{5.4}$$

where the subscript "da" denotes "double angle" and alludes to the two angles used in the calculation. E_e is the incident electron energy of 27.6 GeV. From equation 5.4 it is evident that E_{da} is insensitive to the electron energy measurement using the LAr calorimeter E'_e.

The calibration of E'_e is performed by comparing the ratio E'_e/E_{da} for a subset of events from the nominal analysis in the region of low y[10]. The relative uncertainty on the electron energy measurement $\delta E'_e$ is determined by considering the level of agreement between between the E'_e/E_{da} distributions for data and signal MC as a function of the z-coordinate of the electron impact position on the surface of the LAr calorimeter z_{im}. The uncertainties are summarized in table 5.2 and ranges between 1-5% from the backward to forward regions of the calorimeter.

z_{im} range [cm]					$\delta E'_e$ [%]
		z_{im}	$\leqslant$	-151.5	1
-151.5	$<$	z_{im}	$\leqslant$	24.0	1
24.0	$<$	z_{im}	$\leqslant$	112.0	2
112.0	$<$	z_{im}	$\leqslant$	201.25	3
201.25	$<$	z_{im}			5

Table 5.2: *The relative uncertainty* $\delta E'_e$ *on the electron energy scale.*

To check that the quoted uncertainties are valid in the region of the high y analysis, the calibrated electron energy E'_e is compared to the energy measurement of the track associated to the electron E_{tr}. The ratio E'_e/E_{tr} (times the electron charge Q) is shown in figure 5.1(b) for the data and signal MC (central value of E'_e as well as $\pm 1\sigma$ shifts on the electron energy scale). The data is well described by the MC within the uncertainty.

5.4 Hadronic & Noise Energy

Hadronic Calibration

The algorithm which defines the hadronic final state is referred to as *Hadroo2*[46] and uses as input both tracks and clusters. Since a charged particle produces a track in the tracker as well as cluster(s) in the calorimeter, two potential particle candidates for the particle can result. The inclusion of both candidates in the hadronic final state would lead to double counting. By comparing the expected energy resolution associated to the track with that associated to the cluster, either the track particle candidate or cluster particle candidate is chosen. Where the cluster is chosen the track energy is suppressed. In the case the track is chosen, the cluster energy is partially or fully suppressed. What results at the end of the algorithm is a set of particles of which the hadronic final state (all particles except the scattered electron) comprises.

From the hadronic final state (HFS) it is useful to define the quantities Σ_h, P_t^h, and γ_h:

$$\Sigma_h = \sum_i (E_i - p_{zi}) \tag{5.5}$$

$$P_t^h = \sqrt{(\sum_i p_{xi})^2 + (\sum_i p_{yi})^2} \tag{5.6}$$

$$\tan\frac{\gamma_h}{2} = \frac{\Sigma_h}{P_t^h} \tag{5.7}$$

where E_i, p_{xi}, p_{yi} and p_{zi} are the energy and momentum components of the ith particle.

Σ_h is the longitudinal momentum of the HFS and P_t^h is its transverse momentum; in the QPM, γ_h is the polar angle of the struck quark.

The calibration of the hadronic final state is performed using events from the nominal analysis containing only one jet and one electron. The reference quantity is the transverse momentum of the hadronic final state calculated using the double angle method P_t^{da}:

$$P_t^{da} = \frac{2E_e}{\tan\frac{\theta_e}{2} + \tan\frac{\gamma_h}{2}}. \tag{5.8}$$

P_t^{da} is independent of the LAr energy calibration to a good approximation. The ratio $P_{tbal} = P_t^h / P_t^{da}$ as a function of P_t^{da} for given ranges of γ_h is used to determine the jet calibration constants. The calibration constants are applied only to the cluster particle candidates of the hadronic final state since the tracks are already calibrated. For a full description of the calibration procedure, see[46].

The uncertainty on the hadronic energy scale is obtained by comparing distributions of P_{tbal} in the data to those of signal MC using events from the nominal analysis. It can be shown that the agreement of the means $\langle P_{tbal}^{DATA}\rangle / \langle P_{tbal}^{MC}\rangle$ is within 2%, taken as the hadronic calibration uncertainty.

Noise Suppression

The contribution of LAr calorimeter noise to the hadronic final state becomes increasingly significant at lower values of inelasticity y where the hadronic final state goes very forward. An uncertainty of 10% on the amount of energy identified as LAr calorimeter noise [10] is used.

In the high y analysis the noise contribution is negligible since the HFS is scattered towards the central part of the detector. Since the event kinematics are calculated purely from the scattered electron (section 8.6), the role of the hadronic final state is limited to its contribution to the total longitudinal momentum $E - P_z$ of the event (HFS + scattered electron contribution) which has the cut $E - P_z > 35$ GeV (table 7.8). Figure 5.2 shows the $E - P_z$ distribution from the high y analysis for the e^+ period for data and signal MC (central value as well as the corresponding distribution for $\pm 1\sigma$ shifts on the hadronic energy scale). The data is within the uncertainty of the MC.

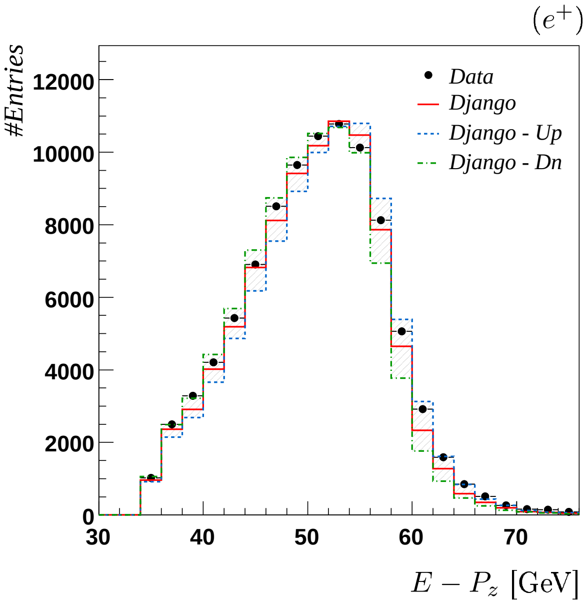

Figure 5.2: *The total longitudinal momentum $E - P_z$ distribution of the high y analysis, e^+ sample. Included are the distributions in data and signal MC (central value as well as $+1\sigma$ ("Up") and -1σ ("Dn") shifts on the hadronic energy scale).*

Chapter 6

Event Selection I - The Nominal Analysis Event Selection

Resolving signal events from background events requires an understanding of the various types of processes involved, as well as the detector response to these processes. This chapter lays out in a step by step fashion the method used to reduce the sample of data stored on tape having a significant amount of background to the final sample used to measure the cross section. An estimation of the various efficiencies as well as their use in correcting the simulation is also presented. A determination of the integrated luminosity for the e^+ *period of running is also explained. The chapter ends with control plots comparing the data (after background subtraction) to simulation (after all corrections are applied).*

6.1 NC Event Signature

Figure 6.1 shows a neutral current event as observed by the H1 detector. The incoming electron e travels in the negative z direction and collides with the incoming proton p travelling in the positive z direction. At the interaction point in the central part of the detector a vertex V at $z_{vtx} = 2.9$ cm is reconstructed by the tracker from the set of tracks shown. The scattered electron e' is clearly "visible" as it produces a track T as well as a high energy deposit C in the LAr Calorimeter, mainly in the EM section (green). The hadronic final state h comprises particles scattered mainly in the forward direction as seen by both the reconstructed tracks and the clusters in the calorimeter. In the $r\phi$ view, the scattered electron appears to be well balanced by the hadronic final state. As the detector covers most of the 4π solid angle, the total reconstructed longitudinal momentum[1] of 53.2 GeV is approximately equal to that before the interaction of 2×27.6 GeV. The kinematics

---

[1] Longitudinal momentum of a four-vector quantity is defined as the energy - z-component of the momentum.

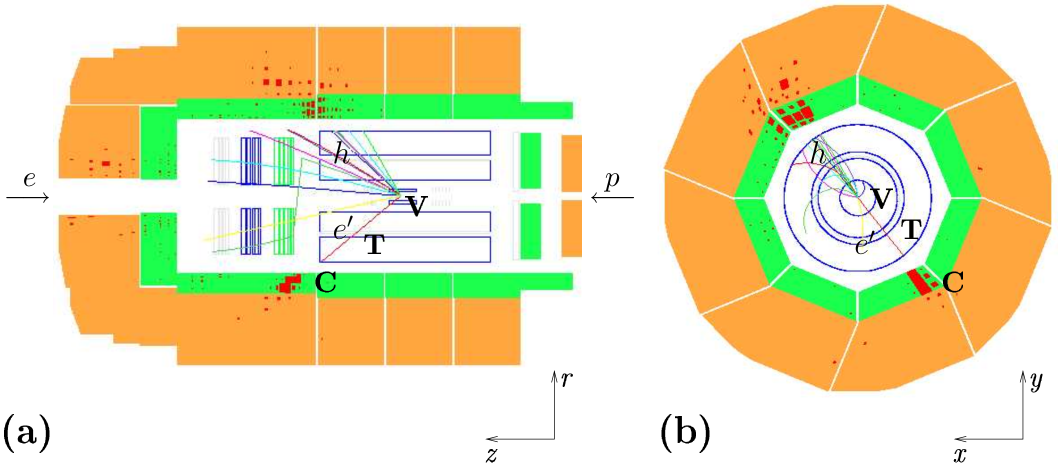

Figure 6.1: *A high Q^2 neutral current event in the (a) rz and (b) $r\phi$ planes with reconstructed kinematics $Q_e^2 = 10056$ GeV^2 and $y_e = 0.56$. The electromagnetic parts (EM) of the calorimeters are shown in green and the hadronic parts (HAD) in orange. The other detectors form the tracking system.*

of this event are $Q^2 = 10056$ GeV^2 and $y = 0.56$.

The cluster C is *the* signature of a NC event - it is used to reconstruct the scattered electron as well as to trigger the event.

6.2 Trigger

The main subtrigger used to select events for the nominal analysis is s67. For an event to fire s67 it must satisfy three Level 1 conditions simultaneously: the LAr Calorimeter condition, LAR, the timing condition, T0 and the veto condition VET. s67 is therefore defined logically as:

$$s67 \equiv LAR \ \ \&\& \ \ T0 \ \ \&\& \ \ VET. \tag{6.1}$$

with && representing the logical AND.

LAR & T0 Condition

The LAR condition requires the `LAr_electron_1` TE to fire, section 2.7. To measure the LAR efficiency ϵ_{lar}, a monitor sample is made by first removing the Subtrigger and Fiducial Volume cuts from the final selection, table 6.7. From the resulting sample, those events that fire s67 constitute the LAR monitor sample used to measure ϵ_{lar}.

As shown in section 7.2, the big towers can be fired by the electron (e-fired) or the hadronic final state (hfs-fired). As these two conditions are independent, the hfs-fired sample can be used to monitor the e-firing efficiency; similarly the e-fired sample can be used to monitor the hfs-firing efficiency. Suppose for the LAR monitor sample:

- n_{eo} = Number of events fired only by the electron *only*
- n_{ho} = Number of events fired only by the hfs *only*
- n_{eh} = Number of events fired by *both* the electron and the hfs
- n_s = Number of events fired which do not meet the classification criteria of being either e-fired or hfs-fired (see figure 7.11).

The e-firing efficiency ϵ_e can then be determined from:

$$\epsilon_e = \frac{n_{eh}}{n_{ho} + n_{eh}} \tag{6.2}$$

which can be used to deduce the total number of events N_{tot} (triggered + untriggered):

$$N_{tot} = \frac{n_{eo} + n_{eh}}{\epsilon_e} = (n_{eo} + n_{eh}) \frac{n_{ho} + n_{eh}}{n_{eh}} \tag{6.3}$$

from which the LAR triggering efficiency can be determined:

$$\epsilon_{lar} = \frac{n_{eo} + n_{ho} + n_{eh} + n_s}{N_{tot}} = \frac{(n_{eo} + n_{ho} + n_{eh} + n_s) n_{eh}}{(n_{eo} + n_{eh})(n_{ho} + n_{eh})} \tag{6.4}$$

As the various n's are independent, their statistical errors can be added in quadrature to get the statistical uncertainty of ϵ_{lar}.

Figure 6.2(a) and (b) show the LAR efficiency ϵ_{lar} for the e^- sample as a function of electron energy and polar angle before and after the Fiducial Volume cut, FV(t). Before the FV(t) cut is made, the trigger efficiency shows E_e' and θ_e dependencies. As a function of the electron impact position on the calorimeter – the z-coordinate (z_{im}) versus the ϕ-coordinate (ϕ_{im}) of the impact position – figure 6.3(a), ϵ_{lar} is close to 100% in most regions but suffers from inefficiencies in several localized parts of the calorimeter. Typically the inefficiencies are due to trigger cells switched off because of high noise or malfunctioning hardware. When these areas are removed as indicated by the hatched areas, the LAR efficiency becomes close to 100%, figure 6.2.

The removal of those regions of significant inefficiency constitutes the FV(t) cut. As some trigger cells are fixed during the course of running of the experiment, some regions are excluded only for some periods (red downward hatched areas); however other areas need to be removed for the entire data taking (black upward hatched areas). The FV(t) cut is therefore a function of time.

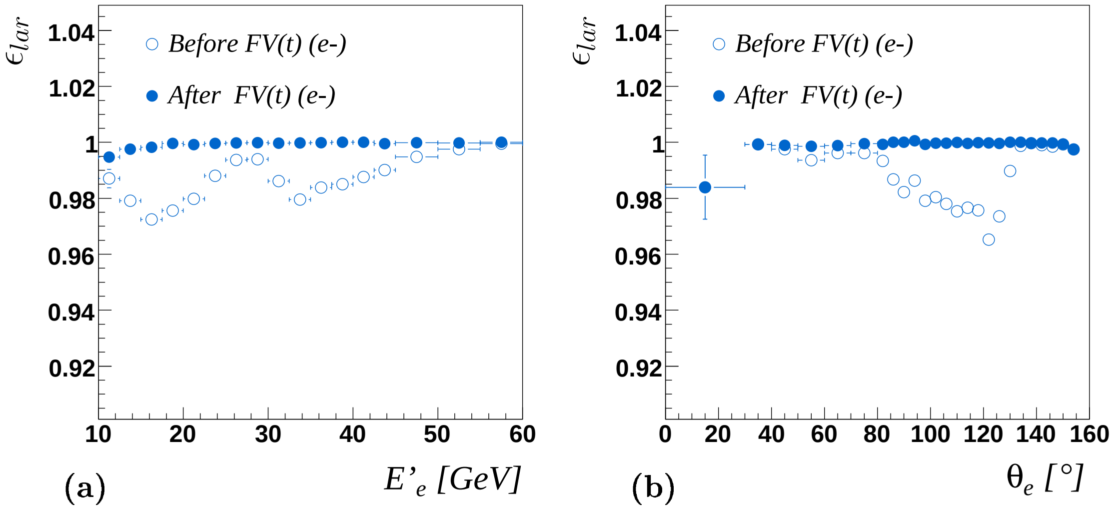

Figure 6.2: *The LAR efficiency ϵ_{lar} as a function of (a) electron energy and (b) electron polar angle for the e^- sample. For each plot, the efficiency is shown before and after the Fiducial Volume cut FV(t) is applied.*

Both the LAr calorimeter and the CIP selector deliver the T0 signals as part of the definition of s67. As these two detectors are independent, each can monitor the other in a similar way the e-fired and hfs-fired LAR conditions act as monitors for each other. The T0 efficiency ϵ_{t0} is therefore determined using equation 6.4 where the subscripts now refer to events where the T0 is fired by the LAr calorimeter *only* (n_{eo}), the CIP detector *only* (n_{ho}), the LAr calorimeter *and* CIP detector (n_{eh}) giving:

$$\epsilon_{t0} = \frac{(n_{eo} + n_{ho} + n_{eh})n_{eh}}{(n_{eo} + n_{eh})(n_{ho} + n_{eh})} \tag{6.5}$$

(n_s=0 as the event must be fired either by the LAr calorimeter or the CIP detector). If ϵ_{cal} is the T0 efficiency from the LAr calorimeter ($= n_{eh}/(n_{ho} + n_{eh})$) and ϵ_{cip} from the CIP($= n_{eh}/(n_{eo} + n_{eh})$), ϵ_{t0} can be rewritten in a more familiar form:

$$\epsilon_{t0} = \epsilon_{cal} + \epsilon_{cip} - \epsilon_{cal}\epsilon_{cip} \tag{6.6}$$

Figure 6.4(a) and (b) show ϵ_{t0} as a function of electron energy and electron polar angle respectively for the e^- and e^+ periods after the FV(t) cut; ϵ_{t0} is close to 100%.

Since both the LAR and T0 efficiencies are close to 100%, no correction is made to the MC. A systematic uncertainty of 1% on the combined efficiency $\epsilon_{lar} \times \epsilon_{t0}$ is quoted.

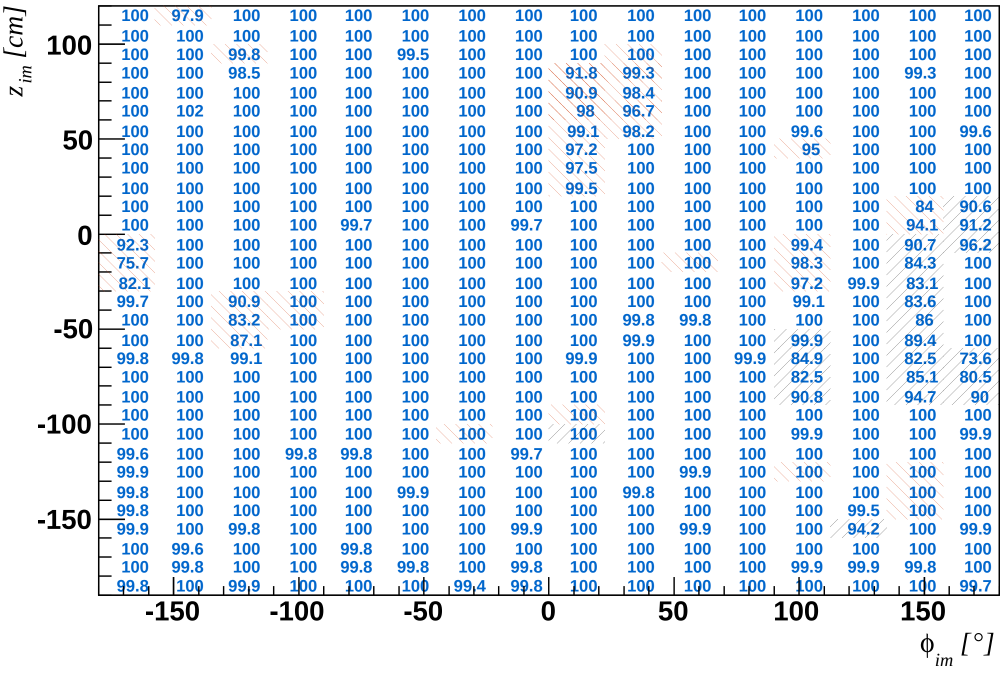

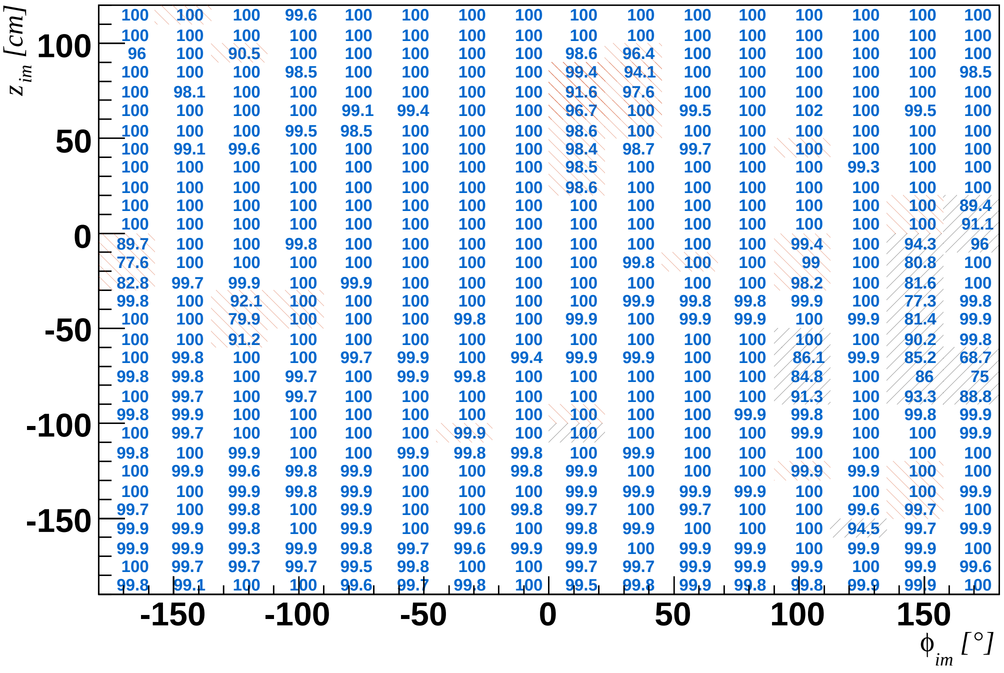

Figure 6.3: *The LAR efficiency ϵ_{lar} as a function of the electron impact position (z_{im} vs. ϕ_{im}). The hatched areas correspond to regions of low efficiency that are removed either for the whole analysis (black upward hatched) or for a particular interval of time (red downward hatched).*

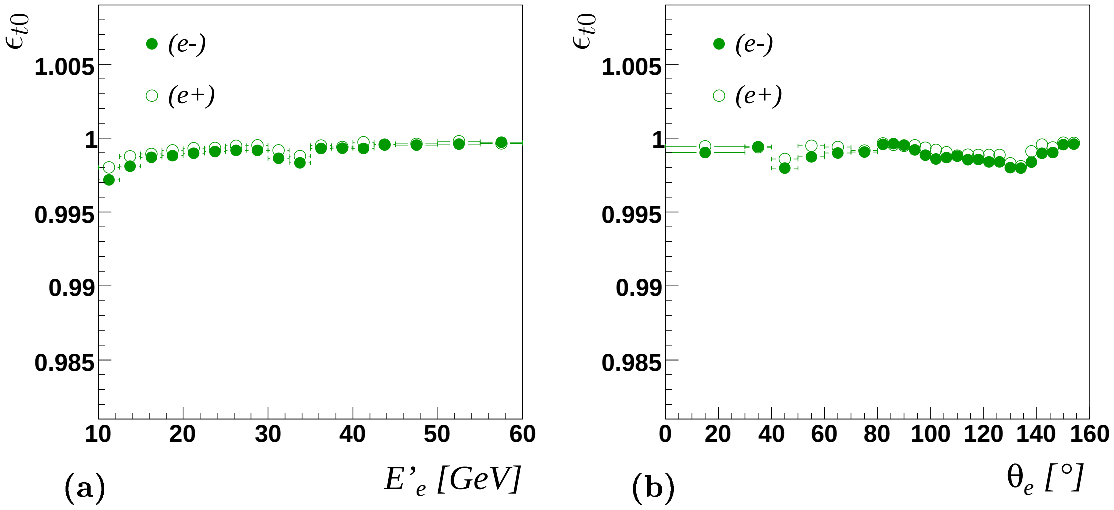

Figure 6.4: *The T0 efficiency ϵ_{t0} as a function of (a) electron energy and (b) electron polar angle for the e^- and e^+ samples. The efficiencies are shown after the Fiducial Volume cut is applied.)*

Veto Condition

The veto condition VET used in the definition of s67 is summarized in table 6.1 as a function of time. The trigger elements are explained in section 2.6. There are three contributions to the veto:

- Time of Flight (ToF) : Two monitor samples are used to measure ϵ_{tof} - Events triggered by s57 (which has no veto condition except for the run range R$\leqslant$382137 where ToF information is included) in the run range R>382137 (ϵ^{s57}_{tof}) and a sample composed of Bethe-Heitler events (ϵ^{bh}_{tof}). The ToF efficiencies from both samples are shown in figure 6.5 with their difference ($\Delta\epsilon = \epsilon^{s57}_{tof} - \epsilon^{bh}_{tof}$) and $\Delta\epsilon = constant$ fits over several run ranges. It can be seen that ϵ^{s57}_{tof} and ϵ^{bh}_{tof} are consistent with each other for most of the sample runs. Where there is a significant difference, it is used to estimate the systematic uncertainty.

- CIP : Monitored using s57.

- MUON : Monitored using s57. This condition was implemented in October 2006 (run number R=483314) to veto events where muons originating from non-*ep* background triggered the LAr calorimeter. The efficiency of the MUON condition is measured to be $\epsilon_{muon} = 100\%$.

Run No	VET
First Run	!VETO_BG && !BToF_BG && !SToF_BG && !(!FIT_IA && FIT_BG)
358934	!VETO_BG && !BToF_BG && !SToF_BG && !(!FIT_IA && FIT_BG) && `!(CIP_mul==7 && CIP_sig==0)`
372718	!VETO_BG && !BToF_BG && !SToF_BG && !(!FIT_IA && FIT_BG) && `!(CIP_mul>7 && CIP_sig==0)`
450139	!VETO_BG && !(BToF_BG&&BToF_Gl&&(!BToF_IA)) && !SToF_BG && !(!FIT_IA && FIT_BG) && `!(CIP_mul>7 && CIP_sig==0)`
483314	!VETO_BG && !(BToF_BG&&BToF_Gl&&(!BToF_IA)) && !SToF_BG && !(!FIT_IA && FIT_BG) && `!(CIP_mul>7 && CIP_sig==0)` && **!(CIP_mul==0&&Mu_BIEC)**

Table 6.1: *The VET condition as a function of time. The time of flight ToF contribution is written in* normal script , *CIP contribution in* `typed script` *and MUON contribution in* **bold script**.

Period	Efficiency[%]			
	ToF	CIP	MUON	VET
e^-	99.44±0.03[stat.]±0.42[sys.]	99.38±0.03[stat.]	N/A	98.83±0.42
e^+	99.52±0.01[stat.]±0.24[sys.]	99.61±0.02[stat.]	100.00±0.00[stat.]	99.13±0.24

Table 6.2: *Summary of the veto efficiencies for the* e^- *and* e^+ *periods.*

Table 6.2 summarizes the the ToF, CIP, MUON and VET ($\epsilon_{vet} = \epsilon_{tof}\cdot\epsilon_{cip}\cdot\epsilon_{muon}$) efficiencies for the e^- and e^+ samples. The VET efficiency is used as a correction to the MC.

6.3 Tracker Requirement

The requirement of a vertex within 0 ± 35 cm plays a significant role in limiting the amount of non-*ep* background in the sample. Figure 6.6 shows the z_{vtx} distribution for a luminosity run[25]. Events where particles originate from interactions at the collimators C5A and C5B are clearly visible. Such events are effectively rejected by the limiting the distance of the z_{vtx} to the nominal interaction point. Having a reconstructed vertex also allows for a more precise calculation of the event kinematics. The requirement of a track linked to

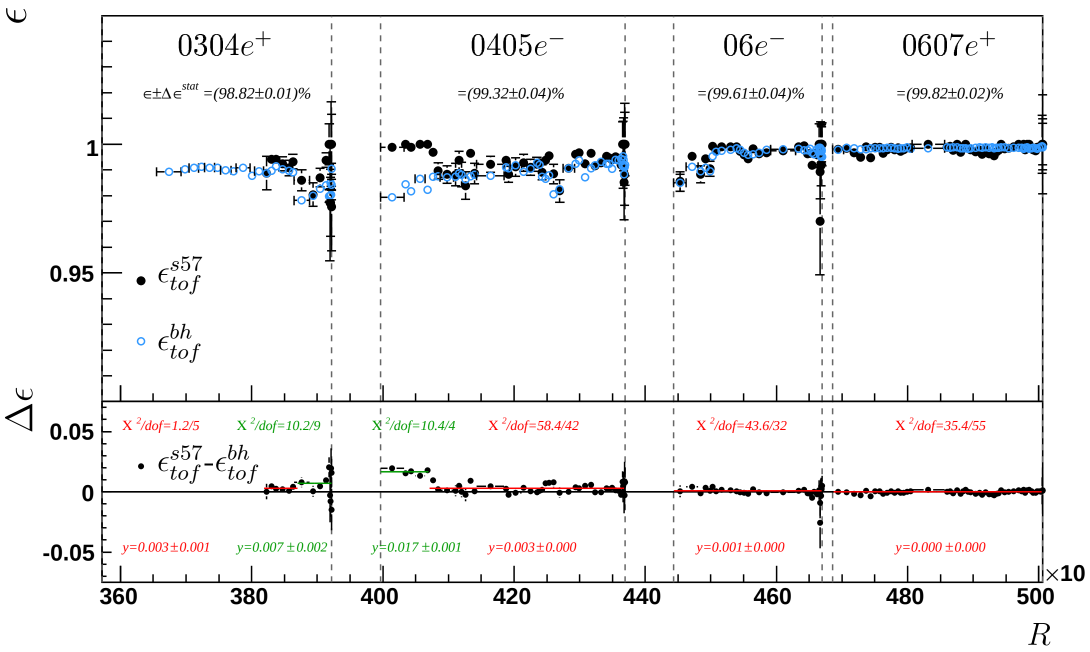

Figure 6.5: *(a) The ToF efficiency as a function of time (run number R) as determined from the S57 and Bethe-Heitler monitor samples. Indicated are the measured efficiency for each period (using ϵ^{bh}_{tof} for the 0304e^+ period and ϵ^{s57}_{tof} for later periods) with its statistical error. In the bottom plot the difference between the efficiencies of the two samples $\Delta\epsilon = \epsilon^{s57}_{tof} - \epsilon^{bh}_{tof}$ is plotted and $\Delta\epsilon =$ constant fits are made over the indicated run ranges.*

the electron candidate - *electron validation* - reduces the possibility of a photon or other neutral particles faking the electron. The vertex (VTX) and electron validation (VAL) requirements are closely related as the vertex position is used as a constraint in the fitting algorithm[47]. As such the vertex and electron validation requirements together constitute the tracker requirement (TRNA), that is:

$$TRNA \quad = \quad VTX \quad \&\& \quad VAL. \tag{6.7}$$

After the track finding and vertex fitting algorithm is completed, tracks that are successfully fitted to the vertex are termed DTRA tracks; those that are not are termed DTNV (section 2.4). There are 3 types of electron validation[48]:

- DTRA-validation where the distance of closest approach to the cluster d^{cls}_{ca} is limited to $d^{cls}_{ca} < 12$ cm to reduce photoproduction background[28].
- DTNV-validation where the distance of closest approach to the cluster d^{cls}_{ca} is limited to $d^{cls}_{ca} < 12$ cm and the distance of closest approach to the vertex (or beam-line

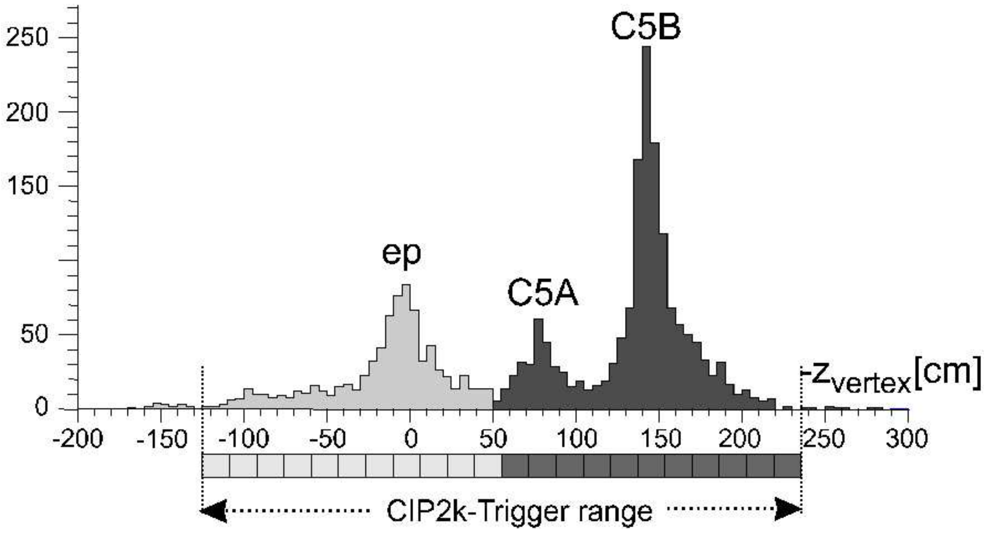

Figure 6.6: *Distribution of the reconstructed z position of the interaction vertex for a luminosity run. Peaks appear at the nominal vertex (0 cm) and at the position of the collimators C5A(-80 cm) and C5B (-145 cm)[25].*

where there is no vertex) d_{ca}^{vtx} is limited to $d_{ca}^{vtx} < 2$ cm.

- CIP-validation where there are more than 2 hits in the CIP detector associated to the electron.

The vertex reconstructed after the track finding and vertex fitting algorithm is completed is termed a CJC-vertex. It is also possible to reconstruct a DTNV-vertex using the DTNV track which validated the electron whose $z-$position is determined from the position at its d_{ca}^{vtx}. With this in mind there are 4 types of vertex-validation that are possible:

1. CJC-vertex with DTRA-validation.
2. CJC-vertex with DTNV-validation.
3. CJC-vertex with CIP-validation.
4. DTNV-vertex with DTNV-validation (the validation is true by default).

The TRNA tracker requirement (used in the nominal analysis) is summarized in table 6.3. If any of the 4 types of vertex-validation is met, the TRNA requirement is fulfilled; in addition if the polar angle of the electron is outside the tracker's acceptance (θ_e<30°) only a CJC-vertex is required (no validation).

Analysis	TrackerRequirement	
NominalAnalysis	TRNA	Any of: CJC-vertex with DTRA-validation CJC-vertex with DTNV-validation CJC-vertex with CIP-validation DTNV-vertex with DTNV-validation CJC-vertex with θ_e<30°

Table 6.3: *The TRNA tracker requirement.*

Period	$\langle r \rangle$[%]	Δ_r^{sys}[%]
e^-	99.30	2.0
e^+	99.38	2.0

Table 6.4: *The TRNA correction factors $\langle r \rangle$ applied to the MC together with its systematic uncertainty Δ_r^{sys}.*

TRNA Efficiency

In order to study the TRNA efficiency ϵ_{trna}, a monitor sample independent of the TRNA requirement yet background free is needed. This sample called the “clean sample” is obtained by removing the TRNA requirement from the final selection, table 6.7, and imposing the following additional cuts: $E'_e > 18$ GeV, $45 < E - P_z < 65$ GeV and $0.5 < P_{tbal} < 1.4$. By limiting the electron energy and ensuring a tight balance in longitudinal and transverse momenta characteristic of ep collisions, a sample with negligible background is obtained[28, 10].

Figure 6.7 show ϵ_{trna} for the e^- period as determined from the clean sample in data and signal MC as a function of y_e in $\log(Q_e^2)$ intervals corresponding to the cross section binning, section 8.1. In figure 6.8 the ratio r of the efficiency in data to that of MC is shown; the average value of r, $\langle r \rangle$ as obtained from the whole sample is also shown together with the quoted systematic uncertainty Δ_r^{sys} of 2%. It can be seen that this uncertainty together with the central value of $\langle r \rangle$ sufficienctly describes the level of agreement between data and MC. The same holds for the e^+ sample, figure 6.9. The MC therefore is corrected with a weighting $\langle r \rangle$ and the systematic uncertainty Δ_r^{sys} is propagated to the cross section measurement, table 6.4.

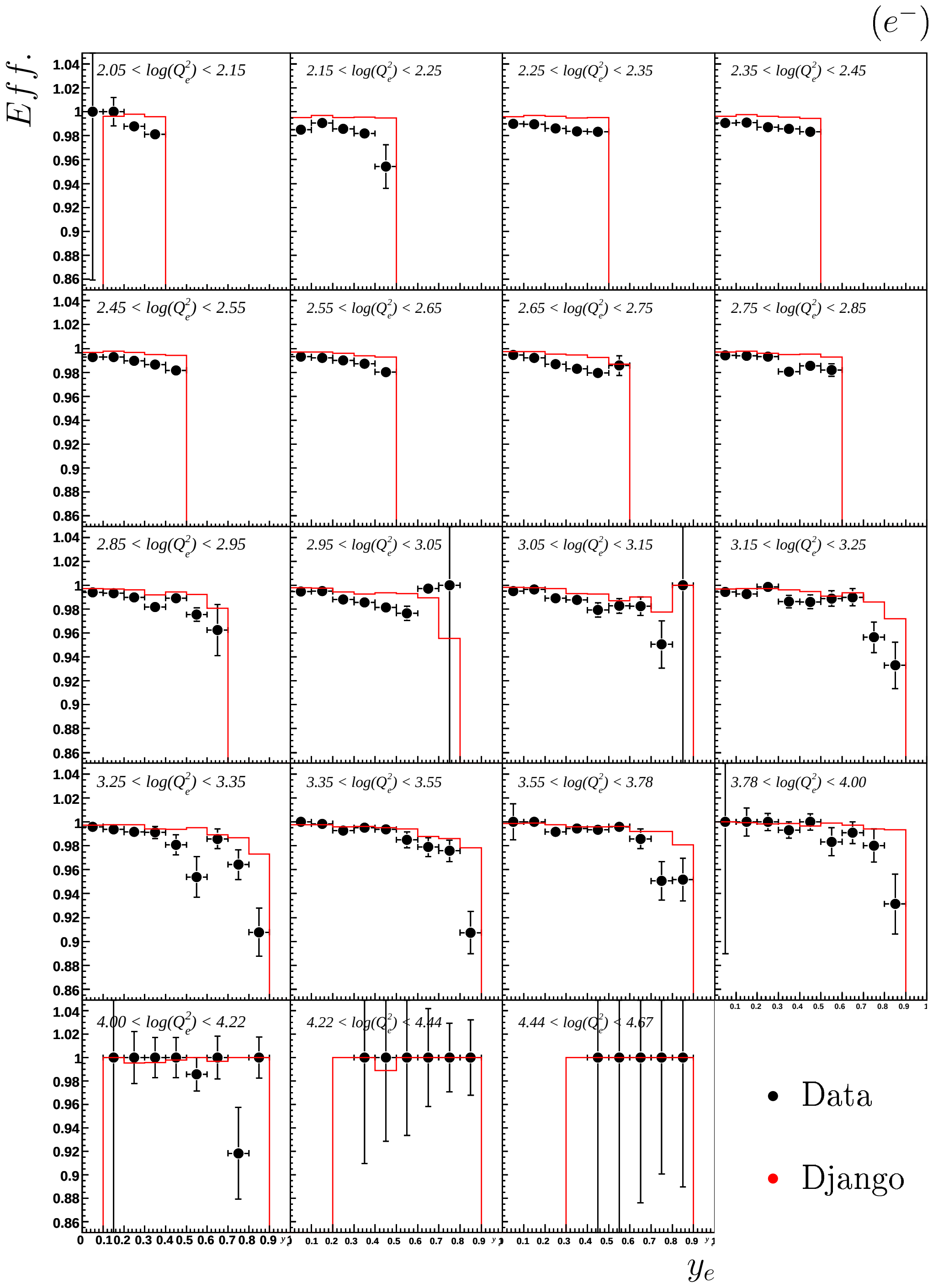

Figure 6.7: *The TRNA efficiency as a function of y_e in log(Q_e^2) intervals corresponding to the cross section binning, section 8.1. The efficiencies shown correspond to data and signal MC for the e^- period.*

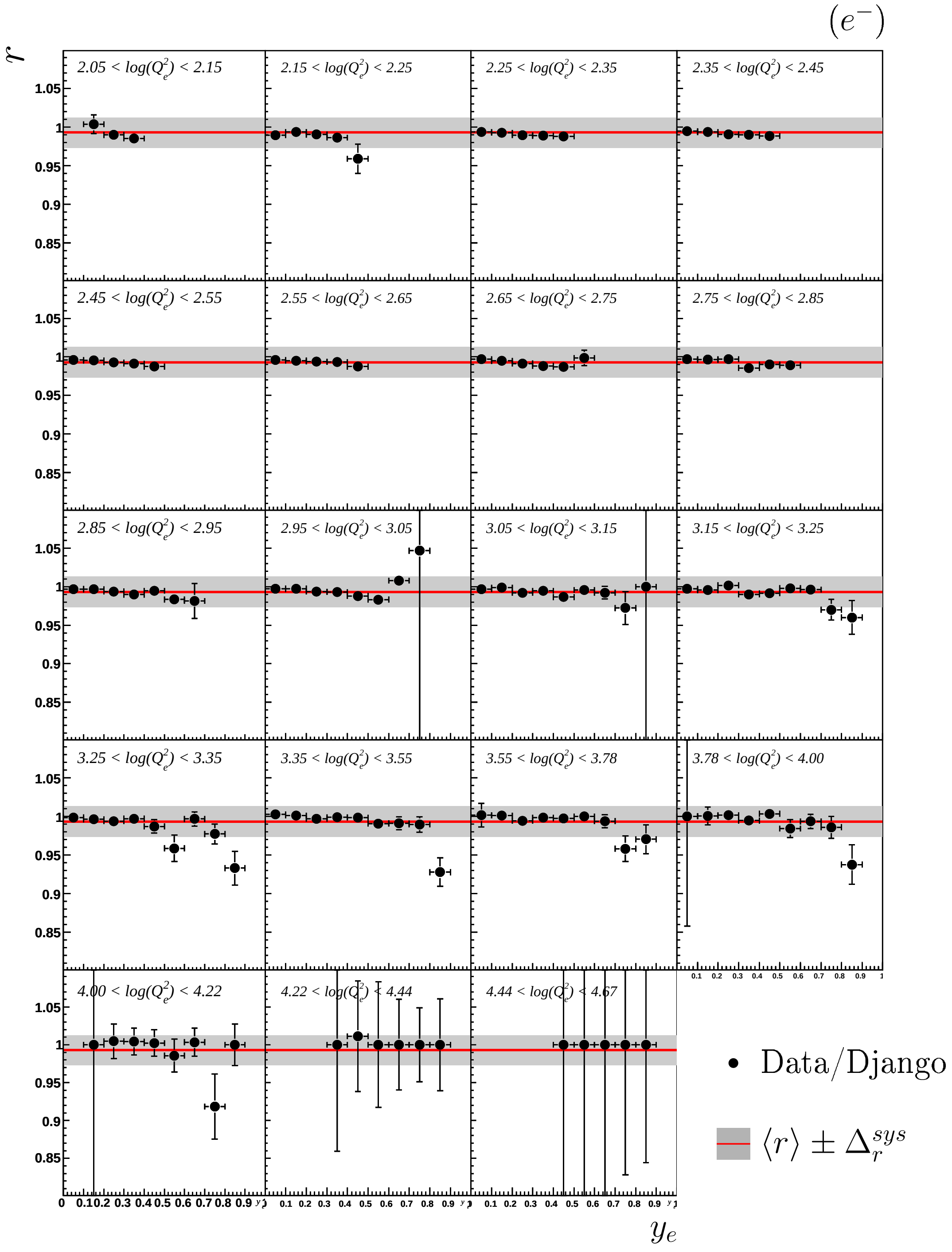

Figure 6.8: *The ratio of the TRNA efficiency in data to that in signal MC for the* e^- *period, as a function of* y_e *in log(*Q_e^2*) intervals. Shown are the average value of* r*,* $\langle r \rangle$ *for the whole sample (red line) together with the quoted systematic uncertainty (grey box).*

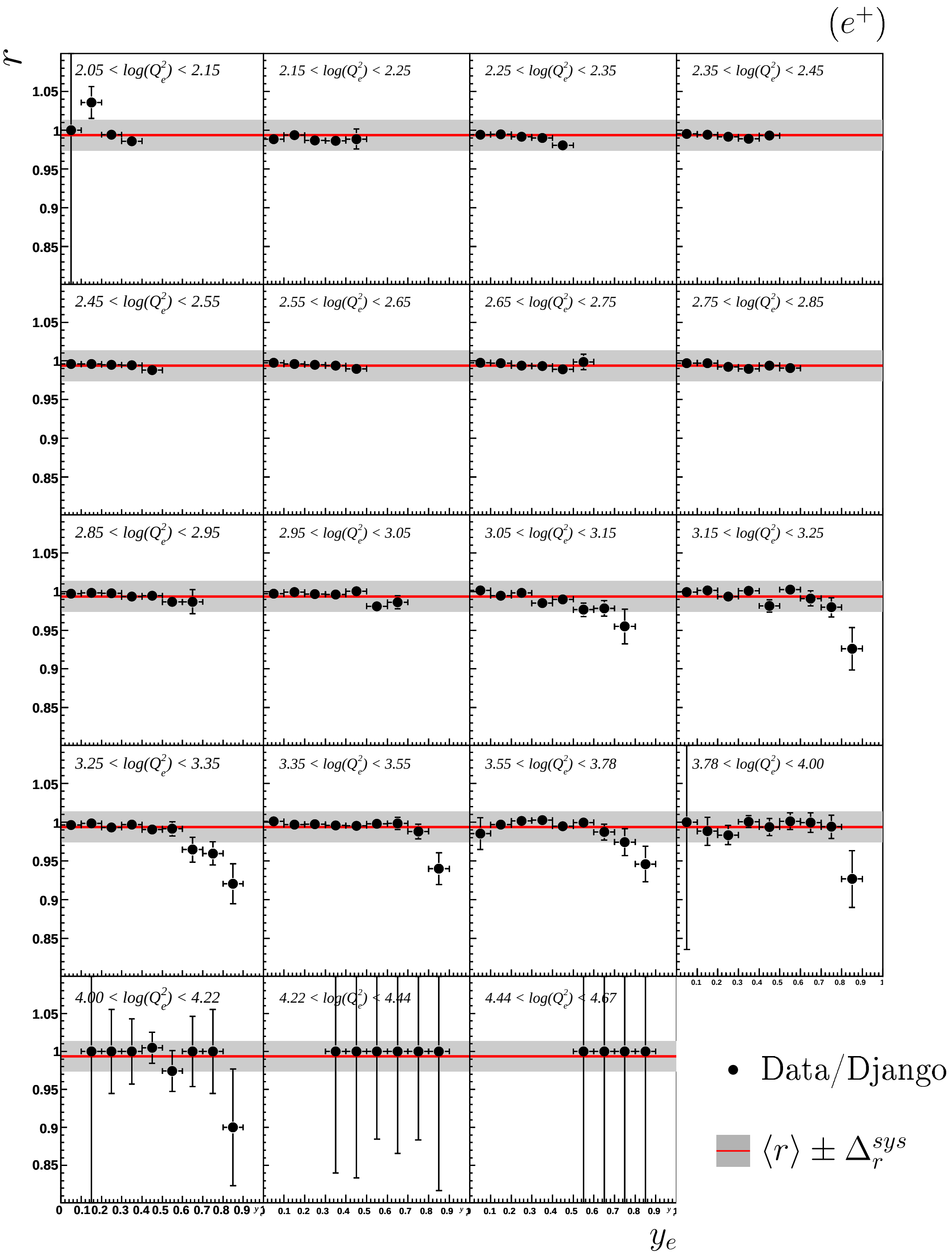

Figure 6.9: *The ratio of the TRNA efficiency in data to that in signal MC for the* e^+ *period, as a function of* y_e *in* $log(Q_e^2)$ *intervals. Shown are the average value of* r, $\langle r \rangle$ *for the whole sample (red line) together with the quoted systematic uncertainty (grey box).*

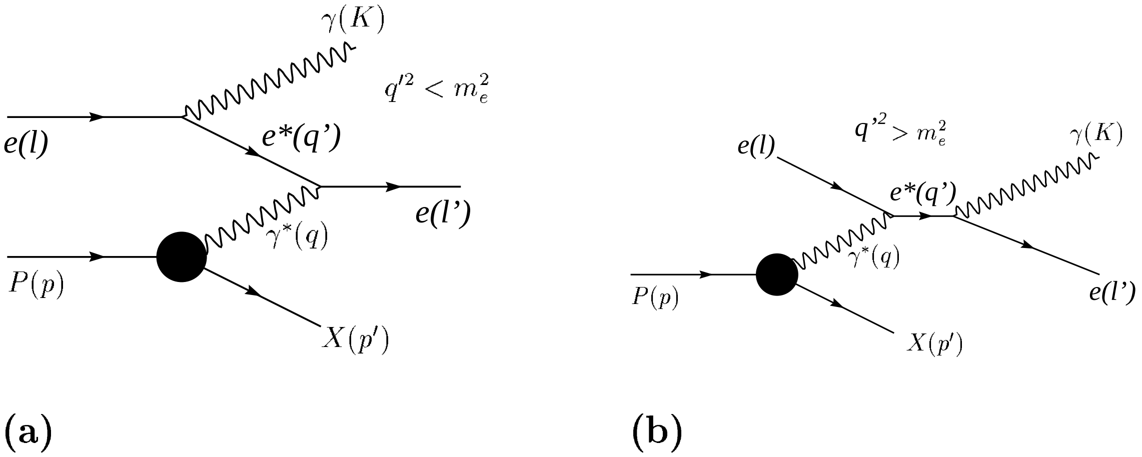

Figure 6.10: *Feynman diagrams of the QED Compton process, (a) and (b). Here* K *and* q' *are the four-momenta of the radiated photon* γ *and virtual electron* e^* *respectively.*

6.4 *ep* Background

Sources of Background

Background from *ep* processes arise when particles from the hadronic final state fake the *scattered* electron. These processes include:

- **Photoproduction (γp)**: In photoproduction ($ep \rightarrow eX$), $Q^2 < 0.01$ GeV^2 so that the exchanged photon is quasi-real[49]. The electron is scattered through such a small angle that it escapes the main detector. Photoproduction is the most significant *ep* background contributor due to the size of the cross section, $\sim$ 165,000 nb.
- **Low Q^2 DIS events**: If $1 \lesssim Q^2 \lesssim 60$ GeV^2 the scattered electron may enter the SPACAL.
- **Elastic QED Compton**: The Feynman diagrams that contribute to the QED Compton cross section ($ep \rightarrow ep\gamma$) are shown in Figure 6.10. If the negative four-momentum transfer squared (-q^2) of the virtual photon $\gamma*$ is small, and that of the virtual electron $e*$ is relatively large in magnitude ($|q'^2|$), then the scattered electron may enter the LAr calorimeter, making the event appear as a high Q^2 event.
- **Lepton pair production (l^+l^-)**: In lepton pair-production ($ep \rightarrow eXl^+l^-$) the final state has a lepton pair l^+l^- comprising electrons, muons or tauons.

Estimation of Background

The *ep* background contribution is estimated from MC simulations. For photoproduction the PYTHIA event generator is used, for elastic QED the WABGEN generator is used and for lepton pair production the GRAPE generator is used (section 3.2). An uncertainty of 30%[50] on the MC background estimate is applied.

6.5 Relative Luminosity

In comparing cross sections or event rates from the e^- and e^+ samples, the relative luminosity between the two must be considered as it enters directly into the comparison. In particular, the error on the relative luminosity may determine to a large extent the strength of the comparison. For example, in the high y analysis, the amount of negatively charged lepton tracks from the e^+ sample is compared to the amount of positively charged lepton tracks from the e^- sample to measure the background charge asymmetry, (section 7.7). As the integrated luminosity measured by the H1 Luminosity System has a large uncertainty of between 2.5-5.0% (section 6.6) the relative luminosity is measured using NC events from the nominal analysis and is described in this section.

Figure 6.11(a) shows the NC reduced cross sections $\tilde{\sigma}_{NC}$ at fixed inelasticity y as a function of Q^2 for e^-p and e^+p interactions as determined from the H1 PDF 2000 fit[1]. At large values of y and Q^2, the $x\tilde{F}_3$ structure function contributes positively to the e^-p cross section and negatively to the e^+p cross section, causing the two cross sections to separate, section 1.2. The ratio of the e^-p to the e^+p reduced cross section is shown in figure 6.11(b). At $Q^2 = 1000$ GeV^2 the e^-p cross section is greater than the e^+p cross section by less than 4% for all values of y shown. Figure 6.11(c) shows the ratio between the e^-p and e^+p ***total*** NC cross sections σ_{tot} for the kinematic range $y < 0.6$, $133 < Q^2 < Q^2_{cut}$ GeV^2 and $\theta_e < 145°$ as determined from the H1 PDF 2000 fit and MRSH. At $Q^2_{cut} = 1000$ GeV^2, this ratio is 1.005343±0.00008; the central value of the ratio quoted here is from the H1 PDF 2000 fit and the error on the ratio is taken as the difference between the ratios from the H1 PDF 2000 fit and MRSH, table 6.5. As the difference in the total cross sections is relatively small in this limited kinematic range, the process σ_{lumi} used to measure the relative luminosity is thus defined as:

$$\sigma_{lumi} = \sigma_{tot}(y < 0.6, 133 < Q^2 < 1000\ GeV^2, \theta_e < 145^\circ)$$

and shown in figure 6.11(d).

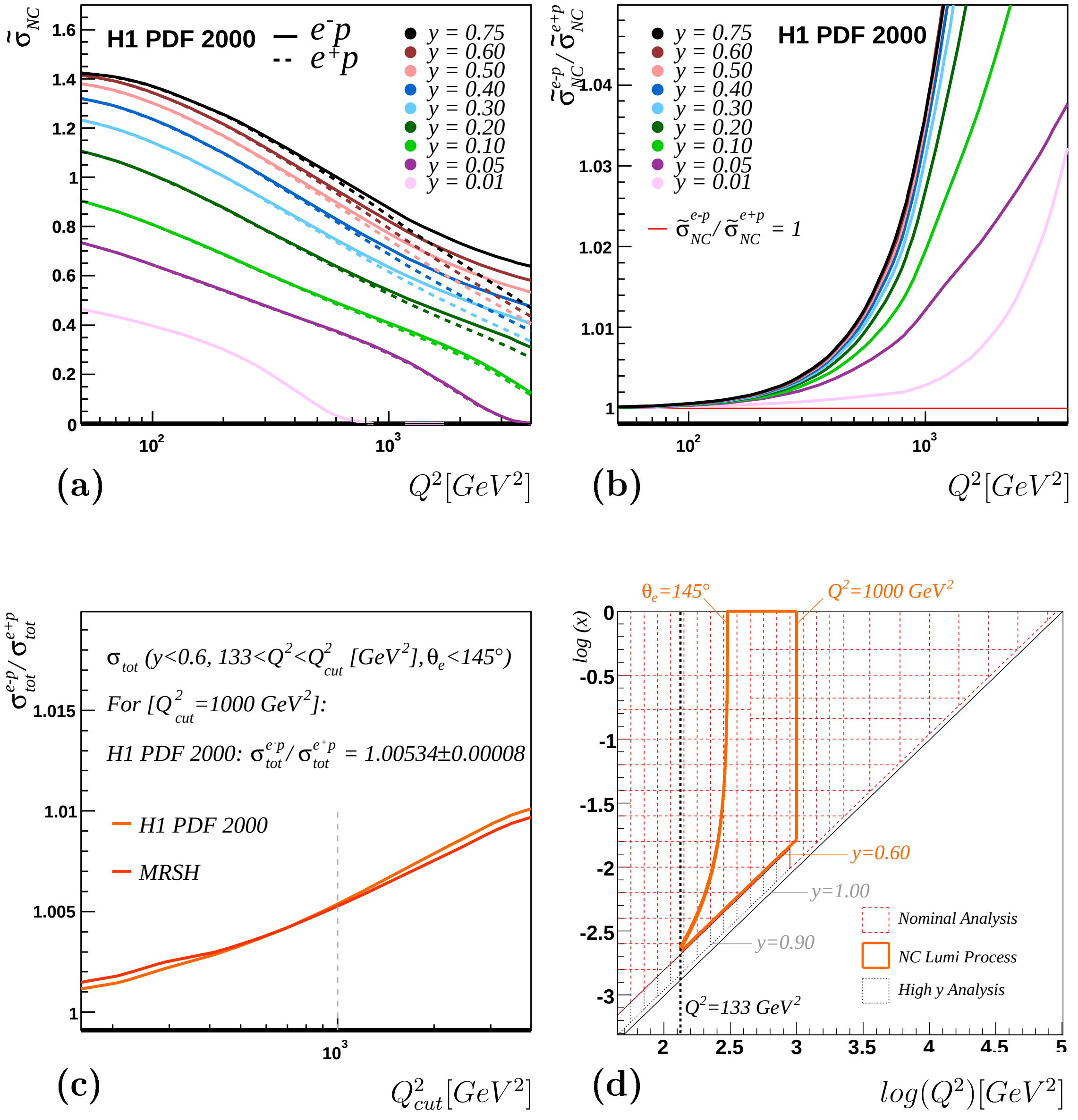

Figure 6.11: *(a) The NC reduced cross section at fixed inelasticity y values as a function of Q^2 for e^-p and e^+p interactions. The cross sections are taken from the H1 2000 PDF fit. (b) The ratio between the e^-p and e^+p reduced cross sections at fixed y as a function of Q^2. (c) The ratio between the e^-p and e^+p total NC cross sections for the kinematic range of inelasticity $y < 0.6$, $133 < Q^2 < Q^2_{cut}$ GeV^2 and $\theta_e < 145°$ as determined from the H1 2000 PDF fit and MRSH. The dashed line shows the cut at $Q^2_{cut} = 1000$ GeV^2 used to measure the relative luminosity between the e^-p and e^+p samples. (d) The kinematic range used to define the process σ_{lumi} for measuring the relative luminosity shown on the xQ^2 plane.*

σ_{tot}[pb]	H1 PDF 2000 fit	MRSH
e^-p	1567.42	1473.31
e^+p	1559.09	1465.60

Table 6.5: *The total NC cross sections for the kinematic range $y < 0.6$, $133 < Q^2 < 1000$ GeV^2 and $\theta_e < 145°$ as determined from the H1 PDF 2000 fit and MRSH.*

Event Selection and Measurement

With the NC "Lumi" process σ_{lumi} defined, the relative luminosity of the e^- sample with respect to the e^+ sample $\Gamma_{\mathcal{L}}$ is[2]:

$$\Gamma_{\mathcal{L}} = \mathcal{L}^{e^-p}/\mathcal{L}^{e^+p}$$

and can be measured from:

$$\Gamma_{\mathcal{L}} = \left(\frac{N^{e^-p}_{lumi}}{N^{e^+p}_{lumi}}\right) \cdot \left(\frac{\epsilon^{e^+p}_{H1}}{\epsilon^{e^-p}_{H1}}\right) \cdot \left(\frac{\sigma^{e^+p}_{lumi}}{\sigma^{e^-p}_{lumi}}\right) \tag{6.8}$$

where $N^{e^\pm p}_{lumi}$ is the number of events from the process σ_{lumi} observed in each sample and $\epsilon^{e^\pm p}_{H1}$ is the detector efficiencies for each sample.

The detector efficiency is a product of the trigger, tracker and electron identification efficiencies. Assuming the electron efficiency between the e^-p and e^+p samples are equal, equation 6.8 can be rewritten as:

$$\Gamma_{\mathcal{L}} = \left(\frac{N^{e^-p}_{lumi}}{N^{e^+p}_{lumi}}\right) \cdot \left(\frac{\epsilon^{e^+p}_{tof}}{\epsilon^{e^-p}_{tof}}\right) \cdot \left(\frac{\epsilon^{e^+p}_{cip}}{\epsilon^{e^-p}_{cip}}\right) \cdot \left(\frac{\epsilon^{e^+p}_{lar}}{\epsilon^{e^-p}_{lar}}\right) \cdot \left(\frac{\epsilon^{e^+p}_{t0}}{\epsilon^{e^-p}_{t0}}\right) \cdot \left(\frac{\epsilon^{e^+p}_{trna}}{\epsilon^{e^-p}_{trna}}\right) \cdot \left(\frac{\sigma^{e^+p}_{lumi}}{\sigma^{e^-p}_{lumi}}\right) \tag{6.9}$$

or more succinctly as:

$$\Gamma_{\mathcal{L}} = \Gamma_{N_{lumi}} \cdot \Gamma^{-1}_{\epsilon_{tof}} \cdot \Gamma^{-1}_{\epsilon_{cip}} \cdot \Gamma^{-1}_{\epsilon_{lar}} \cdot \Gamma^{-1}_{\epsilon_{t0}} \cdot \Gamma^{-1}_{\epsilon_{trna}} \cdot \Gamma^{-1}_{\sigma_{lumi}}. \tag{6.10}$$

The ratio $\Gamma_{\epsilon_{tof}}$ of the ToF efficiency from the e^- sample to the efficiency of the e^+ sample is shown in figure 6.12(a.1) as a function of electron energy and figure 6.12(a.2) as a function of electron polar angle. The data is fitted by a $\Gamma = constant$ assumption. As the quality of the fit is good over the kinematic variables, $\Gamma_{\epsilon_{tof}}$ can be assumed to be well described by the single value of 0.9984±0.0044, taken as the average, table 6.6. The systematic error on $\Gamma_{\epsilon_{tof}}$ has two contributions: (a) an overall systematic error of 0.0039

---

[2] Throughout the thesis Γ_q will represent the ratio of a quantity q as obtained from the e^- sample to the same quantity as obtained from the e^+ sample, that is: $\Gamma_q = q^{e^-p}/q^{e^+p}$.

taken as the difference between $\Gamma_{\epsilon_{tof}^{s57}}$ and $\Gamma_{\epsilon_{tof}^{bh}}$, using the ToF efficiencies as determined from the s57 and Bethe-Heitler samples respectively (b) an additional systematic error of 0.002 due to the uncertainty in ϵ_{tof} at the start of the 0304e^+ data taking ($\approx$ 16% of the total e^+p sample) when s57 included ToF information, section 7.4. The ratio $\Gamma_{\epsilon_{cip}}$, $\Gamma_{\epsilon_{lar}}$ and $\Gamma_{\epsilon_{t0}}$ are also shown in figure 6.12; no dependence on kinematics is observed and Γ is well described by the average value indicated in table 6.6. Figure 6.13 (a) and (b) shows the ratio of the e^-p to e^+p TRNA tracker efficiency $\Gamma_{\epsilon_{trna}}$ as determined in section 6.3 as a function of electron energy and the inclusive polar angle γ_h and is consistent with a $\Gamma_{\epsilon_{trna}} = constant$ assumption as seen by the corresponding fit. Its average value is given as well in table 6.6.

The *luminosity* sample used to determine N_{lumi} in equation 6.9 from the NC Lumi process is selected using the final selection cuts of table 6.7 and applying the following additional cuts:

- $y_e < 0.6$, $133 < Q_e^2 < 1000$ GeV^2
- $\theta_e < 145°$ thus removing the dependence of the acceptance on the z_{vtx} distribution
- Applying each rejection region in the FV(t) cut to *all* runs thus removing the time dependence

Figure 6.14 shows the distribution of events from the e^- and e^+ luminosity samples in (a) electron energy and (b) electron polar angle. The ratio $\Gamma_{N_{lumi}}$ of the e^- to e^+ number of entries is shown in the bottom part of each plot, together with a fit to the data of the form $\Gamma_{N_{lumi}} = constant$; it is found to be 0.8658±0.0026. This value is corrected using equation 6.10, from which the relative normalization is measured[3] to be $\Gamma_{\mathcal{L}} = 0.8667 \pm 0.0046$, table 6.6. This value is consistent with that obtained from the H1 Luminosity System of 0.886±0.035, but has significantly greater precision.

---

[3] The uncertainty due to the electron energy, electron polar angle, hadronic energy scale and noise is assumed to cancel in the numerator $N_{norm}^{e^-p}$ and denominator $N_{norm}^{e^+p}$ terms, and therefore neglected in the measurement.

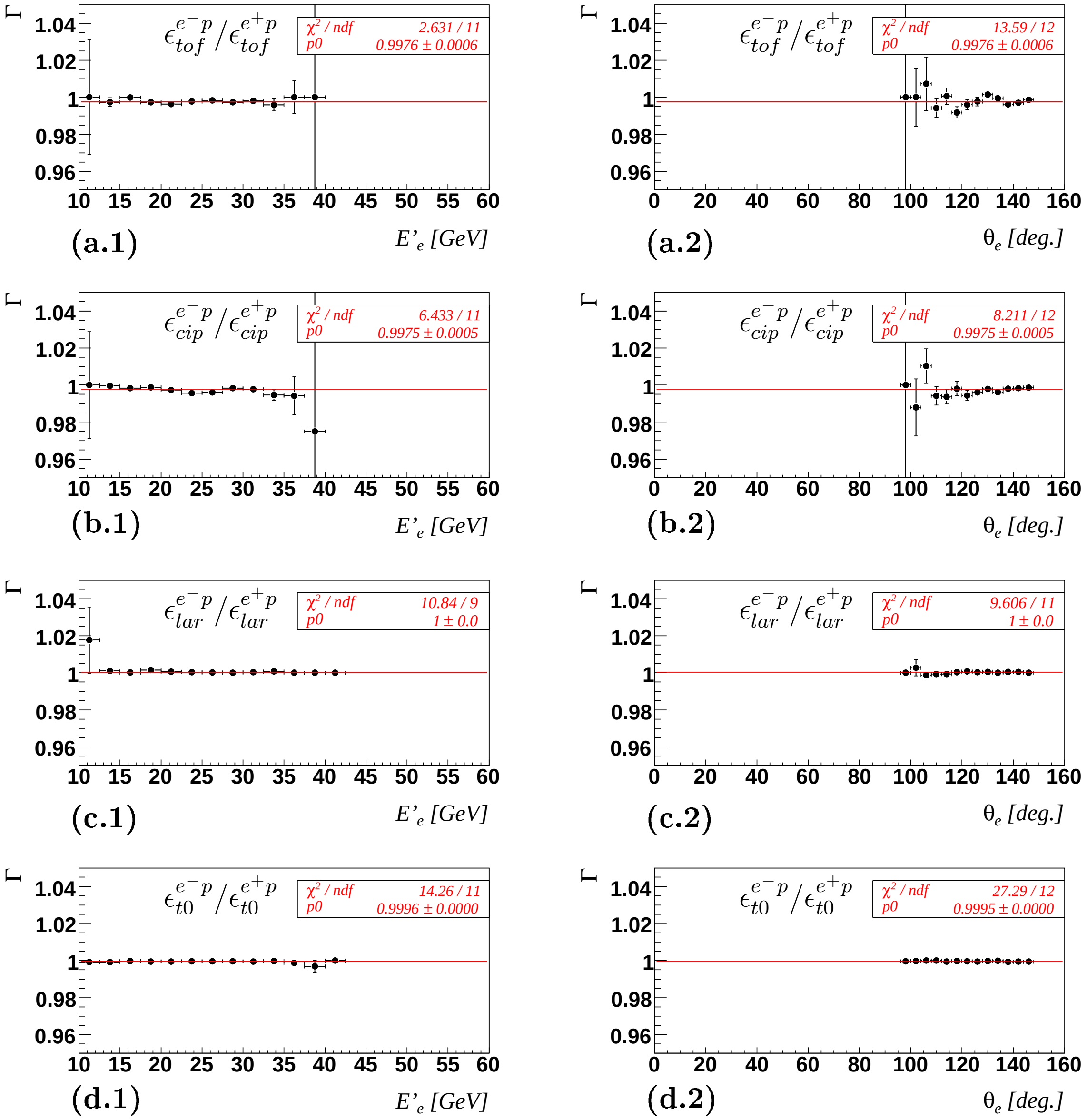

Figure 6.12: *(a) The ratio* Γ *of the* e^- *to the* e^+ *trigger efficiency components: (a.1-2) ToF, (b.1-2) CIP, (c.1-2) LAR and (d.1-2) T0 as a function of (a-d.1) electron energy and (a-d.2) electron polar angle. The data is fitted by a* $\Gamma = constant = p0$ *assumption, shown as the red line.*

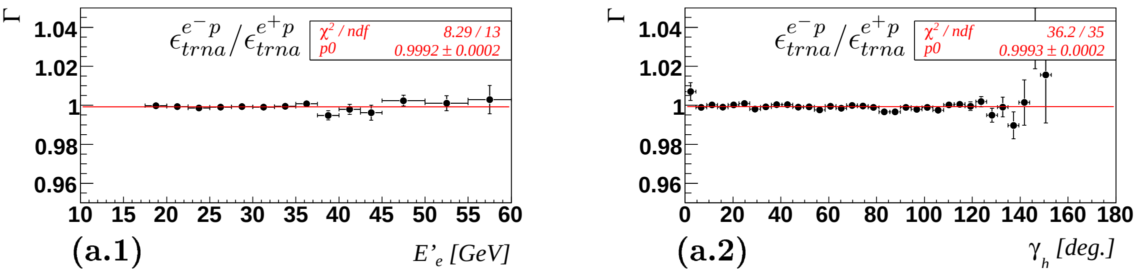

Figure 6.13: *(a) The ratio* Γ *of the* e^- *to the* e^+ *TRNA tracker efficiency as a function of (a) electron energy and (b) inclusive polar angle* γ_h*. The data is fitted by a* $\Gamma = constant = p0$ *assumption, shown as the red line.*

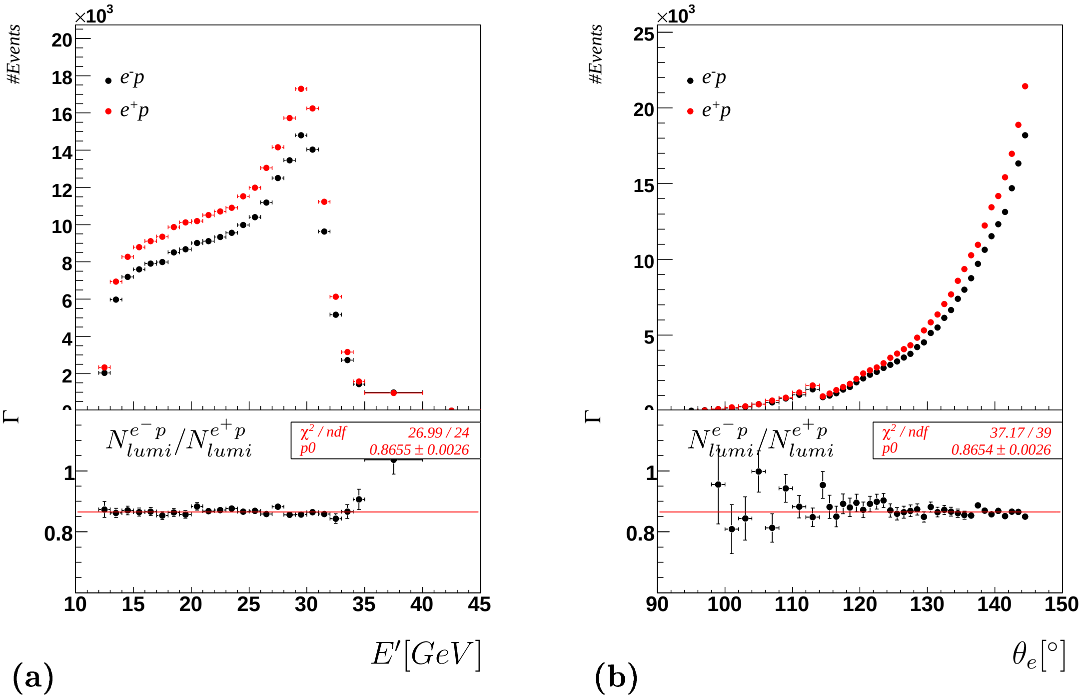

Figure 6.14: *The distribution of events from the* e^- *and* e^+ *luminosity samples in (a) electron energy and (b) electron polar angle. The ratio* Γ *of the* e^- *to* e^+ *number of entries is shown in the bottom part of each plot, together with a fit to the data of the form* $\Gamma = constant = p0$.

Quantity q	Γ_q
σ_{lumi}	1.005343±0.00008
ϵ_{tof}	0.9977±0.0006[stat.]±0.0032[syst.[a]]±0.0020[syst.[b]]
ϵ_{cip}	0.9975±0.0005[stat.]
ϵ_{lar}	1.0004±0.0001[stat.]
ϵ_{t0}	0.99954±0.00003[stat.]
ϵ_{trna}	0.9992±0.0003[stat.]
N_{lumi}	0.8658±0.0026[stat.]
$\mathcal{L}$	0.8661±0.0043

---

[a] Taken as the difference between $\Gamma_{\epsilon_{tof}}$ as measured using the s57 monitor sample and the Bethe-Heitler monitor sample.

[b] Taken as the uncertainty in the first 27 pb^{-1} of 0304e^+data where s57 cannot be used as a monitor.

Table 6.6: *The e^-p/e^+p Γ ratio of the quantities σ_{lumi}, ϵ_{tof}, ϵ_{cip}, ϵ_{lar}, ϵ_{t0}, ϵ_{trna} and N_{lumi} used to determine the relative luminosity $\Gamma_{\mathcal{L}}$.*

6.6 Cut Summary, Event Yield & Control Plots

Cut Summary

Table 6.7 lists the nominal analysis selection cuts used to obtain the final sample upon which the cross section measurement is made.

Event Yield

The event yield Y_F for a given interval of data-taking is defined as:

$$Y_F = \frac{N_F^D}{\mathcal{L}^{H1}} \tag{6.11}$$

where N_F^D is the number of events in the final sample and $\mathcal{L}^{H1}$ is the integrated luminosity as measured by the H1 Luminosity System.

For a given z_{vtx}, the electron polar angle acceptance is set by the minimum cut on z_{im}, $z_{im}^{min} = -190$ cm. This is shown schematically in figure 6.15 where electrons scatter from vertices at ±35 cm unto the surface of the LAr calorimeter. For the vertex at +35 cm, the maximum polar angle is $\theta_e^{max} \approx 155°$; for the vertex at -35 cm, the maximum polar angle is $\theta_e^{max} \approx 145°$. This dependence of θ_e^{max} on z_{vtx} makes the yield defined equation 6.11 dependent on the z_{vtx} distribution of *ep* events. If say for one period of data-taking most events are at large ***positive*** z_{vtx}, then the yield would be greater than a similar period of data-taking where the events were at large ***negative*** z_{vtx}. This makes Y_H sensitive to the z_{vtx} distribution and hence beam conditions.

Cut Name	Description
Run Selection[a]	Require CJC1,CJC2,LAr,ToF,Luminosity,CIP Require runs with subtrigger s75,s67,s77
Subtrigger	Require s67 or s77
Fiducial Volume FV(t)	**Reject** regions indicated in figure 6.3.
Scattered Electron	
LAr Candidate	Require scattered electron candidate in LAr
ϕ-crack	**Reject** $\phi_{wheel} \in [-2^\circ, +2^\circ]$ if $z_{im} < 300$ cm
z-crack 1	**Reject** $z_{im} < -190$cm
z-crack 2	**Reject** $15 < z_{im} < 25$cm
Tracker	TRNA Requirement (see table 6.3)
Kinematics	$(Q_e^2 > 133 \text{ GeV}^2)$ and $(y_e < 0.9)$ **Reject** $((Q_e^2 < 891.25) \text{ GeV}^2$and $(0.63 < y_e < 0.9))$
ISR	$E - P_z > 35$ GeV
non-ep Background Cut	**Reject if:**
Topological Cut	EP Topological Finders Fail and ($P_{tbal} < 0.5$ or $P_{tbal} > 2.0$ or $\eta_{max} < 3$)
Timing Cut	CJC Timing Fail and ($\eta_{max} < 3$)

---

[a] One common run selection requiring s75, s67 and s77 is used for the high y analysis and the nominal analysis.

Table 6.7: *Summary of the cuts used to obtain the final sample in the nominal analysis.*

To remove this sensitivity, the yield Y is defined as:

$$Y = \frac{N^D_{\theta_e < 145^\circ}}{\mathcal{L}^{H1}} \tag{6.12}$$

where $N^D_{\theta_e<145^\circ}$ is the number of events in the final sample with electron polar angle $\theta_e < 145^\circ$, since for this angular range, z_{im} is limited to -185 cm, figure 6.16(a). Figure 6.16(b) shows the electron polar angle distribution for two samples: the final sample where $z_{im}^{min} = -190$ cm and the sample obtained by removing the minimum z_{im} cut. Since for the angular range $\theta_e < 145^\circ$ the two samples are identical - showing that the number of events is unaffected by the z_{im}^{min} cut - events at large positive z_{vtx} have equal likelihood of passing the z_{im}^{min} cut as events at large negative z_{vtx}.

Thus by limiting the electron polar angle to $\theta_e < 145^\circ$, the yield is insensitive to the z_{vtx} distribution, making it a good indicator of the overall detector efficiency.

Figure 6.17(a) shows Y for the 0304e^+ period as a function of the run number R where each yield measurement corresponds to an integrated luminosity of ≈ 400 nb^{-1}. The data is fitted by a $y = constant$ assumption. The inner plot shows the yield *distribution* fitted to a Gaussian assumption. Since the yield is proportional to the overall detector efficiency

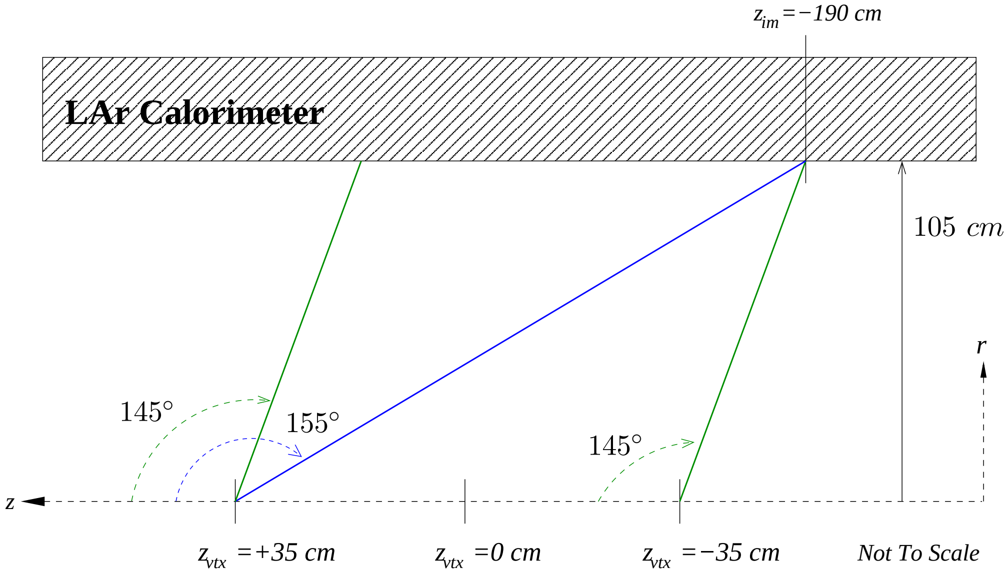

Figure 6.15: *Schematic showing the dependence of the electron polar angle acceptance on the* $z-$*coordinate of the reconstructed vertex.*

ϵ^{H1} and inversely proportional to the integrated luminosity $\mathcal{L}^{H1}$

$$Y \propto \left(\frac{\epsilon^{H1}}{\mathcal{L}^{H1}}\right),$$

an abnormally low or high yield may indicate a period where the detector efficiency or measured integrated luminosity is not well understood. No abnormalities are present as indicated by the fits. The same is true for the 0405e^-period, figure 6.17(b).

Figures 6.18(a) and (b) show similar plots for the 06e^- and 0607e^+ periods. At run number $R \approx 464600$ the yield drops from 1.69 nb^{-1} to 1.62 nb^{-1} as indicated by the fits over the run ranges indicated. The lower yield appears to continue into the 0607e^+ period up to run number $R \approx 477000$ where it inceases from 1.64 nb^{-1} to 1.73 nb^{-1}. Similar changes in the yield have been observed by other independent analyses[51] and have been attributed to biases in the integrated luminosity measurement the cause of which is yet uncertain but most likely related to the acceptance of the photon tagger. Apart from the discontinuity of the yield due to the integrated luminosity measurement, the yield appears to be stable over the fitted run ranges indicated.

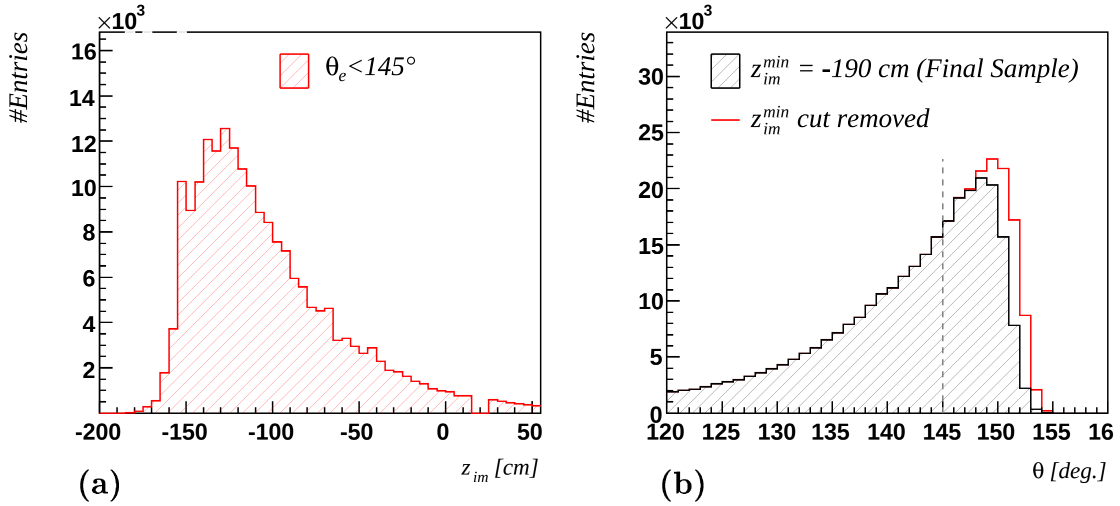

Figure 6.16: *(a) The z_{im} distribution of events from the final sample whose electron polar angle is limited to the range $\theta_e < 145°$. (b) The electron polar angle θ_e distribution for events from the final sample as well as from the sample obtained by removing the minimum z_{im} cut of $z_{im}^{min} = -190$ cm.*

Control Plots

The relative error on the integrated luminosity as measured by the H1 Luminosity System for the various subperiods are[52]:

- 2.5% for 0304e^+, 0405e^- and 06e^-
- 5.0% for 0607e^+.

Due to the large relative error of the 0607e^+ subperiod, the integrated luminosity of the e^+ sample is obtained using the *relative* luminosity of the e^- to the e^+ sample, $\Gamma_{\mathcal{L}}$ (section 7.7), so that:

$$\mathcal{L}^{e^+} = \frac{\mathcal{L}^{e^-}}{\Gamma_{\mathcal{L}}}. \tag{6.13}$$

In this way $\mathcal{L}^{e^+}$ is calculated to be 167.25±4.26 pb^{-1} compared to that measured by the H1 Luminosity System of 163.6 pb^{-1}. The integrated luminosities with their corresponding errors are summarized in table 6.8 for the e^- and e^+ periods.

The control plots and cross sections of both the nominal analysis and the high y analysis correspond to the integrated luminosities given in table 6.8.

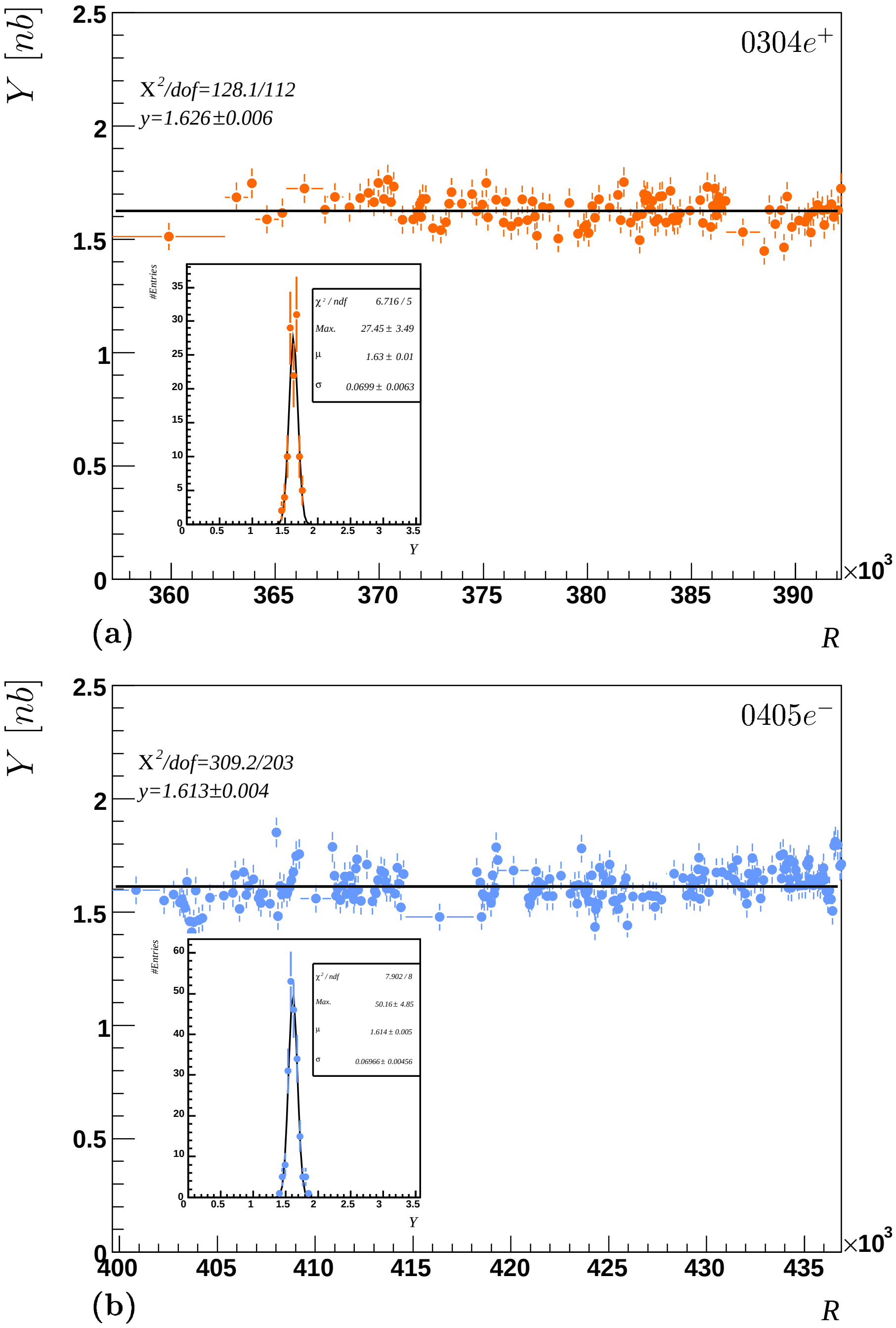

Figure 6.17: *(b) The event yield Y for the $0304e^+$ period as a function of the run number R. Fitted to the data is the function $Y = constant$. The inner plot shows the result of a Gaussian fit to the yield distribution. (b) Similar plots for $0405e^-$ period.*

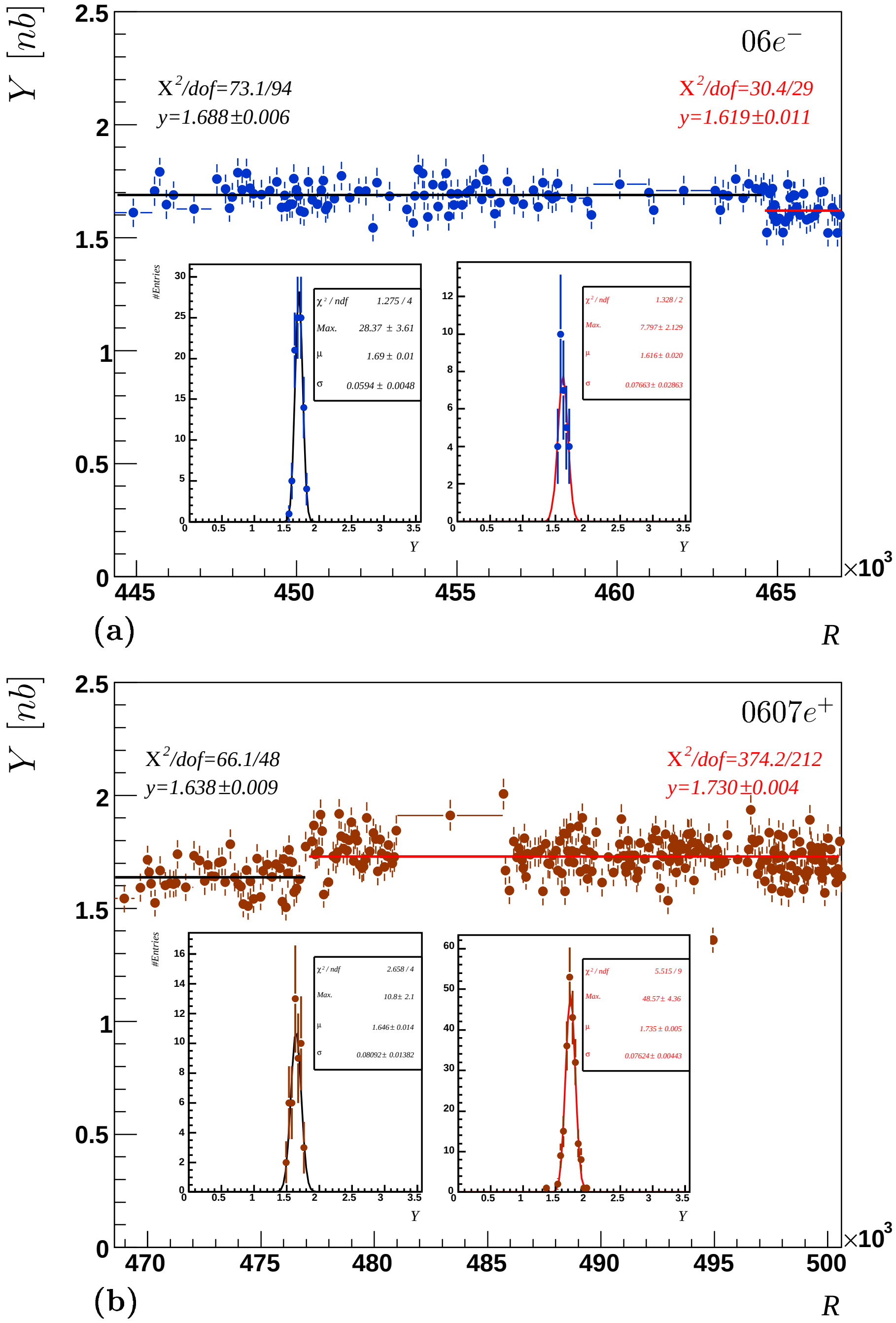

(a)

(b)

Figure 6.18: *(b) The event yield Y for the 06e$^-$ period as a function of the run number R. Fitted to the data are two functions of the form Y = constant over the indicated run ranges. The inner plots show the result of a Gaussian fit to the two yield distributions corresponding to the fitted runranges. (b) Similar plots for 0607e$^+$ period.*

Period	$\mathcal{L}$ [pb^{-1}]	$\Delta_{\mathcal{L}}$ [pb^{-1}]	$\delta_{\mathcal{L}}$ [%]
e^-	144.86	3.62	2.50
e^+	167.25	4.26	2.55

Table 6.8: *The integrated luminosity $\mathcal{L}$ of the e^- and e^+ periods together with their absolute ($\Delta_{\mathcal{L}}$) and relative ($\delta_{\mathcal{L}}$) uncertainties.*

Control plots comparing the signal+background MC to the data are shown for the e^- and e^+ periods in figures 6.19 and 6.20 respectively for (a) electron energy, (b) electron polar angle and inelasticities as measured from the (c) electron y_e and (d) hadronic final state y_h. All MC corrections including the efficiencies described in this chapter have been applied. The background-only MC contribution scaled by the factor ×5 is also shown. The MC reasonably describes the data. The normalization r of the total number of events in the data to the total number of events in the signal+background MC is $r = 1.015 \pm 0.002$ for e^- sample and 1.017 ± 0.002 for the e^+ sample.

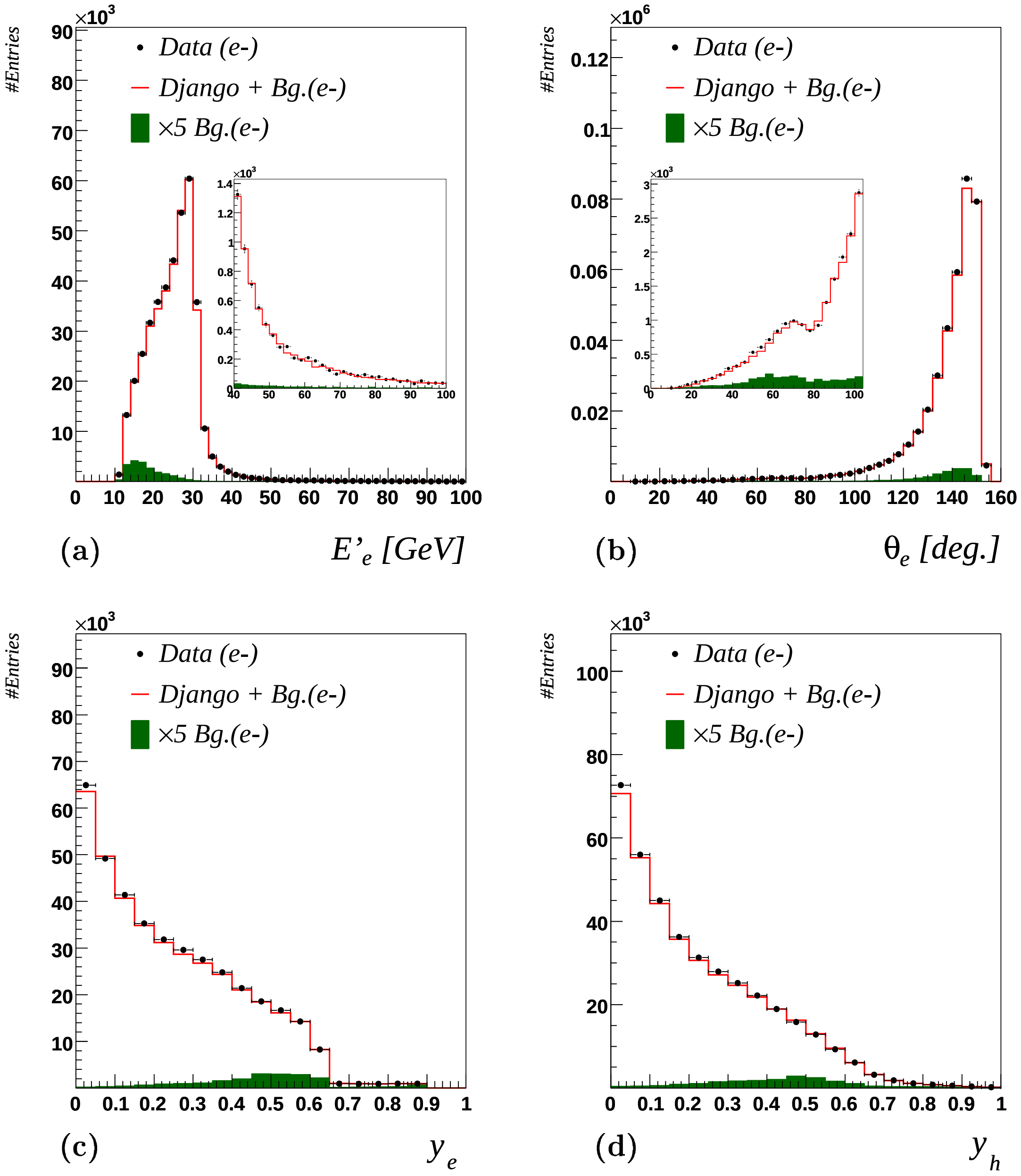

Figure 6.19: *The e^- control distributions for the quantities (a) electron energy E'_e, (b) electron polar angle θ_e and inelasticity y as determined from the (c) electron y_e and (d) hadronic final state y_h. Data, signal+background MC and background-only MC are shown. The background-only MC is scaled by a factor $\times 5$. The inner plots of (a) and (b) correspond to the respective quantities over the indicated ranges.*

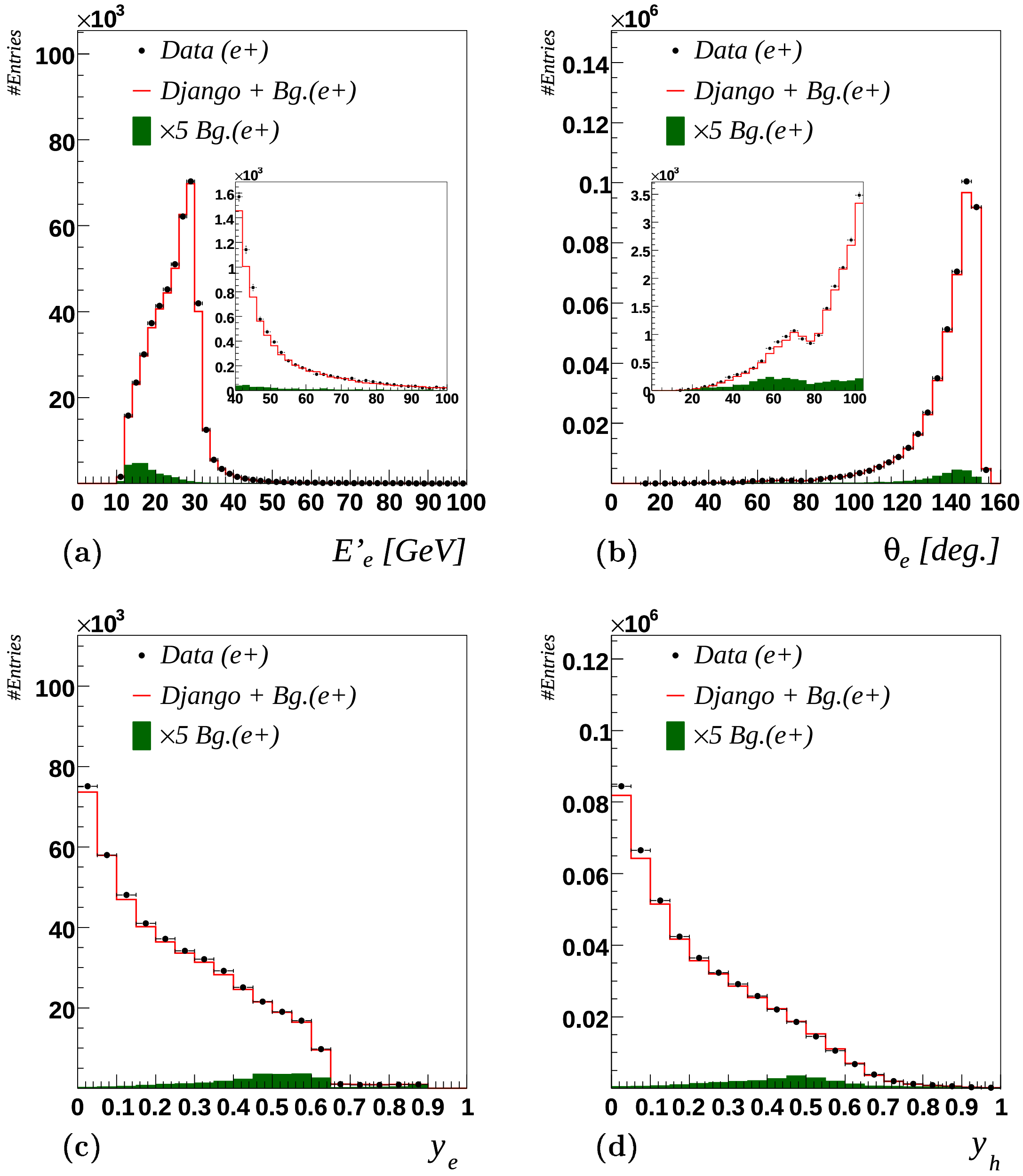

Figure 6.20: *The e^+ control distributions for the quantities (a) electron energy E'_e, (b) electron polar angle θ_e and inelasticity y as determined from the (c) electron y_e and (d) hadronic final state y_h. Data, signal+background MC and background-only MC are shown. The background-only MC is scaled by a factor ×5. The inner plots of (a) and (b) correspond to the respective quantities over the indicated ranges.*

Chapter 7

Event Selection II - The High y Analysis Event Selection

The event selection for the high y analysis is presented here. The lower electron energies compared to the nominal analysis brings with it different trigger strategies and background subtraction procedures. As will be shown, the nominal analysis complements the high y analysis as it offers a means of estimating the tracker efficiency. The relative luminosity of the e^- to the e^+ sample measured in the nominal analysis is also used to determine the charge asymmetry of the background to a very good precision. As in chapter 6, control plots comparing the data (after background subtraction) to simulation (after all corrections are applied) are presented.

7.1 Trigger

The subtrigger used to select events for the high y analysis is “s75”. For s75 to fire, the event must satisfy four level I conditions simultaneously: the level I LAr Calorimeter condition, LAR1, the track condition TRK, the timing condition, T0 and the veto condition VET. s75 also has a level II electron validation requirement, LAR2. Summarizing then, the s75 subtrigger is defined as:

$$s75 \equiv LAR1 \;\; \&\& \;\; TRK \;\; \&\& \;\; T0 \;\; \&\& \;\; VET \;\; \&\& \;\; LAR2. \tag{7.1}$$

with && representing the logical AND.

In this analysis, the trigger behaviour is not included in the detector simulation but applied as an efficiency reweight to the MC events. In the following each of the conditions are explained and efficiency studies are presented. In all the trigger efficiency measurements presented here, background is subtracted using the wrong charge background subtraction procedure, section 7.7.

7.2 Liquid Argon Condition - LAR

The LAR1 condition is met when the `LAr_electron_2` TE fires (section 2.7). As the final high y analysis event selection (table 7.8) limits the z-coordinate of the electron impact position to $-190 < z_{im} < 45$ cm, the electron is confined to sectors 10-13 (table 2.1) having energy thresholds of 3.5 GeV (sectors 10,11,12) and 5 GeV (sector 13). The lower cut on the electron energy and the high y kinematics restrict the energy of the scattered electron to $5 < E'_e < 20$ GeV.

Since both the scattered electron (e') and the hadronic final state (HFS) can deposit considerable amounts of energy in the LAr calorimeter, the big towers can be fired by either of the two. Figure 7.1(a) shows the $r\phi$-view of an event where the HFS is approximately 180° to the scattered electron making energy depositions by the two clearly distinguishable. Figure 7.1(b) shows the difference Δz between the z-position of a big tower, z_{BT} and the z-coordinate of electron impact position z_{im}, $\Delta z = z_{BT} - z_{im}$, plotted against the difference $\Delta\phi$ between the ϕ-position of a big tower, ϕ_{BT} and ϕ-coordinate of electron impact position ϕ_{im}, $\Delta\phi = \phi_{BT} - \phi_{im}$, for all big towers fired for a set of signal events. Events are classified to have been e-fired LAR1 if there is big tower fired inside the blue solid box and hfs-fired LAR1 if $|\Delta\phi| > 50°$ (red dashed lines). In the high y analysis events are required to be e-fired LAR1, that is:

$$LAR \equiv e - fired\ LAR1 \ \ \&\& \ \ LAR2. \tag{7.2}$$

Monitor Samples

To measure the LAR trigger efficiency, a monitor sample independent of the LAR condition is required otherwise the resulting efficiency is biased. The selection used to obtain the monitor sample begins with a basic selection S^{trig} comprising all final selection cuts (table 7.8) minus the "Subtrigger", "LAR" and "Fiducial Volume" cuts. *Two* monitor samples are then built from S^{trig}:

- SPA monitor sample, S_M^{spa}- Those events firing any of the SPACAL subtriggers s0, s1, s2, s3, s8 or s9.
- LAR67 monitor sample, S_M^{lar67}- Those events firing subtrigger s67 by the HFS. (See section 2.6 for subtrigger definitions.)

The SPA monitor sample is independent of the LAR requirement since the SPACAL subtriggers do not contain signals from the LAr Calorimeter (on any of the trigger levels). As the scattered electron is in the LAr calorimeter, the events in the SPA sample can be

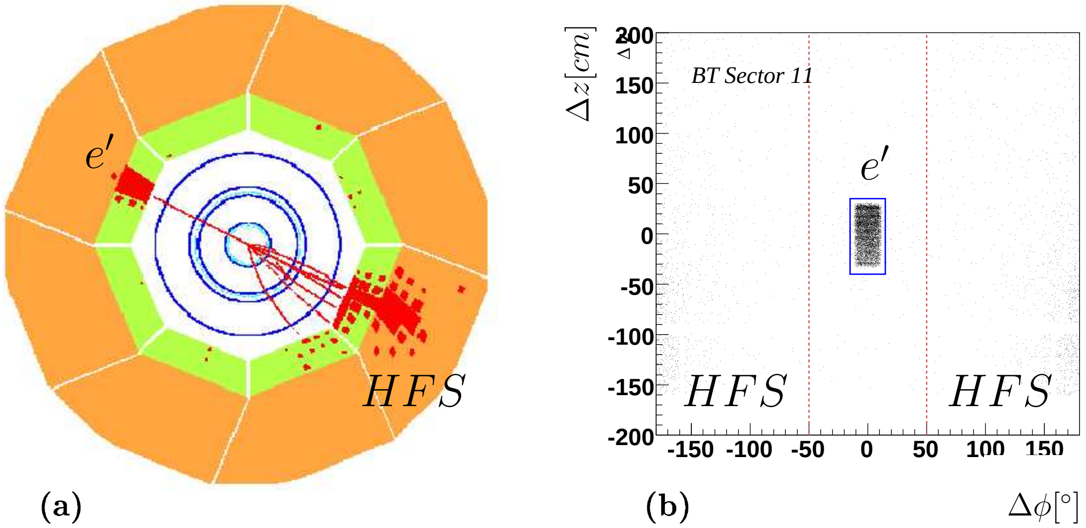

Figure 7.1: *(a)Both the scattered electron (e') and the hadronic final state (HFS) deposit energy in the LAr Calorimeter and can thus fire a big tower. In this $r\phi$-view of an NC event both final state objects are clearly distinguishable. (b)Big Tower distribution in ϕ and z with respect to the electron impact position for the cases where the electron hit BT Sector 11. BTs considered to have been fired by the electron e' are within the blue solid box; those considered fired by the HFS correspond to $|\Delta\phi| > 50^\circ$ as seen by the red dashed lines.*

regarded as being fired by the HFS depositing energy in the SPACAL detector. Events from the LAR67 monitor sample are by definition hfs-fired LAR1, and are also independent of the e-fired LAR1 condition since e-fired BTs are well separated from hfs-fired BTs (last section). s67 carries no level II conditions.

Figure 7.2(a) shows the distribution of the inclusive hadronic polar angle γ_h for both monitor samples where the LAR67 distributions are normalized to the number of entries in the SPA distributions. It can be seen that events in the SPA sample are at larger γ_h compared to the LAR67 sample since the scattered electron is in the LAr calorimeter so that the SPACAL subtriggers are triggered in large part by the HFS. As the very backward HFS triggers the SPACAL subdetector there is less chance that it will trigger the LAr calorimeter. The actual number of hfs-fired events from the SPA sample is shown in figure 7.2(a). The *fraction* of events from the SPA sample that is hfs-fired, f_h^{spa} is shown in figure 7.2(b). This fraction is at most 40% in contrast to the LAR67 sample which is $\approx$100% hfs-fired by definition ("$\approx$"100% and not "$=$" since the `LAr_electron_2` threshold is actually *higher* than the `LAr_electron_1` threshold for sector 13).

Events common to both monitor samples are those events that are hfs-fired from the SPA sample that trigger s67 with its `LAr_electron_1` threshold. The contribution of these common events to each monitor sample f_{com}^{spa} and f_{com}^{lar67} are:

$$f_{com}^{spa} = N^{com}/N^{spa}, \qquad f_{com}^{lar67} = N^{com}/N^{lar67}$$

where N^{spa} is the number of events from the SPA sample, N^{lar67} the number of events from the LAR67 sample and N^{com} is the number of events common to both samples. So for example if the number of events in the SPA sample is 100, in the LAR67 sample is 200 and the number of common events is 10, then $N^{com}/N^{spa} = 10\%$ and $N^{com}/N^{lar67} = 5\%$. These contributions are shown in figures 7.2(c) and (d) for the $z_{im} < -115$ cm and $-115 < z_{im} < 45$ cm. Since common events contribute $\lesssim 20\%$ to each of the monitor samples, the two samples can be treated as statistically independent.

Efficiency Determination

The liquid argon level I efficiency, the fraction of events which meet the e-fired LAR1 condition, is determined from each of the monitor samples: ϵ_{l1}^{spa} for the SPA sample and ϵ_{l1}^{lar67} for the LAR67 sample. These are shown in figures 7.3 and 7.4 for the e^- and e^+ periods respectively. For $z_{im} < -115$ cm which corresponds to a `LAr_electron_2` threshold of 5 GeV, the efficiency falls steeply with electron energy. Such a drop-off is not observed at higher z_{im} due to a lower threshold of 3.5 GeV. Due to the large associated relative statistical uncertainty $(\Delta\epsilon_{l1}/\epsilon_{l1})$ in this threshold region, events with electron energies $E_e' < 7$ GeV and $z_{im} < -115$ cm are removed from the analysis as indicated by the vertical dashed lines of figures 7.3 and 7.4.

Figure 7.5 (a) and (b) show ϵ_{l1}^{spa} and ϵ_{l1}^{lar67} respectively as a function of z_{im} for electron energies $7 < E_e' < 10$ GeV and above 10 GeV. At lower energies there is a discontinuity in the efficiency across the transition region from sector 12 → 13 (shown as the pair of dashed lines). This may be due to lost energy in dead material joining the 2 BT sectors. At higher energies the transition is smooth. Thus events with electron energies $7 < E_e' < 10$ GeV and in the transition region $-125 < z_{im} < -115$ cm are also removed from the analysis.

For those points not removed from the analysis, the agreement between the efficiency measurements from the two monitor samples is checked by calculating the significance, $sig(\Delta)$ of the difference, Δ:

$$\Delta = \epsilon_{l1}^{lar67} - \epsilon_{l1}^{spa}, \qquad \delta\Delta = \Delta\epsilon_{l1}^{lar67} \oplus \Delta\epsilon_{l1}^{spa}, \qquad sig(\Delta) = \Delta/\delta\Delta$$

where $\delta\Delta$ is the error on the difference made by adding the statistical errors of each measurement ($\Delta\epsilon_{l1}^{lar67}$, $\Delta\epsilon_{l1}^{spa}$) in quadrature, treating the monitor samples as independent (last section). Figure 7.6 shows the difference while figure 7.7 shows the significance of the difference for the e^- and e^+ periods. Significance bands at ±1, ±2 and ±3 are included. It can be seen that the LAR67 measurement is consistent with the SPA measurement

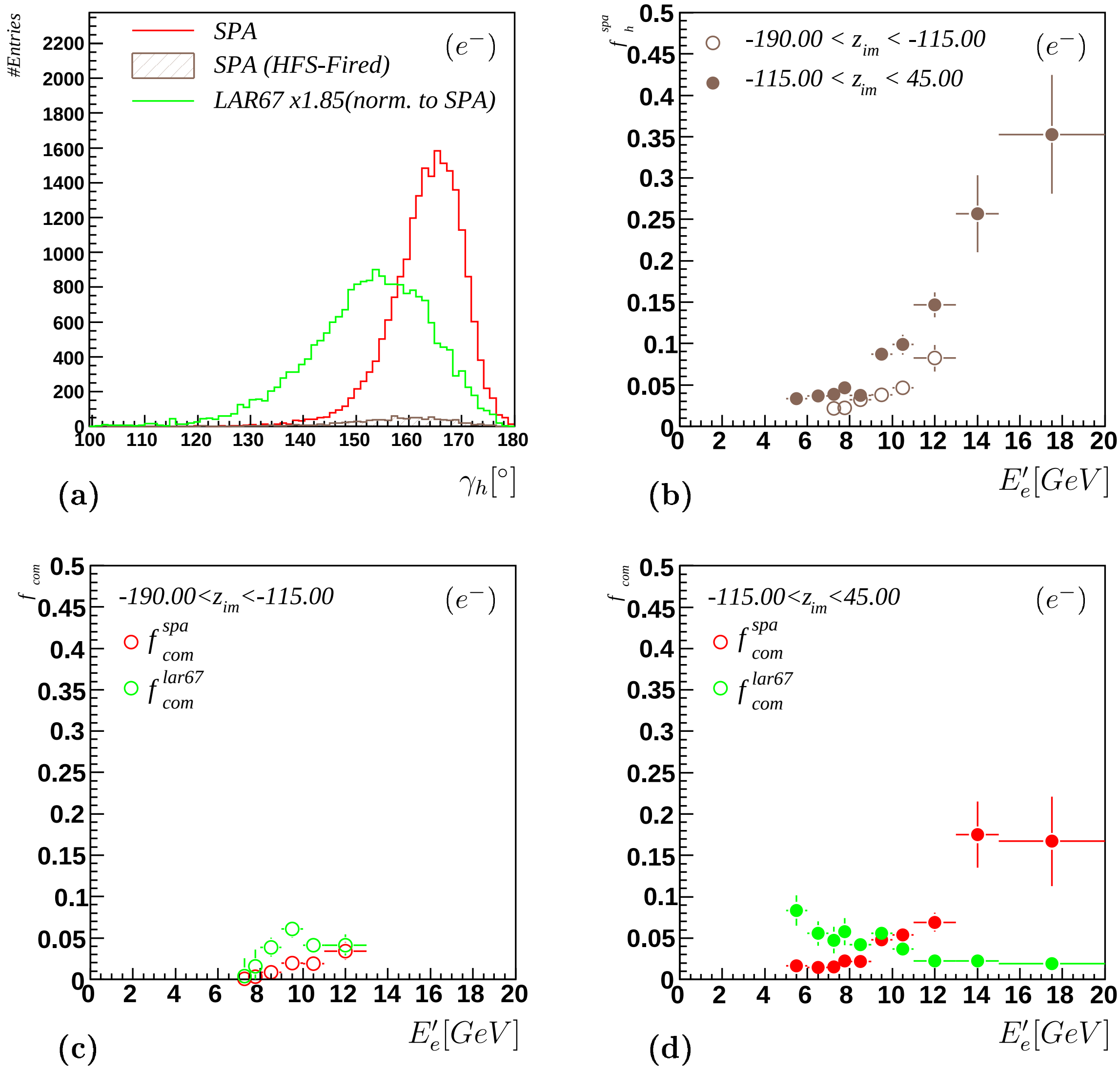

Figure 7.2: *(a) The inclusive hadronic polar angle γ_h distribution for the SPA and LAR67 monitor samples. The LAR67 sample is normalized to the number of entries in the SPA sample. Also shown are the number of events from the SPA sample fired by the HFS. In (b) the fraction of events from the SPA sample that are hfs-fired f_h^{spa} as a function of E'_e for $z_{im} < -115$ cm and $-115 < z_{im} < 45$ cm. The contribution of common events to each of the monitor samples, f_{com}^{spa} and f_{com}^{lar67} for (c) $z_{im} < -115$ cm and (d) $-115 < z_{im} < 45$ cm. Plots shown are for the e^- sample and are similar for the e^+ sample.*

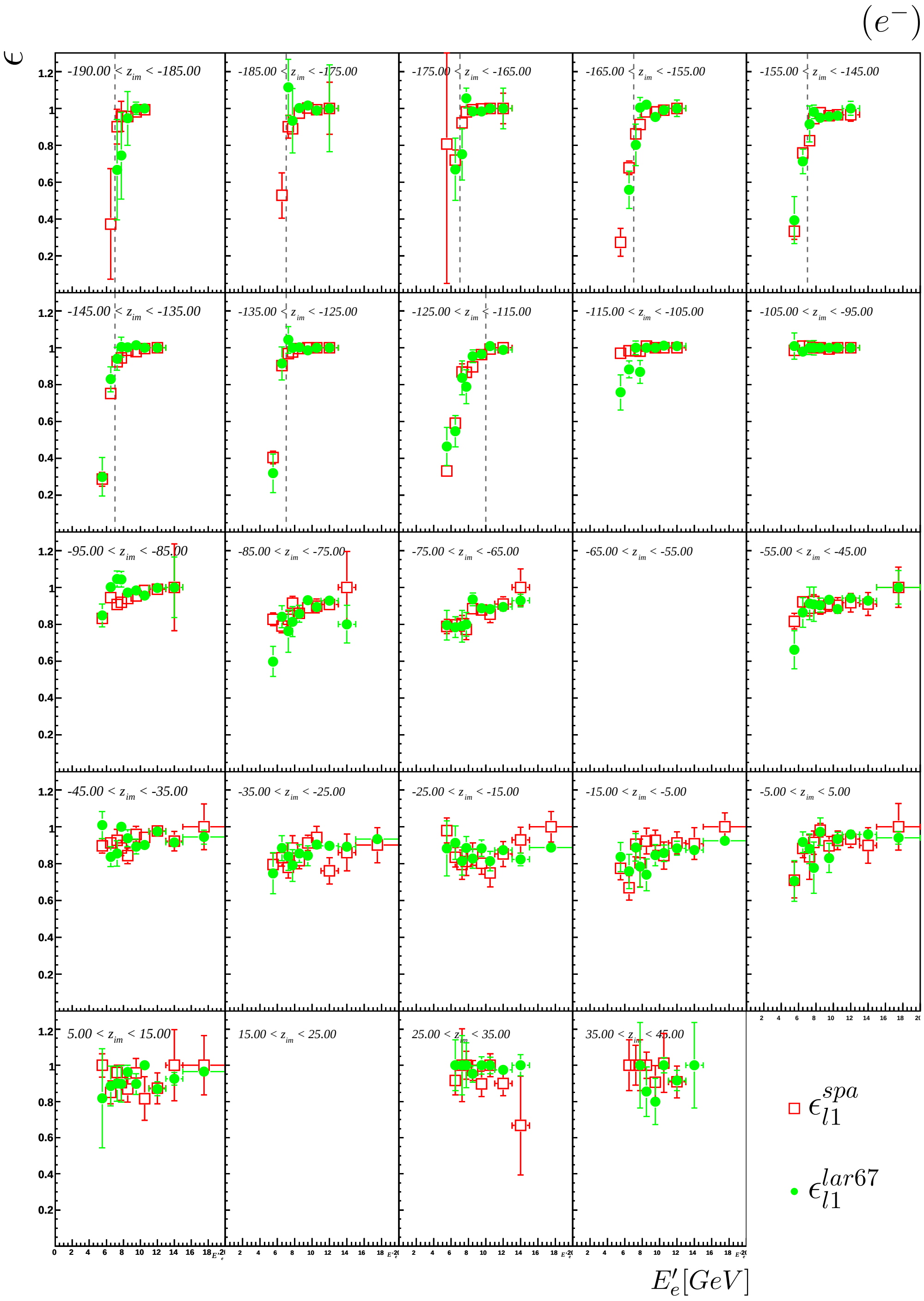

Figure 7.3: *The e-fired LAR1 efficiency binned in z_{im} as a function of electron energy E'_e as determined from the SPA and LAR67 monitor samples. Electrons with energies to the left of the vertical dashed lines for the given z_{im} bin are removed from the analysis. The measurements shown are for the e^- period.*

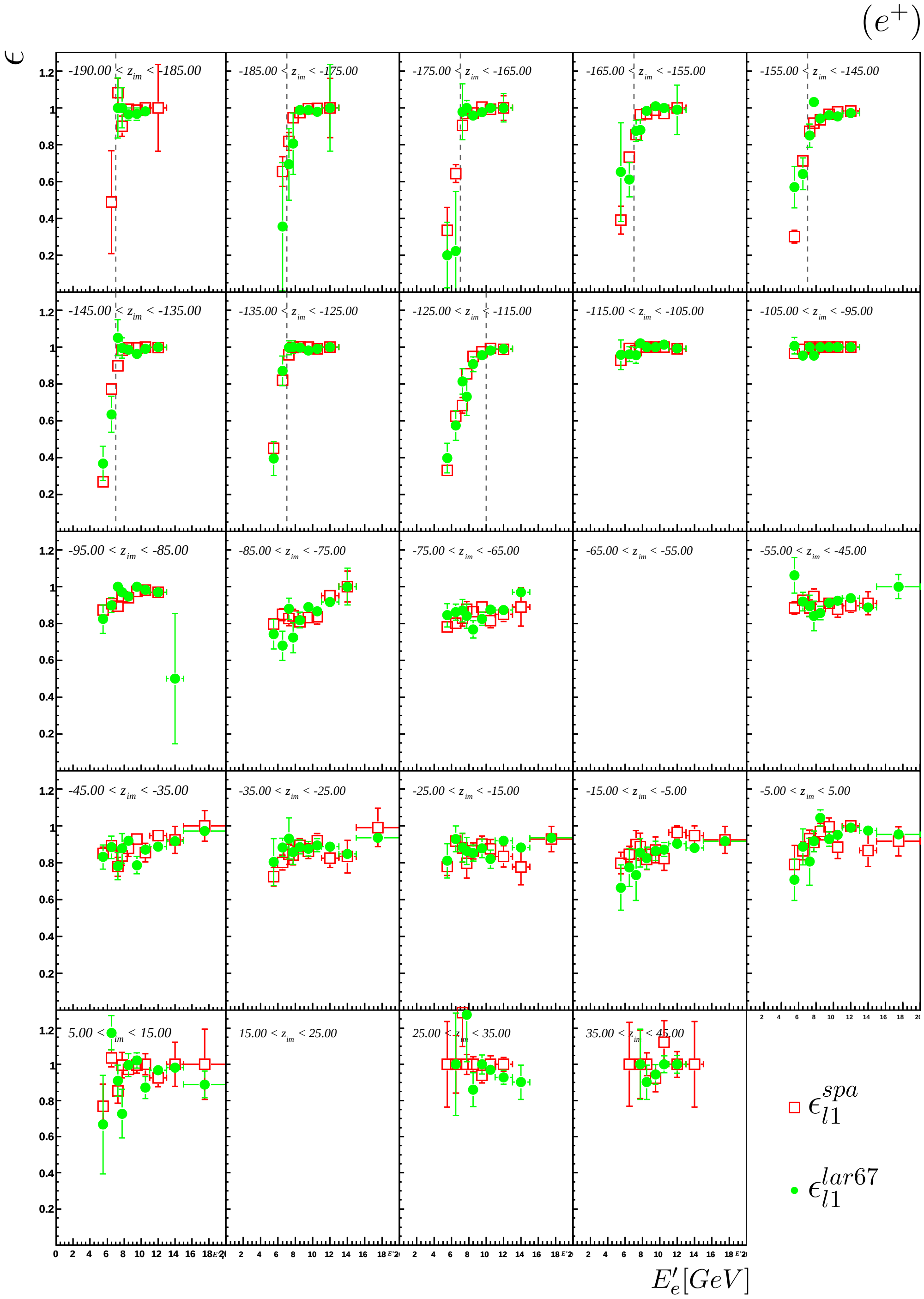

Figure 7.4: *The e-fired LAR1 efficiency binned in* z_{im} *as a function of electron energy* E'_e *as determined from the SPA and LAR67 monitor samples. Electrons with energies to the left of the vertical dashed lines for the given* z_{im} *bin are removed from the analysis. The measurements shown are for the* e^+ *period.*

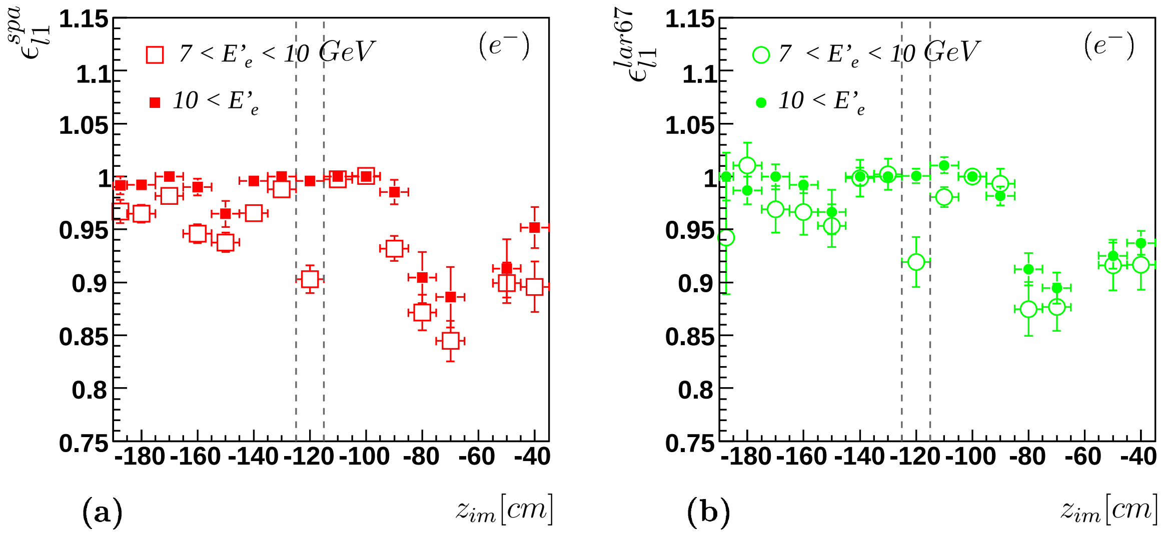

Figure 7.5: *The e-fired LAR1 efficiency binned in electron energy* E'_e *as a function* z_{im} *as determined from the (a) SPA and (b) LAR67 monitor samples. The transition region from* BT *sector* $12 \rightarrow 13$ *(*$-125 < z_{im} < -115$ *cm) is shown as the pair of dashed lines.*

as most of the significance values falls within ±1 and ±2. Figures 7.8(a) and (b) also show the distribution of the significance for the e^- and e^+ periods respectively, together with the sample mean (consistent with 0) and sample standard deviation. Since the main difference between the SPA and LAR67 samples is the amount of hadronic activity, it can be concluded that the e-fired LAR1 efficiency does not depend on the amount of hadronic activity in the event.

Having passed the level I requirement, an event must then satisfy the level II condition, LAR2. The conditional efficiency of firing on level II given that level I is already fired, $\epsilon_{l2|l1}$, is determined for each of the monitor samples and shown in figures 7.9 and 7.10 for the e^- and e^+ periods respectively. For the region $z_{im} > -115$ cm, $\epsilon_{l2|l1}$ is consistent with 1 for both the SPA and LAR67 samples. However for $z_{im} < -115$ cm, both the SPA and LAR67 measurements drop with decreasing electron energy. This is seen more clearly in figure 7.11(a), determined for the $z-$impact range $z_{im} < -115$ cm. From $\lesssim 10$ GeV the LAR67 efficiency becomes greater than the SPA efficiency, the difference increasing as the efficiency decreases. This difference in efficiencies occurs since the hadronic final state also contributes to the firing of level II, a condition which favours the LAR67 sample over the SPA sample due to its comparatively higher hadronic activity ($f_h^{lar67} > f_h^{spa}$).

Figure 7.11(b) shows events from a monitor sample classified as e-fired and h-fired as already discussed. From those events that are e-fired (n_e), some are triggered by the

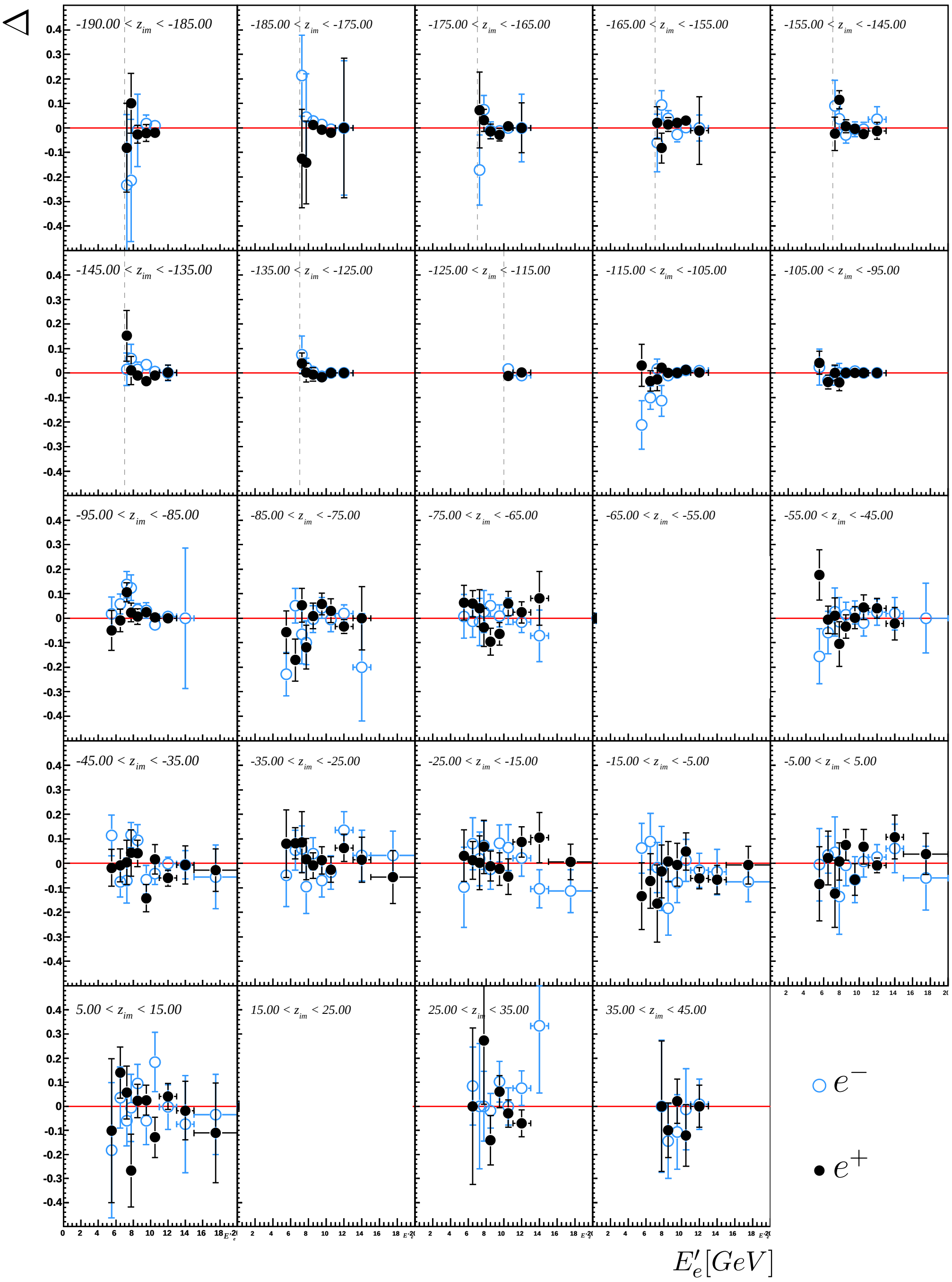

Figure 7.6: *The difference Δ between the SPA and LAR67 determined e-fired LAR1 efficiency, $\Delta = \epsilon_{l1}^{lar67} - \epsilon_{l1}^{spa}$. Results shown are for the $e^-$and e^+periods.*

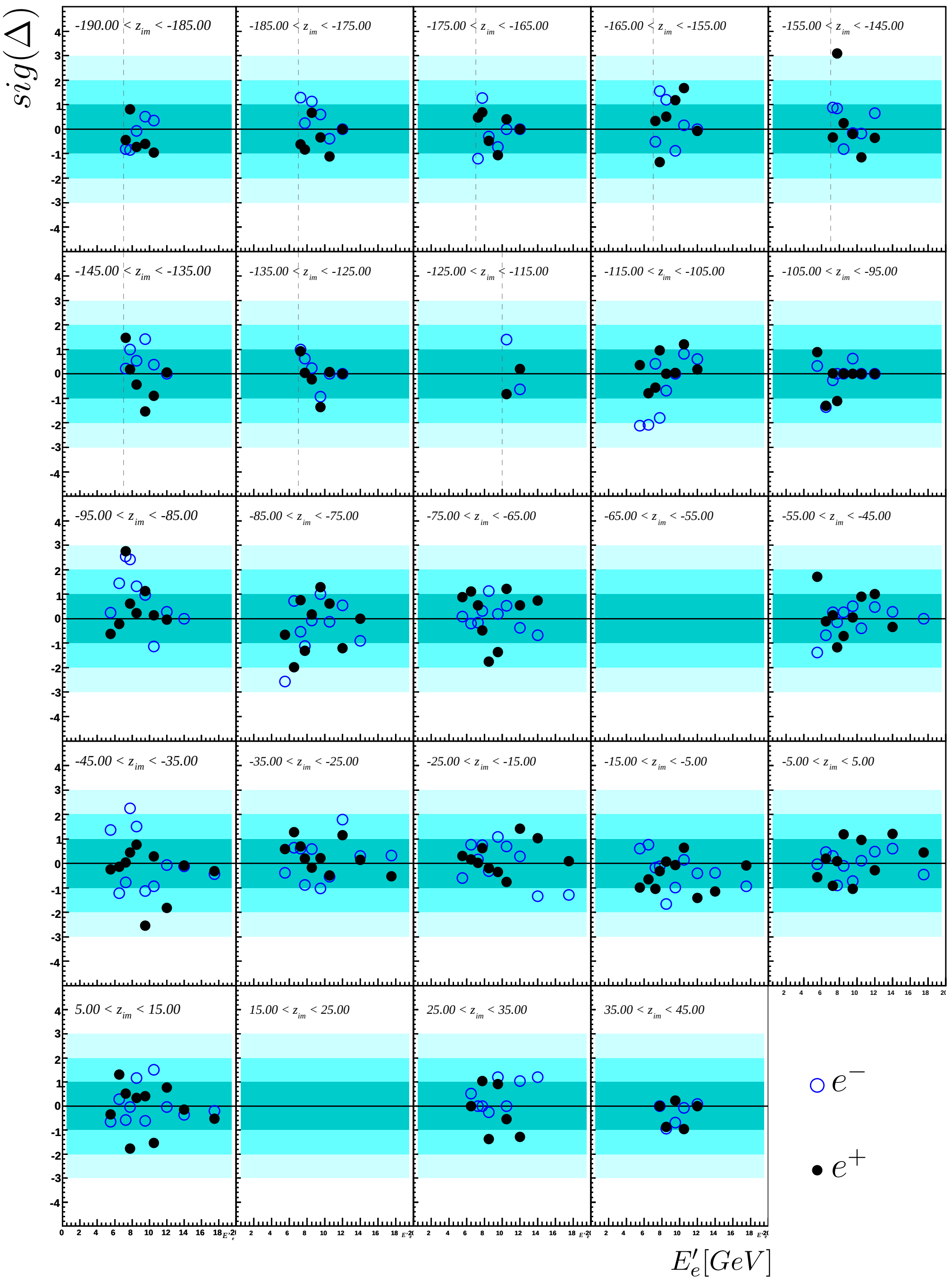

Figure 7.7: *The significance of the difference* $sig(\Delta)$ *between the SPA and LAR67 determined e-fired LAR1 efficiency. Significance bands at* ±1,±2 *and* ±3 *as indicated. Results shown are for the* e^- *and* e^+ *periods.*

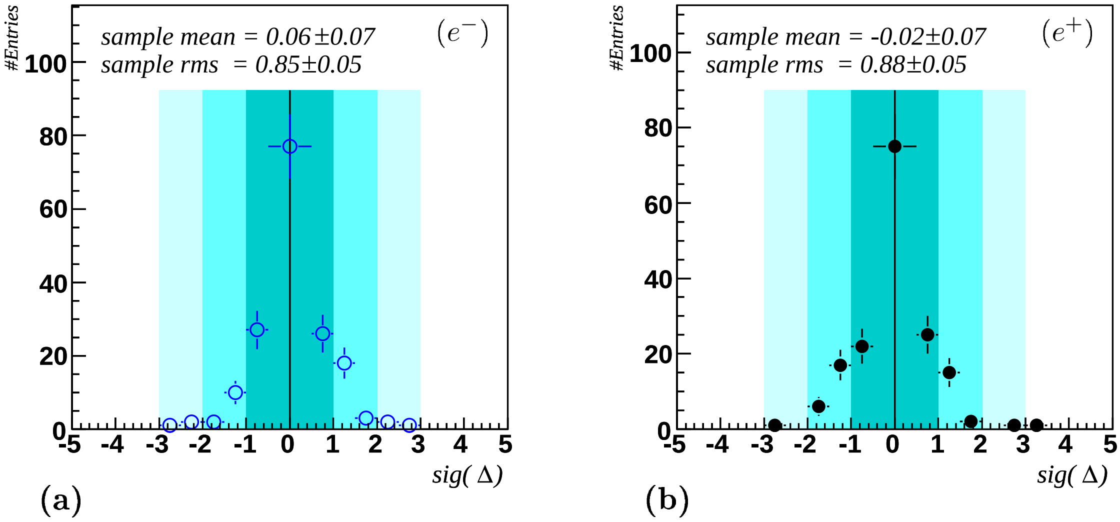

Figure 7.8: *The distribution of the significance of the difference* $sig(\Delta)$ *between the SPA and LAR67 determined e-fired LAR1 efficiency,* $\Delta = \epsilon_{l1}^{lar67} - \epsilon_{l1}^{spa}$*; (a) for the* e^- *period and (b) for the* e^+ *period.*

electron *only* (n_{eo}) and the remainder are both e-fired *and* hfs-fired (n_{eh}), that is, $n_e = n_{eo} + n_{eh}$. The conditional efficiency of firing on level II given that level I was triggered by the electron *only* (eonly-fired), was determined. The monitor sample used was those events from S^{trig} which passed s67 and were eonly-fired. The resulting efficiency $\epsilon_{l2|l1eo}^{lar67}$is also shown in figures 7.9, 7.10 and 7.11(a). Since $\epsilon_{l2|l1eo}^{lar67} \simeq \epsilon_{l2|l1}^{spa}$ the gain inefficiency $\epsilon_{l2|l1}^{lar67} - \epsilon_{l2|l1}^{spa}$ is due to the contribution of the hadronic final state firing level II. This difference introduces an added uncertainty to the efficiency determination, and is treated below in "Uncertainty on the Efficiency".

The liquid argon trigger efficiency, ϵ_{lar}, the fraction of events firing *both* the e-fired LAR1 and LAR2 conditions, determined from the SPA and LAR67 monitor samples, is shown in figures 7.12 and 7.13 for the e^- and e^+periods respectively. The efficiency used in the analysis is determined from a *combined* sample, S_M^{comb} composed of events from S_M^{spa} *or* S_M^{lar67}, that is:

$$S_M^{comb} = S_M^{spa} \cup S_M^{lar67}.$$

Since the amount of events common to the SPA and LAR67 samples is small, the size of the combined sample is approximately equal to that of the SPA and LAR67 samples added together, resulting in increased statistical precision of the resulting efficiency. The efficiency from the combined sample, ϵ_{lar}^{comb}, is also shown in figures 7.12 and 7.13.

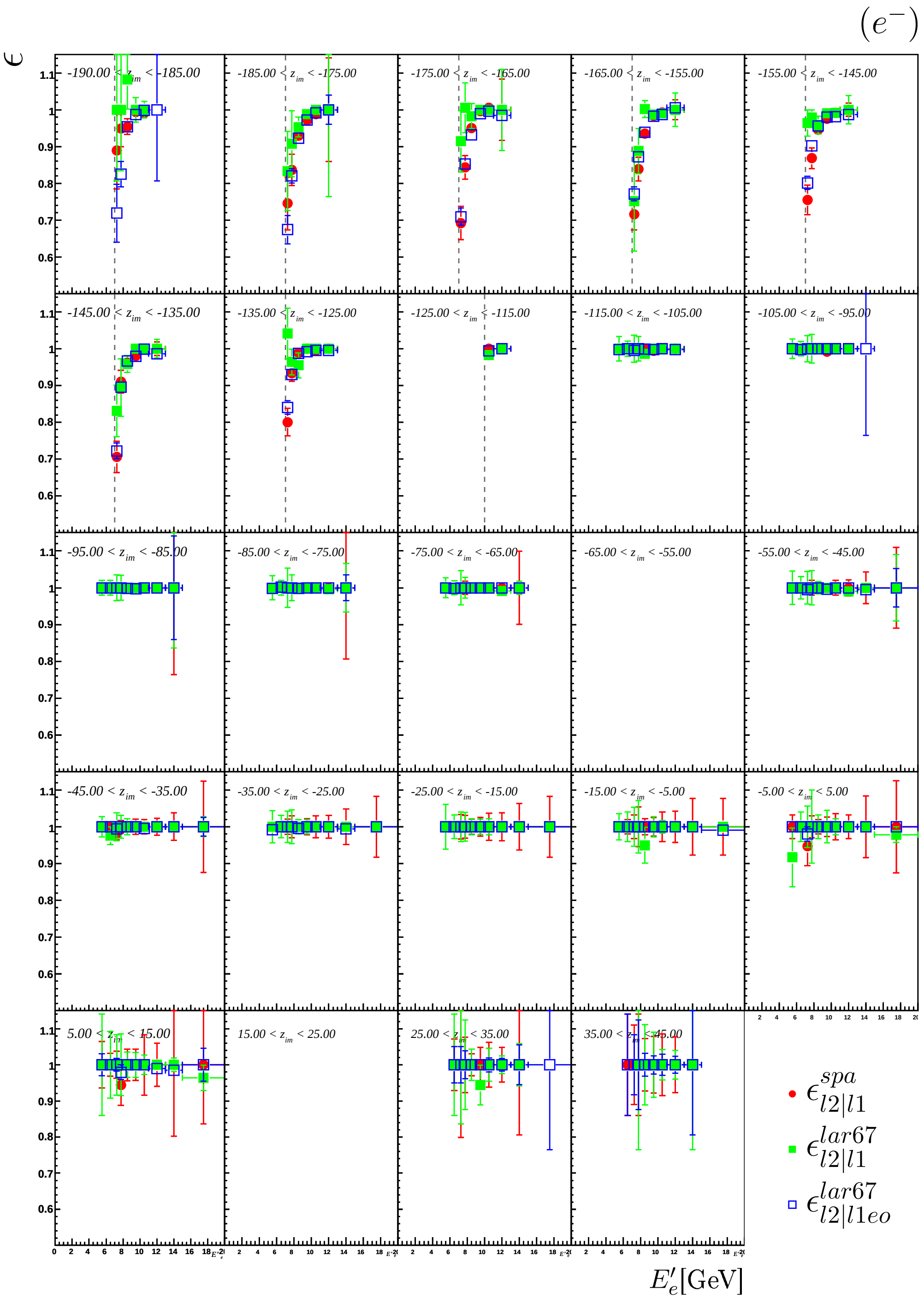

Figure 7.9: *The conditional efficiency of firing on level II (LAR2) given that the e-fired LAR1 condition is already met, $\epsilon_{l2|l1}$, binned in z_{im} as a function of electron energy E'_e as determined from the SPA ($\epsilon^{spa}_{l2|l1}$) and LAR67 ($\epsilon^{lar67}_{l2|l1}$) monitor samples. Also shown is the conditional efficiency of firing on level II given that the eonly-fired LAR1 condition is already met, $\epsilon^{lar67}_{l2|l1eo}$. The measurements shown are for the e^- period.*

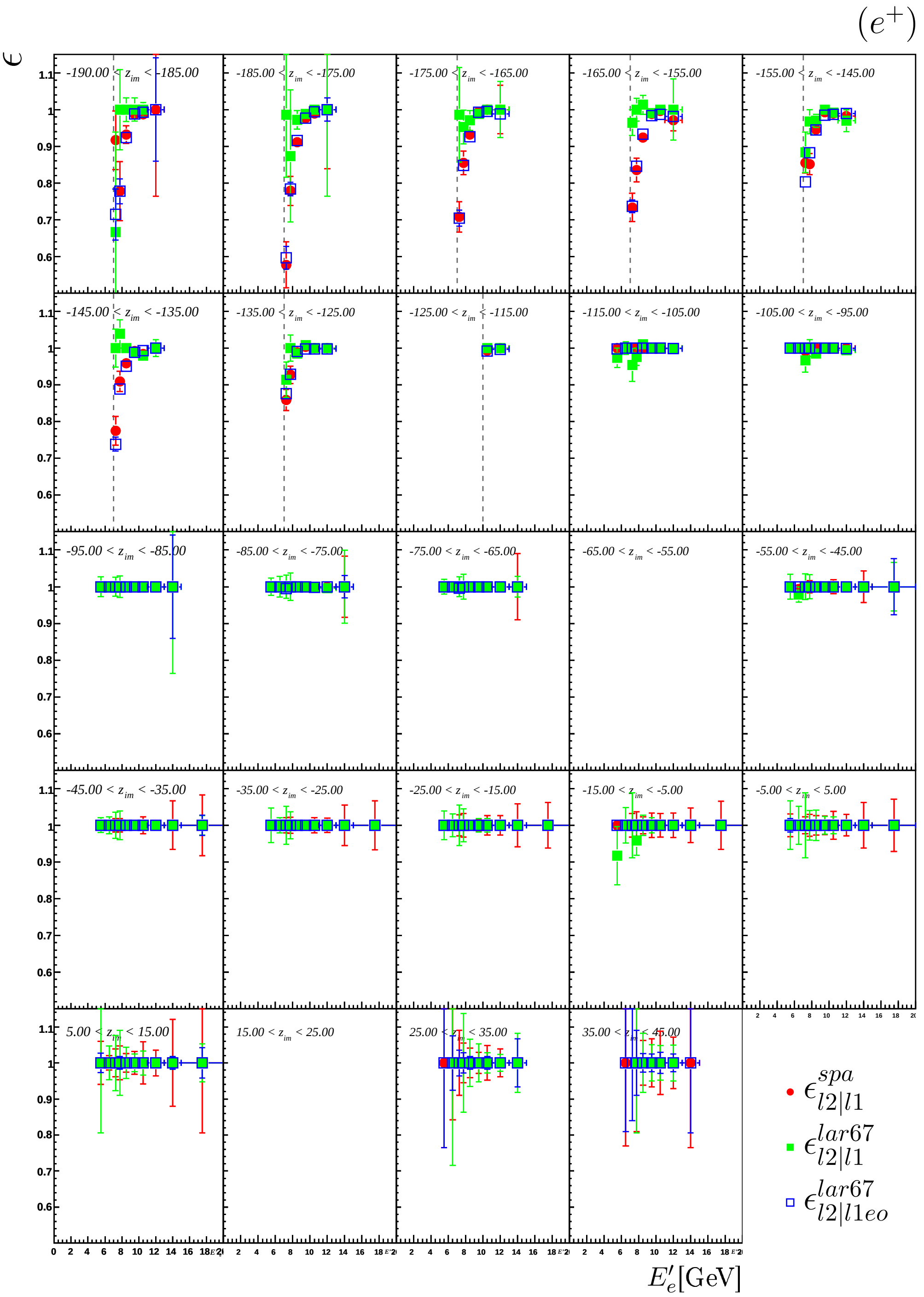

Figure 7.10: *The conditional efficiency of firing on level II (LAR2) given that the e-fired LAR1 condition is already met,* $\epsilon_{l2|l1}$*, binned in* z_{im} *as a function of electron energy* E'_e *as determined from the SPA (*$\epsilon^{spa}_{l2|l1}$*) and LAR67 (*$\epsilon^{lar67}_{l2|l1}$*) monitor samples. Also shown is the conditional efficiency of firing on level II given that the eonly-fired LAR1 condition is already met,* $\epsilon^{lar67}_{l2|l1eo}$*. The measurements shown are for the* e^+ *period.*

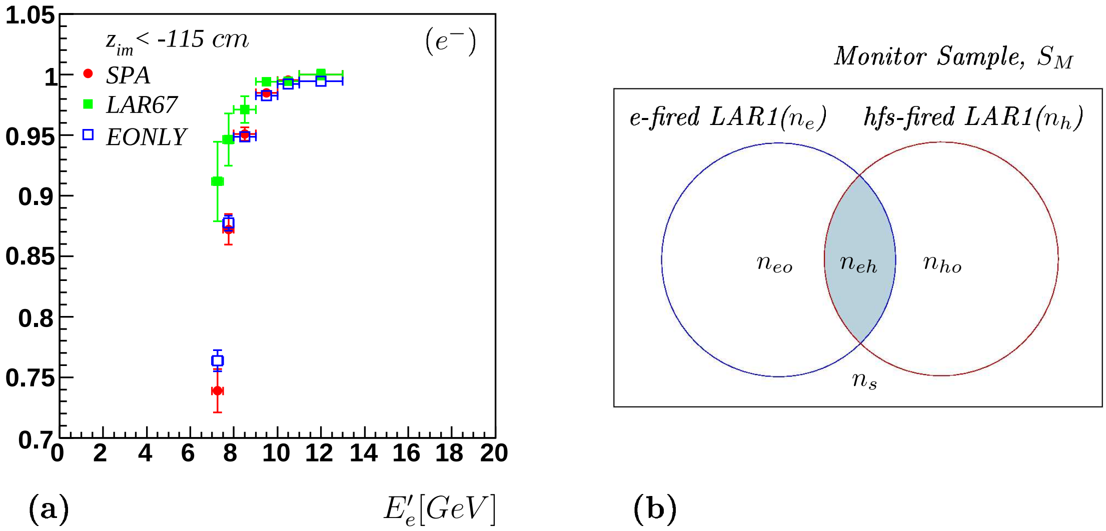

(a) (b)

Figure 7.11: *(a) The conditional efficiency of firing on level II (LAR2) given that the e-fired LAR1 condition is already met as determined from the SPA and LAR67 monitor samples as well as the conditional efficiency given that the eonly-fired LAR1 condition is already met, EONLY. The measurements shown are for the e^- period. (b) LAR1 Event classification: e-fired (n_e), hfs-fired (n_h), eonly-fired (n_{eo}), hfs only-fired (n_{ho}), e-fired and hfs-fired (n_{eh}), fired but neither classified as e-fired (not within blue box of figure 7.1) nor as hfs-fired ($|\Delta\phi| \not> 50°$), (n_s).*

The liquid argon trigger efficiency used in the analysis to reweight the MC events, ϵ_{lar}, is taken from the combined sample, that is:

$$\epsilon_{lar} = \epsilon_{lar}^{comb}. \tag{7.3}$$

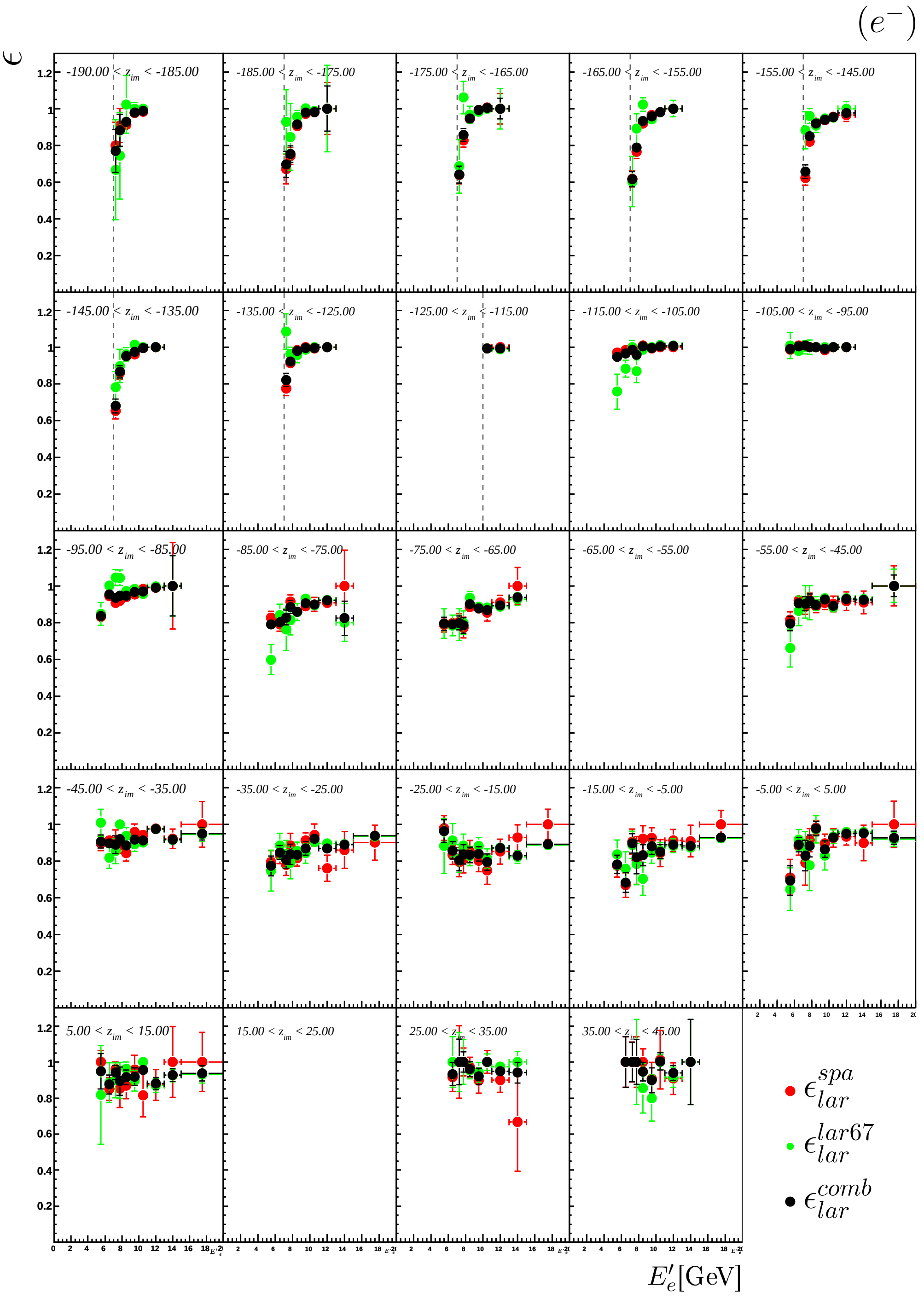

Figure 7.12: *The LAR efficiency ϵ_{lar}, binned in z_{im} as a function of electron energy E'_e as determined from the SPA, LAR67 and COMB monitor samples. The measurements shown are for the e^- period.*

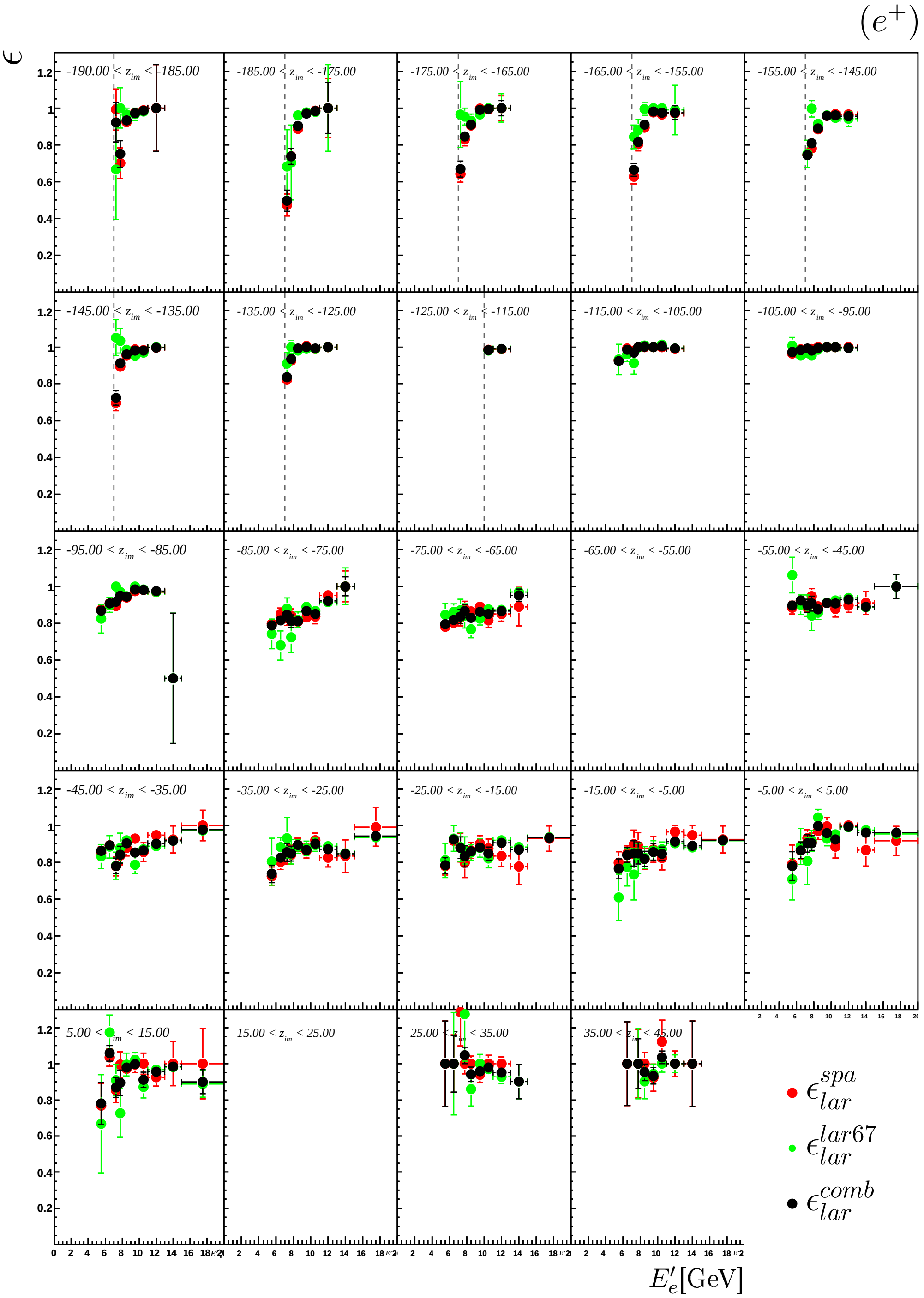

Figure 7.13: *The LAR efficiency ϵ_{lar}, binned in z_{im} as a function of electron energy E'_e as determined from the SPA, LAR67 and COMB monitor samples. The measurements shown are for the e^+ period.*

Testing the Reweight Variables and Bin Size

In order to test that the LAR efficiency, ϵ_{lar}, is adequately described by the reweighting variables E'_e and z_{im}, and that the chosen E'_e-z_{im} binning is of suitable size, the combined monitor sample S_M^{comb} is divided into two statistically independent subsamples $S_M^{comb,even}$ and $S_M^{comb,odd}$ defined by:

$$\begin{aligned} S_M^{comb,even} &\equiv \{0th\ event, 2nd\ event, 4th\ event...\} \\ S_M^{comb,odd} &\equiv \{1st\ event, 3rd\ event, 5th\ event...\}. \end{aligned}$$

Corresponding even and odd efficiencies $\epsilon_{lar,even}$ and $\epsilon_{lar,odd}$ are measured from the even and odd subsamples respectively and are shown in figure 7.14, together with the "full" efficiency ϵ_{lar}.

A prediction n'_e for the number of events triggered from the even subsample in a given bin for any variable is then made by summing the number of events from the even subsample weighted by the odd efficiency $\epsilon_{lar,odd}$; so that for a given bin:

$$n'_e = \sum_{i=1}^{N_e} \epsilon^i_{lar,odd}(E'_e, z_{im}) \qquad : i \in S_M^{spa,even}, \tag{7.4}$$

where N_e is the number of events in the given bin from the even subsample and E'_e and z_{im} are the electron energy and z-impact of the ith event in the bin. The prediction n'_e is then compared to the number of events actually triggered from the even subsample by the LAR condition, n_e. Since the odd efficiency is statistically independent from the even subsample, fluctuations in the prediction n'_e and the number of events actually triggered n_e are uncorrelated.

Figures 7.15(a) shows the z_{im} distribution for the even subsample, the triggered events and the prediction. Also shown is the ratio of triggered events to prediction, r $(=n_e/n'_e)$ using statistical errors for n_e and zero error for the prediction n'_e. A $y = constant$ fit is also made. The bin size used in the plot is 5cm. The bin size used to measure the odd efficiency is shown as the grid of dashed lines which is *not* the grid used in the analysis but approximately corresponds to the BT sector divisions (the electron energy is binned using the analysis binning). It can be observed that there is significant disagreement between prediction and actually triggered events *within* an efficiency bin as the ratio r fluctuates systematically upward (where the prediction is too low) and downward (prediction too high). This occurs because the interval in z_{im} is too large to perform an averaging of the efficiency. The fluctuations are correspondingly seen in the electron polar angle distribution, figure 7.15(b). In 7.15(c) the odd efficiency is binned using the analysis binning (10 cm for all bins except the first bin of 5 cm) and the fluctuations in r are smoothened to

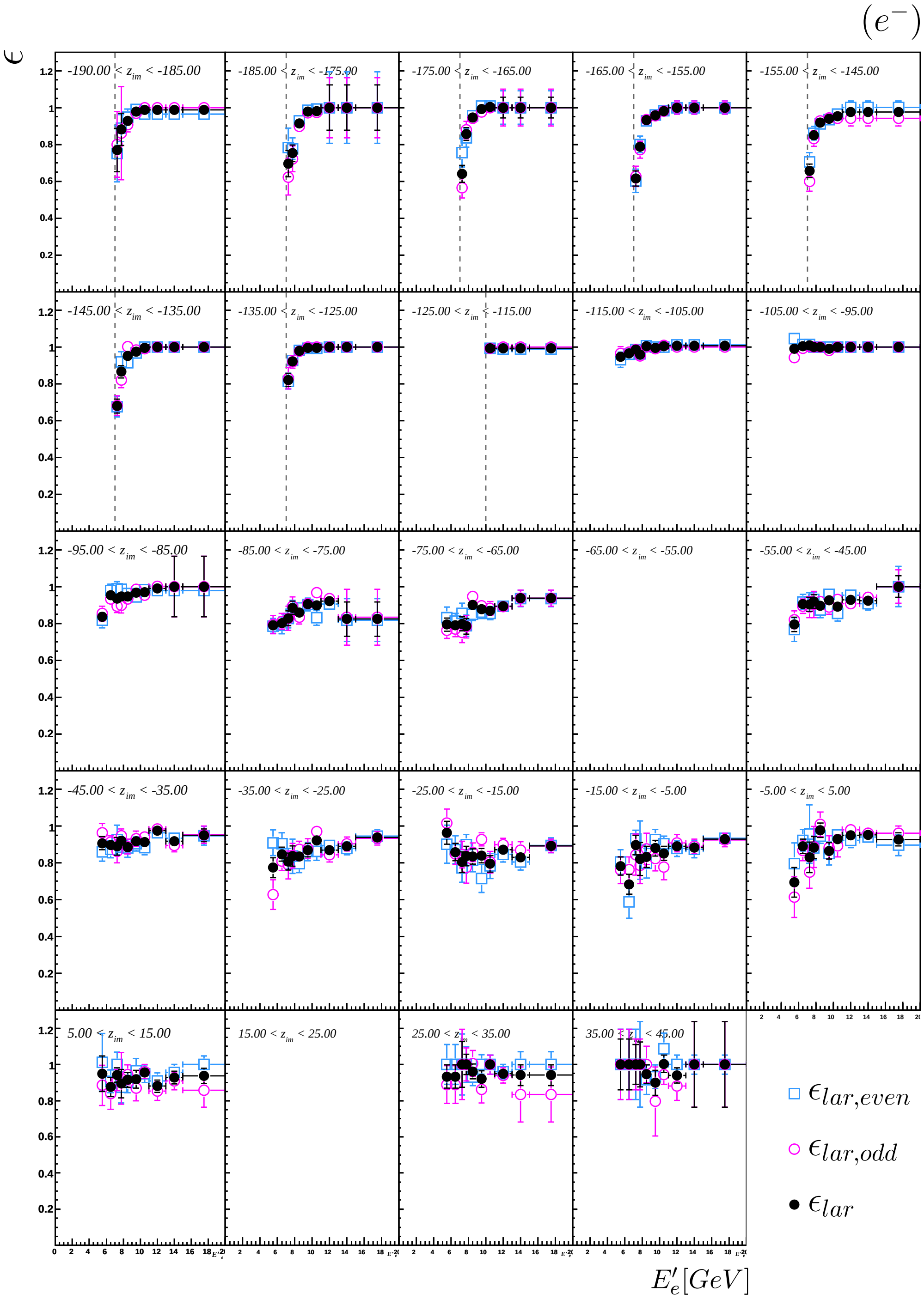

Figure 7.14: *The LAR efficiency as determined from the even subsample, $\epsilon_{lar,even}$, odd subsample, $\epsilon_{lar,odd}$ and the full sample, ϵ_{lar}. The measurements shown are for the e^- period.*

within ±5 %. The corresponding improvement is seen in figure 7.15(d) for the electron polar angle.

In figure 7.16(a) the electron energy distribution for the even subsample, the triggered events and the prediction (using the analysis E'_e-z_{im} binning) is shown, while figure (b) shows the inelasticity y_e which has a strong dependence on electron energy, equation 8.1. In both plots the level of agreement between the prediction and the actual events triggered are good. In figures 7.16(c) and (d) the corresponding distributions for Q^2 is given for the e^- and e^+ periods respectively.

Figure 7.17(a) shows the ϕ_{im} distribution as well as r as a function of ϕ_{im} using the analysis E'_e-z_{im} binning. As expected, the prediction *overestimates* where the ϵ_{lar} is *low* and underestimates where ϵ_{lar} is high, figure 7.17(b). This occurs since the reweighting function does not take into account the ϕ_{im} dependence for a given (E'_e-z_{im}) bin but averages over all ϕ_{im}. This does not affect the kinematics (figures 7.16 (b) and (c)).

Since the agreement is good between the prediction and the number of events actually triggered for the kinematic variables a shown, it can be concluded that the LAR condition is sufficiently described by the detector variables E'_e and z_{im} in the chosen binning scheme.

Uncertainty on the Efficiency

The relative statistical error[1] $\delta^{stat}_{\epsilon_{lar}}$ on ϵ_{lar} is shown in figure 7.18 for the e^- and e^+ periods. Were it not for the role of the hadronic final state in firing the level II liquid argon condition, the efficiencies measured from the SPA and LAR67 samples would be consistent. The differences between ϵ^{spa}_{lar} and ϵ^{lar67}_{lar} exist only in the region $z_{im} < -115$ cm for electron energies $E'_e \lesssim 9$ GeV. The systematic uncertainty on ϵ_{lar} in each E'_e-z_{im} bin is thus estimated from the difference Δ between the efficiencies of the two monitor samples times the fraction of the events in the final analysis selection that are fired by both the electron and the HFS, f_{eh}:

$$\Delta^{sys}_{\epsilon_{lar}} = f_{eh} \times \Delta.$$

The difference between the LAR67 and SPA efficiencies is shown in figures 7.19(a) and (b) for the e^- and e^+ periods where the z_{im} range is limited to $z_{im} < -115$ cm. Since the difference $\epsilon^{lar67}_{lar} - \epsilon^{spa}_{lar}$ is similar for both periods, a Δ function that characterizes both periods is used as indicated by the histogram, and table 7.1. The fraction of the final event sample that are both e-fired and hfs-fired is shown in figure 7.20 with the Δ function.

---

[1] The convention used throughout this thesis is that the symbol Δ_S is used for the 1σ absolute error and δ_S for the 1σ relative error on the *source* of error S. The *effect* on the cross section of the source S by its 1σ variation is indicated by Δ^S for absolute and δ^S for relative error. The super- and sub-scripts *stat* and *sys* will represent statistical and systematic contributions to the error respectively. So for example, the relative statistical error on the efficiency ϵ, δ^{stat}_{ϵ} ($=\Delta^{stat}_{\epsilon}/\epsilon$) results in a relative error on the cross section of δ^{ϵ}_{stat} ($=\Delta^{\epsilon}_{stat}/\sigma$). The terms "error" and "uncertainty" are used interchangeably.

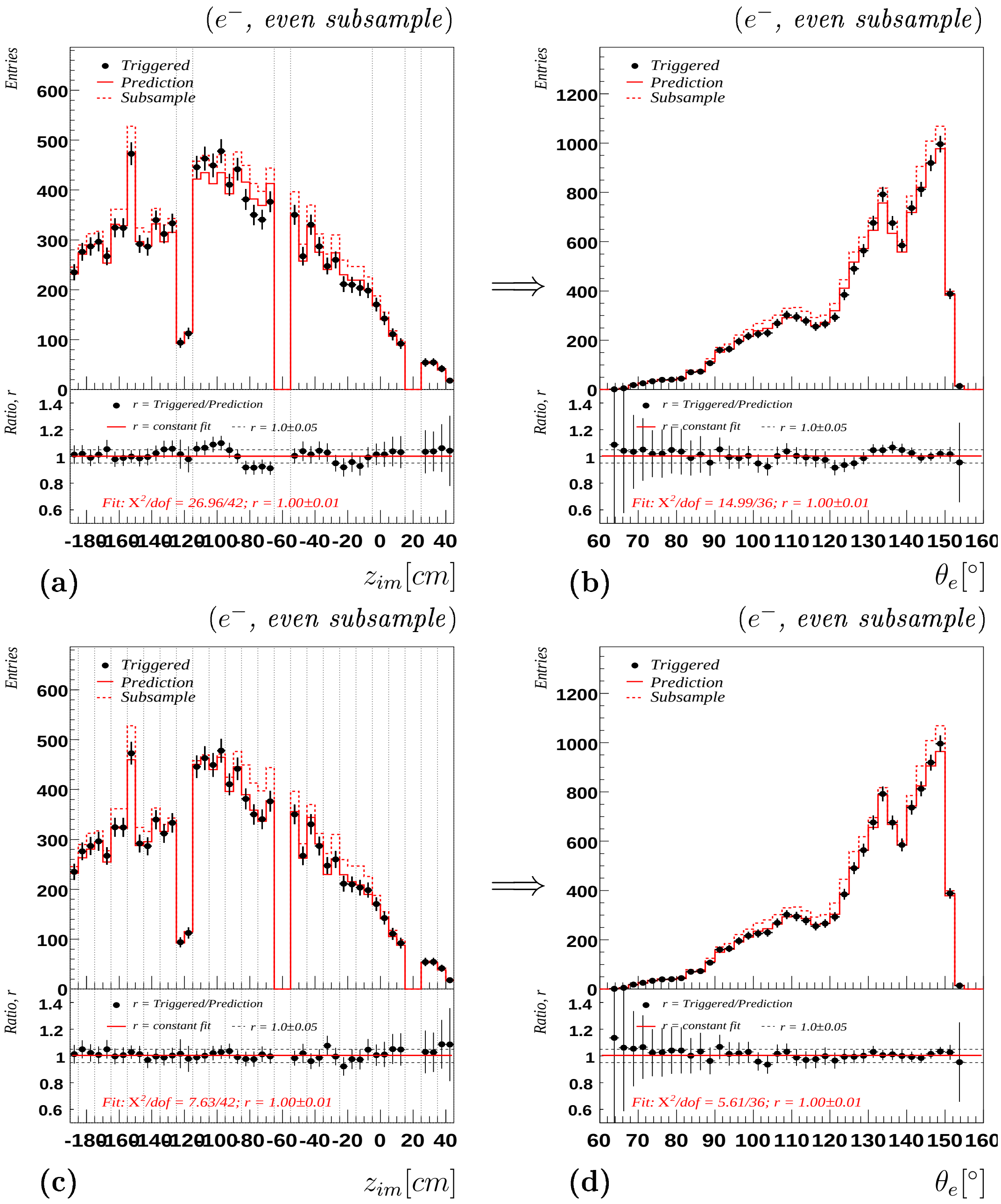

Figure 7.15: *Testing the* z_{im} *binning: (a) The* z_{im} *distribution for the even subsample, LAR triggered events and the prediction. The ratio* $r = n_e/n'_e$ *between the number of triggered events and the prediction together with a* $y = constant$ *fit are shown. The* E'_e*binning used for the odd efficiency is the same as in the analysis, but the* z_{im} *binning is much wider than that used in the analysis as seen by the dashed lines. (b) The resulting electron polar angle distributions using the* z_{im} *binning in (a). In (c) the efficiency is binned in* z_{im} *using the analysis* z_{im} *binning and in (d) the resulting distributions in the electron polar angle are shown. Plots are for the* e^- *period, even subsample.*

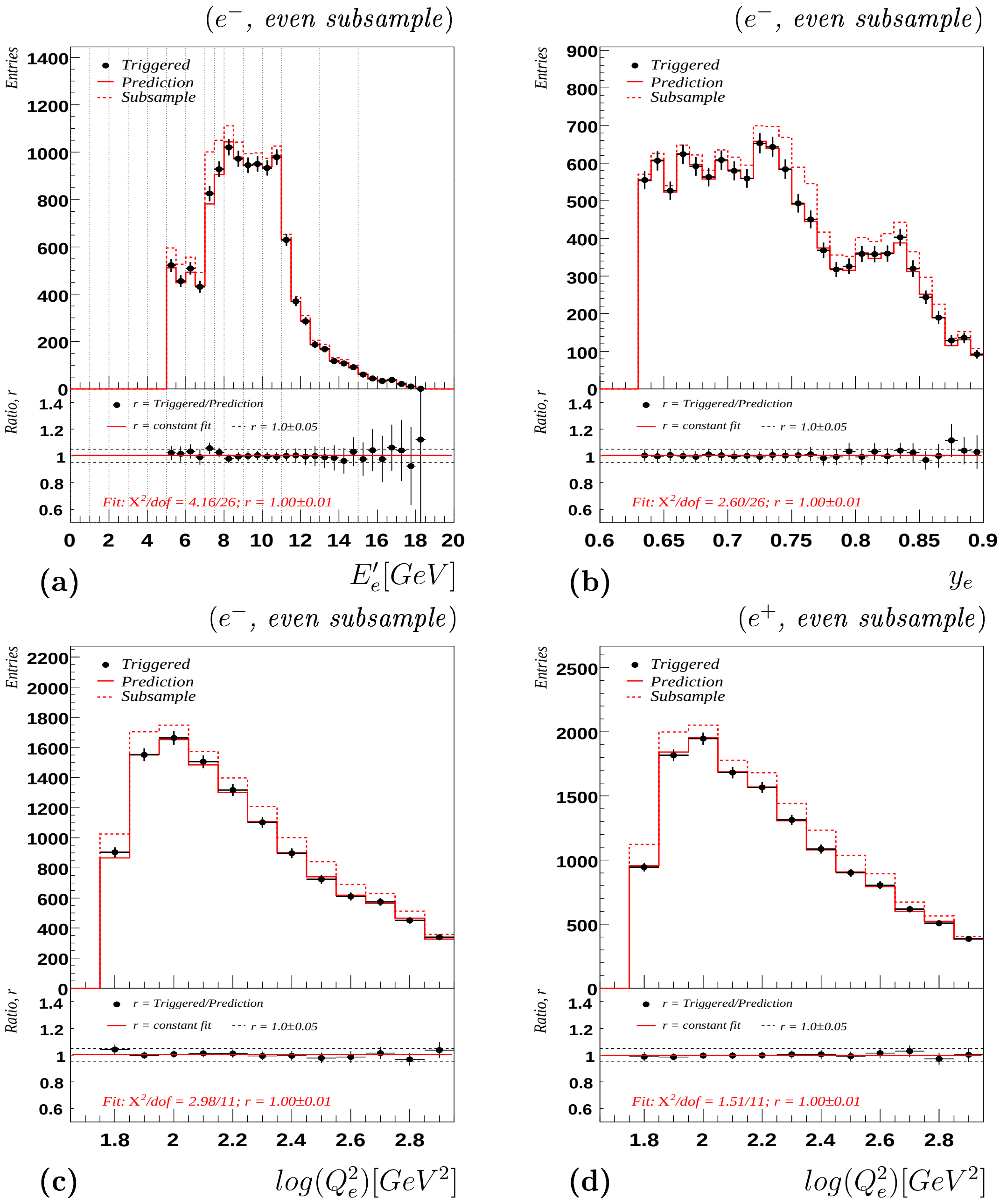

Figure 7.16: *The (a) electron energy, (b) inelasticity y_e and (c) Q^2_e distributions for the e^- even subsample, LAR triggered events and the prediction. The ratio $r = n_e/n'_e$ between the number of triggered events and the prediction together with a $y =$ constant fit are shown. The E'_e-z_{im} binning used for the odd efficiency corresponds to that used in the analysis. In (d) similar plots are given for the Q^2_e distributions for the e^+ even subsample.*

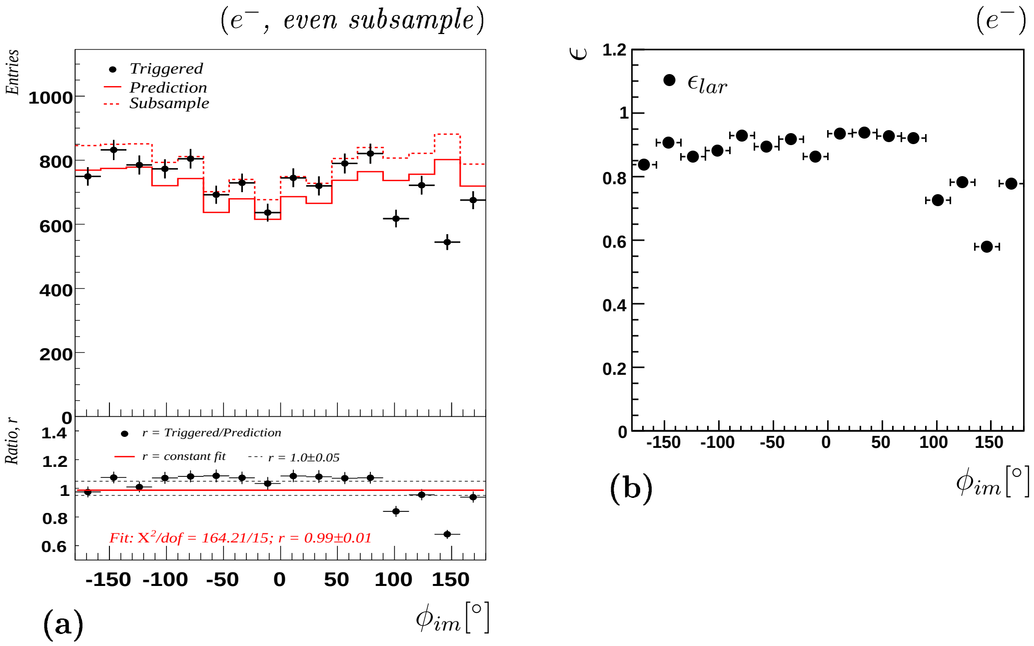

Figure 7.17: *(a) The ϕ-impact ϕ_{im} distribution for the even subsample, LAR triggered events and the prediction. The ratio $r = n_e/n'_e$ between the number of triggered events and the prediction together with a $y = constant$ fit are shown. The E'_e-z_{im} binning used for the odd efficiency corresponds to that used in the analysis. (b) ϵ_{lar} as a function of ϕ_{im}.*

Finally the relative LAR systematic uncertainty $\delta^{sys}_{\epsilon_{lar}}$ is shown on the same plot. The low values of f_{eh} in the region where a systematic uncertainty is quoted, $\lesssim 10\%$ results in relative systematic uncertainties of typically 2% and less.

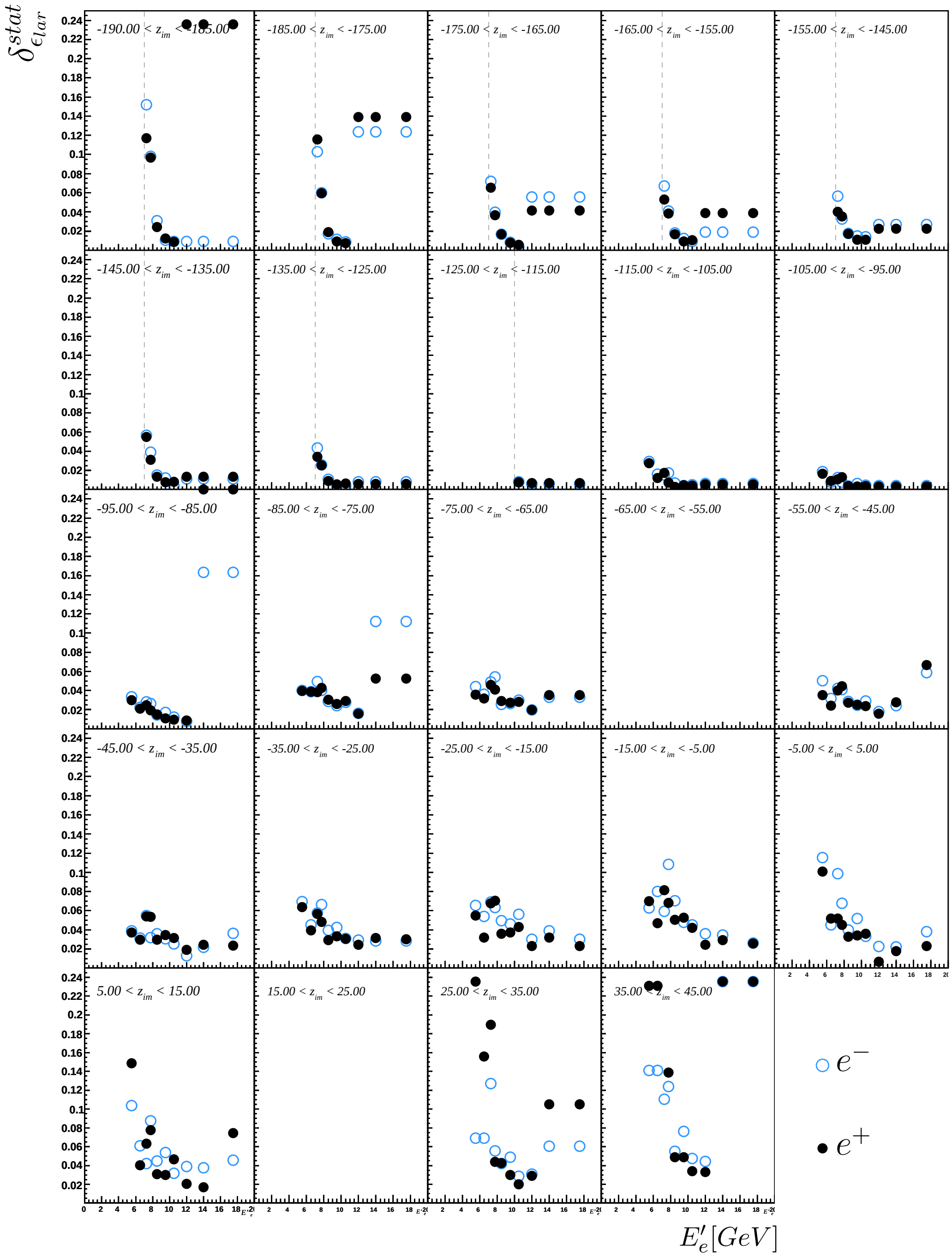

Figure 7.18: *The relative statistical error* $\delta^{stat}_{\epsilon_{lar}}$ *on* ϵ_{lar} *for the* e^- *and* e^+ *periods.*

Range in z_{im}	Range in E'_e	LAR Systematic Uncertainty ($=f_{eh} \times \Delta$)
$z_{im} < -115cm$	$7.0 < E'_e < 7.5$	$f_{eh}(E'_e, z_{im}) \times 17.0$ %
	$7.5 < E'_e < 8.0$	$f_{eh}(E'_e, z_{im}) \times 12.0$ %
	$8.0 < E'_e < 9.0$	$f_{eh}(E'_e, z_{im}) \times 3.50$ %
	$9.0 < E'_e$	0.0
$z_{im} > -115cm$		0.0

Table 7.1: *The systemtic uncertainty on the LAR efficiency. The values given apply to both the* e^+ *and* e^- *samples.*

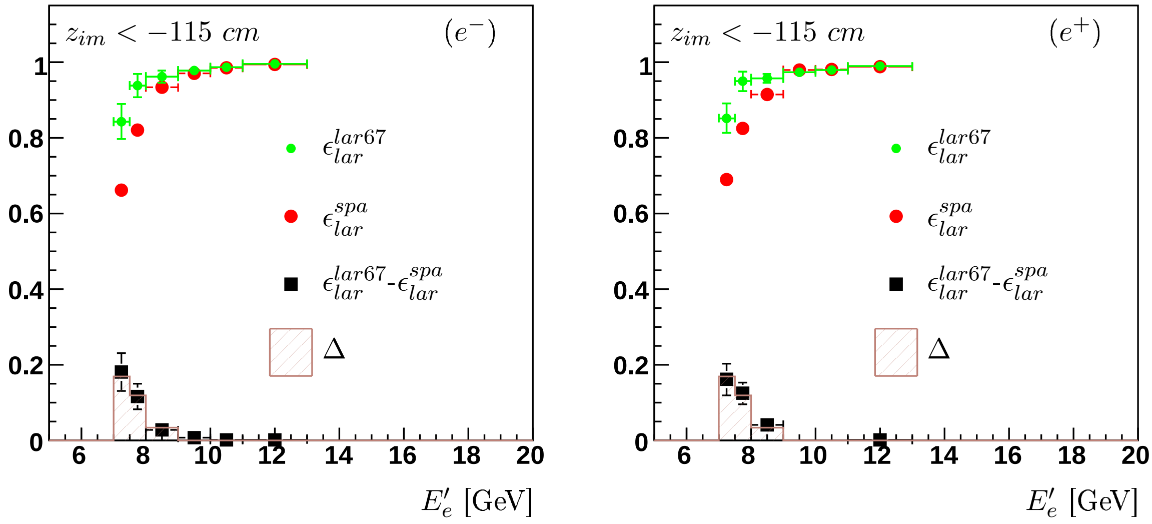

Figure 7.19: *The difference between the LAR efficiencies as determined from the SPA and LAR67 samples, (a) for the* e^- *sample and (b) for the* e^+ *sample as a function of electron energy for the range* $z_{im} < -115$ *cm. One function* Δ *is used to characterize this difference for both periods.*

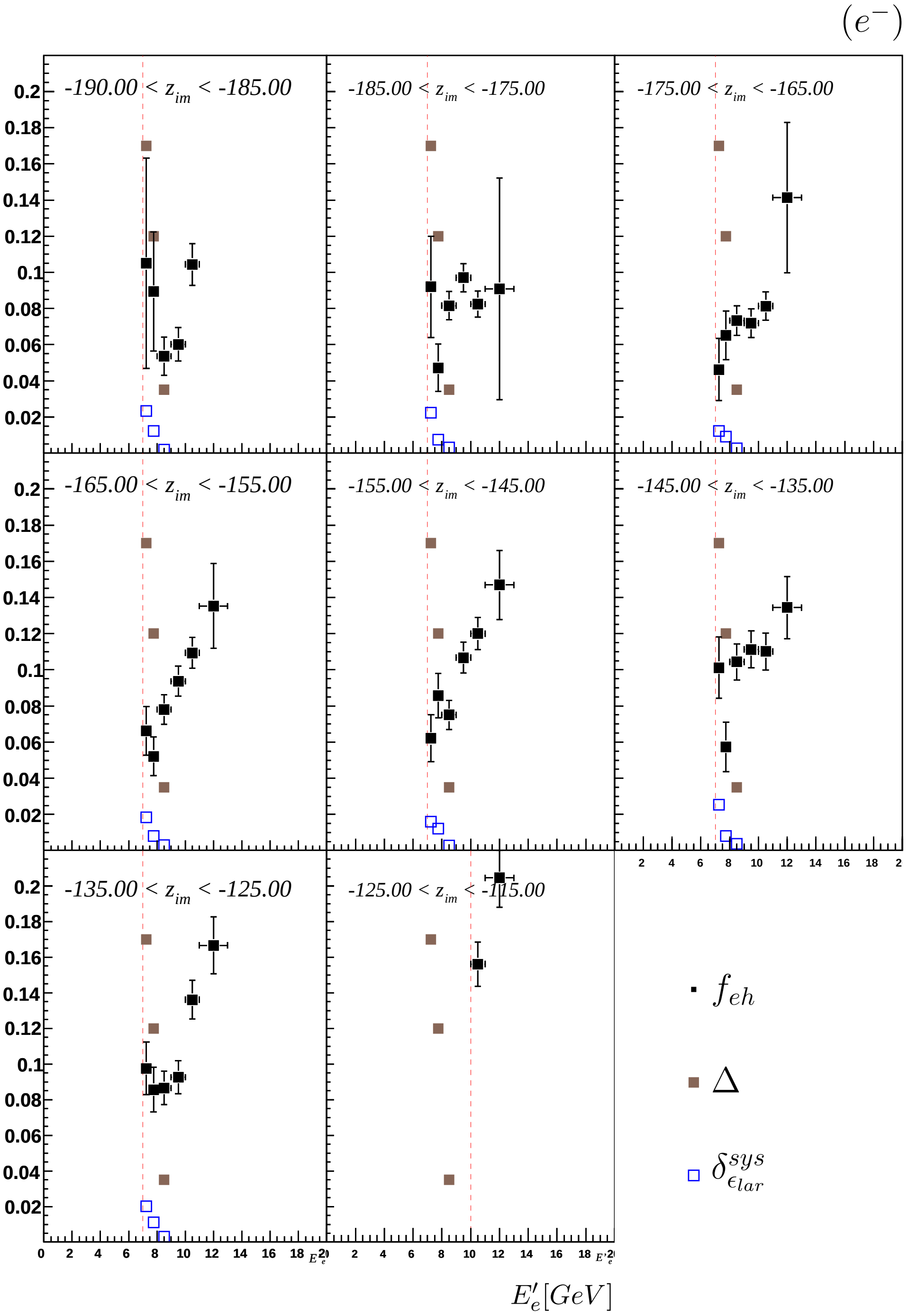

Figure 7.20: *The fraction of the final event sample where the LAR condition is met by both the electron and hadronic final state at level I, f_{eh}, the difference function Δ between ϵ_{lar} as determined from the LAR67 and SPA monitor samples and the relative systematic error on the LAR efficiency $\delta^{sys}_{\epsilon_{lar}}$. The plot is for the e^- sample.*

Run No	TRK	T0	TT0
357149-401616	`DCRPh_THig`	`CIP_T0`	`DCRPh_THig` && `CIP_T0`
$\geqslant$401617	`FTT_mul_Td>0`	`CIP_T0`	`FTT_mul_Td>0` && `CIP_T0`

Table 7.2: *The TRK, T0 and TT0 conditions as a function of time.*

7.3 Track and Timing Conditions - TT0

The TRK condition included in the s75 definition requires the presence of at least one track of minimum transverse momentum p_t. Over the course of the data taking, the trigger system used to define the TRK condition changed from the dcrϕ trigger (where the `DCRPh_THig` trigger element was used) to the the Fast Track Trigger (`FTT_mul_Td` trigger element used), table 7.2 and section 2.6. The difference between the two trigger elements is more than the minimum cut on p_t would suggest - 800 MeV for the dcrϕ trigger and 900 MeV for the FTT - as the FTT has a much more precise track counting and a better p_t-resolution than the dcrϕ system. The `CIP_T0` trigger element (section 2.6) is also included in the definition of s75 and is asserted to 1 if the CIP detector reconstructs a central track. Together the TRK and T0 conditions constitute the TT0 condition:

$$TT0 = TRK \ \ \&\& \ \ T0$$

as shown in table 7.2.

The TT0 efficiency is studied using a LAR monitor sample built from S^{trig} where events are required to be triggered by s67 and which has the `LAr_T0` condition asserted to 1; the Fiducial Volume cuts of table 7.8 are applied. Figure 7.21(a) and (b) show the measured efficiency as a function of $N_{trk}^{0.75}$, the number of tracks in an event with minimum transverse momentum of 0.75 GeV, for the e^- and e^+ periods respectively. The sub-periods are also shown. The first bin, $N_{trk}^{0.75} = 1$ corresponds to the efficiency of the scattered electron triggering the TT0 condition. As $N_{trk}^{0.75}$ increases the HFS tracks contribute to the efficiency which quickly plateaus once there are $N_{trk}^{0.75} \approx 5$ tracks in the event. The TT0 efficiency for the 0304e^+sub-period (and hence the e^+ period) is significantly lower compared to the other periods indicating the improvement in switching from the dcrϕ trigger to the FTT.

Testing the Reweight Variable

The suitability of $N_{trk}^{0.75}$ as a MC reweighting variable for the TT0 efficiency is tested using the same procedure used to test the suitability of electron energy and impact position for the LAR efficiency, section 7.2. Figure 7.22(a) to (d) show the results of the test for electron energy, electron polar angle, y_e and Q_e^2 for the e^- sample. The agreement between the number of actual triggered events and the prediction is good.

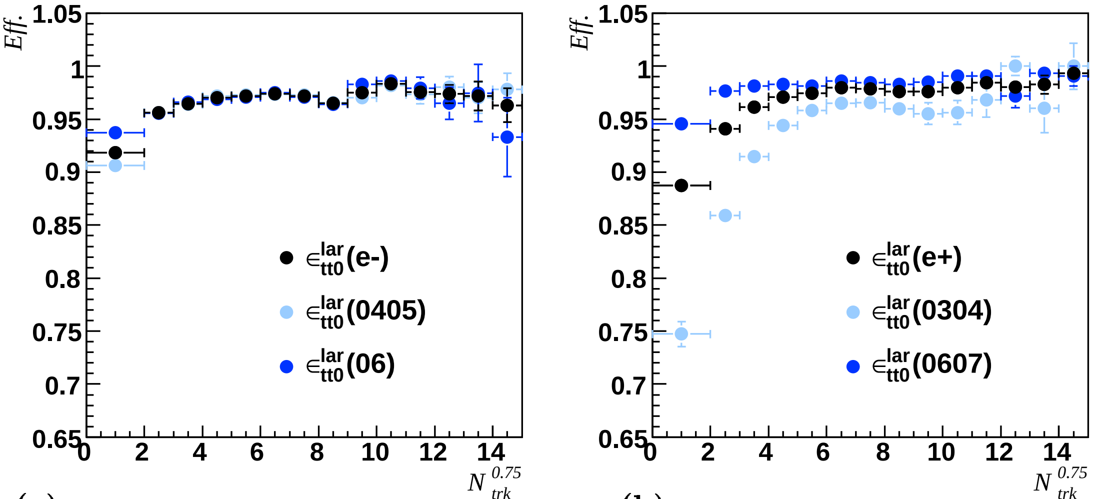

(a) (b)

Figure 7.21: *The TT0 trigger efficiency as a function of the number of tracks with minimum transverse momentum of 0.75 GeV as determined from the LAR sample shown for the* e^- *and* e^+ *periods. The efficiency for the sub-periods 0304*e^+*, 0405*e^-*, 06*e^- *and 0607*e^+ *are also shown.*

The $N_{trk}^{0.75}$ distribution is shown in figures 7.23(a) and (b) for the e^- and e^+ periods in data and signal MC with the signal MC normalized to the number of entries in the data. It can be observed that the MC has more tracks compared to the data. To correct for this, in cases where $N_{trk}^{0.75} > 1$, 6% of the second, third, ... MC tracks are randomly not counted. The MC distribution after this correction is in good agreement with the data as their ratio is now within 5%.

Uncertainty on the Efficiency

The systematic uncertainty on ϵ_{tt0} is estimated by using the γ_h dependence of the efficiency, figure 7.24(a), and defining two monitor samples - the SPA sample where γ_h is very backward and the HAD sample where γ_h is more central, figure 7.24(b):

- SPA sample - events from S^{trig} and triggered by one of s0, s1, s2 or s3
- HAD sample - events from the LAR sample which are fired by the HFS on level I

In figure 7.24(a) it can be seen that the TT0 efficiency drops with increasing γ_h for the LAR and SPA samples as the HFS tracks have a higher probability of falling outside the CJC acceptance; the HAD sample is statistically limited at large γ_h. Figure 7.25(a) shows the TT0 efficiency as a function of $N_{trk}^{0.75}$ for the e^- sample. Where there is only one

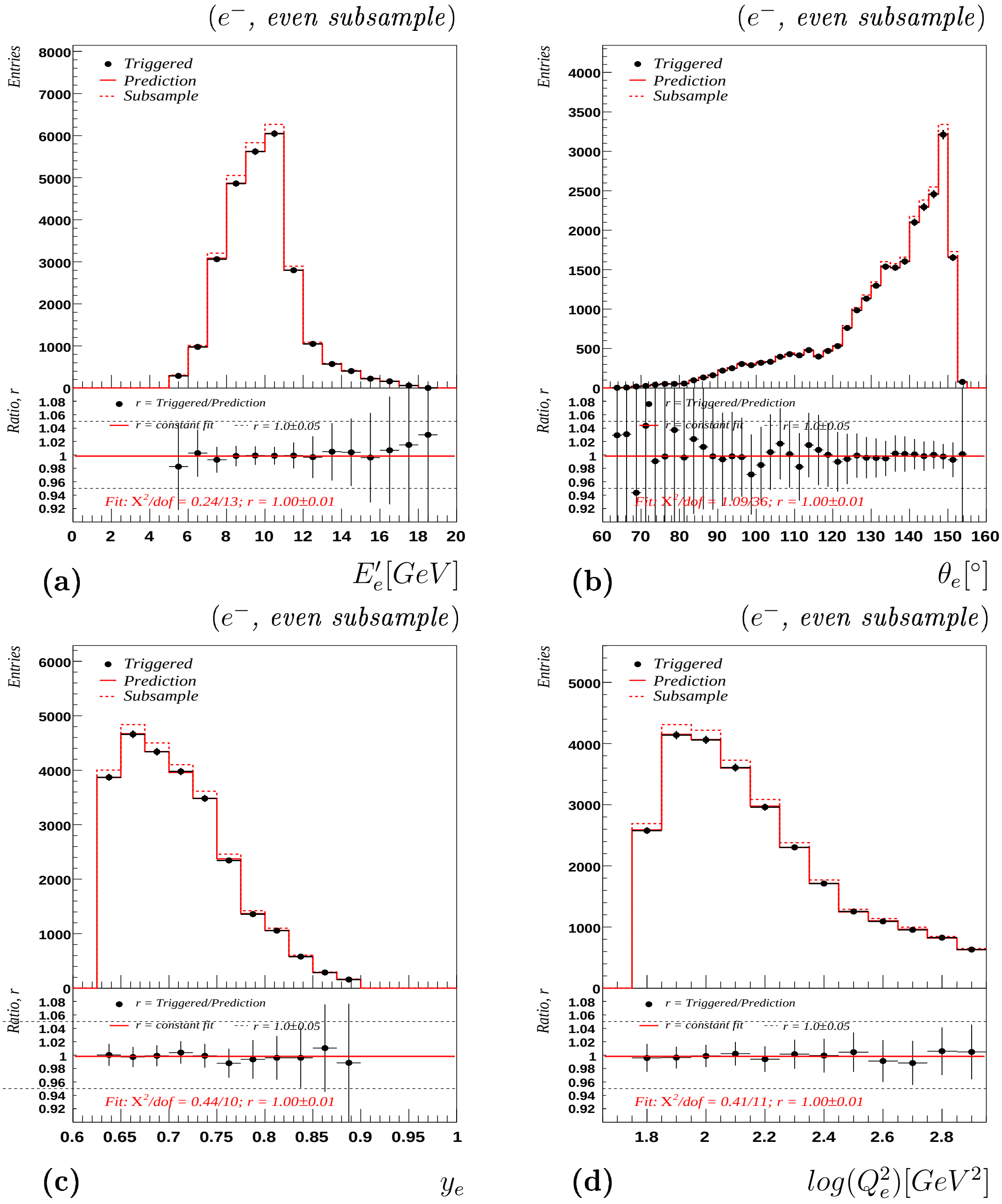

Figure 7.22: *The (a) electron energy, (b) electron polar angle, (c) inelasticity y_e and (d) Q_e^2 distributions for the e^- even subsample, TT0 triggered events and the prediction. The ratio between the number of triggered events and the prediction together with a $y =$ constant fit are shown.*

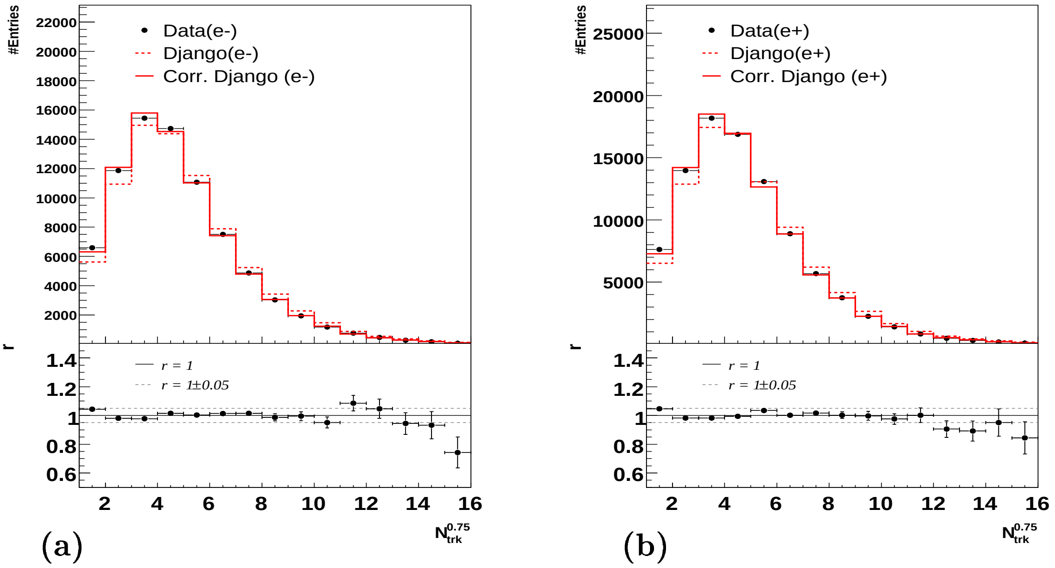

(a) (b)

Figure 7.23: *The* $N_{trk}^{0.75}$ *distribution in data and signal MC before (dashed line) and after (solid line) correction for (a) the* e^- *period and (b) the* e^+ *period. The MC distributions are normalized to the number of entries in the data. The ratio between data and corrected MC is shown in the bottom part of the plot.*

track (first bin), the SPA and HAD efficiencies agree as this represents the efficiency of the electron track firing the TT0 condition. At $N_{trk}^{0.75} = 2$, the HAD efficiency is significantly higher since its HFS track is more within the CJC's acceptance compared to the HFS track of the SPA sample. This difference is shown in the bottom plot of figure 7.25(a). A systematic uncertainty of 4% is thus ascribed in this bin as indicated. For $N_{trk}^{0.75} \geqslant 3$ there is no significant difference between the samples indicating there are enough tracks in either sample such that at least 1 will fire the trigger and so no systematic uncertainty is ascribed. For the e^+ sample however, figure 7.25(b), the difference between the HAD and SPA samples remain significant up to $N_{trk}^{0.75} = 4$. This is due to the lower efficiency of the $0304e^+$ period, figure 7.25(c) compared to the $0304e^+$ period, figure 7.25(d). This lower single track efficiency implies that more tracks are needed to ensure at least on will fire the trigger. The TT0 systematic uncertainty is summarized in table 7.3.

Period	Range in $N_{trk}^{0.75}$	TT0 Systematic Uncertainty [%]
e^-	$N_{trk}^{0.75} = 1$	0.0
	$N_{trk}^{0.75} = 2$	4.0
	$N_{trk}^{0.75} \geqslant 3$	0.0
e^+	$N_{trk}^{0.75} = 1$	0.0
	$N_{trk}^{0.75} = 2$	4.0
	$N_{trk}^{0.75} = 3$	4.0
	$N_{trk}^{0.75} = 4$	1.0
	$N_{trk}^{0.75} \geqslant 5$	0.0

Table 7.3: *The systemtic uncertainty on the TT0 efficiency for the e^- and e^+ samples.*

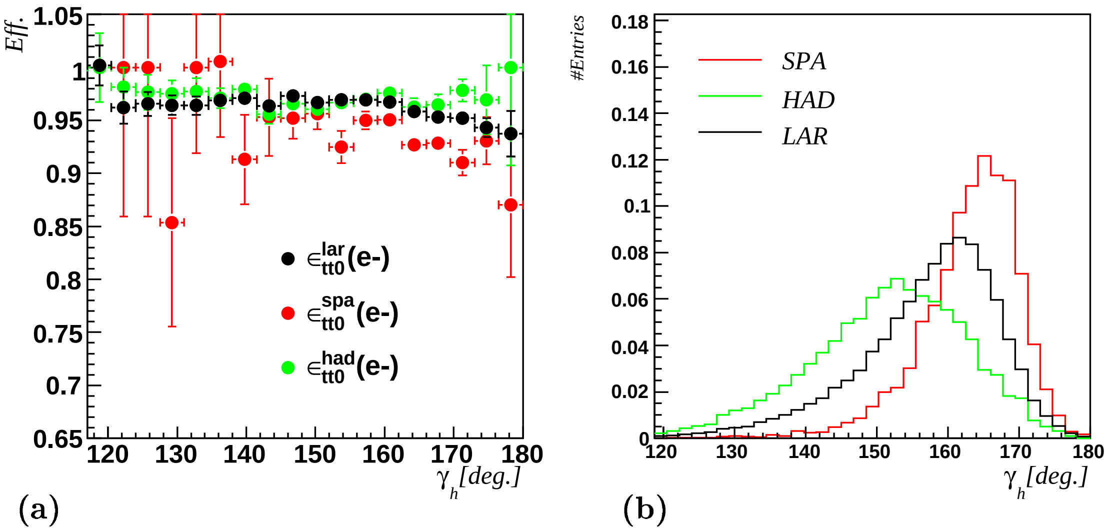

(a) **(b)**

Figure 7.24: *(a) The γ_h dependence of the TT0 efficiency for the LAR, SPA and HAD monitor samples. (b) The γ_h distribution of the 3 monitor samples; the distributions are normalized to an integral of 1.*

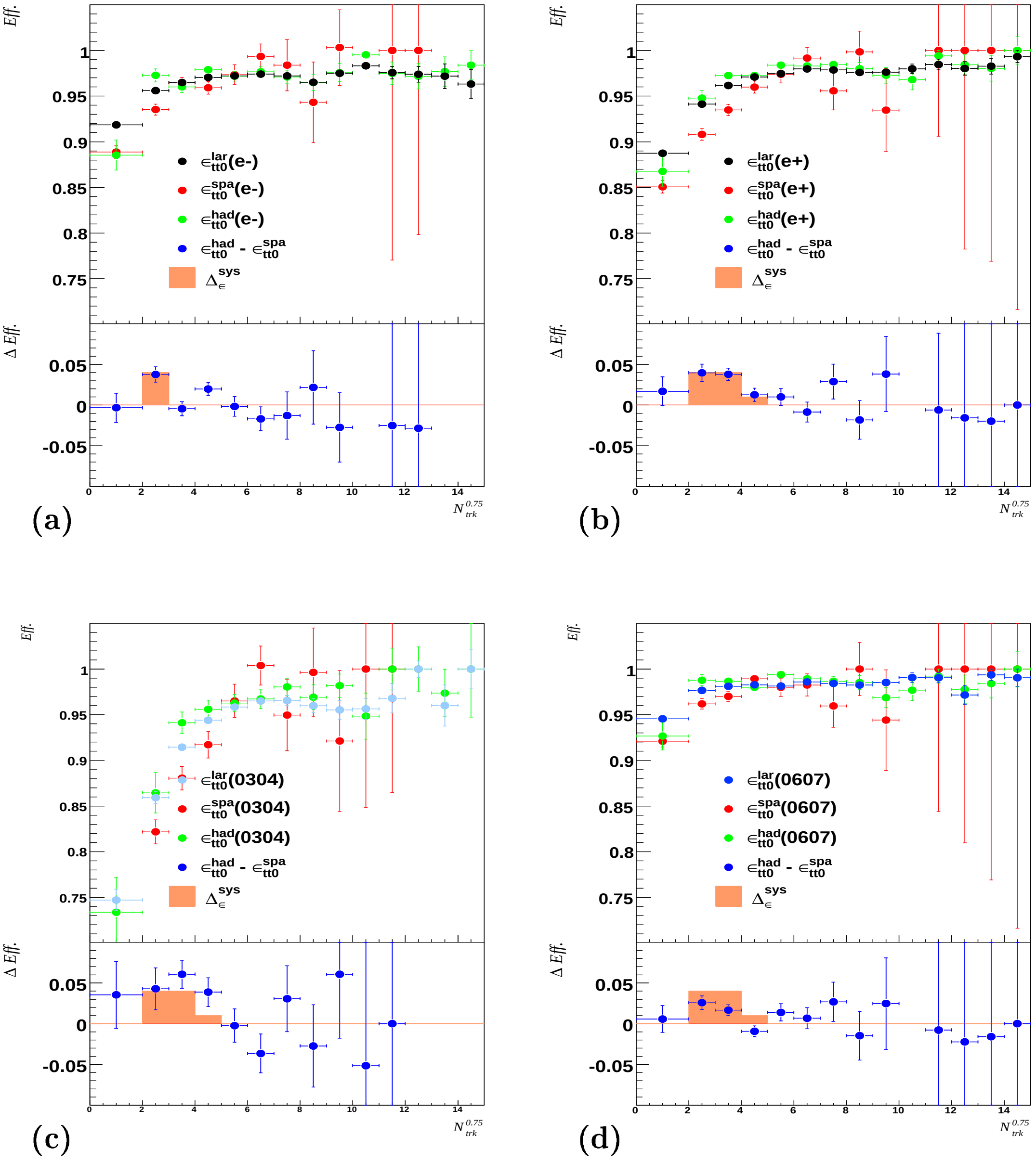

(a) **(b)**

(c) **(d)**

Figure 7.25: *The TT0 efficiency as a function of the number of tracks with transverse momentum greater than 0.75 for the (a) e^-, (b) e^+, (c) 0304$e^+$and (d) 0607e^+periods. Shown are ϵ_{tt0} as determined from the LAR, SPA and HAD monitor samples as well as the difference between the HAD and SPA samples. The systematic uncertainty of ϵ_{tt0} based on this difference is also indicated.*

Run No	VET
First Run	!VETO_BG && !BToF_BG && !SToF_BG && !(!FIT_IA && FIT_BG)
358934	!VETO_BG && !BToF_BG && !SToF_BG && !(!FIT_IA && FIT_BG) && `!(CIP_mul==7 && CIP_sig==0)`
372718	!VETO_BG && !BToF_BG && !SToF_BG && !(!FIT_IA && FIT_BG) && `!(CIP_mul>7 && CIP_sig==0)`
444307	!VETO_BG && !BToF_BG && !SToF_BG && !(!FIT_IA && FIT_BG) && `!(CIP_sig==0)`
450139	!VETO_BG && !(BToF_BG&&BToF_Gl&&(!BToF_IA)) && !SToF_BG && !(!FIT_IA && FIT_BG) && `!(CIP_sig==0)`

Table 7.4: *The VET condition as a function of time. The time of flight ToF contribution is written in* normal script *and the CIP contribution in* `typed script`.

7.4 Veto Condition - VET

The veto condition VET uses signals from various subdetectors to reject events based on event timing or toplogy. The time-of-flight (ToF) detectors – BToF, SToF, FIT and the Veto Wall (secton 2.6) – use timing information to produce the trigger elements that constitute the ToF condition of s75. Trigger elements built using information from the CIP detector are used to veto events based on event topology - if too many tracks originate from the backward direction – and form the CIP condition. That is:

$$VET \equiv ToF \ \ \&\& \ \ CIP. \tag{7.5}$$

The VET definition as a function of time is outlined in table 7.4.

In order to study the VET efficiency ϵ_{vet}, the S57 monitor sample S_M^{s57} is defined as comprising those events from $S^{trig'}$ that fire subtrigger s57 (which has no veto condition except for the run range R$\leqslant$382137 where ToF information is included – approximately half the luminosity of 0304e^+). Figure 7.26(a) to (c) show the ToF (ϵ_{tof}^{s57}) and CIP (ϵ_{cip}) efficiencies determined from this sample as a function of electron energy, electron polar angle and Q_e^2 respectively for the e^- period together with $\epsilon = constant$ fits. For the e^+ period as a function of Q_e^2, the ToF efficiency is shown in figure 7.26(d.1) for the 0607e^+ period only since s57 includes ToF information for the run range R$\leqslant$382137. The CIP efficiency is shown in figure 7.26(d.2) for the e^+ period. From these plots it is evident that the ToF and CIP efficiencies show no dependence on event kinematics.

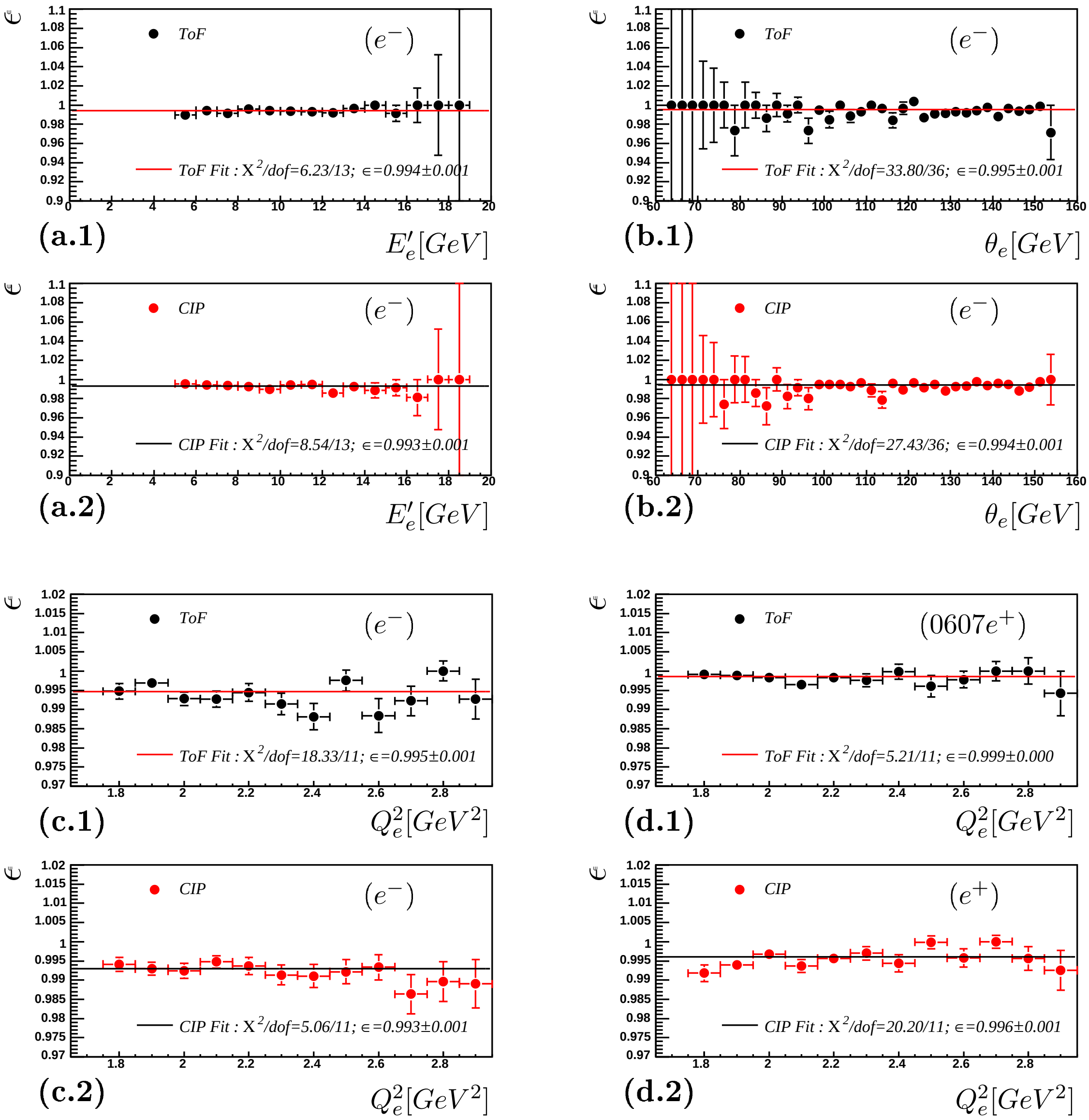

Figure 7.26: *The ToF efficiency* ϵ_{tof}^{s57} *and CIP efficiency* ϵ_{cip} *as a function of (a) electron energy, (b) electron polar angle and (c)* Q_e^2 *for the* e^-*period.* ϵ = *constant fits are also made. (d)* ϵ_{tof}^{s57} *and* ϵ_{cip} *as a function of* Q_e^2 *for the* e^+ *sample.*

Period	Efficiency[%]		
	ToF	CIP	VET
e^-	99.37±0.07[stat.]±0.42[sys.]	99.26±0.07[stat.]	98.63±0.43
e^+	99.52±0.03[stat.]±0.24[sys.]	99.52±0.06[stat.]	99.04±0.25

Table 7.5: *Summary of the veto efficiencies for the e^- and e^+ periods.*

The ToF efficiency as determined from the S57 monitor sample, ϵ_{tof}^{s57}, is shown as a function of time in figure 7.27(a). Also shown on the same figure is the ToF efficiency using Bethe-Heitler events $ep \rightarrow ep\gamma$, ϵ_{tof}^{bh}. For this sample, the electron is tagged in the electron tagger and the photon in the photon tagger; the events are triggered using s91 (section 2.6). The difference $\Delta\epsilon = \epsilon_{tof}^{s57} - \epsilon_{tof}^{bh}$ together with $\Delta\epsilon = constant$ fits are provided in the bottom part of the plot. For most of the 0304e^+ and 0405e^- periods the difference is approximately 0.5% which is used as the systematic uncertainty on ϵ_{tof} for this run range. However, in the range $387000 < R < 407000$ the ToF efficiency from both analyses show uncharacteristic deviations, and so the systematic uncertainty in this region is conservatively estimated at 2%, as seen from the fits. For the 06e^- and 0607e^+ periods no systematic uncertainty is quoted as the efficiencies from both analyses are consistent with each other. The systematic uncertainty averaged over the e^- and e^+ periods are 0.42% and 0.24% respectively, table 7.5. Using the efficiency from the Bethe-Heitler sample for the 0304e^+period and the S57 efficiency ϵ_{tof}^{s57} for all other periods, the Tof efficiency averaged over the e^- and e^+ periods and are shown in table 7.5 with its uncertainties.

The CIP efficiency as a function of time is shown in figure 7.27(b) together with its value averaged over each period with statistical error. The efficiency averaged for the e^- and e^+ periods with statistical uncertainty is given in table 7.5. No systematic uncertainty on ϵ_{cip} is assumed.

Finally the VET efficiency ϵ_{vet} which is applied as a correction to the signal MC is calculated as:

$$\epsilon_{vet} = \epsilon_{tof} \cdot \epsilon_{cip}$$

with errors added in quadrature since the ToF system and CIP detector are independent. The VET efficiency and its uncertainty is summarized in table 7.5.

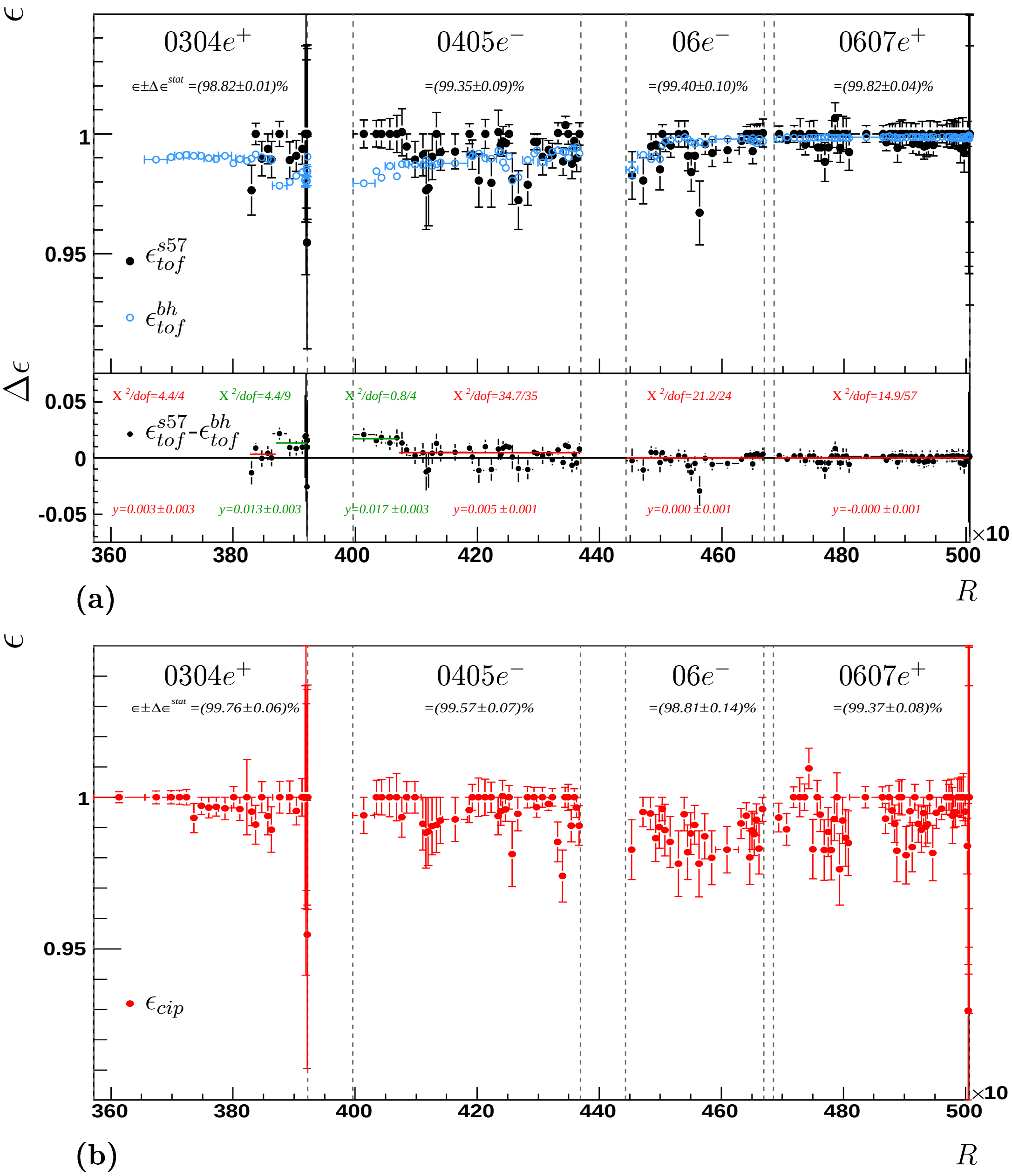

Figure 7.27: *(a) The ToF efficiency as a function of time (run number R) as determined from the S57 and Bethe-Heitler monitor samples. Indicated are the measured efficiency for each period (using ϵ_{tof}^{bh} for the 0304e^+ period and ϵ_{tof}^{s57} for later periods) with its statistical error. In the bottom plot the difference between the efficiencies of the two samples $\Delta\epsilon = \epsilon_{tof}^{s57} - \epsilon_{tof}^{bh}$ is plotted and $\Delta\epsilon =$ constant fits are made over the indicated run ranges. (b) The CIP efficiency as a function of time. The efficiency averaged over each of the four periods is indicated with its statistical error.*

7.5 Electron Identification

To study the electron finding efficiency ϵ_{id} [2], events fullfilling all final selection cuts (table 7.8) apart from:

- LAr Candidate
- ϕ-crack
- z-crack 1
- z-crack 2

are selected. From these events, a monitor sample is defined as the set of events where the scattered electron is found using the track-based electron finder [53]. The efficiency can then be written as:

$$\epsilon_{id} = \frac{N'_{both}}{N'_{both} + N'_{trk}}. \tag{7.6}$$

Here N'_{both} is the number events where the scattered electron is found by both the LAr and the track-based electron finders, and N'_{trk} is the number of events where the scattered electron is found by the track-based electron finder *only*. N' is after background subtraction using the wrong charge background subtraction procedure, section 7.7.

In figures 7.28(a) to (d) distributions for the sample where the electron is found only by the track-based finder is shown after background correction (N'_{trk}) together with its background component (N^{bg}_{trk}). These distributions are compared to the sample where the LAr electron finder finds the electron, corresponding to the final cuts in table 7.8 and control plot figures 7.42 and 7.43. The LAr signal MC distribution is normalized to the track-based distribution after background correction (N'_{trk}) and the LAr background distribution is normalized to the track-based background distribution. It can be observed that the track-based sample has significantly more background than the LAr sample. This is seen particularly in the $E-P_z$ distribution where most of the background is found at low $E-P_z$ values ($\lesssim$45 GeV). The track-based background compared to the LAr background is similar in shape. After background correction, the track-based distributions are well described by the signal MC. Therefore it can be assumed that the track-based only sample, once corrected for background, does indeed represent the signal.

Figure 7.29(a) shows the the electron identification efficiency ϵ_{id} as a function of ϕ_{oc}, the relative position of the electron impact position on the LAr calorimeter with respect to the nearest ϕ-crack, section 2.3. The efficiency is determined for both data (ϵ_{id}^{data}) and signal MC (ϵ_{id}^{mc}) and wrong charge background subtraction is used in its calculation (section 7.7).

---

[2] the electron finder is described in section 5.1

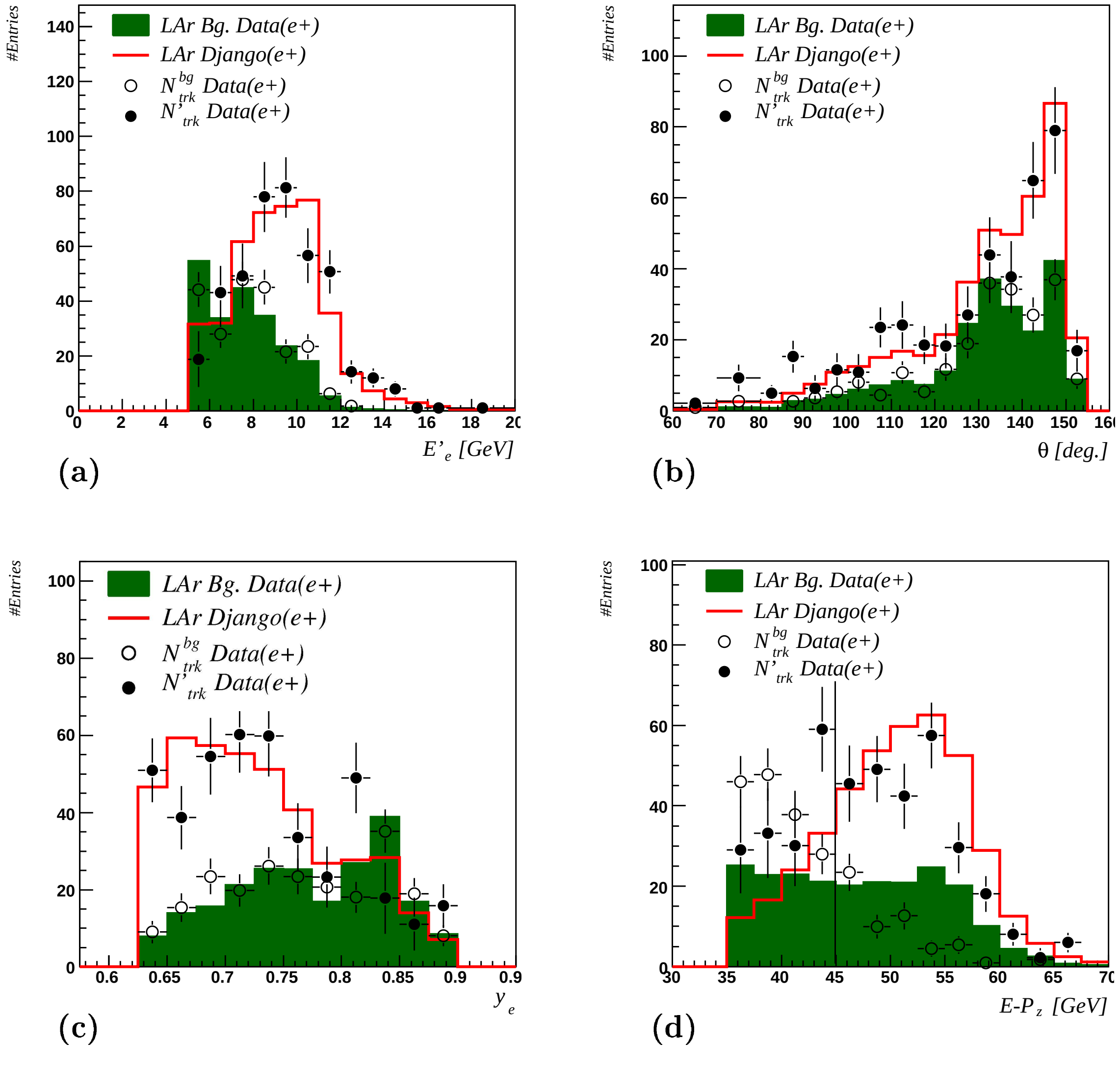

(a) (b)

(c) (d)

Figure 7.28: *The track-based electron finder distributions compared to that of the LAr electron finder for signal after background subtraction as well as the background. Distributions in (a) electron energy, (b) electron polar angle, (c) inelasticity y_e and (d) longitudinal momentum $E - P_z$ are shown. The LAr Django distribution is normalized to the track-based signal N'_{trk} and the LAr background distribution is normalized to the track-based background N^{bg}_{trk}.*

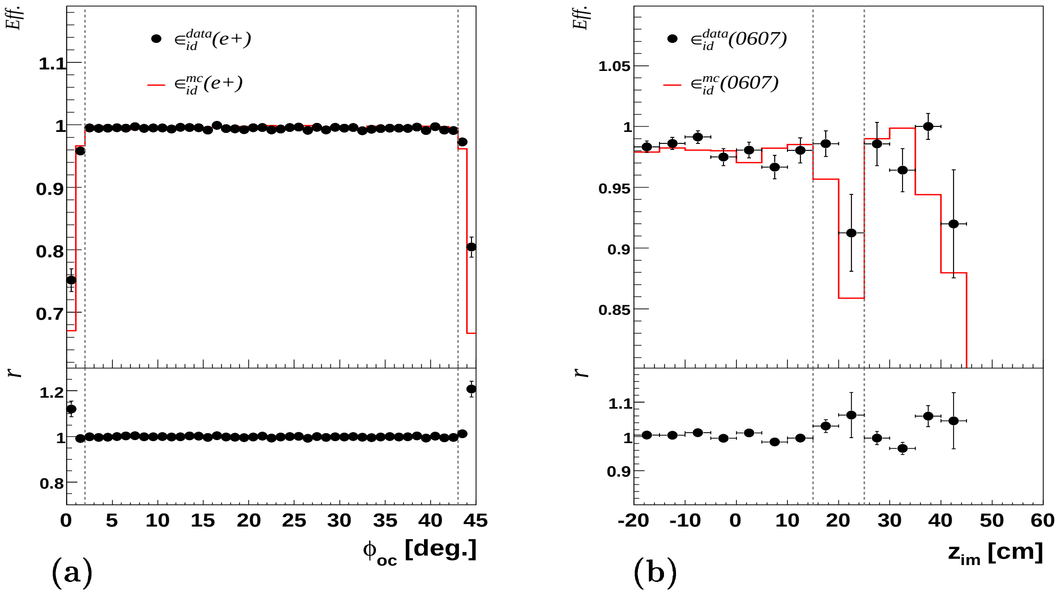

Figure 7.29: *The electron identification efficiency ϵ_{id} as a function of (a) ϕ-octant (relative position of the ϕ-coordinate of the impact position of the electron to the nearest LAr ϕ-crack) and (b) z_{im}, for data and signal MC.*

If the electron is within 2° of the ϕ-crack ($\phi_{oc} < 2°$ or $\phi_{oc} > 43°$) the simulation poorly describes the data. This region is thus removed from the analysis (cut ϕ-crack, table 7.8). Figure 7.29(b) shows the efficiencies as a function of z_{im}. The simulation does not describe the data well in the regions $15 < z_{im} < 25$ cm, the CB2/CB3 wheel boundary, section 2.3. This region together with the CB1/CB2 boundary at $-65 < z_{im} < 55$ cm are removed from the analysis (cuts z-crack 1 and z-crack 2, table 7.8).

Figure 7.30 shows the electron identification efficiency as a function of electron energy, polar angle, Q_e^2 and $E - P_z$ for the e^- sample after the $z-$ and ϕ-cracks are removed. To cross check the data efficiency against the assumption that the monitor sample is background free, ϵ_{id} is also measured using events from the monitor sample with $E - P_z >$ 45 GeV. This part of the sample has significantly lower background as can be seen in figure 7.28. The resulting efficiency ϵ_{empz} (calculated using wrong charge background subtraction) is also shown in figure 7.30: ϵ_{id}^{data} and ϵ_{empz}^{data} are consistent. Figure 7.31 shows similar plots for the e^+ period.

The level of agreement between data and signal MC efficiencies can be seen in the bottom part of the plots where the ratio $r = \epsilon_{id}^{data}/\epsilon_{id}^{mc}$ is given. The ratio is fitted with a $r = constant = p0$ assumption; the quality of the fit is good. It can be concluded that the electron identification efficiency is well modelled in the MC across the full kinematic range of the analysis. The average value of r is 99.88% ±0.05% for the e^- period and 99.86%±0.05% for the e^+ period. A relative systematic uncertainty $\delta^{sys}_{\epsilon_{id}}$ is conservatively quoted at 1% for both periods; no correction is applied to the MC.

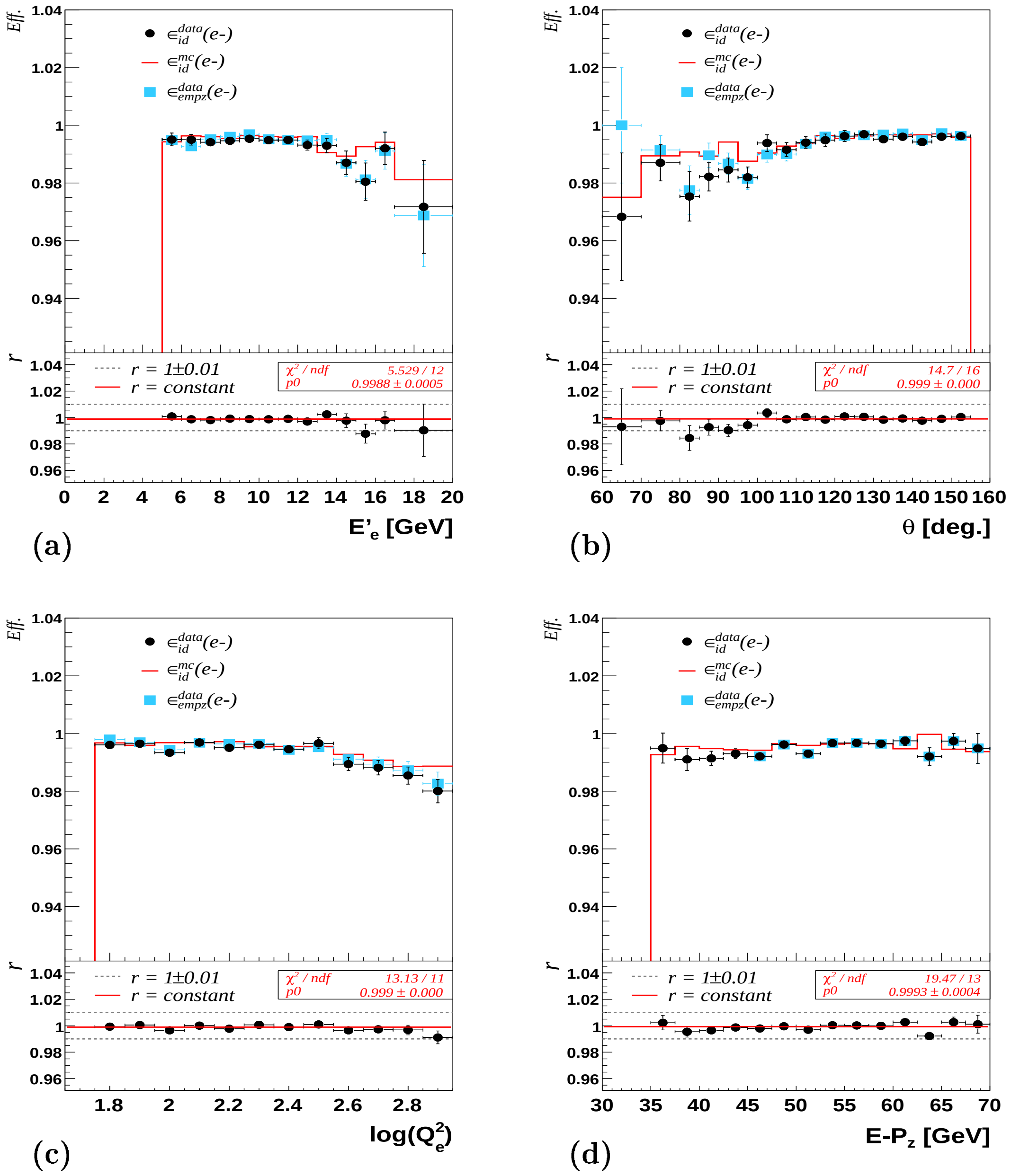

Figure 7.30: *The electron identification efficiency ϵ_{id} as a function of (a) electron energy, (b) electron polar angle, (c) log(Q_e^2) and (d) longitudinal momentum $E - P_z$ as determined from data (ϵ_{id}^{data}) and signal MC (ϵ_{id}^{mc}) for the e^- period. Also shown is ϵ_{id} as determined from events with $E - P_z > 45$ GeV from the data sample (ϵ_{empz}^{data}). The ratio $r = \epsilon_{id}^{data}/\epsilon_{id}^{mc}$ is shown in the bottom part of the plot and is fitted to an $r = constant = p0$ assumption.*

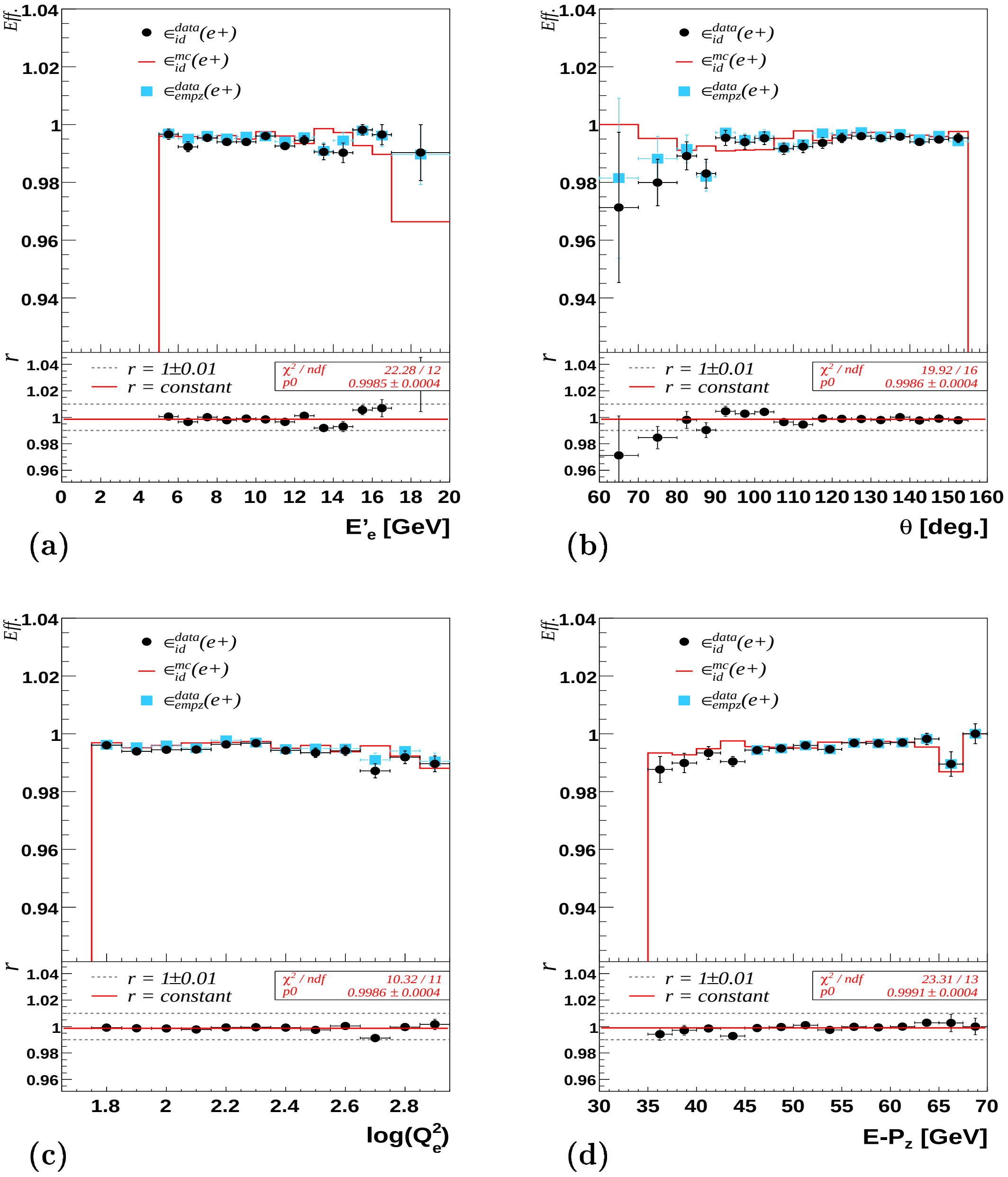

Figure 7.31: *The electron identification efficiency* ϵ_{id} *as a function of (a) electron energy, (b) electron polar angle, (c) log(*Q_e^2*) and (d) longitudinal momentum* $E - P_z$ *as determined from data* (ϵ_{id}^{data}) *and signal MC* (ϵ_{id}^{mc}) *for the* e^+ *period. Also shown is* ϵ_{id} *as determined from events with* $E - P_z > 45$ *GeV from the data sample* (ϵ_{empz}^{data})*. The ratio* $r = \epsilon_{id}^{data}/\epsilon_{id}^{mc}$ *is shown in the bottom part of the plot and is fitted to an* $r = constant = p0$ *assumption.*

7.6 Tracker Requirement - Vertex and Track Link, Charge Identification

The tracker requirement of the high y analysis (TRHY) demands a CJC-vertex together with a DTRA track (vertex-validation type 1, section 6.3) such that the DCA to the cluster to less than 6 cm, that is:

$$TRHY = CJC - vertex \ \&\& \ DTRA - validation \ \&\& \ d_{ca}^{cls} < 6cm.$$

Because the track linked to the electron is used to estimate the ep background, the TRHY efficiency is estimated using the 'clean' sample from the nominal analysis used to estimated the TRNA tracker efficiency (where the background is removed), section 6.3. The TRHY efficiency ϵ_{trhy} is measured using events from this clean sample in a limited part of phase space where the kinematics approach that of the high y analysis. This region is called the "NA high y limit" and is shown in figure 7.32(a). The NA high y limit sample is defined by the following cuts applied to the clean sample:

- $y_e > 0.3$ and $y_{e\Sigma} > 0.3$. This cut is motivated by a study presented in section 8.6 showing that for $y > 0.3$ the kinematics is best determined using only the scattered electron properties - the kinematic reconstruction technique used in the high y analysis.
- $Q_e^2 < 2000$ GeV^2.
- $\theta_e > 60°$. Figure 7.32(b) shows the TRHY efficiency as a function of the electron polar angle using the full clean sample, in data and signal MC. For very forward θ_e the efficiency in both data and simulation drop and the level of agreement worsens. Since the high y analysis selection effectively limits the electron polar angle to $\theta_e > 60°$, events with $\theta_e < 60°$ are excluded from the NA high y limit sample.

Figure 7.33 shows the TRHY efficiency in data and signal MC as a function of electron energy, electron polar angle, $\log(Q_e^2)$ and y_e for the e^- period; the ratio r of the efficiency in the data to the MC is shown in the bottom part of each plot. Also indicated is the average efficiency $\langle r \rangle$ for the entire sample with an error band of $\pm 2\%$. The data to MC agreement can be seen to be within the uncertainties quoted. The same is true for the e^+ sample, figure 7.34. The MC is therefore corrected using $\langle r \rangle$ with its systematic uncertainty, table 7.6.

Charge Identification Efficiency

Since the NA high y limit sample is low in ep background, it is also used to estimate the efficiency of correctly identifying the *sign* of the charge of the track associated to the

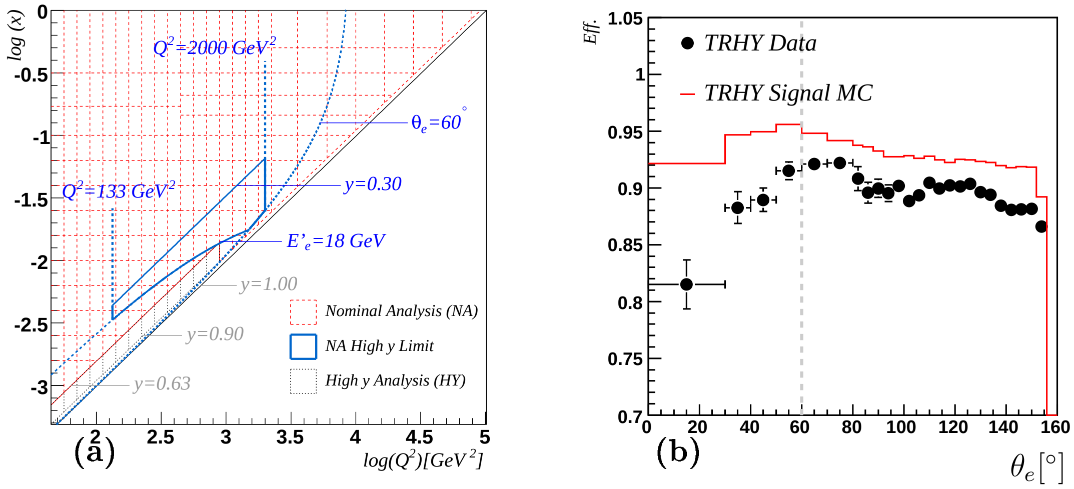

Figure 7.32: *(a) The $x - Q^2$ kinematic plane showing the cuts used to define the NC High y limit sample - $133 < Q^2 < 2000\ GeV^2$, $y > 0.3$, $E'_e > 18\ GeV$ and $\theta_e > 60°$. (b) The TRHY efficiency in data and signal MC for the clean sample as a function of the electron polar angle. Events with electron polar angles less than 60° (vertical line) are excluded from the NC High y limit sample.*

Period	$\langle r \rangle [\%]$	$\Delta_r^{sys} [\%]$
e^-	96.01	2.0
e^+	96.23	2.0

Table 7.6: *The TRHY correction factors $\langle r \rangle$ applied to the MC together with its systematic uncertainty Δ_r^{sys}.*

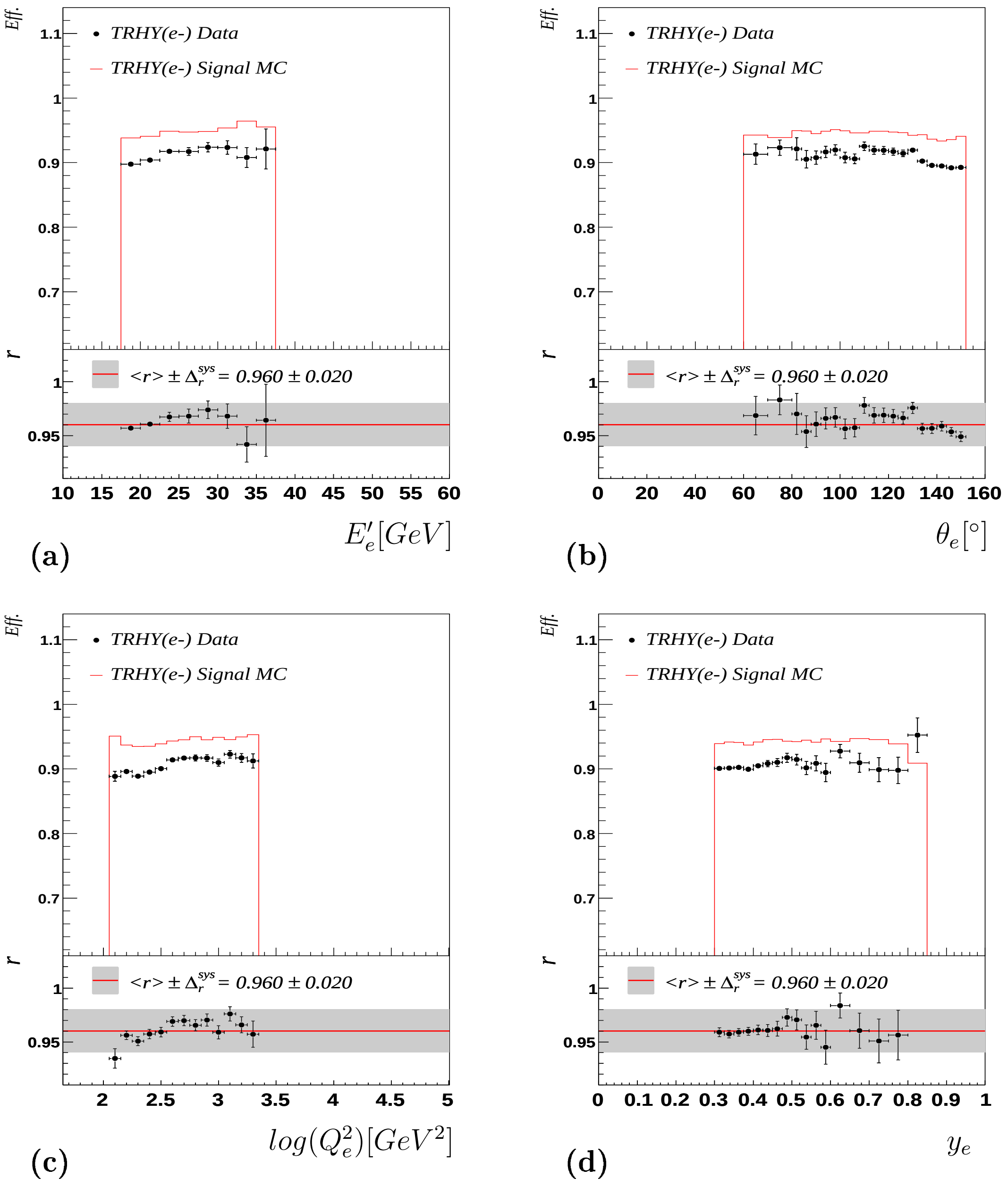

Figure 7.33: *The TRHY efficiency in data and signal MC for the e^- period as a function of (a) electron energy, (b) electron polar angle, (c) $log(Q_e^2)$ and (d) y_e. The ratio r of the efficiency in data to MC is shown in the bottom part of each plot. The average ratio $\langle r \rangle$ together with its systematic uncertainty is indicated as the red line and grey box.*

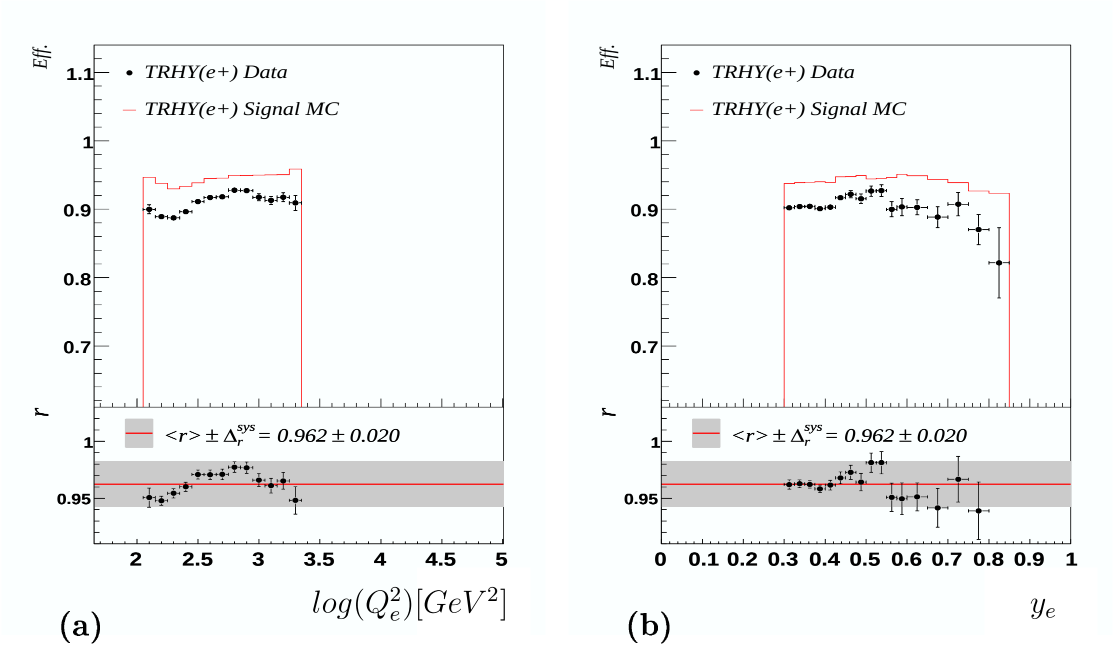

Figure 7.34: *The TRHY efficiency in data and signal MC for the* e^+ *period as a function of (a) log(*Q_e^2*) and (b)* y_e*. The ratio* r *of the efficiency in data to MC is shown in the bottom part of each plot. The average ratio* $\langle r \rangle$ *together with its systematic uncertainty is indicated as the red line and grey box.*

electron ϵ_{qid}. This efficiency is taken as the fraction of events from the sample with a charge matching the beam lepton charge and is shown as a function of the electron polar angle θ_e for the e^- and e^+ samples in figures 7.6(a) and (b) respectively for data and signal MC. Also shown in the bottom part of each plot is the ratio of data to MC efficiency; lines at 1±0.005 are also indicated. The agreement between data and MC is better than 0.5%, that is, $|r-1| < 0.5\%$. No correction is applied to either data or MC, but a systematic uncertainty on the cross section is quoted accordingly (section 9.3).

7.7 *ep* Background

The sources of *ep* background of the high y analysis are similar to those of the nominal analysis (section 6.4).

Estimation of Background

The uncertainty of 30% on the background contribution as estimated from MC (section 6.4) would lead to large errors on the high y analysis cross section measurements since the background contribution increases at lower electron energies. Therefore in the high y

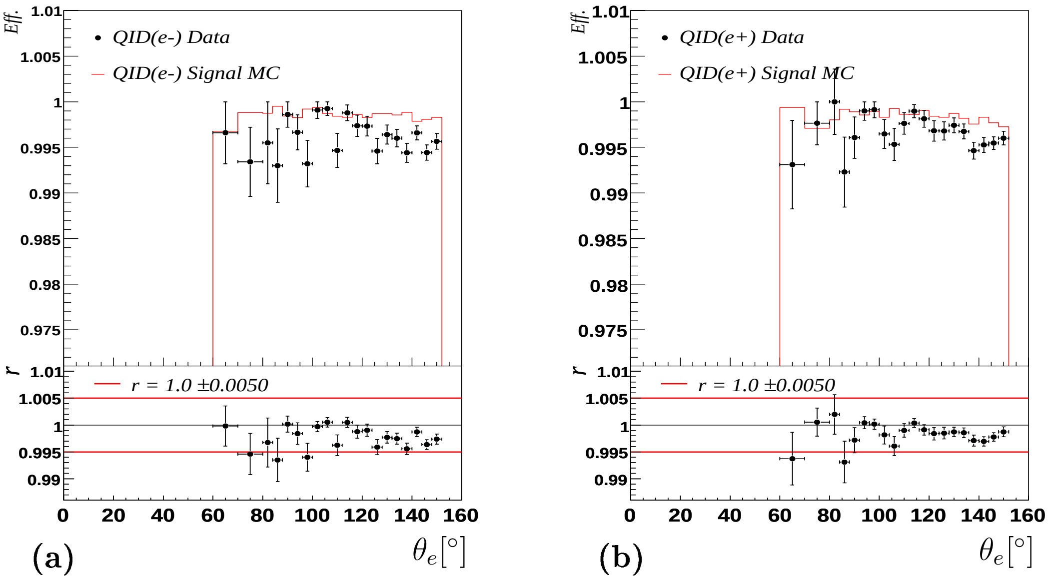

Figure 7.35: *The* e^- *(a) and* e^+*(b) charge identification efficiency* ϵ_{qid} *as a function of the electron polar angle* θ_e *for data and signal MC. The ratio* r *of the data to MC efficiency is shown in the bottom part of the plot together with lines at* $r = \pm 1.005$.

analysis the sign of the charge of the track linked to the scattered electron candidate is used to estimate the amount of ep background present in the sample. A positive track from an e^-p interaction can be regarded as coming from a background process since the efficiency of correctly identifying the sign of the track is close to 1, section 7.6. Assuming that the charge distribution of background events is symmetric, the number of background events in the e^- sample can be estimated as:

$$N_{e^-p}^{bg} = N_{e^-p}^{+} \tag{7.7}$$

where in the notation, the *process* is indicated as e^-p, e^+p or background "*bg*" and the *track charge* indicated as "+" or "−" in the superscript. If however there is a charge asymmetry in the background which is defined as the ratio of negative to positive background, $\kappa \equiv N_{bg}^-/N_{bg}^+$ - which can arise due to the CJC's asymmetry in ϕ for example - then equation 7.7 needs to be rewritten as:

$$N_{e^-p}^{bg} = \kappa N_{e^-p}^{+}. \tag{7.8}$$

The *measurement* of κ uses the wrong charge of the e^+p sample ($N_{e^+p}^-$) as an estimate for N_{bg}^- and the wrong charge of the e^-p sample ($N_{e^-p}^+$) as an estimate for N_{bg}^+ so that:

$$\kappa = \left(\frac{N_{e^+p}^-}{N_{e^-p}^+}\right) \cdot \left(\frac{\epsilon_{H1}^{e^-p}}{\epsilon_{H1}^{e^+p}}\right) \cdot \left(\frac{\mathcal{L}^{e^-p}}{\mathcal{L}^{e^+p}}\right) \tag{7.9}$$

Differences in the detector for the two periods are taken into account by the detector efficiency terms ϵ_{H1} in equation 7.9; the difference in the luminosity is taken into account by the $\mathcal{L}^{e^{\pm}p}$ terms. As ϵ_{H1} equals the product of the trigger (ϵ_{trig}), electron finder (ϵ_{id}) and tracker (ϵ_{trhy}) efficiencies (presented in the last three sections) equation 7.9 can be rewritten as:

$$\kappa = \left(\frac{N^{-}_{e^+p}}{N^{+}_{e^-p}} \right) \cdot \left(\frac{\epsilon^{e^-p}_{trig}}{\epsilon^{e^+p}_{trig}} \right) \cdot \left(\frac{\epsilon^{e^-p}_{id}}{\epsilon^{e^+p}_{id}} \right) \cdot \left(\frac{\epsilon^{e^-p}_{trhy}}{\epsilon^{e^+p}_{trhy}} \right) \cdot \left(\frac{\mathcal{L}^{e^-p}}{\mathcal{L}^{e^+p}} \right) \tag{7.10}$$

or more succinctly as:

$$\kappa = \left(\frac{N^{-}_{e^+p}}{N^{+}_{e^-p}} \right) \cdot \left(\frac{\epsilon^{e^-p}_{trig}}{\epsilon^{e^+p}_{trig}} \right) \cdot \left(\Gamma_{\epsilon_{id}} \right) \cdot \left(\Gamma_{\epsilon_{trhy}} \right) \cdot \left(\Gamma_{\mathcal{L}} \right) \tag{7.11}$$

where in the notation Γ_q represents the ratio of a quantity q as obtained from the e^- sample to the same quantity as obtained from the e^+ sample, that is: $\Gamma_q = q^{e^-p}/q^{e^+p}$. Figure 7.36(a.1-2) shows $\Gamma_{\epsilon_{id}}$ as a function of electron energy (a.1) and electron polar angle (a.2) together with fits to the data of the form $\Gamma_{\epsilon_{id}} = constant$. As the quality of the fit is good, $\Gamma_{\epsilon_{id}}$ is well described by its average value of 1.0000 ± 0.0006 taken over the kinematic range of the samples. The same is true for $\Gamma_{\epsilon_{trhy}}$, figures 7.36(b.1-2) whose average value is 0.9980 ± 0.0019. The relative luminosity $\Gamma_{\mathcal{L}}$ between the e^-p and e^+p samples is determined in section to be 0.8661 ± 0.0043. The various Γ values are summarized in table 7.7.

The trigger efficiency $\epsilon^{e^{\pm}p}_{trig}$ in equation 7.11 is applied as a reweight to each background event: $1/\epsilon^{e^+p}_{trig}$ for background events events with a negative charged track (coming from the e^+p sample) and $1/\epsilon^{e^-p}_{trig}$ for the positively charged background events (coming from the e^-p sample); $\epsilon^{e^{\pm}p}_{trig}$ has 3 components:

- ϵ_{lar} determined in section 7.2 and parametrized as a function of (E'_e,z_{im})
- ϵ_{tt0} determined in section 7.3 and parametrized as a function of ($N^{0.75}_{trk}$)
- ϵ_{vet} determined in section 7.4 and parametrized by a constant.

Figures 7.37(a) and (b) show the electron energy and electron polar angle distributions for the negative background ($N^{-}_{bg'} = N^{-}_{e^+p} \times 1/\epsilon^{e^+p}_{trig}$) and positive background ($N^{+}_{bg'} = N^{+}_{e^-p} \times 1/\epsilon^{e^+p}_{trig}$) samples corrected for the trigger efficiency. The ratio $\Gamma_{N_{bg'}}$ of the negative to positive background is shown in the bottom part of the plot together with a $\Gamma_{N_{bg'}} = constant$ fit; the quality of the fit is good. The average value of $\Gamma_{N_{bg'}}$ is 1.1824±0.0218[stat.], table 7.7.

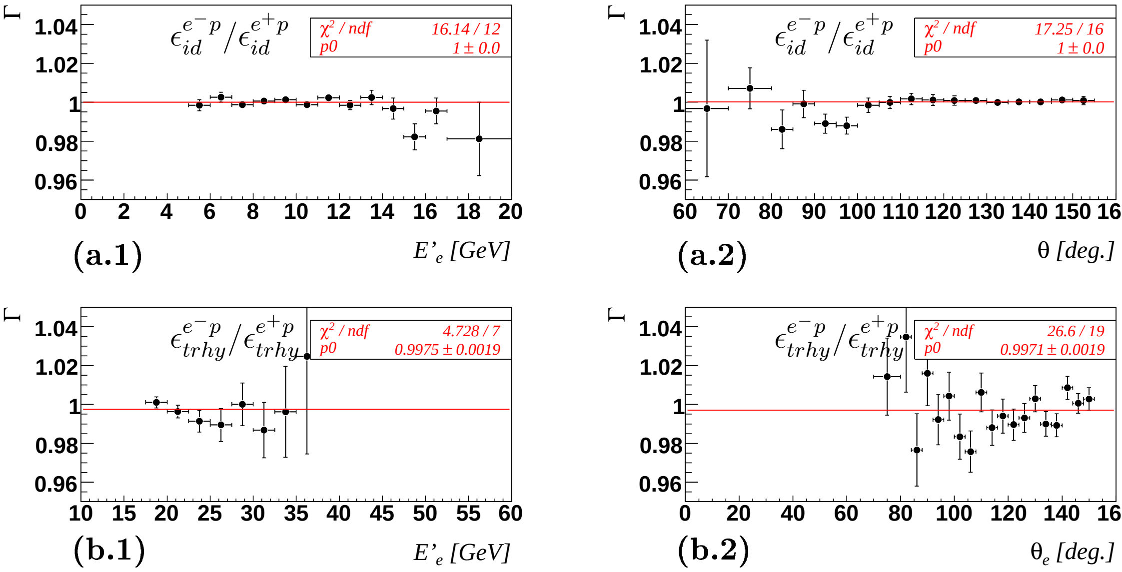

Figure 7.36: *(a) The ratio Γ of the e^- to the e^+ (a.1-2) electron identification efficiency and (b.1-2) tracker TRHY efficiency as a function of (a-b.1) electron energy and (a-b.2) electron polar angle. The data is fitted by a $\Gamma = constant = p0$ assumption, shown as the red line.*

Finally using equation 7.11, κ is calculated to be 1.022±0.021(0.020[stat.]±0.006[syst.]). The systematic error of 0.006 is taken to be the difference between κ as calculated using equation 7.11 and its value assuming $\epsilon_{H1}^{e^{\pm}p} = 1$, effectively taking the systematic error on the various efficiencies as their corresponding inefficiency. The systematic error contribution is negligible.

κ is consistent with the value of 0.99±0.07 corresponding to the HERA I data[50] determined using a similar method adopted here. The present measurement of κ is much more precise than the HERA I measurement due to increased statistics (the relative statistical error on the positive background from the e^- sample in HERA I was ≈6%). κ can also be estimated from events where the scattered electron is detected in the electron tagger and taking the ratio of the negative fake “scattered” electrons to the positive ones. It was found[50] to be 1.13±0.2 (e^-p data) and 0.98±0.09 (e^+p data) which are also consistent with the value obtained in this analysis.

Background Subtraction Procedure

The procedure used to correct for background is to statistically subtract the number of wrongly charged tracks from the rightly charged sample. In the case of the e^-p data, the

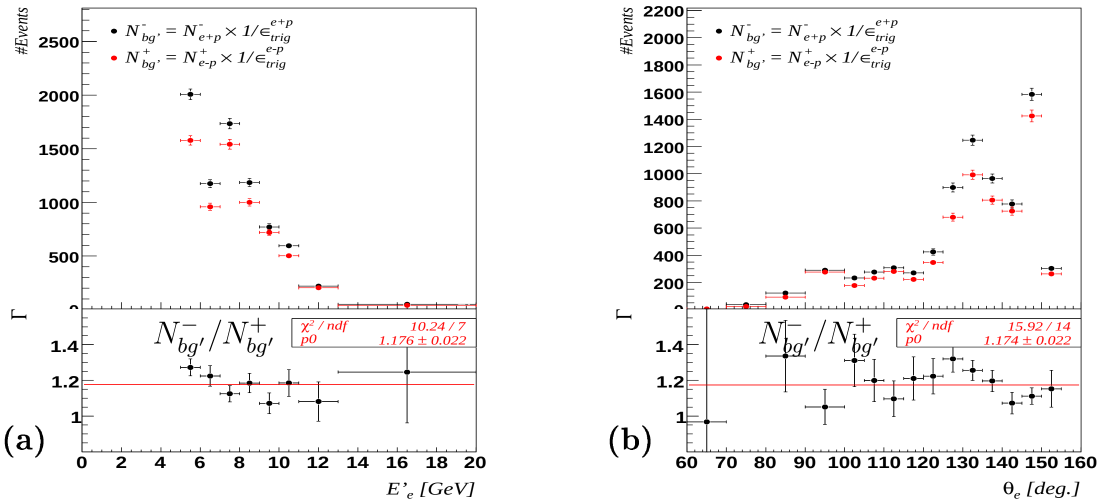

Figure 7.37: *The background sample distributions for negatively charged tracks corrected for trigger efficiency* ($N^-_{bg'} = N^-_{e^+p} \times 1/\epsilon^{e^+p}_{trig}$) *and positively charged tracks corrected for trigger efficiency* ($N^+_{bg'} = N^+_{e^-p} \times 1/\epsilon^{e^-p}_{trig}$) *in (a) for electron energy and (b) for electron polar angle. The ratio* Γ *of the negative to positive tracks is shown in bottom part of the plot and fitted by a* $\Gamma = constant = p0$ *assumption, shown as the red line.*

background corrected N' number of events is:

$$N' = N^- - \kappa N^+ \tag{7.12}$$

where "$-$" and "$+$" indicates the sign of the track associated to the electron. For the e^+p sample:

$$N' = N^+ - (1/\kappa)N^- \tag{7.13}$$

The procedure is termed "wrong charge background subtraction," and is performed both on data and MC.

7.8 Cut Summary, Event Yield & Control Plots

Cut Summary

Table 7.8 lists the selection cuts used to obtain the final high y analysis sample upon which the cross section measurement is made.

Event Yield

The yield Y is defined in equation 6.12 using events from the high y analysis final sample with a maximum electron polar angle of 145° and is shown in figures 7.38 and 7.39 for

Quantity q	Γ_q
ϵ_{id}	1.0000±0.0006[stat.]
ϵ_{trhy}	0.9980±0.0019[stat.]
$\mathcal{L}$	0.8661±0.0043
$N_{bg'}$	1.1824±0.0218[stat.]
κ	1.022±0.021 (0.020[stat.]±0.006[syst.])

Table 7.7: *The e^-p/e^+p Γ ratio of the quantities ϵ_{id}, ϵ_{trhy}, luminosity $\mathcal{L}$ and number of background events N_{bg} used to determine the charge asymmetry κ.*

the 0304e^+, 0405e^-, 06e^- and 0607e^+ periods respectively. Apart from the sudden change in yield attributed to the luminosity measurement (section 6.6), no abnormalities in the yields are observed over the indicated fit ranges.

Control Plots

Control plots[3] comparing the signal MC to the data are shown for the e^- and e^+ periods in figures 7.40 to 7.43 for various kinematic as well as detector quantities. All MC corrections including the efficiencies described in this chapter have been applied. The background subtraction procedure is also applied to both the data and MC. The ratio r of the data to the MC is also shown in the bottom part of each plot with the results of an $r = constant$ fit. Apart from the difference in normalization between the data and MC samples - $r = 1.040 \pm 0.005$ and 1.045 ± 0.005 for the e^- and e^+ periods respectively - the agreement in the shape of the distributions is good as shown by the fit results. The level of agreement in the $E - P_z$ distribution though is not as well described, but still within the uncertainties of the hadronic energy scale, section 5.4. Figure 7.44 shows the (a) electron energy and (b) electron polar angle distributions for events where the electron is in the backward part of the calorimeter, $z_{im} < -115$ cm; the level of agreement between data and MC is good. For reference the distribution of the background events (= wrong charged data events × charge asymmetry κ) is also shown.

From these plots it can be concluded that the simulation reasonably describes the data and that the detector's response to expected physics is well understood and represented by the various efficiency reweights and detector simulation. The nature of the background is also well accounted for.

---

[3] The control plots and cross sections correspond to the integrated luminosities given in table 6.8 (section 6.6).

Cut Name	Description
Run Selection[a]	Require CJC1,CJC2,LAr,ToF,Luminosity,CIP Require runs with subtrigger s75,67,77
Subtrigger	Require s75
LAR	**e**-Fired LAR1 (section 7.1)
Fiducial Volume	$E'_e > 7$ GeV if $z_{im} < -115$ cm $E'_e > 10$ GeV if $-125 < z_{im} < -115$ cm $z_{im} < 45$ cm
Scattered Electron	
LAr Candidate	Require scattered electron candidate in LAr
Minimum E'_e	$E'_e > 5$ GeV
	Reject:
ϕ-crack	$\phi_{wheel} \notin [-2^\circ, +2^\circ]$
Minimum z_{im}	$z_{im} > -190$ cm
z-crack 1	$-65 < z_{im} < -55$ cm
z-crack 2	$15 < z_{im} < 25$ cm
Tracker (TRHY)	
Central Vertex	Require Central Vertex
Vertex Range	Require $z_{vtx} \in [-35, 35]$cm
Electron Validation	DTRA Track with Distance to Cluster $d_{ca}^{cls} < 6$ cm
Kinematics	$(56 < Q_e^2 < 891)$ GeV^2 and $(0.63 < y_e < 0.9)$
ISR	$E - P_z > 35$ GeV
ep Background Cut	Use wrong charge background subtraction
non-*ep* Background Cut	Reject if:
Topological Cut	EP Topological Finders Fail and ($P_{tbal} < 0.5$ or $P_{tbal} > 2.0$ or $\eta_{max} < 3$)
Timing Cut	CJC Timing Fail and ($\eta_{max} < 3$)

---

[a] One common run selection requiring s75, s67 and s77 is used for the high y analysis and the nominal analysis.

Table 7.8: *Summary of the cuts used to obtain the final sample of the high y analysis.*

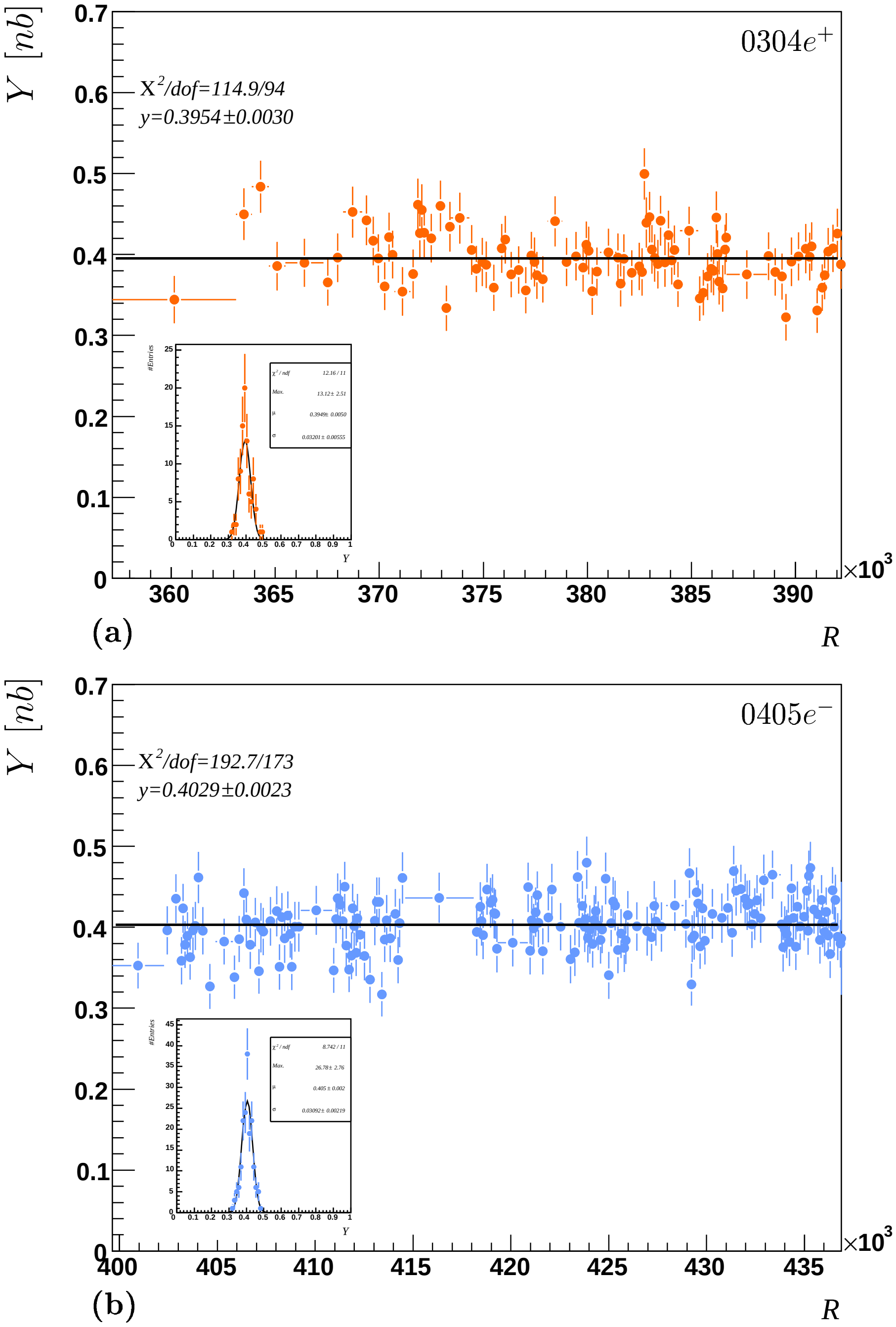

Figure 7.38: *(b) The event yield Y for the 0304e^+ period as a function of the run number R. Fitted to the data is the function Y = constant. The inner plot shows the result of a Gaussian fit to the yield distribution. (b) Similar plots for 0405e^- period.*

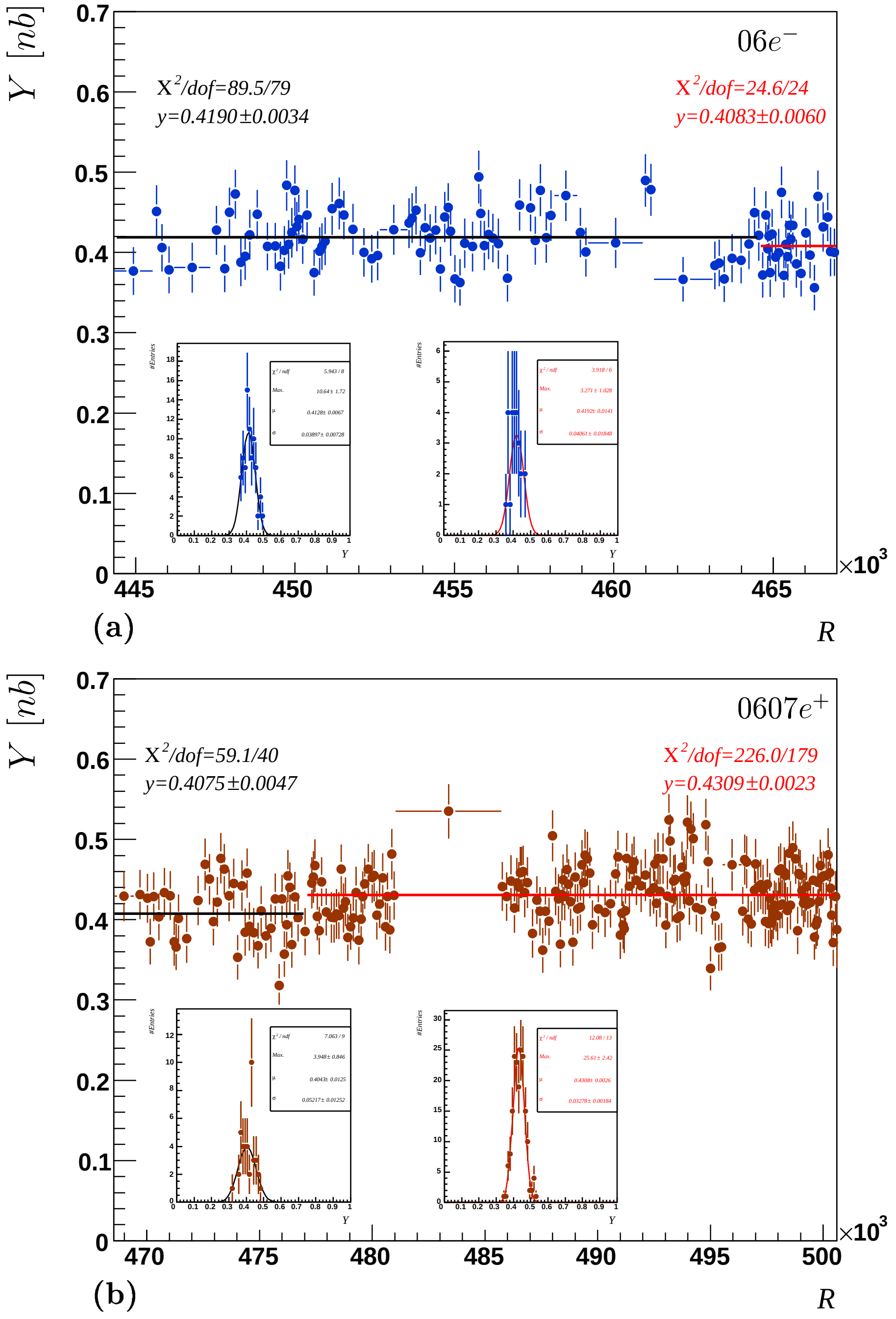

Figure 7.39: *(b) The event yield Y for the $06e^-$ period as a function of the run number R. Fitted to the data are two functions of the form Y = constant over the indicated run ranges. The inner plots show the result of a Gaussian fit to the two yield distributions corresponding to the fitted runranges. (b) Similar plots for $0607e^+$ period.*

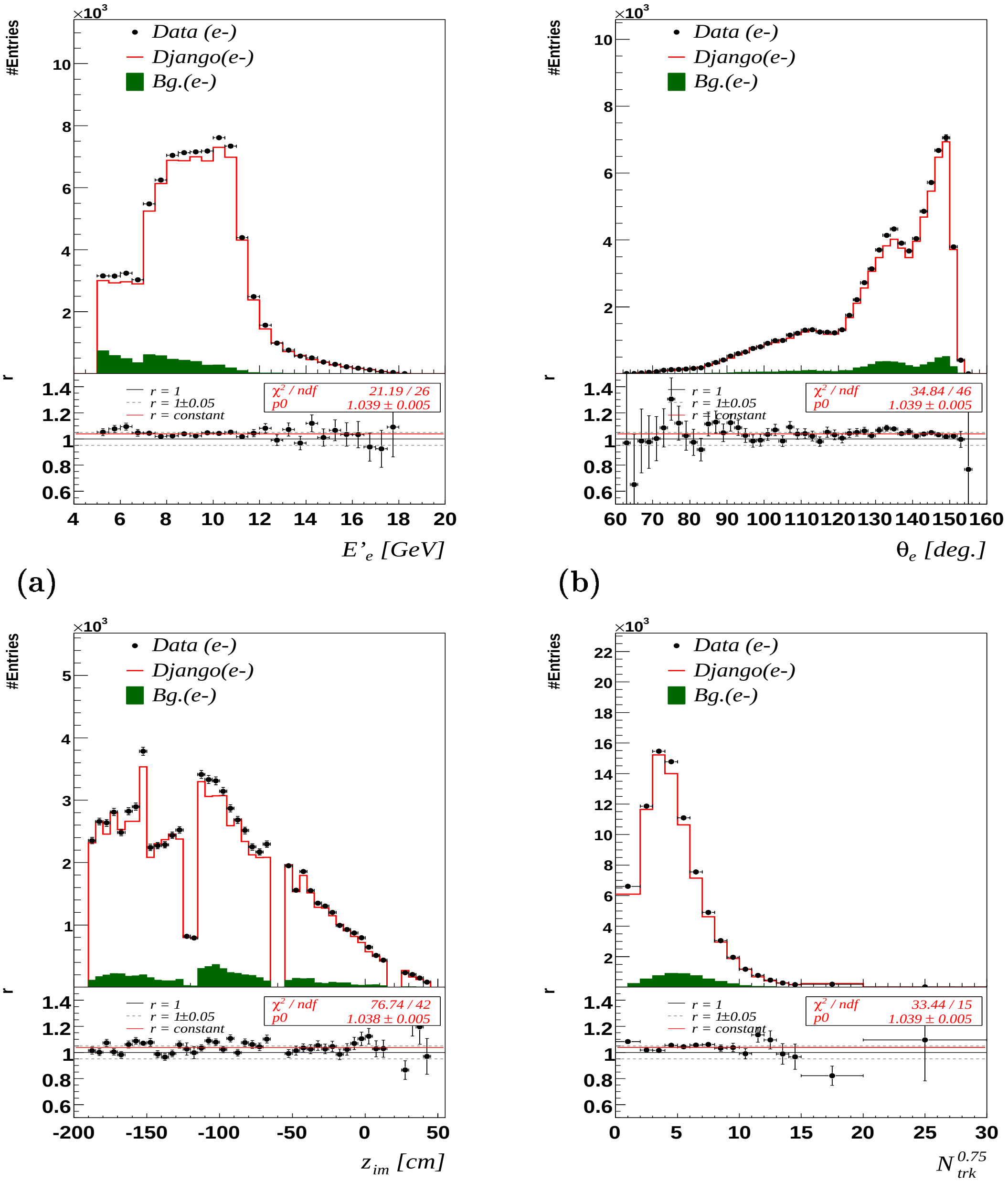

(a) (b) (c) (d)

Figure 7.40: *Control plots comparing the signal MC to the data distributions for (a) electron energy, (b) electron polar angle, (c) z-coordinate of the impact position and (d) number of tracks with* $p_t > 0.75$ *GeV for the* e^- *period. The distribution of the background (wrong charge data events × asymmetry) is also shown. The ratio r of data to MC is given in the bottom part of the plot and fitted by a* $r = constant$ *hypothesis. All correctons are applied to the MC; background subtraction is applied to both the data and MC.*

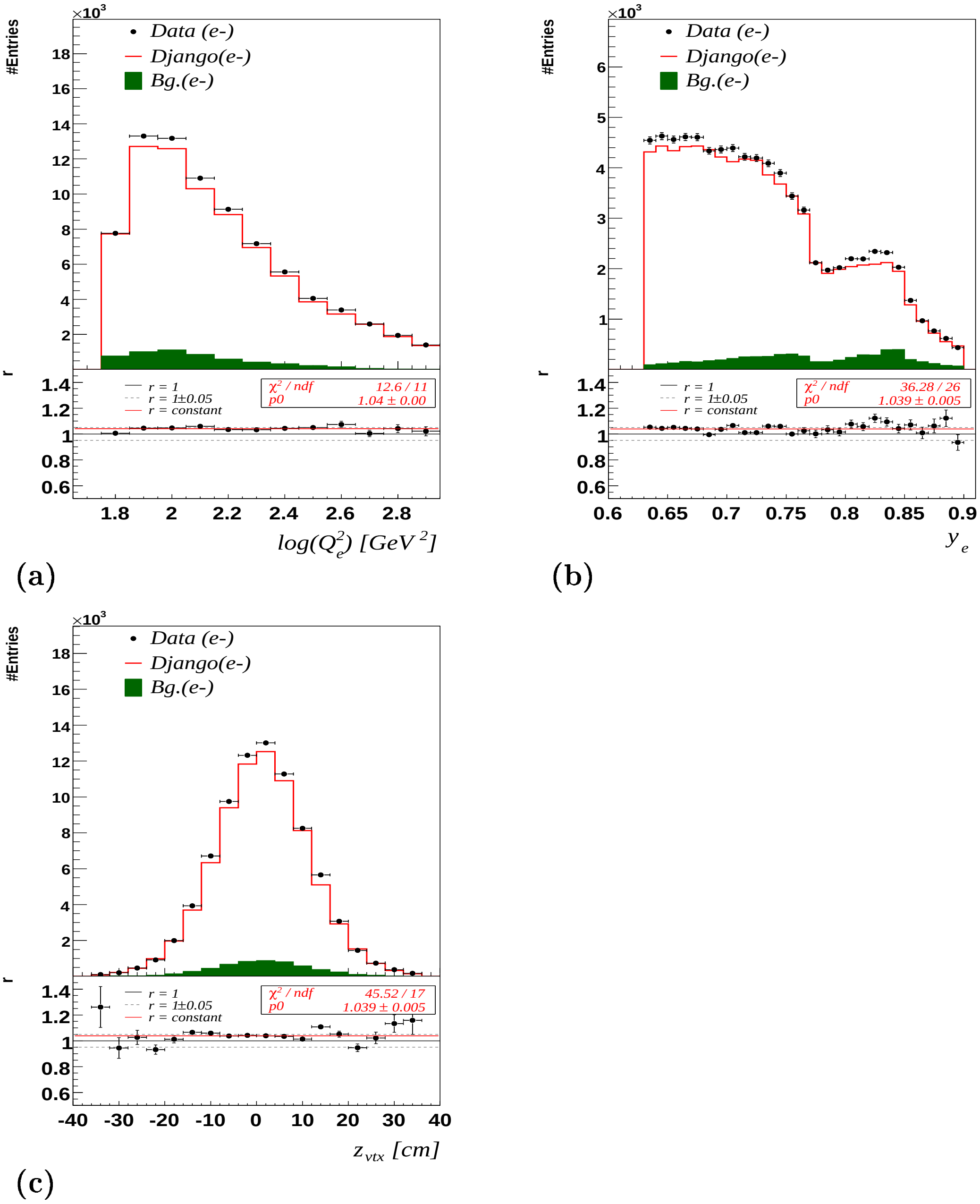

(a)

(b)

(c)

Figure 7.41: *Control plots comparing the signal MC to the data distributions for (a) log*(Q_e^2)*, (b) inelasticity* y_e *and (c) z-position of the reconstructed vertex. The distribution of the background (wrong charge data events × asymmetry) is also shown. The ratio* r *of data to MC is given in the bottom part of the plot and fitted by a* $r = constant$ *hypothesis. All corrections are applied to the MC; background subtraction is applied to both the data and MC.*

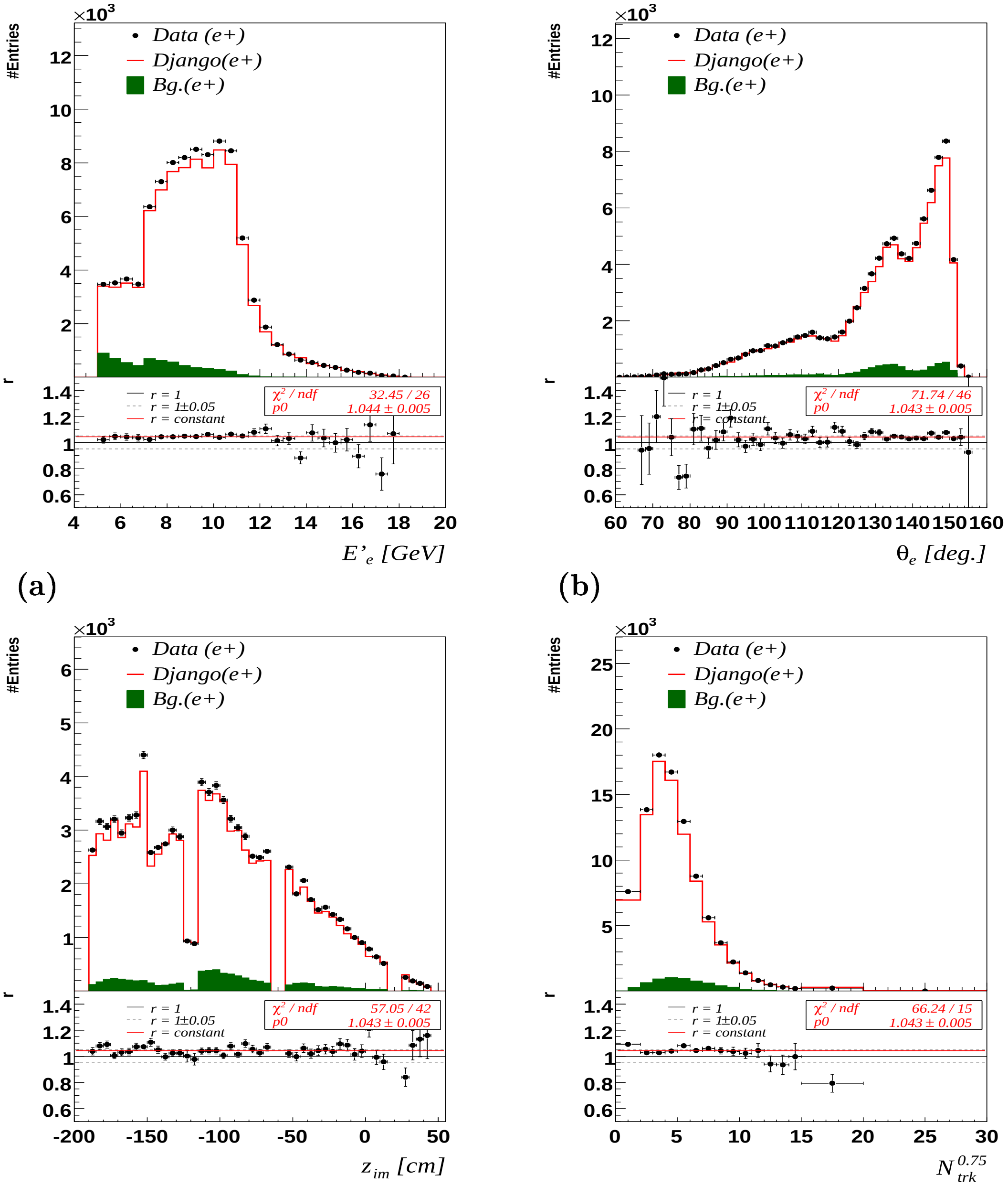

(a) (b)

(c) (d)

Figure 7.42: *Control plots comparing the signal MC to the data distributions for (a) electron energy, (b) electron polar angle, (c) z-coordinate of the impact position and (d) number of tracks with* $p_t > 0.75$ *GeV, for the* e^+ *period. The distribution of the background (wrong charge data events × asymmetry) is also shown. The ratio r of data to MC is given in the bottom part of the plot and fitted by a r = constant hypothesis. All correctons are applied to the MC; background subtraction is applied to both the data and MC.*

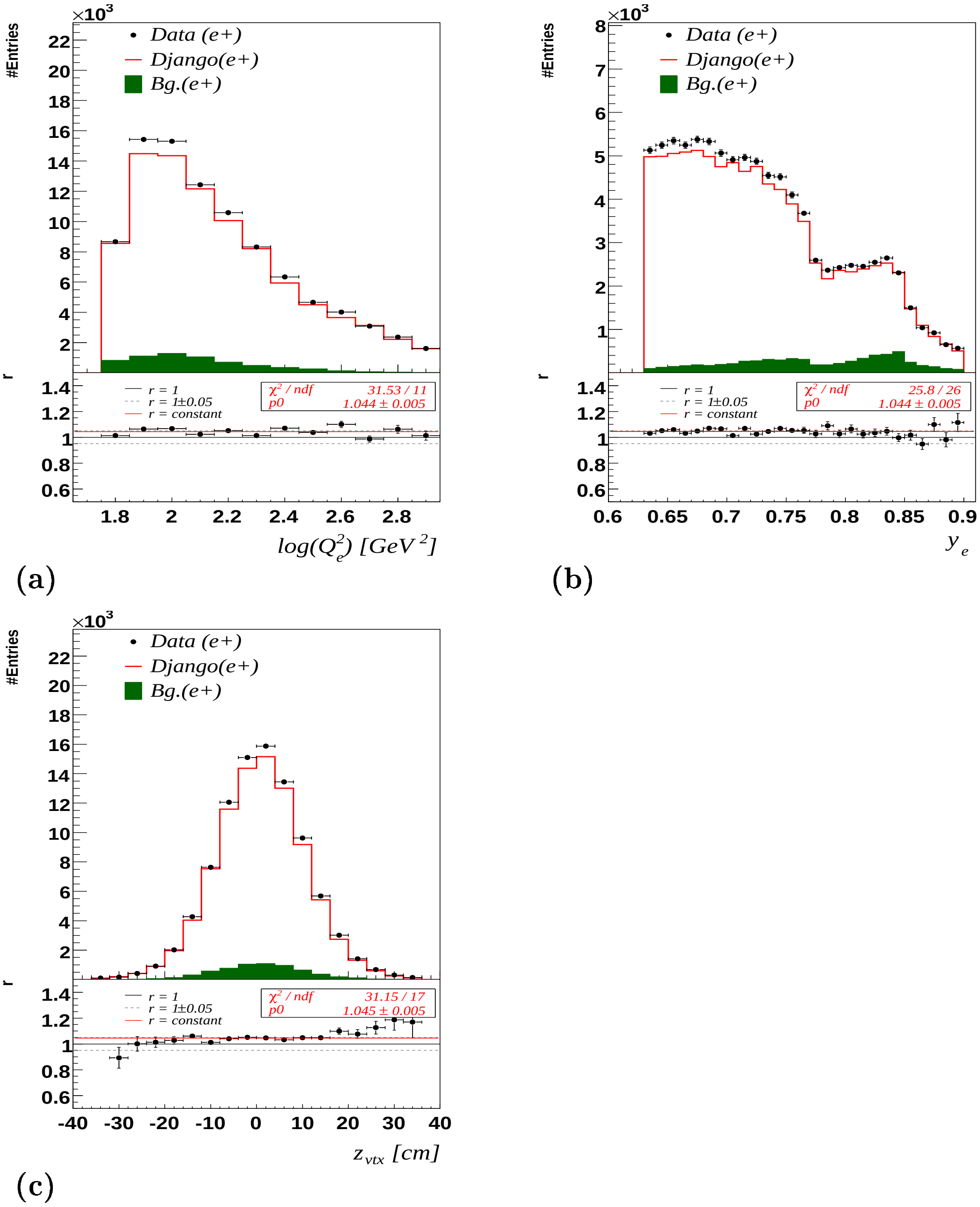

(a) (b) (c)

Figure 7.43: *Control plots comparing the signal MC to the data distributions for (a) log(Q_e^2), (b) inelasticity y_e and (c) z-position of the reconstructed vertex for the e^+ period. The distribution of the background (wrong charge data events × asymmetry) is also shown. The ratio r of Data to MC is given in the bottom part of the plot and fitted by a $r =$ constant hypothesis. All corrections are applied to the MC; background subtraction is applied to both the data and MC.*

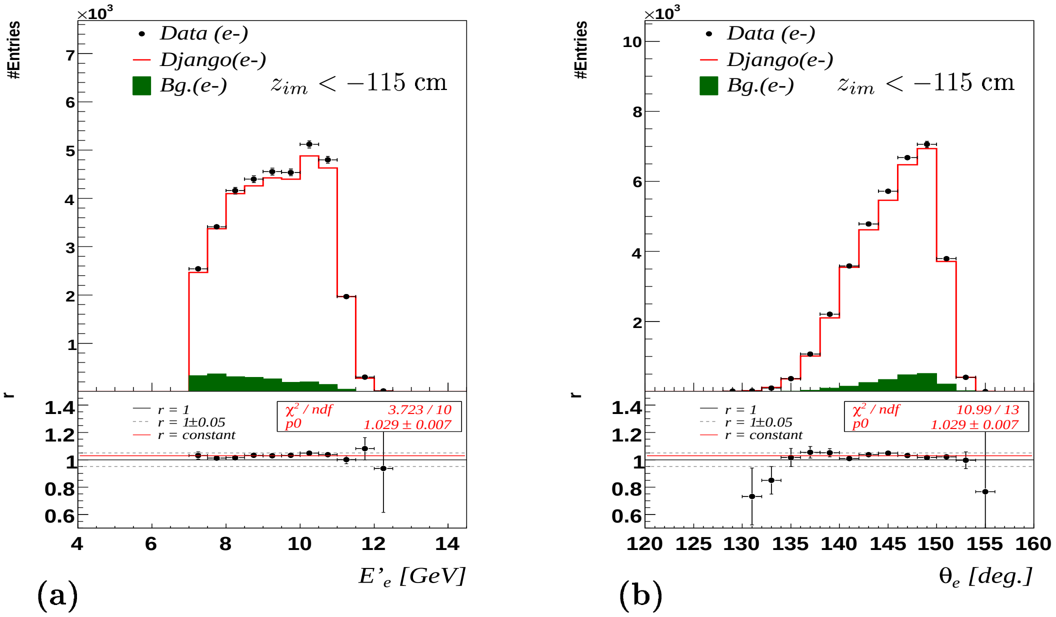

(a) **(b)**

Figure 7.44: *Control plots comparing the signal MC to the data distributions for (a) electron energy and (b) electron polar angle for the* e^- *period in the region* $z_{im} < -115$ *cm. The distribution of the background (wrong charge data events* × *asymmetry) is also shown. The ratio* r *of Data to MC is given in the bottom part of the plot and fitted to a* $r =$ *constant hypothesis. All corrections are applied to the MC; background subtraction is applied to both the data and MC.*

Chapter 8

Measurement I: Kinematic Reconstruction and the Binning Scheme

As ***both*** *final states - the scattered electron and the hadronic final state - are measured at H1, the kinematics of neutral current processes can be reconstructed exclusively from either final state or using information from both. The redundancy afforded by such an overdetermined process is taken one step further in this thesis. Using resolution and systematic error on the cross section as indicators of reliability and precision, the phase space is divided into regions best suited for a particular reconstruction method. As the final states correspond to parts of the detector that are largely independent, this sets the stage for a combination of the cross section measurements whereby the two final states effectively cross calibrate one another, Chapter 9 - Extracting the Cross Section.*

8.1 Binning Scheme

The events in the final sample are binned in x and Q^2 using a bin grid depicted in figure 8.1. For the nominal analysis the bin grid is shown as the red dashed lines and defined by the following bin boundaries:

$log(Q^2)$ [GeV^2] Bin Boundaries

1.6500	1.7500	1.8500	1.9500	2.0500	2.1500	2.2500	2.3500	2.4500
2.5500	2.6500	2.7500	2.8500	2.9500	3.0500	3.1500	3.2500	3.3500
3.5500	3.7782	4.0000	4.2222	4.4437	4.6659	4.8881	log(101568.0)	

$log(x)$ Bin Boundaries for $log(Q^2) < 2.65$ GeV^2

-3.3110 -2.8000 -2.6000 -2.4000 -2.2000 -2.0000 -1.8000 -1.6000
-1.4000 -1.2000 -1.0000 -0.7670 -0.5000 0.0000

$log(x)$ Bin Boundaries for $log(Q^2) > 2.65$ GeV^2

-3.3110 -2.8000 -2.6000 -2.4000 -2.2000 -2.0000 -1.8000 -1.6000
-1.4000 -1.2000 -1.0000 -0.8386 -0.6800 -0.5000 -0.3000 0.0000

The size of the bins increases with increasing Q^2 and decreasing x in order to limit the statistical error on the corresponding cross sections. The bin sizes are also large enough to ensure that the Q^2 and x resolutions are better than the bin width, Chapter 8, and that the statistical errors between the bins are uncorrelated.

For the high y analysis the bin grid is shown as the black dotted lines in figure 8.1 and defined by the following bin boundaries:

$log(Q^2)$ [GeV^2] Bin Boundaries

1.6500 1.7500 1.8500 1.9500 2.0500 2.1500 2.2500 2.3500 2.4500
2.5500 2.6500 2.7500 2.8500 2.9500

The high y analysis bin edges follow exactly those of the nominal analysis and are bounded by the y cuts of 0.63 and 0.9.

In this thesis the cross sections are quoted at *points* in the the x-Q^2 kinematic plane following a bin centre correction procedure described in section 9.1. These points (not necessarily at the center of the bin) are the *bin centres* (Q_c^2, x_c) for the corresponding bins and are shown figure 8.1. For the nominal analysis (red circles) the bin centres are:

Q_c^2 [GeV^2] Bin Centres

50 65 80 100 120 150 200 250 300
400 500 650 800 1000 1200 1500 2000 3000
5000 8000 12000 20000 30000 50000 90000

x_c Bin Centres for $log(Q^2) < 2.65$ GeV^2

0.0010 0.0020 0.0032 0.0050 0.0080 0.0130 0.0200 0.0320
0.0500 0.0800 0.1300 0.2500 0.4000

x_c Bin Centres for $log(Q^2) > 2.65$ GeV^2

0.0010 0.0020 0.0032 0.0050 0.0080 0.0130 0.0200 0.0320
0.0500 0.0800 0.1300 0.1800 0.2500 0.4000 0.6500

The high y analysis bin centres (black circles, figure 8.1) follow those of the nominal analysis:

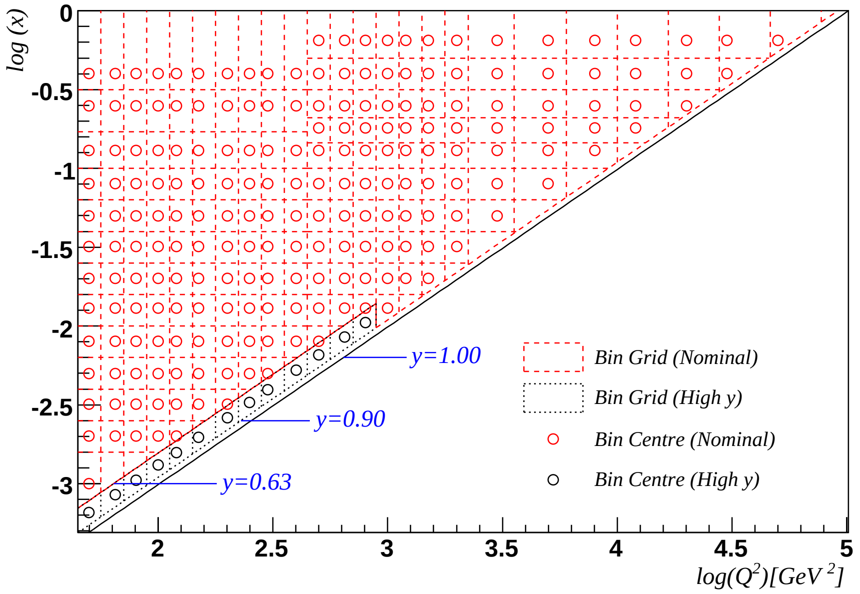

Figure 8.1: *The x-Q^2 kinematic plane showing the bin grids used in the nominal analysis (red dashed lines) and the high y analysis (black dotted lines). Also shown are the nominal analysis and high y analysis bin centres where the cross sections are quoted (red and black circles respectively).*

Q^2_c [GeV^2] Bin Centres								
50	65	80	100	120	150	200	250	300
400	500	650	800					

8.2 Bin Integrity

A bin is considered acceptable for extracting its corresponding differential cross section if it passes certain quality cuts. It is useful to define the reconstruction efficiency $\epsilon_{\mathcal{R}}$, stability $\mathcal{S}$, purity $\mathcal{P}$ and acceptance $\mathcal{A}$ for a given bin in the following way:

$$\epsilon_{\mathcal{R}} = \frac{N^{MC}_{pass}}{N^{MC}_{gen}}$$

$$\mathcal{S} = \frac{N^{MC}_{stay}}{N^{MC}_{pass}}$$

$$\mathcal{P} = \frac{N^{MC}_{stay}}{N^{MC}_{rec}}$$

$$\mathcal{A} = \frac{N^{MC}_{rec}}{N^{MC}_{gen}}$$

where:

- N^{MC}_{gen} is the number of events generated *in* the given bin
- N^{MC}_{pass} is the number of events reconstructed (passes final selection) *from* the given bin.
- N^{MC}_{stay} is the number of events reconstructed *from* the given bin and reconstructed *in* the given bin.
- N^{MC}_{rec} is the number of events reconstructed *in* the given bin

The events used are those from the signal MC. It can be shown that:

$$\mathcal{A} = \frac{\epsilon_{\mathcal{R}} \cdot \mathcal{S}}{\mathcal{P}}$$

As an example suppose that 100 events were generated in a particular bin. Out of the 100, 80 were reconstructed. And out of the 80, 55 remained in the bin (so that 25 migrated out). Also, 65 events were reconstructed in total in the bin (that is, 10 events migrated *in* from neighbouring bins). Then:

$N^{MC}_{gen} = 100$,

$N^{MC}_{pass} = 80$,

$N^{MC}_{stay} = 55$,

$N^{MC}_{rec} = 65$,

$\epsilon_{\mathcal{R}} = 80/100$ (80%),

$\mathcal{S} = 55/80$ (68.75%),

$\mathcal{P} = 55/65$ ($\approx$ 85%),

$\mathcal{A} = 65/100$ (65%).

8.3 Electron Method

Perhaps the most natural way to reconstruct NC kinematics is from measurements of the scattered electron's energy E'_e and polar angle θ_e according to

$$Q^2_e = 2E_eE'_e(1+\cos\theta_e), \qquad y_e = \frac{2E_e - E'_e(1-\cos\theta_e)}{2E_e} \quad \text{and} \quad x_e = \frac{Q^2_e}{sy_e}. \tag{8.1}$$

This is known as the electron method (**e-method**) of reconstruction. At the experiment both E'_e and θ_e are measured using the LAr Calorimeter, with energy depositions mainly contained in the EM section. The corresponding Q^2 and x resolutions are shown in figures 8.2 and 8.3 respectively for the Nominal Analysis x - Q^2 binning where the resolution of say Q^2 (Q^2_{res}) for a given bin is defined as:

$$Q^2_{res} = \sigma(\frac{Q^2_{rec} - Q^2_{gen}}{1/2 - bin - width}) \tag{8.2}$$

so that $Q^2_{res} = 1$ corresponds to a resolution equal to half of the bin-width (1/2-bin-width). It can be seen that the Q^2_e resolution is better than the 1/2-bin-width for most of the phase space. The x_e resolution however degrades rapidly with decreasing y (increasing x) since the relative resolution of x_e , $\sigma(x_e)/x_e$ is given by

$$\frac{\sigma(x_e)}{x_e} = \frac{1}{y_e}\frac{\sigma(E'_e)}{E'_e} \oplus tan\frac{\theta_e}{2}(x_e\frac{E_p}{E_e} - 1)\sigma(\theta_e) \tag{8.3}$$

where $\sigma(E'_e)$ and $\sigma(\theta_e)$ are the electron energy and polar angle resolutions respectively.

The e-method of reconstruction does not take into account initial state radiation (ISR) where a photon γ is emitted before the hard interaction, figure 8.4, thereby reducing the incoming electron energy from E_e to E^*_e . Thus Q^2 and y are overestimated, while x is underestimated.

8.4 Sigma Method

The limitations of the e-method (poor x resolution at low y and ISR bias) are somewhat overcome by the sigma method (**s-method**) of reconstruction [54]. The interaction is

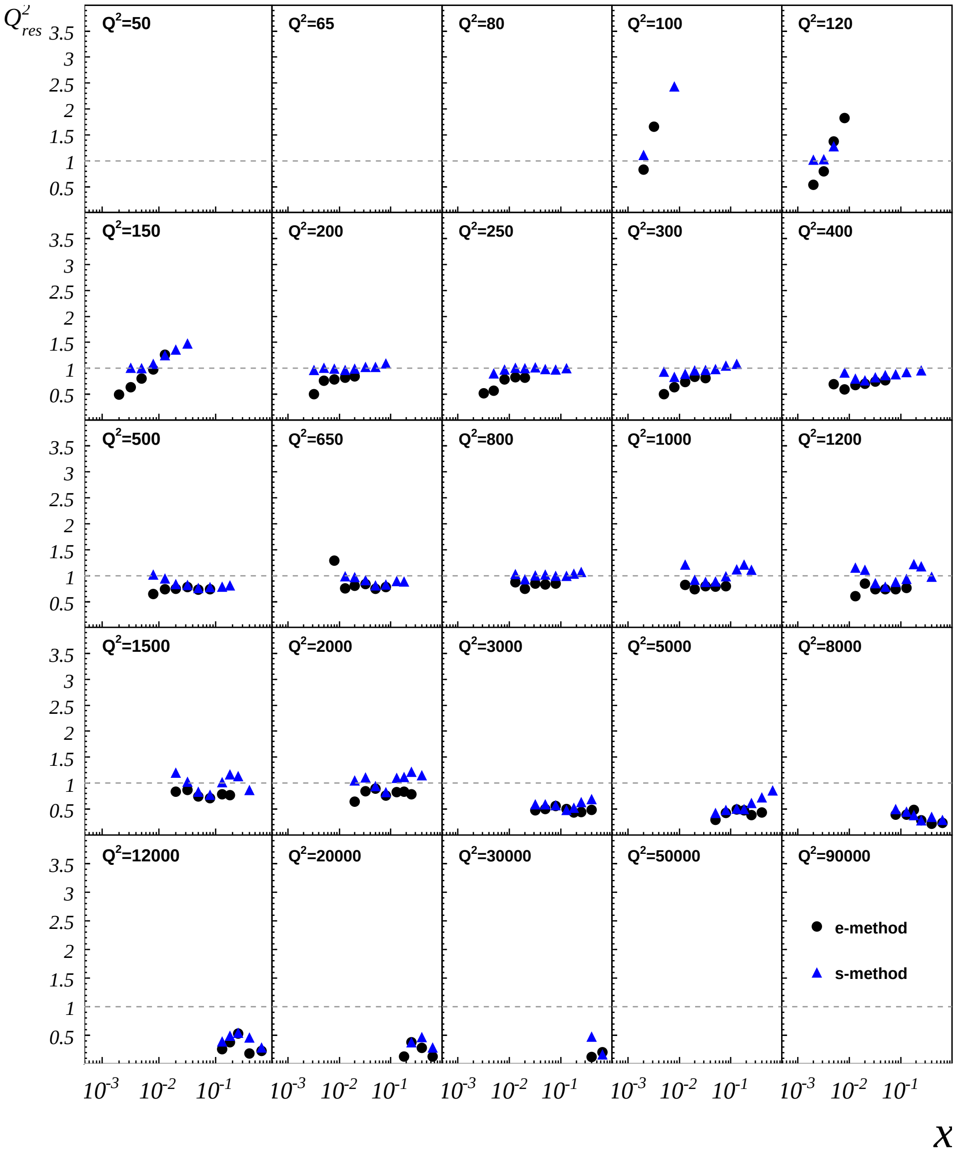

Figure 8.2: *The Q^2 resolution Q^2_{res} at fixed $Q^2[GeV^2]$ as a function of x using the Nominal Analysis binning scheme. The e-method and s-method are shown for comparison.*

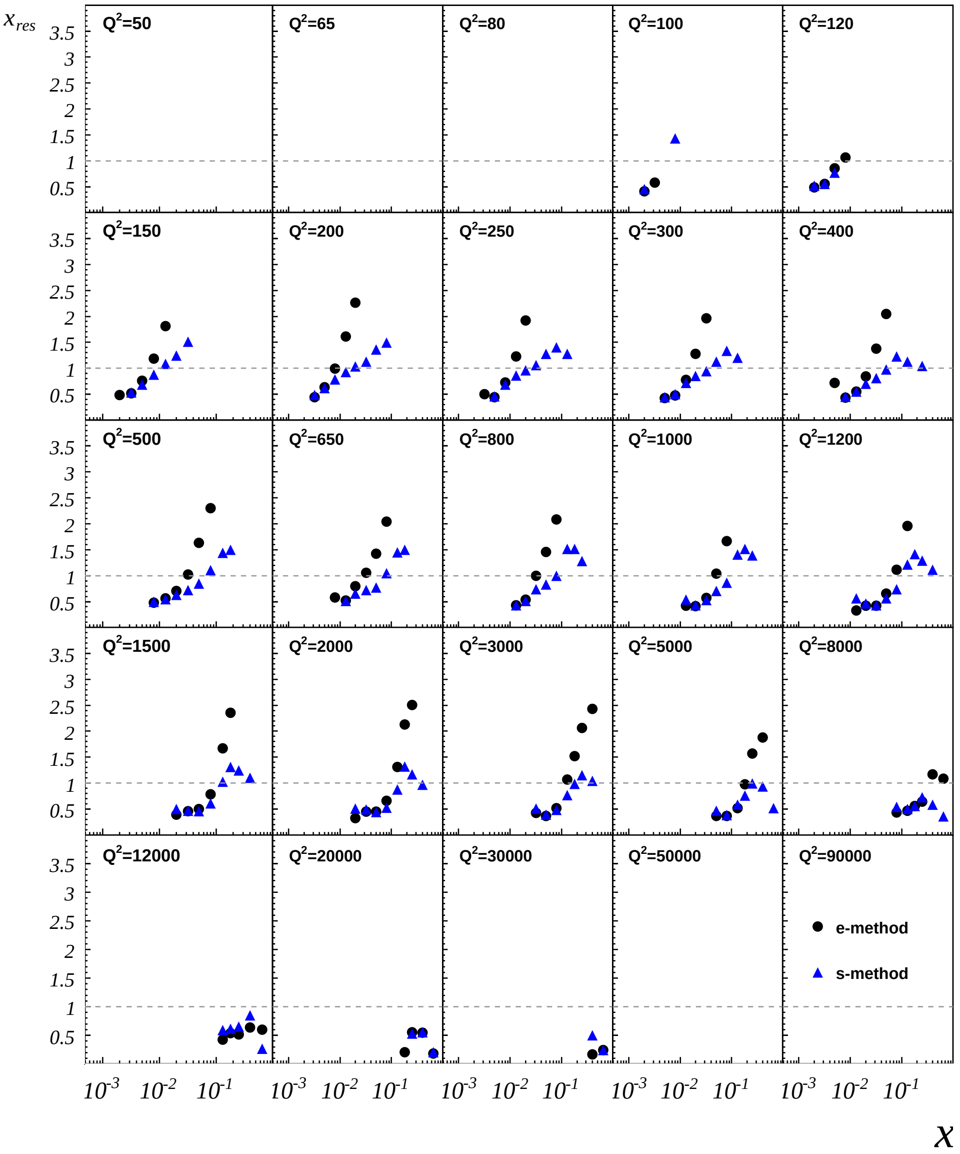

Figure 8.3: *The x resolution x_{res} at fixed $Q^2[GeV^2]$ as a function of x using the Nominal Analysis binning scheme. The e-method and s-method are shown for comparison.*

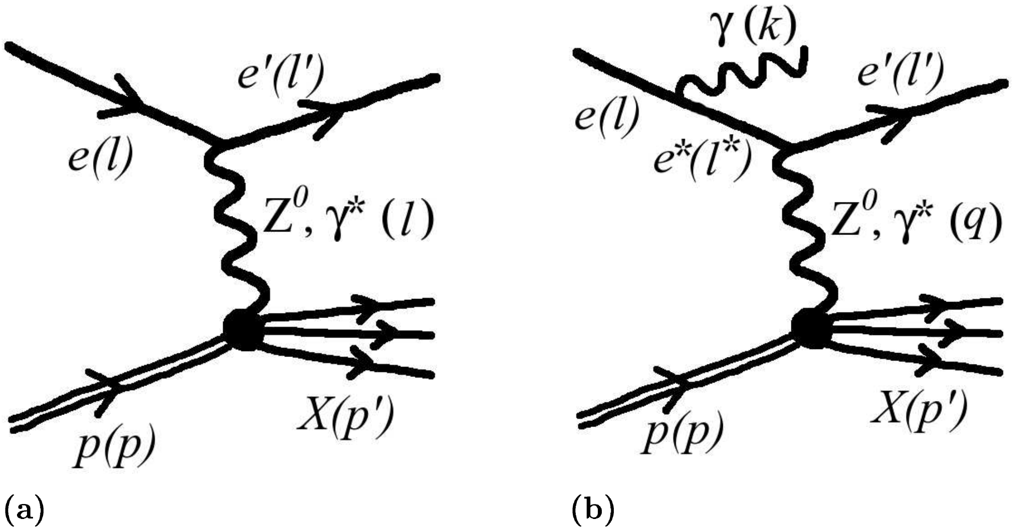

Figure 8.4: *Feynman diagrams for neutral current scattering without (a) and with (b) initial state radiation. The quantities in parenthesis are the corresponding four-vectors.*

assumed to have ISR with the photon radiated in the direction of the incoming lepton. This results in a reduction of the effective incoming lepton beam and centre of mass energies by the factor E_e^*/E_e. To correct for this, one extra variable is needed and this comes from the HFS, Σ_h(equation 5.7).

If the energy of the ISR photon γ is E_γ and the $E - Pz$ of the scattered electron is denoted by Σ_e' , the *reduced* incoming lepton energy E_e^* (=$E_e - E_\gamma$) can be estimated by conserving longitudinal momentum

$$2E_e^* = \Sigma_h + \Sigma_e' \tag{8.4}$$

since the ISR photon will miss the main detector. Replacing E_e by E_e^* in equations 8.1 gives the s-method kinematics

$$y_\Sigma = \frac{\Sigma_h}{\Sigma_h + 2E_e'(1-\cos\theta_e)}, \qquad Q_\Sigma^2 = \frac{(E_e'\sin\theta_e)^2}{1-y_\Sigma} \quad \text{and} \quad x_\Sigma = \frac{Q_\Sigma^2}{s y_\Sigma}. \tag{8.5}$$

Note that Q_Σ^2 and y_Σ takes into account ISR while x_Σ is underestimated since the reduced centre of mass energy s_Σ (= $4E_e^* E_p$) is not used.

From figure 8.3 it can be seen that the x resolution from the s-method is significantly better at low y compared to the e-method since

$$\frac{\sigma(x_\Sigma)}{x_\Sigma} = (\frac{4E_e(1-y_e)}{\Sigma} + 1)\frac{\sigma(E_e')}{E_e'} \oplus tan\frac{\theta_e}{2}(\frac{Q_e^2}{\Sigma E_e} - 1)\sigma(\theta_e) \oplus (2y_\Sigma - 1)\frac{\sigma(\Sigma_h)}{\Sigma_h} \tag{8.6}$$

where $\Sigma = \Sigma_h + \Sigma'_e$. Comparing equations 8.3 and 8.6, the contribution to the x resolution due to E'_e in the e-method is much greater than the s-method at low y . At higher values of y this advantage is lost due to greater uncertainties in the HFS reconstruction as more particles enter the central part of the detector. The Q^2 resolution of the s-method is worse than that of the e-method due to the uncertainty introduced by using the HFS in the calculation, figure 8.2.

8.5 Electron-Sigma Method

The electron-sigma method (**es-method**) is designed to take advantage of the Q^2 reconstruction from the e-method and x reconstruction from the s-method. Thus the kinematics are calculated by

$$Q^2_{e\Sigma} = Q^2_e, \qquad x_{e\Sigma} = x_\Sigma \qquad \text{and} \qquad y_{e\Sigma} = \frac{Q^2_e}{s x_\Sigma}. \tag{8.7}$$

The stability and purity are shown in figures 8.5 and 8.6 demonstrating the virtue of such a combination. At lower values of y the es-method outperforms both the e-method and s-method since it takes the binning variables from the best method (Q^2 from the e-method and x from the s-method). However this is not optimum at higher values of y where the best resolution for both binning variables come from the e-method. As a further motivation to optimize the kinematic reconstruction, the systemtic errors on the cross section measurement arising from the electron energy, electron polar angle, hadron energy and calorimeter noise contributions, δ_{sys} , are shown in figure 8.7 for the e- and es-methods. It is evident that the gain in precision by using the e-method over the es-method is significant for high y measurements.

8.6 Splitting the Kinematic Plane

The kinematic plane is thus partitioned into a low y region where the cross section is quoted using the es-method and a high y region where the cross sections is quoted using the e-method. Bins with bin centres having y values < 0.3 define the low y region; all other bins constitute the high y region. This partitioning is shown as the vertical line in figures 8.5, 8.6 and 8.7. Bins to the right of the vertical line define the low y region and to the left the high y region. All bins with bin centres having Q^2 values > 12000 GeV^2 are in the high y region.

For a given event, y_e may be greater than $y_{e\Sigma}$ due to either ISR or detector resolution. This can lead to *double counting* if the event is binned in both the low and high y regions. To investigate the statistical correlation between the number of reconstructed events in

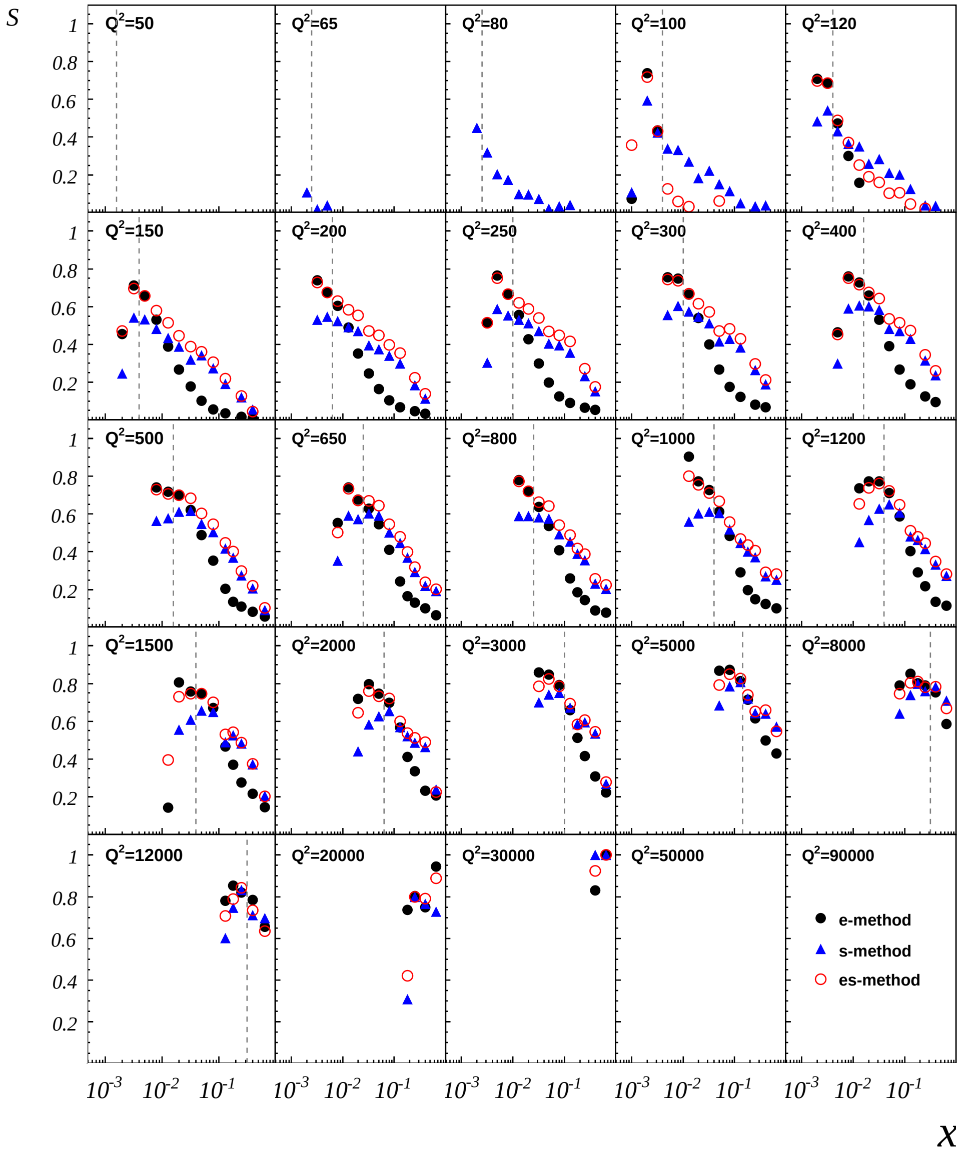

Figure 8.5: *The stability* $\mathcal{S}$ *at fixed* Q^2*[GeV*^{2}*] as a function of* x *using the Nominal Analysis binning scheme. The e-method, s-method and es-method are shown for comparison. Bins to the right of the vertical line define the low* y *region and to the left the high* y *region. All bins with bin centres having* Q^2 *values* > 12000 *GeV*^{2} *are in the high* y *region.*

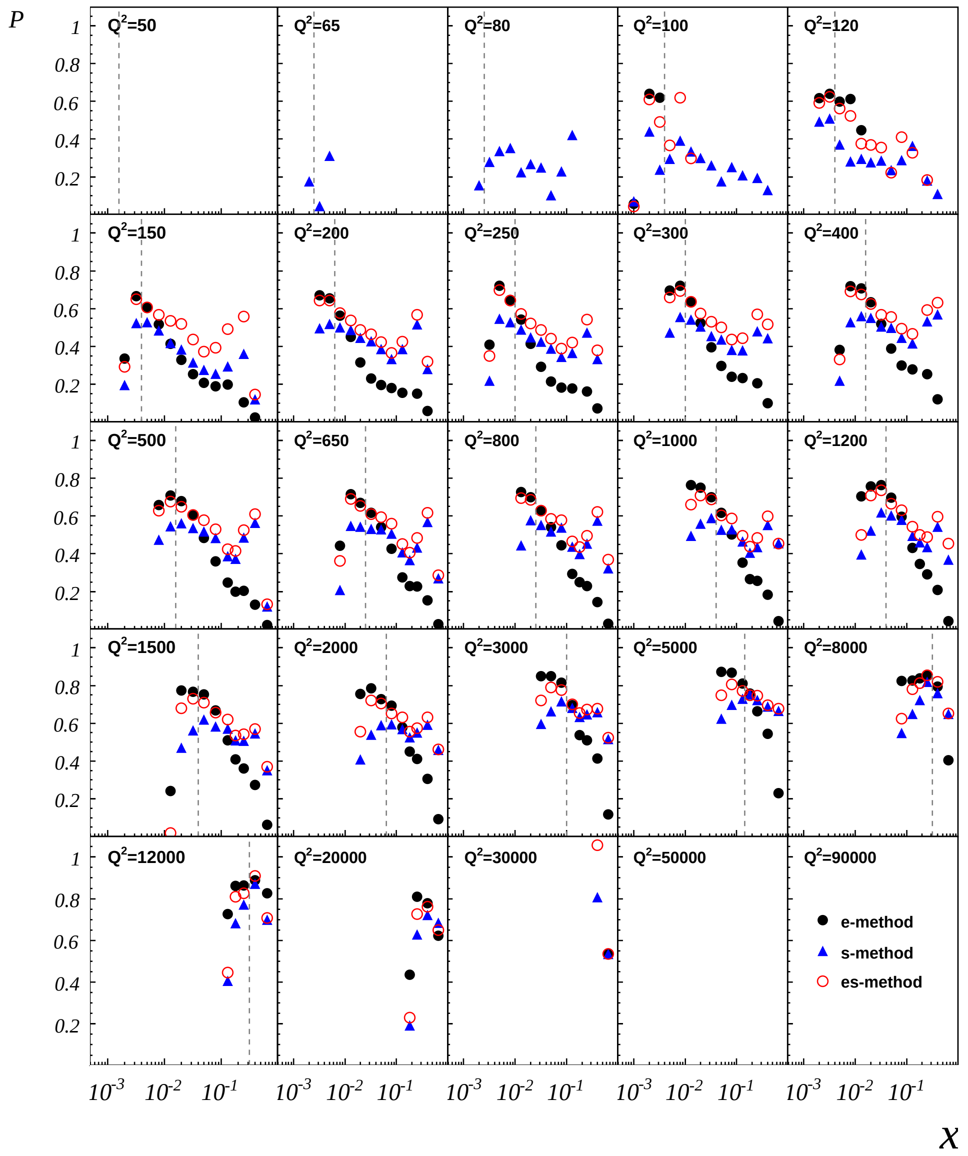

Figure 8.6: *The purity $\mathcal{P}$ at fixed Q^2[GeV^2] as a function of x using the Nominal Analysis binning scheme. The e-method, s-method and es-method are shown for comparison. Bins to the right of the vertical line define the low y region and to the left the high y region. All bins with bin centres having Q^2 values > 12000 GeV^2 are in the high y region.*

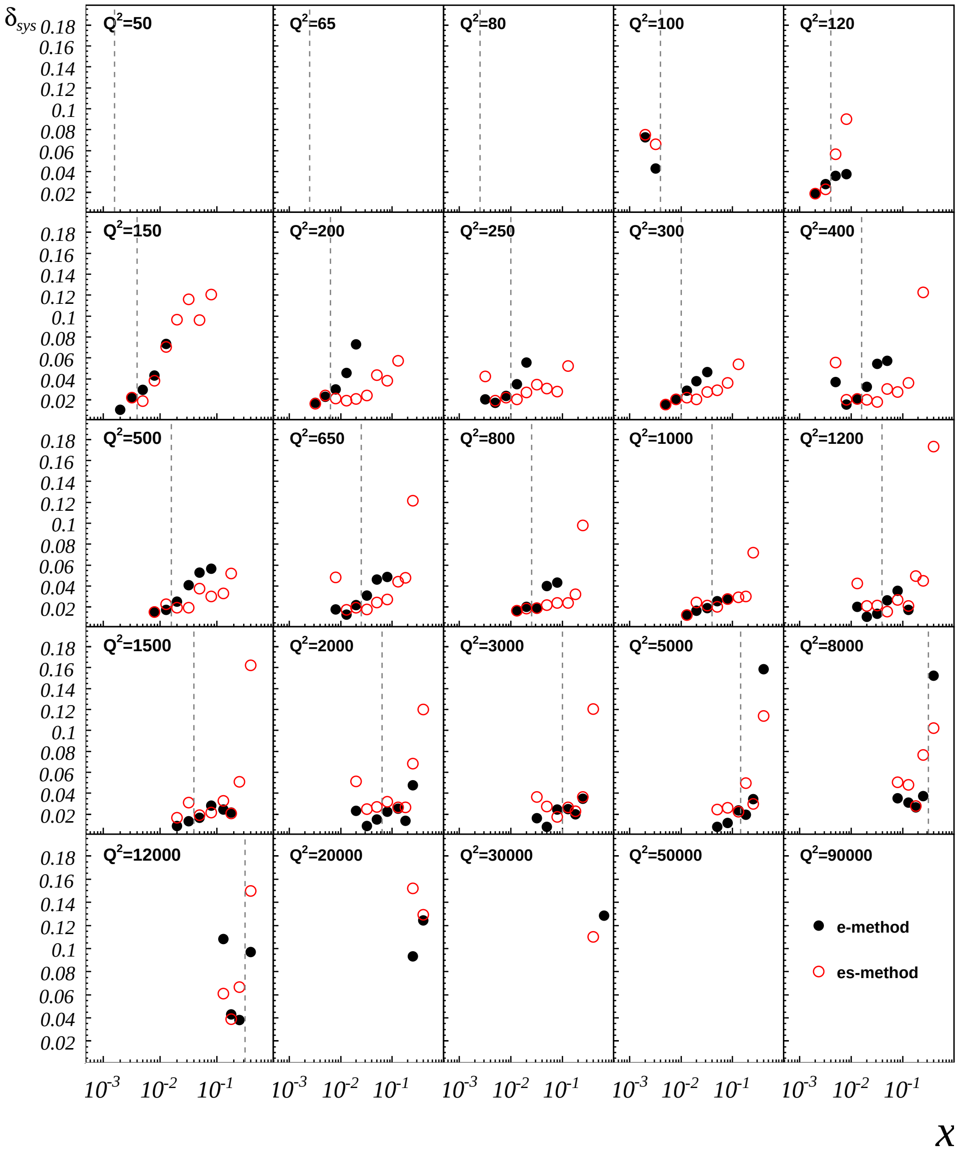

Figure 8.7: *The systematic error δ_{sys} on the cross section measurement arising from the uncertainties in the electron energy E'_e , electron polar angle θ_e , hadron energy and noise energy contributions. Bins to the right of the vertical line define the low y region and to the left the high y region. All bins with bin centres having Q^2 values > 12000 GeV^2 are in the high y region.*

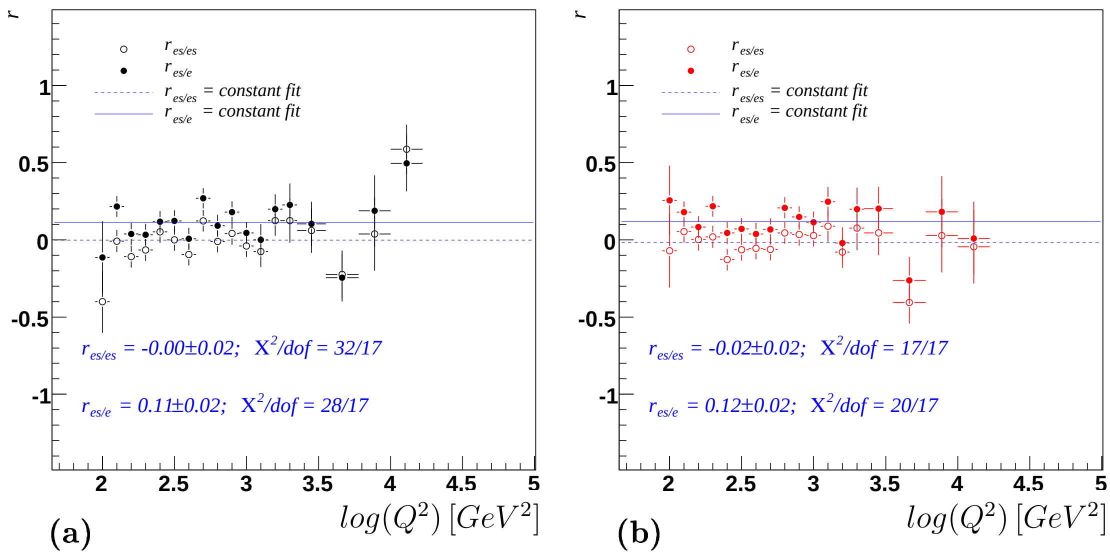

Figure 8.8: *The correlation coefficient r between the highest x bin in the high y region and the lowest x bin in the low y region as a function of Q^2. r is measured in the case where the es-method is used in both bins ($r_{es/es}$ - no double counting) and when the es-method is used in the low y region and the e-method in the high y region ($r_{es/e}$). Both data (a) and signal MC (b) are shown together with the results of $r = constant$ fits.*

adjacent x bins for a given Q^2 bin, the correlation coefficient r was measured between the highest x bin in the high y region and the lowest x bin in the low y region, first for the es-method of reconstruction in both bins ($r_{es/es}$ - no double counting) and then for the e-method in the high y region and es-method in the low y region ($r_{es/e}$ double counting possible). The correlation coefficient r of Q^2 is shown for data and signal MC in figures 8.8(a) and (b) respectively. The measurements are fitted by a $r = constant$ assumption. It can be seen that the increase in r^2 ($=r^2_{es/e} - r^2_{es/es}$) is of the order 1%, showing that the correlations introduced by double counting can be neglected. The statistical errors are therefore treated as uncorrelated across bins.

8.7 High y Stability and Purity

All cross section bins of the high y analysis have bin centres at $y_c = 0.75$, thus the e-method of reconstruction is used. The resulting stability and purity are shown in figures 8.9(a) and (b) for the e^- and e^+ periods respectively taking values greater than ≈70% in all bins.

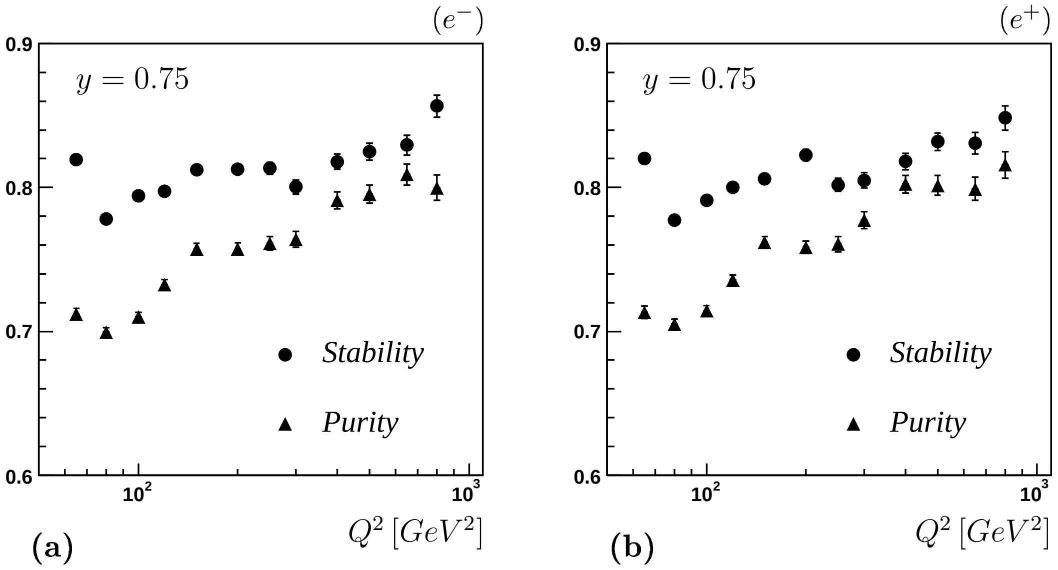

Figure 8.9: *The stability and purity of high* y *analysis bins for the (a)* e^- *and (b)* e^+ *periods.*

Chapter 9

Measurement II: Cross Section Extraction

The work done in the previous chapters produced data samples upon which the cross sections are to be measured. The last chapter explained the method to be used in reconstructing the kinematics. This chapter describes the process of extracting the cross section. The use of signal Monte Carlo and its faithfulness in reproducing the data allows correction of the data for efficiency losses, radiative effects and the limited precision of reconstructed four-momentum quantities (including energy calibration and detector alignment). All corrections have their respective uncertainties, and these are taken into account in the extraction process.

The measured reduced cross sections are then presented and compared to previous measurements as well as expectations as determined from various QCD fits.

9.1 Cross Section Extraction

In this thesis, double differential cross sections in the kinematic variables x and Q^2 are measured. Each measurement, $\mathrm{d}^2\sigma/\mathrm{d}x\mathrm{d}Q^2$, is quoted at a particular *point* (Q_c^2, x_c) corresponding to one of the bin centres defined in section 8.1. Each bin centre is associated to a particular 2-dimensional bin in the bin grid – the measurement originating from the number of events observed in the particular bin. Figure 9.1 shows one such point (full dot) together with the bin associated to it (shaded rectangle).

In the **nominal analysis** the cross section at (Q_c^2, x_c) is measured using

$$\frac{d^2\sigma}{dxdQ^2} = \frac{N^D - N^B}{\mathcal{A} \cdot \mathcal{L}} \cdot \delta^{bc}(Q_c^2, x_c) \tag{9.1}$$

where:

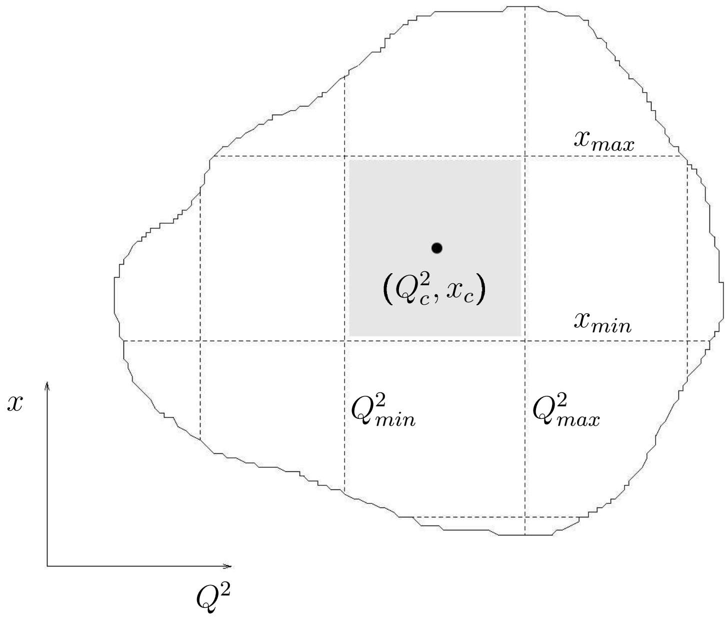

Figure 9.1: *A "patch" of phase space in the xQ^2 analysis plane. The dashed lines represent the bin grid. Each bin has a bin centre (Q^2_c, x_c) defined where the cross section measurement is quoted. The bin centre for the shaded bin is shown as the full dot.*

N^D is the number of events in the data
N^B is the number of background events, estimated from the simulation as the sum of the photoproduction, Compton and lepton pair production contributions
$\mathcal{A}$ is the acceptance introduced in section 8.2, and is determined using the signal MC which contains radiative events (section 9.3). $\mathcal{A}$ contains all corrections (apart from background) including efficiency and radiative corrections, as well as the effects due to measurement of the final states including absolute scales and resolutions of reconstructed quantities.
$\mathcal{L}$ is the luminosity of the data set
δ^{bc} is the bin centre correction.

The bin centre correction is defined by

$$\delta^{bc} = \frac{\left.\left(\dfrac{d^2\sigma^{MC}}{dxdQ^2}\right)\right|_{Q^2=Q^2_c, x=x_c}}{\sigma^{MC}_{bin}} \tag{9.2}$$

where $d^2\sigma^{MC}/dxdQ^2$ is the theoretical cross section implemented in the signal MC, here taken from the H1 PDF 2000 fit. σ^{MC}_{bin} is the integrated cross section in the associated bin and is given by

$$\sigma_{bin}^{MC} = \int_{x_{min}}^{x_{max}} \int_{Q^2_{min}}^{Q^2_{max}} \frac{d^2\sigma^{MC}}{dxdQ^2} dxdQ^2. \tag{9.3}$$

The bin centre correction allows the cross section at a *point* (bin centre) to be extracted from an observation in a *region* (bin) of phase space. The acceptance $\mathcal{A}$ is given by

$$\mathcal{A} = \frac{N_{rec}^{MC}}{N_{gen}^{MC}} = \frac{N_{rec}^{MC}}{\sigma_{bin}^{MC}\mathcal{L}} \tag{9.4}$$

where N_{gen}^{MC} is the number of events generated in the signal MC corresponding to the luminosity of the data $\mathcal{L}$; N_{rec}^{MC} is the number of reconstructed events.

Substituting 9.2 and 9.4 in 9.1 gives

$$\frac{d^2\sigma}{dxdQ^2} = \frac{N^D - N^B}{N_{rec}^{MC}} \cdot \left(\frac{d^2\sigma^{MC}}{dxdQ^2}\right)\Bigg|_{Q^2=Q^2_c, x=x_c} \tag{9.5}$$

By expressing the double differential cross section as the dimensionless reduced cross section $\tilde{\sigma}_{NC}$ (section 1.2)

$$\tilde{\sigma}_{NC} \equiv \frac{xQ^4}{2\pi\alpha^2}\frac{1}{Y_+}\frac{d^2\sigma}{dxdQ^2} \tag{9.6}$$

the measurement can be expressed in terms of the number of observed events in data, signal and background Monte Carlos

$$\tilde{\sigma}_{NC} = \frac{N^D - N^B}{N_{rec}^{MC}} \cdot \tilde{\sigma}_{NC}^{MC}. \tag{9.7}$$

In the **high y analysis** the reduced cross section measurement is given by

$$\tilde{\sigma}_{NC} = \frac{N^{D'}}{N_{rec}^{MC'}} \cdot \tilde{\sigma}_{NC}^{MC}. \tag{9.8}$$

where $N^{D'}$ and $N_{rec}^{MC'}$ are the number of events in the data and the number of events reconstructed in the signal MC respectively, each corrected for background using the wrong charge background subtraction procedure, section 7.7.

It is useful to write the cross section measurements expressed in equations 9.7 and 9.8 in the following way:

$$\tilde{\sigma}_{NC} = \chi_{NC} \cdot \tilde{\sigma}_{NC}^{MC} \tag{9.9}$$

where

$$\chi_{NC} = \begin{cases} \dfrac{N^D - N^B}{N^{MC}_{rec}} & \textit{nominal analysis} \\ \\ \dfrac{N^{D'}}{N^{MC'}_{rec}} & \textit{high } y \textit{ analysis.} \end{cases} \tag{9.10}$$

The quantity χ_{NC} is the ratio of the measured cross section to its theoretical value as determined from the H1 PDF 2000 fit.

9.2 Systematic Uncertainties

The systematic uncertainties of the various error sources and their corresponding 1σ effect on the measured cross section is summarized in the following two sections – *Correction Uncertainties* and *Reconstruction Uncertainties*. The first section presents uncertainties in the cross section due to corrections that are applied to the simulation – efficiencies and radiative corrections. Uncertainties due to the precision of the reconstruction of the electron and hadronic final state particles are presented in the second section. This section also includes the uncertainty of the luminosity measurement.

9.3 Correction Uncertainties

Trigger Efficiency

Nominal Analysis

In the nominal analysis a 1% uncorrelated systematic error is attributed to the uncertainty on the LAR && T0 combined efficiency. Correlated errors of 0.42% and 0.24% are attributed to the uncertainty on the veto efficiency VET as indicated in table 6.2.

High y Analysis

For a given cross section bin, the number of events reconstructed from the signal MC, $N^{MC'}_{rec}$ in equation 9.8, can be rewritten as

$$N^{MC'}_{rec} = \sum_i N^{MC'}_{rec}(i). \tag{9.11}$$

Here $N_{rec}^{MC'}(i)$ is the number of events reconstructed in the ith $\epsilon_{lar}(E'_e,\, z_{im})$ reweight bin. If $N_{(\epsilon_{lar})}^{MC'}(i)$ is the number of events reconstructed using all weights *except* $\epsilon_{lar}(i)$, then

$$N_{rec}^{MC'} = \sum_i N_{(\epsilon_{lar})}^{MC'}(i) \cdot \epsilon_{lar}(i) \tag{9.12}$$

since $N_{rec}^{MC'}(i) = N_{(\epsilon_{lar})}^{MC'}(i) \cdot \epsilon_{lar}(i)$. By substituting 9.12 into equation 9.8 and differentiating partially with respect to each $\epsilon_{lar}(i)$, it can be shown that the relative statistical uncertainty on the cross section $\delta_{stat}^{\epsilon_{lar}}$ is given by

$$\delta_{stat}^{\epsilon_{lar}} = \sum_i^{\oplus} f^{MC}(i) \cdot \delta_{\epsilon_{lar}}^{stat}(i) \tag{9.13}$$

where $f^{MC}(i) = N_{rec}^{MC'}(i)/N_{rec}^{MC'}$ is the fraction of the total number of MC events reconstructed in the ith reweight bin and $\delta_{\epsilon_{lar}}^{stat}(i)$ is the relative statistical uncertainty of ϵ_{lar}. The $\oplus$ symbol signifies that the summation is done in quadrature.

The statistical uncertainty on the cross section $\delta_{stat}^{\epsilon_{lar}}$ is so determined using the relative statistical errors $\delta_{\epsilon_{lar}}^{stat}$ shown in figure 7.18. The results are shown in figure 9.2(a) for each cross section bin; e^- period shown. Another procedure to determine $\delta_{stat}^{\epsilon_{lar}}$ begins with assuming that the true efficiency $\epsilon_{lar}^{true}(i)$ for a given reweight bin comes from a Gaussian distribution with mean $\epsilon_{lar}(i)$ and standard deviation $\Delta_{\epsilon_{lar}}^{stat}(i)$. A random efficiency from the Gaussian distribution is then generated (for each reweight bin) and used in equation9.12 to get a random value for $N_{rec}^{MC'}$, $N_{ran}^{MC'}$. If this procedure is iterated several times, the resulting distribution of $N_{ran}^{MC'}$ represents the variation in $N_{rec}^{MC'}$ due to the statistical uncertainty of ϵ_{lar}. The $N_{ran}^{MC'}$ distribution generated in this way is shown in figure 9.2(b) for the cross section bin $Q^2 = 250$ GeV^2 using 2000 iterations. The width is measured to be 34.39 using a Gaussian fit. Since $N_{rec}^{MC'} = 5839.93$, the statistical uncertainty on the cross section $\delta_{stat}^{\epsilon_{lar}}$= 0.59%. It can be observed from figure 9.2(a) that both methods of determining $\delta_{stat}^{\epsilon_{lar}}$ agree to much better than one part per mil. The statistical uncertainty on the cross section increases with Q^2 apart from the first two bins where the analysis cuts reduce the sample size.

The relative systematic uncertainty on the cross section $\delta_{sys}^{\epsilon_{lar}}$ can be deduced by replacing the statistical with the systematic error on ϵ_{lar} in equation 9.13 and adding the contributions linearly (not in quadrature),

$$\delta_{sys}^{\epsilon_{lar}} = \sum_i f^{MC}(i) \cdot \delta_{\epsilon_{lar}}^{sys}(i). \tag{9.14}$$

The systematic uncertainty on the cross section $\delta_{sys}^{\epsilon_{lar}}$ is so determined using the relative systematic errors $\delta_{\epsilon_{lar}}^{sys}$ shown in figure 7.20. The results are shown in figure 9.3. The relative uncertainty on the cross section due to the total uncertainty on ϵ_{lar} is calculated as the sum of the statistical and systematic contributions added in quadrature, $\delta^{\epsilon_{lar}} = \delta^{\epsilon_{lar}}_{stat} \oplus \delta^{\epsilon_{lar}}_{sys}$. The statistical, systematic and total relative uncertainty on the cross section due to the TT0 efficiency ϵ_{tt0}, is calculated similarly using equations 9.13 and 9.14 with ϵ_{tt0}replacing ϵ_{lar}. The results are shown in figures 9.3(a) and (b) together with the uncertainty due to the veto efficiency ϵ_{vet}. Finally the uncertainty on the cross section due to the trigger efficiency is made by summing the individual contributions from the LAR, TT0 and VET conditions in quadrature.

The uncertainty on the e^- cross section can be seen to be ≈1%. The LAR contribution is limited by statistics and so increases with Q^2; its systematic uncertainty only appears where the electron is at low energy and in the backward part of the LAr calorimeter corresponding to the low Q^2 bins. The TT0 contribution is systematically limited and increases with decreasing Q^2 since in these bins the transverse momentum of the electron and hence the hadronic final state is relatively small resulting in a small number of tracks with $p_t > 0.75$ GeV, section 7.3. The TT0 efficiency is the major contributor to the cross section uncertainty in the e^+ period due to the 0304e^+ subperiod where the dcrϕ trigger was used. This results in a total uncertainty between 1 to 2% as seen in figure 9.3(b).

Electron Identification Efficiency – Nominal & High y Analyses

The systematic error of 1% on the electron identification efficiency ϵ_{id} leads to a 1% relative error on the cross section in both the nominal and high y analyses, uncorrelated across all bins.

Tracker Efficiency – Nominal & High y Analyses

The systematic errors of 2% on the TRNA efficiency (nominal analysis) and 2% on the TRHY efficiency (high y analysis) lead to a 2% relative error on the cross section in both analyses, uncorrelated across all bins.

Charge Identification Efficiency – High y analysis only

Figure 9.4 is a schematic representation of the tracker with charge identification efficiency ϵ_{qid}. In total $N^{R^*} + N^{L^*}$ tracks are reconstructed with R^* denoting those tracks whose *true* charge matches the beam charge, and L^* those tracks whose charge do not match. Due to the charge reconstruction efficiency not being 100%, the number of tracks whose *reconstructed* charge matches the beam N^R is composed of those tracks from N^{R^*} whose charge is correctly reconstructed plus those from N^{L^*} whose charge is incorrectly reconstructed.

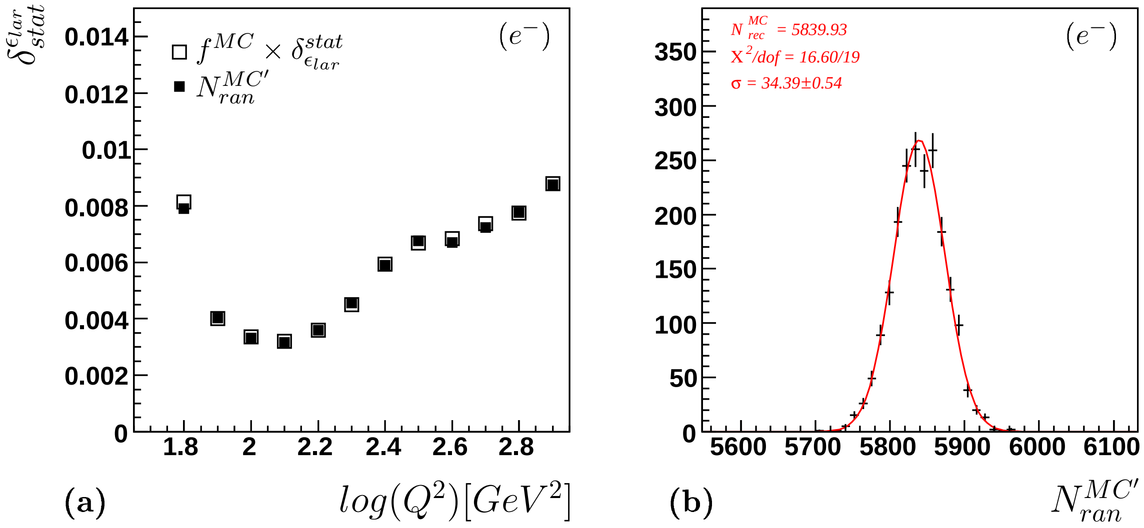

Figure 9.2: *(a) The relative statistical uncertainty on the cross section $\delta_{stat}^{\epsilon_{lar}}$ due to the statistical error on the LAR efficiency ϵ_{lar}. The uncertainty is calculated using MC event fractions ($f^{MC} \times \delta_{\epsilon_{lar}}^{stat}$) according to equation 9.13, as well as parameterizing the efficiencies using Gaussian distributions ($N_{ran}^{MC'}$). (b) The distribution of the random variable $N_{ran}^{MC'}$ for the cross section bin at $Q^2 = 250$ GeV^2 together with the results of a Gaussian fit. Plots shown are for the e^- period.*

This is expressed in the following equations (also given for N^L):

$$N^R = \epsilon N^{R^*} + (1-\epsilon)N^{L^*} \tag{9.15}$$

$$N^L = \epsilon N^{L^*} + (1-\epsilon)N^{R^*}. \tag{9.16}$$

where for simplicity ϵ is used to represent ϵ_{qid}. By rearranging equations 9.15 and 9.16 it can be shown that:

$$N^{R^*} = \frac{\epsilon N^R - (1-\epsilon)N^L}{2\epsilon - 1} \tag{9.17}$$

$$N^{L^*} = \frac{\epsilon N^L - (1-\epsilon)N^R}{2\epsilon - 1}. \tag{9.18}$$

In calculating the cross section, **no** correction is applied to the MC for the charge identification efficiency, resulting in:

$$\chi_{NC} = \frac{N_D^R - \kappa' N_D^L}{N_{MC}^R - \kappa' N_{MC}^L} \tag{9.19}$$

where κ' is the charge asymmetry term having the values κ for the e^- sample and $1/\kappa$ for the e^+ sample (section 7.7). The subscripts D and MC are for data and Monte Carlo

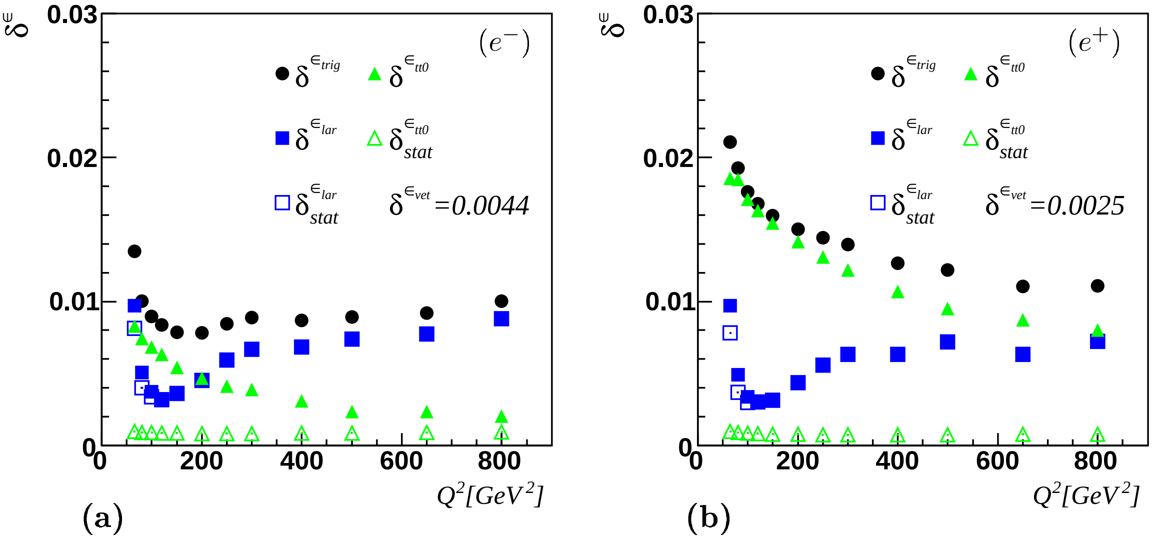

Figure 9.3: *(a) The relative uncertainty on the cross section due to the error on the trigger efficiency as well as the LAR, TT0 and VET contributions for the* e^- *and* e^+ *periods. The statistical contributions of the LAR and TT0 efficiencies are also given; the VET contribution is indicated in the legend.*

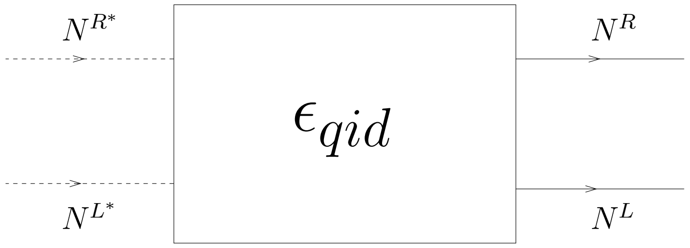

Figure 9.4: *The tracker represented schematically with its charge identification efficiency* ϵ_{qid}*. In total* $N^{R^*}+N^{L^*}$ *tracks are reconstructed. The superscript* R^* *denotes those tracks whose* ***true*** *charge matches that of the beam and* L^* *those tracks whose true charge do not match.* N^R *represents the number of tracks whose* ***reconstructed*** *charge matches the beam charge;* N^L *those that do not.* $N^R+N^L=N^{R^*}+N^{L^*}$*. Since the charge identification efficiency is not 100%,* $N^R \neq N^{R^*}$ *and* $N^L \neq N^{L^*}$*.*

respectively. Were the charge identification efficiency correction applied, the *corrected* value χ^*_{NC} would be given by:

$$\chi^*_{NC} = \frac{N_D^{R^*} - \kappa' N_D^{L^*}}{N_{MC}^{R^*} - \kappa' N_{MC}^{L^*}} \tag{9.20}$$

which on substituting equations 9.17 and 9.18 becomes

$$\chi^*_{NC} = \frac{N_D^R\left[\epsilon_D + (1-\epsilon_D)\kappa'\right] - N_D^L\left[\kappa'\epsilon_D + (1-\epsilon_D)\right]}{N_{MC}^R\left[\epsilon_{MC} + (1-\epsilon_{MC})\kappa'\right] - N_{MC}^L\left[\kappa'\epsilon_{MC} + (1-\epsilon_{MC})\right]}\left(\frac{2\epsilon_{MC}-1}{2\epsilon_D-1}\right). \tag{9.21}$$

It can be shown that since the efficiencies are close to 1 ($\epsilon_D = 0.996$ and $\epsilon_{MC} = 0.998$ for the e^- sample) equation 9.20 is given to a good approximation by:

$$\chi^*_{NC} = \frac{N_D^R - \kappa' N_D^L}{N_{MC}^R - \kappa' N_{MC}^L}\left(\frac{2\epsilon_{MC}-1}{2\epsilon_D-1}\right) \tag{9.22}$$

that is

$$\chi^*_{NC} = \chi_{NC}\left(\frac{2\epsilon_{MC}-1}{2\epsilon_D-1}\right). \tag{9.23}$$

The relative error on the cross section due to the charge identification efficiency $\delta^{\epsilon_{qid}}$ is then given by

$$\delta^{\epsilon_{qid}} = \frac{\chi_{NC} - \chi^*_{NC}}{\chi_{NC}} \tag{9.24}$$

$$= 1 - \left(\frac{2\epsilon_{MC}-1}{2\epsilon_D-1}\right). \tag{9.25}$$

Defining r as the ratio of the charge identification efficiency of data to MC (ϵ_D/ϵ_{MC}) yields:

$$\delta^{\epsilon_{qid}} = \frac{2(r-1)}{2r - \left(\frac{1}{\epsilon_{MC}}\right)}. \tag{9.26}$$

Since ϵ_{MC} is approximately 1, it can be shown that

$$\delta^{\epsilon_{qid}} = \frac{2(r-1)}{\epsilon_{MC} + 2(r-1)} \tag{9.27}$$

so that finally $\delta^{\epsilon_{qid}}$ can be approximated to

$$\delta^{\epsilon_{qid}} = 2|r-1|. \tag{9.28}$$

Since $|r-1| < 0.5\%$ (section 7.6), the relative uncertainty on the cross section is 1.0%, uncorrelated across all bins.

Radiative Correction

An uncorrelated uncertainty of 1% is estimated on the QED radiative corrections by comparing the radiative corrections predicted by the signal MC (DJANGO) with those calculated from HECTOR and EPRC[55]. The uncertainty also includes small missing corrections in DJANGO due to the exchange of two or more photons between the lepton and quark lines.

9.4 Reconstruction Uncertainties

For the next 4 sources of error – electron energy E'_e, electron polar angle θ_e, hadron energy E_h and noise energy E_n – the relative systematic error on the cross section δ^S_{sys} due to the uncertainty of each source S (chapter 5) is calculated such that its magnitude is given by:

$$|\delta^S_{sys}| = \frac{0.5(|c^+ - c| + |c^- - c|)}{c} \tag{9.29}$$

where $c(= N^{MC'}_{rec})$ is the number of events reconstructed by MC (corrected for background in the high y analysis) and $c^\pm$ are the values of $N^{MC'}_{rec}$ corresponding to a $\pm 1\sigma$ change in the source S, σ being the systematic error of S. The sign of δ^S_{sys} is decided in accordance with the following convention:

$$\delta^S_{sys} = \begin{cases} +|\delta^S_{sys}| & for\ c^+ \leqslant c \\ -|\delta^S_{sys}| & otherwise. \end{cases} \tag{9.30}$$

δ^S_{sys} is given in tables 9.1 - 9.3 for the e^- period and tables 9.4 - 9.6 for the e^+ period, found in the appendix.

Electron Energy

Nominal Analysis

The relative error on the cross section due to the electron energy uncertainty increases with increasing Q^2 and decreasing y where it becomes one of the dominant contributions to the total systematic error.

High y Analysis

In the high y analysis the relative error on the cross section is less than 1%.

Electron Polar Angle

Nominal Analysis

The relative error on the cross section due to the electron polar angle uncertainty is generally between 0-2% in most bins and reaches a few percent in bins at higher Q^2, low y.

High y Analysis

In the high y analysis the relative error on the cross section is generally between 1-2% becoming larger at lower values of Q^2.

Hadron Energy

Nominal Analysis

The relative error on the cross section due to the hadron energy uncertainty is $\approx$0.2% for bins using the e-method of kinematic reconstruction ($y > 0.3$). For the other bins the relative error is less than 1% and reaches a few percent at low values of y.

High y Analysis

In the high y analysis the relative error on the cross section is between $\approx$0.3%-0.5%.

Noise Energy

Nominal Analysis

The relative error on the cross section due to the uncertainty on the LAr calorimeter noise is $\approx$0.1% in bins reconstructed using the e-method kinematics. For the other bins the relative error is $\gtrsim$0.5% reaching a few percent at very low values of y.

High y Analysis

In the high y analysis the relative error on the cross section is $\leqslant 0.2\%$ in all bins.

Luminosity – Nominal & High y Analyses

The relative uncertainty on the cross section due to the uncertainty of the integrated luminosity in data is 2.5% and 2.55% for the e^- and e^+ samples respectively (section 6.6).

9.5 Reduced Cross Section Ratios χ_{NC}

To ensure a good reliability of the measurement, cross sections are measured only in bins whose purity and stability (section 8.2) are both greater that 30%. The stability and purity for each measurement bin were presented in chapter 8.

Figure 9.5 shows χ_{NC} – the ratio of the reduced cross section measured in this analysis to its prediction using the H1 PDF 2000 fit for fixed Q^2 as a function of x for the e^- period. The measurements are consistent with 1 within error, demonstrating a good agreement with the prediction in shape as well as in normalization (the 2.5% normalization error is not included in the figure). Measurements from the high y analysis are shown in greater detail in 9.7(a). The corresponding plots for the e^+ period (2.55% normalization error) show similar levels of agreement between measurement and prediction (figures 9.6 and 9.7(b)).

Figure 9.8 shows χ_{NC} for nominal analysis bins as a function of Q^2 for fixed values of x for the e^- (9.8(a) and 9.8(b)) and e^+ (9.8(c) and 9.8(d)) periods. The ratio χ_{NC} is scaled by a factor f as indicated. For comparison, measurements published previously by H1[1] using HERA I data is also given. It can be seen that the measurements of this analysis agree with those previously published.

Figure 9.7 shows the previously published results by H1 for the high y analysis. Measurements of this analysis agree with those previously published. In addition, the measurements at $Q^2 = 65$ GeV^2 and $Q^2 = 80$ GeV^2 represent an extension of the measurement into regions of phase space previously unmeasured. For the e^- cross sections, the precision of this measurement is better than the published measurement – systematic uncertainties of this measurement are better than the published by $0.7 - 5.5\%$. The precision of the e^+ period is similar to that of the previous measurement.

Depending on the method of kinematic reconstruction, the resulting cross section measurement will have varying levels of sensitivity to the measured kinematic variables. For example, the e-method which uses only the scattered electron to reconstruct the kinematics is least sensitive to the hadronic final state quantities(hence hadronic and noise energy scales). It will however be more sensitive to radiative corrections than the es-method. The ratio of the reduced cross section as measured using the e-method to the cross section measured using the es-method ($\tilde{\sigma}^{e}_{NC}/\tilde{\sigma}^{es}_{NC}$) is shown in figure 9.9 as a function of Q^2 for fixed x for the e^- (figure 9.9 (a) and (b)) and e^+(figure 9.9 (c) and (d)) periods. Only bins with stability and purity both greater than 30% are used, limiting the comparison to higher values of y (low x). The cross sections are consistent with each other.

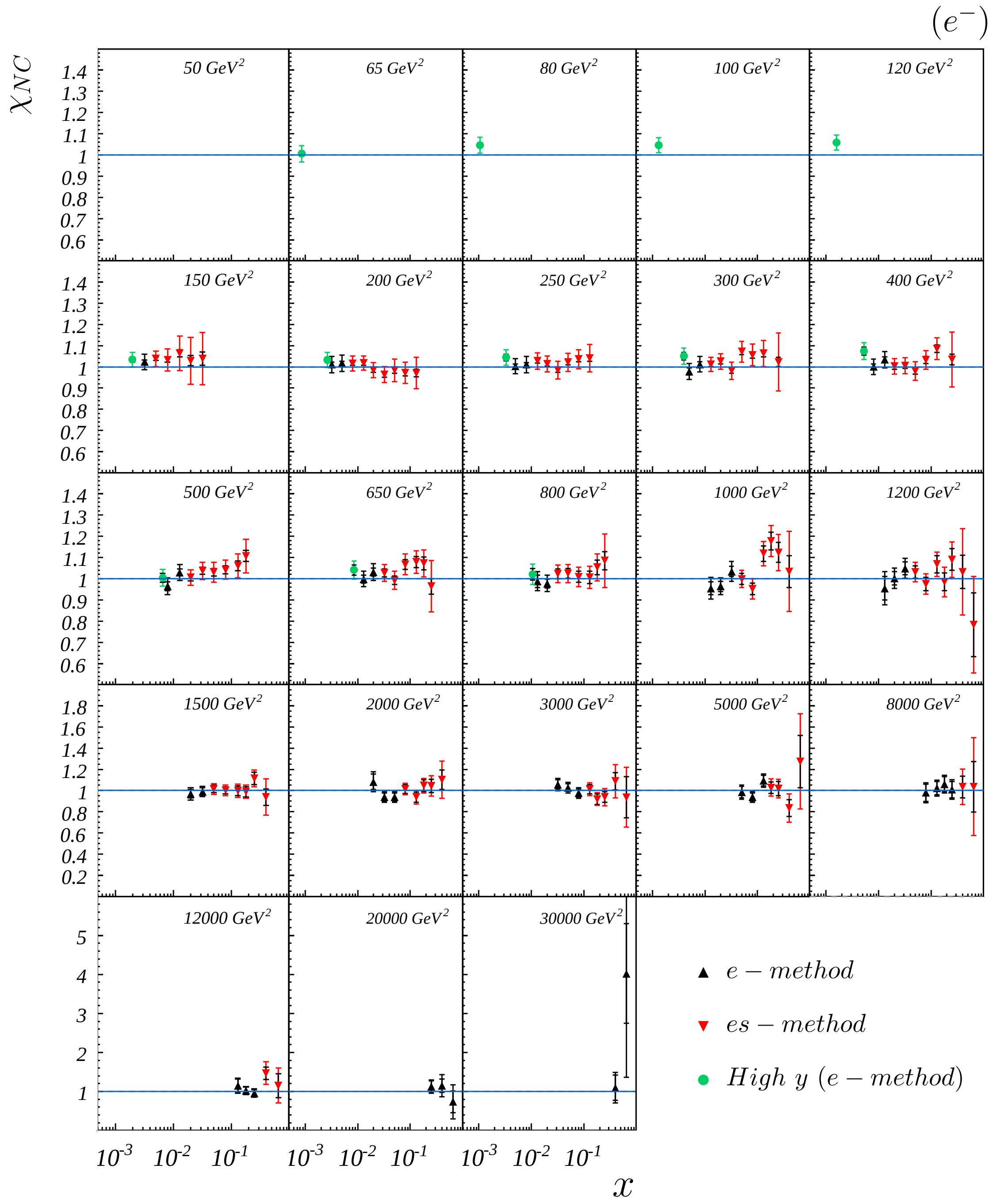

Figure 9.5: *The ratio χ_{NC} of the reduced cross section measurement to its value as predicted by the H1 PDF 2000 fit for the e^- period. χ_{NC} is shown for fixed Q^2 as a function of x. The red downward triangles correspond to cross sections measured using the es-method, black upward triangles using the e-method and the green dots correspond to measurements from the high y analysis (e-method). The inner error bar is the uncertainty due to the statistical error in the data while the outer error bar includes all sources of error apart from the luminosity measurement.*

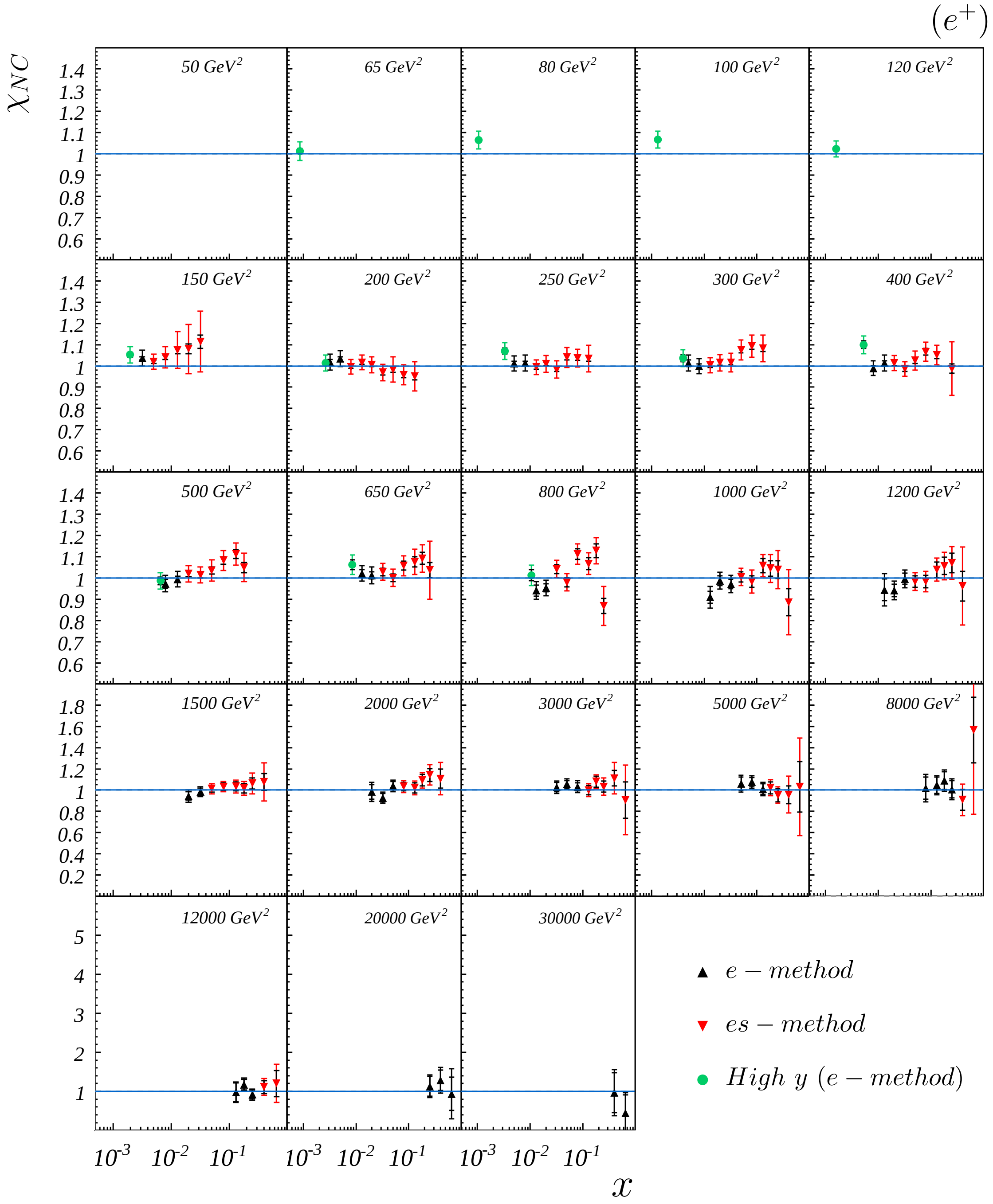

Figure 9.6: *The ratio χ_{NC} of the reduced cross section measurement to its value as predicted by the H1 PDF 2000 fit for the e^+ period. χ_{NC} is shown for fixed Q^2 as a function of x. The red downward triangles correspond to cross sections measured using the es-method, black upward triangles using the e-method and the green dots correspond to measurements from the high y analysis (e-method). The inner error bar is the uncertainty due to the statistical error in the data while the outer error bar includes all sources of error apart from the luminosity measurement.*

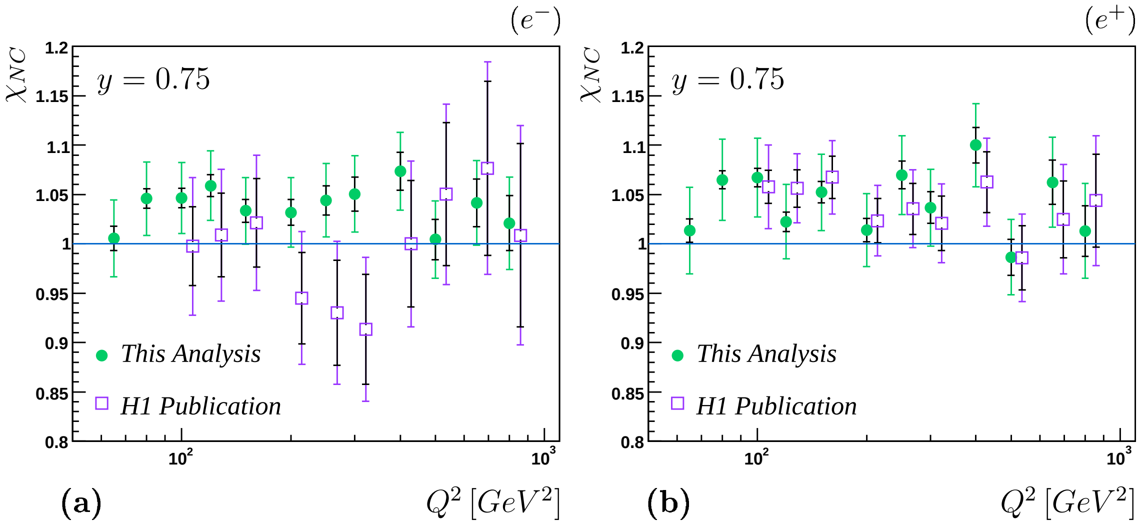

Figure 9.7: *The ratio* χ_{NC} *of the high* y *reduced cross section measurement of this analysis to its value as predicted by the H1 PDF 2000 fit for the (a)* e^- *and (b)* e^+ *periods. The inner error bar is the uncertainty due to the statistical error in the data while the outer error bar includes all sources of error apart from the luminosity measurement.*

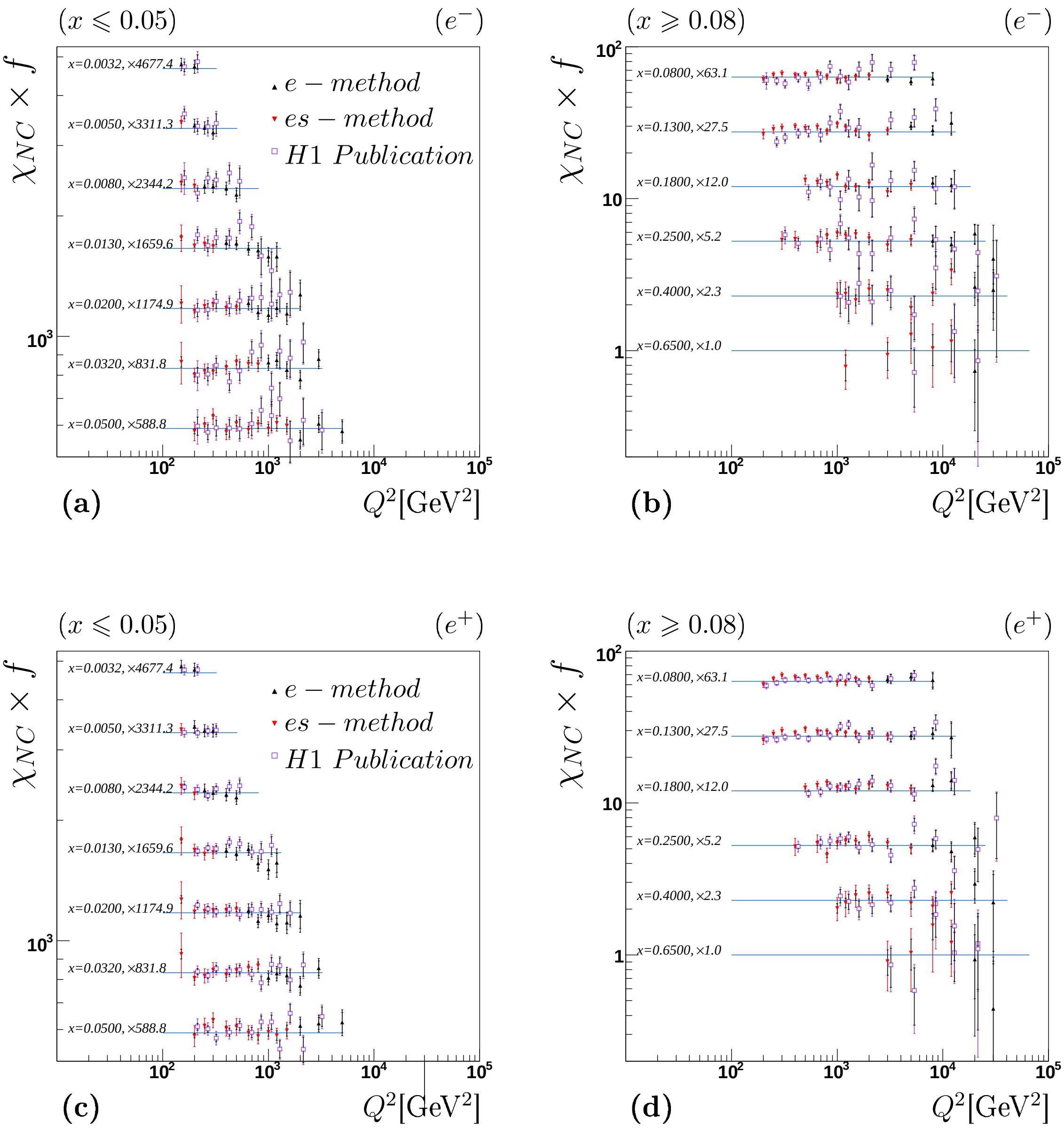

Figure 9.8: *The ratio χ_{NC} of the reduced cross section measurement to its value as predicted by the H1 PDF 2000 fit, for fixed x as a function of Q^2 for the e^- period (a,b) and e^+ period (c,d). Measurements correspond to those of the nominal analysis. χ_{NC} is scaled by a factor f depending on x as indicated. The measurements corresponding to this analysis are distinguished in terms of reconstruction method (red downward triangle for es-method and black upward triangles for e-method). Previously published H1 results [1] are indicated by the open squares. The inner error bar is the uncertainty due to the statistical error in the data while the outer error bar includes all sources of error apart from the luminosity measurement.*

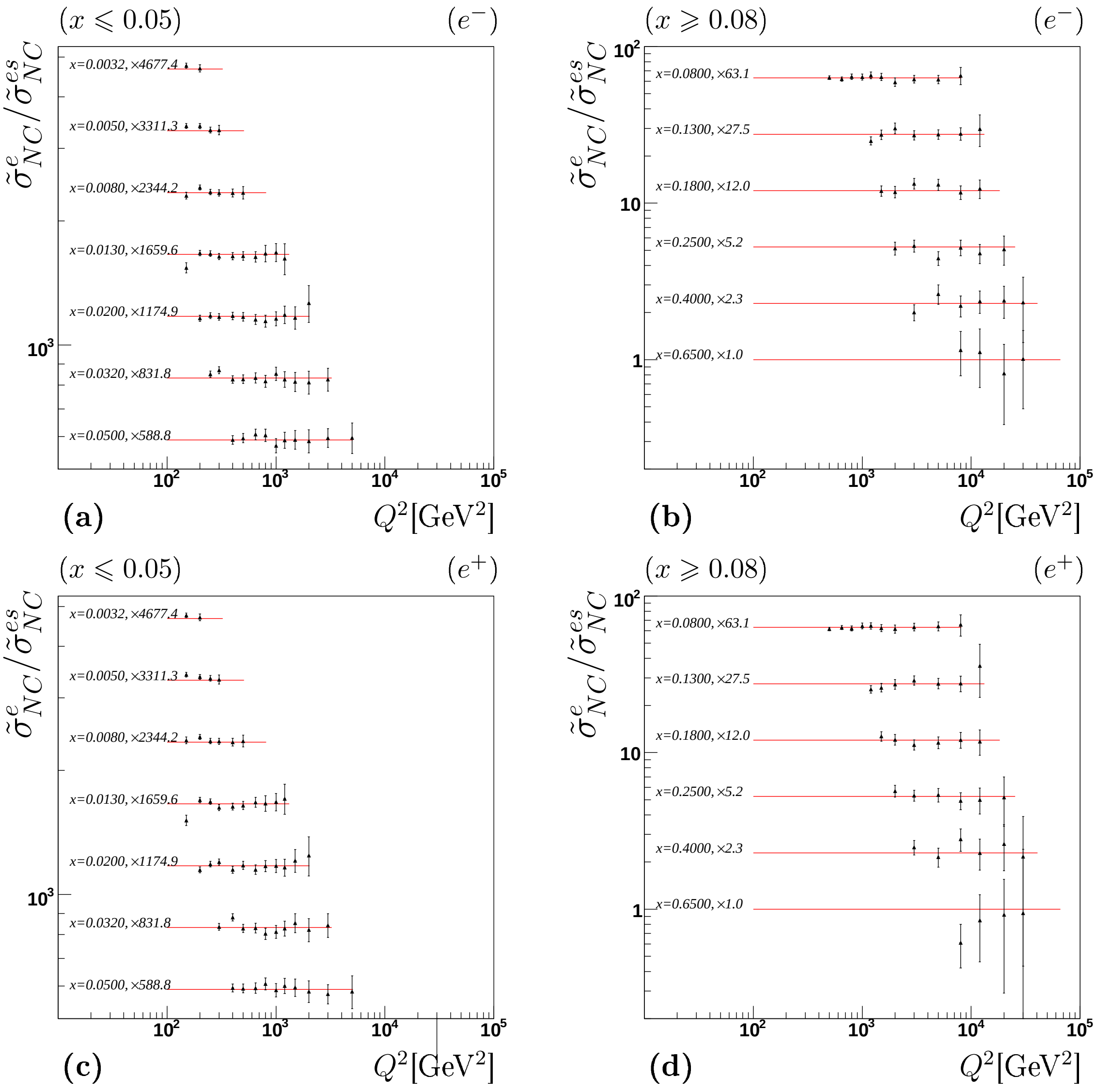

Figure 9.9: *The ratio of the reduced cross section measured using the e-method ($\tilde{\sigma}^e_{NC}$) to the es-method ($\tilde{\sigma}^{es}_{NC}$) of reconstruction for fixed x as a function of Q^2; (a) and (b) correspond to the e^- period for two differnet ranges of x as indicated. The e^+ ratios are shown in (c) and (d).*

9.6 Reduced Cross Sections $\tilde{\sigma}_{NC}$ and the $\tilde{F}_2$ and $x\tilde{F}_3$ Proton Structure Functions

The measurements of this analysis cover the kinematic range $65 \leqslant Q^2 \leqslant 30000$ GeV^2 and $0.00085 \leqslant x \leqslant 0.65$ thus spanning 3 orders of magnitude in Q^2 and 4 orders of magnitude in x. In total there are 142 cross section measurements from the e^- sample and 140 from the e^+ sample.

Figures 9.10 and 9.11 show the reduced cross section measurement $\tilde{\sigma}_{NC}$ as a function of x for fixed Q^2 for the e^- and e^+ periods respectively. Also shown for comparison are predictions as determined by two NLO QCD fits – the H1 PDF 2000 fit and the CTEQ 6m fit. The data is well described by both fits. It can be observed that $\tilde{\sigma}_{NC}$ increases with decreasing x. As $\tilde{\sigma}_{NC} \approx \tilde{F}_2$ in most of the kinematic range, the rise of $\tilde{\sigma}_{NC}$ implies a rise of $\tilde{F}_2$. The rise in $\tilde{F}_2$ at low x can be attributed to a rise in the sea quark distributions. This increase in sea quarks is driven by the increase in gluon density at low x and the process $g \rightarrow q\bar{q}$.

For $Q^2 \lesssim 1000$ GeV^2, $\tilde{\sigma}_{NC}$ is approximately equal to $F_2 - (y^2/Y_+)F_L$ (equation 1.16) as weak contributions can be ignored. At the lowest values of x (highest y), there is a hint that the cross section begins to drop, possibly due the the negative contribution of F_L (the prediction assuming zero F_L contribution is also indicated). This is explored further in section 9.7.

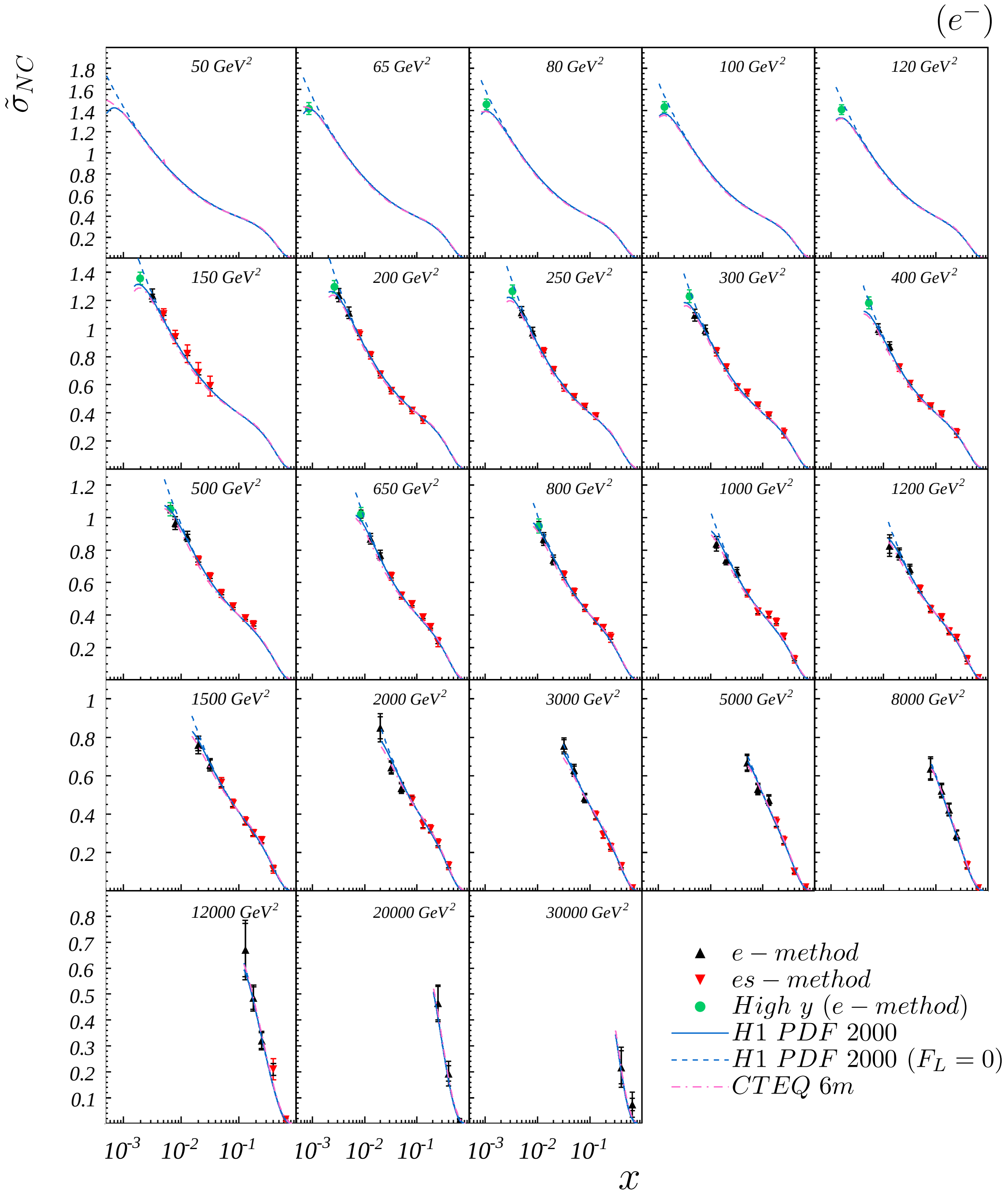

Figure 9.10: *The reduced cross section $\tilde{\sigma}_{NC}$, for fixed Q^2 (indicated in the upper right) as a function of x for the e^- period. The red downward triangles and black upward triangles correspond to the es-method and e-method of reconstruction respectively of the nominal analysis; the high y analysis measurements are the green dots (e-method). The inner error bar is the uncertainty due to the statistical error in the data while the outer error bar includes all sources of error apart from the luminosity measurement. Predictions as determined from the H1 PDF 2000 fit as well as the CTEQ 6m fit are indicated.*

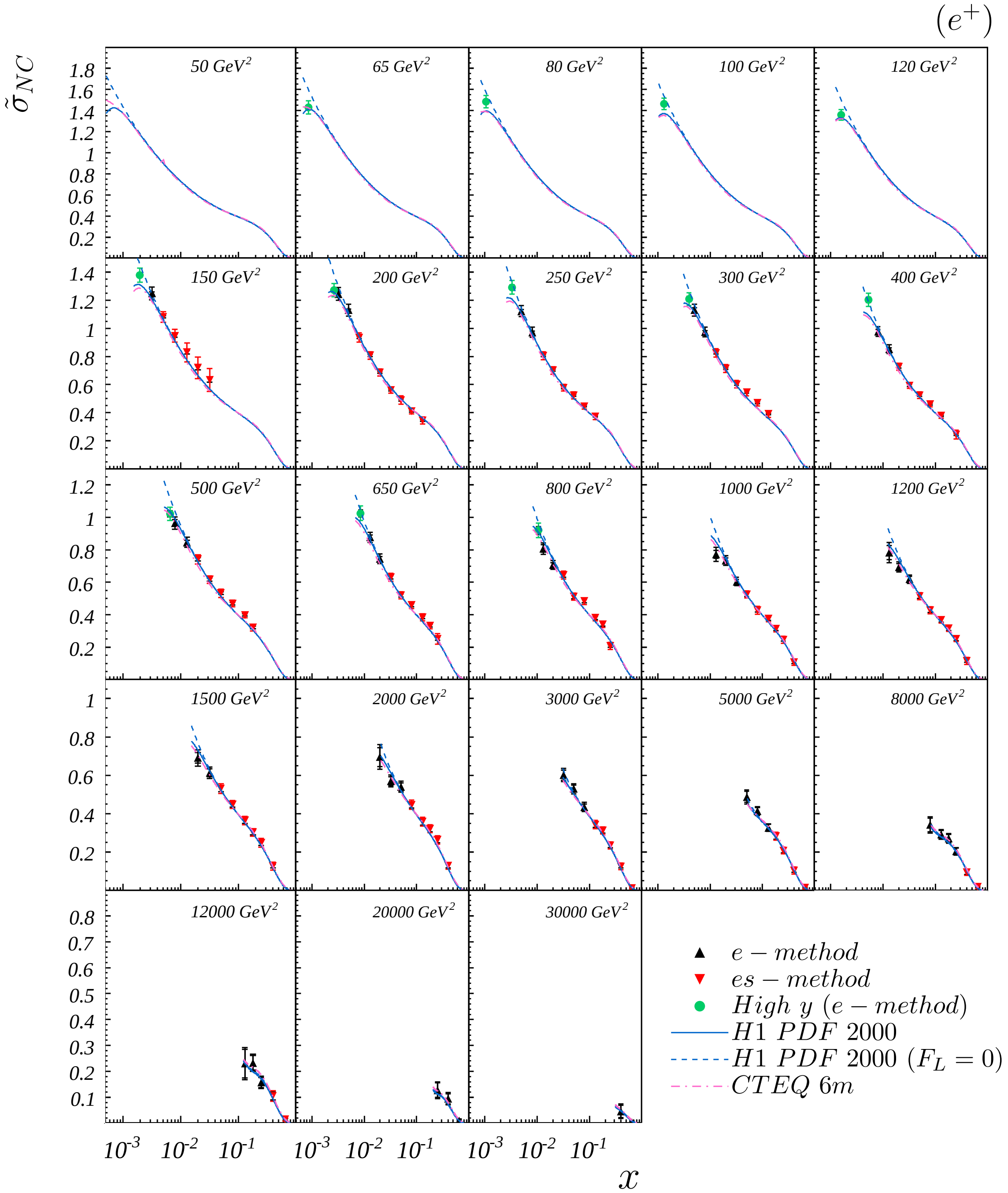

Figure 9.11: *The reduced cross section* $\tilde{\sigma}_{NC}$*, for fixed* Q^2 *(indicated in the upper right) as a function of* x *for the* e^+ *period. The red downward triangles and black upward triangles correspond to the es-method and e-method of reconstruction respectively of the nominal analysis; the high* y *analysis measurements are the green dots (e-method). The inner error bar is the uncertainty due to the statistical error in the data while the outer error bar includes all sources of error apart from the luminosity measurement. Predictions as determined from the H1 PDF 2000 fit as well as the CTEQ 6m fit are indicated.*

Plots showing $\tilde{\sigma}_{NC}$ as a function of Q^2 for fixed x (nominal analysis) are shown in figures 9.12 and 9.13 for the e^- and e^+ periods respectively – the data is well described by both the H1 PDF 2000 and CTEQ 6m NLO QCD fits. In particular, figure 9.14 shows the e^- and e^+ reduced cross section at the fixed values of x as a function of Q^2 for the x-values 0.013, 0.032 and 0.18. The e^- and e^+ H1 PDF 2000 predictions with and without $\tilde{F}_L$ contributions are indicated. Where all four predictions are approximately equal, the $x\tilde{F}_3$ and $\tilde{F}_L$ contributions are small and so the reduced cross section dominated by $\tilde{F}_2$. It can be deduced that $\tilde{F}_2$ rises with Q^2 at low x. The decrease of $\tilde{F}_2$ at large x can be deduced from figures 9.12 and 9.13. The systematic rise of $\tilde{F}_2$ at low x and drop at high x as a function of Q^2 is known as “scaling violation” is well predicted by the QCD fits.

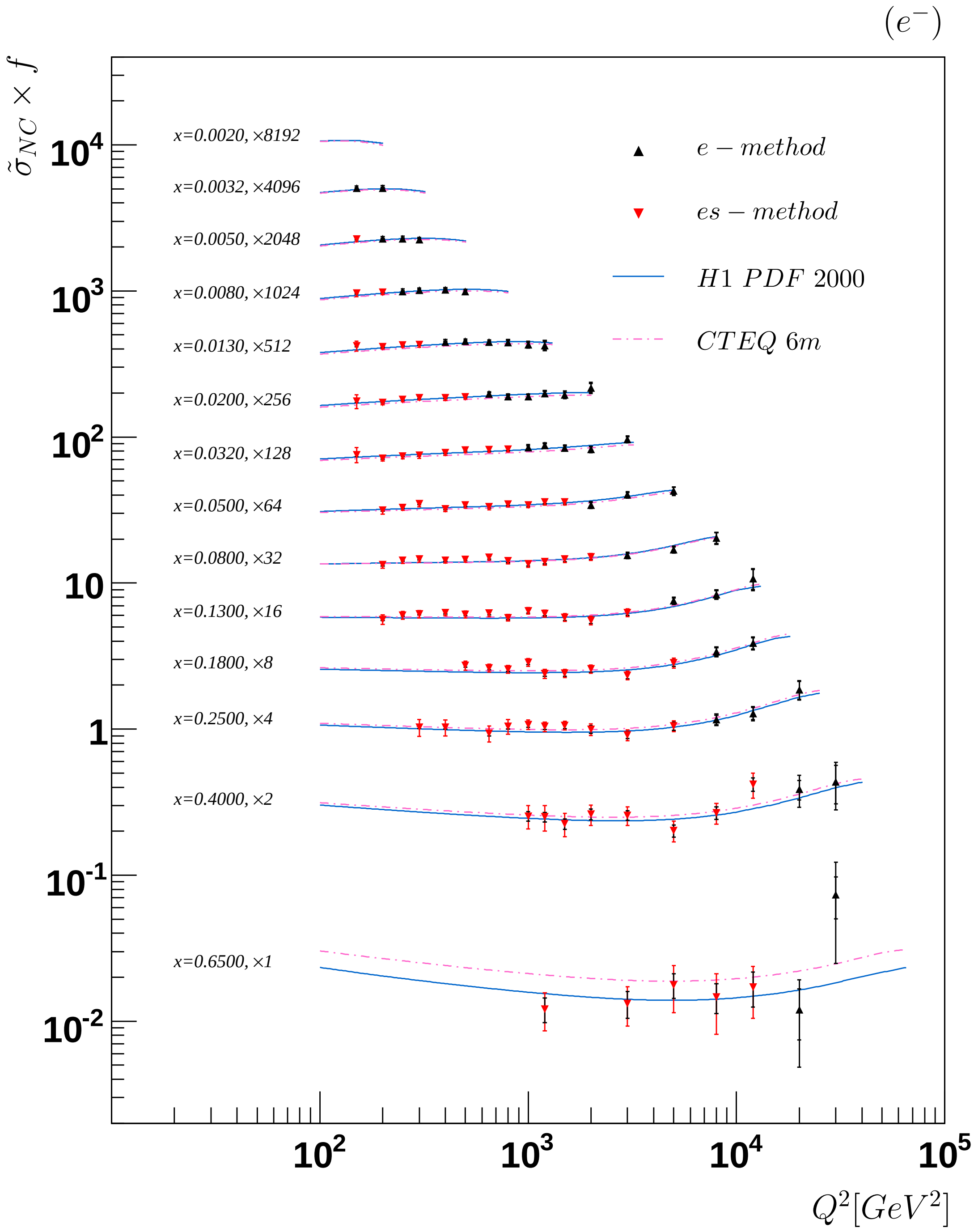

Figure 9.12: *The nominal analysis reduced cross section $\tilde{\sigma}_{NC}$ for fixed x as a function of Q^2 for the e^- period. The mmeasurementsare scaled by a factor f depending on x as indicated; red downward triangles correspond to the es-method of kinematic reconstruction and black upward triangles to the e-method. The inner error bar is the uncertainty due to the statistical error in the data while the outer error bar includes all sources of error apart from the luminosity measurement. Predictions as determined from the H1 PDF 2000 fit as well as the CTEQ 6m fit are indicated.*

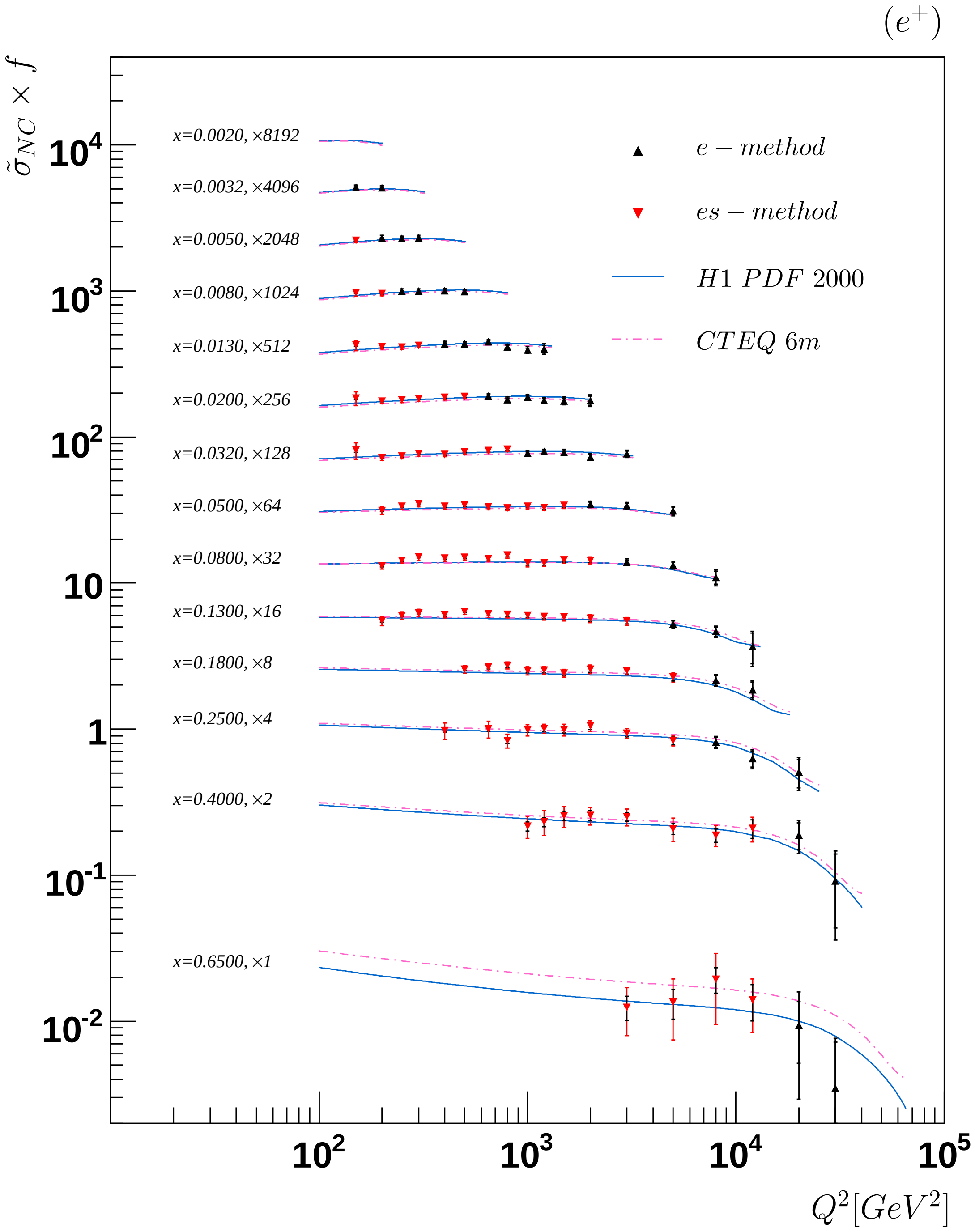

Figure 9.13: *The nominal analysis reduced cross section $\tilde{\sigma}_{NC}$ for fixed x as a function of Q^2 for the e^+ period. The mmeasurementsare scaled by a factor f depending on x as indicated; red downward triangles correspond to the es-method of kinematic reconstruction and black upward triangles to the e-method. The inner error bar is the uncertainty due to the statistical error in the data while the outer error bar includes all sources of error apart from the luminosity measurement. Predictions as determined from the H1 PDF 2000 fit as well as the CTEQ 6m fit are indicated.*

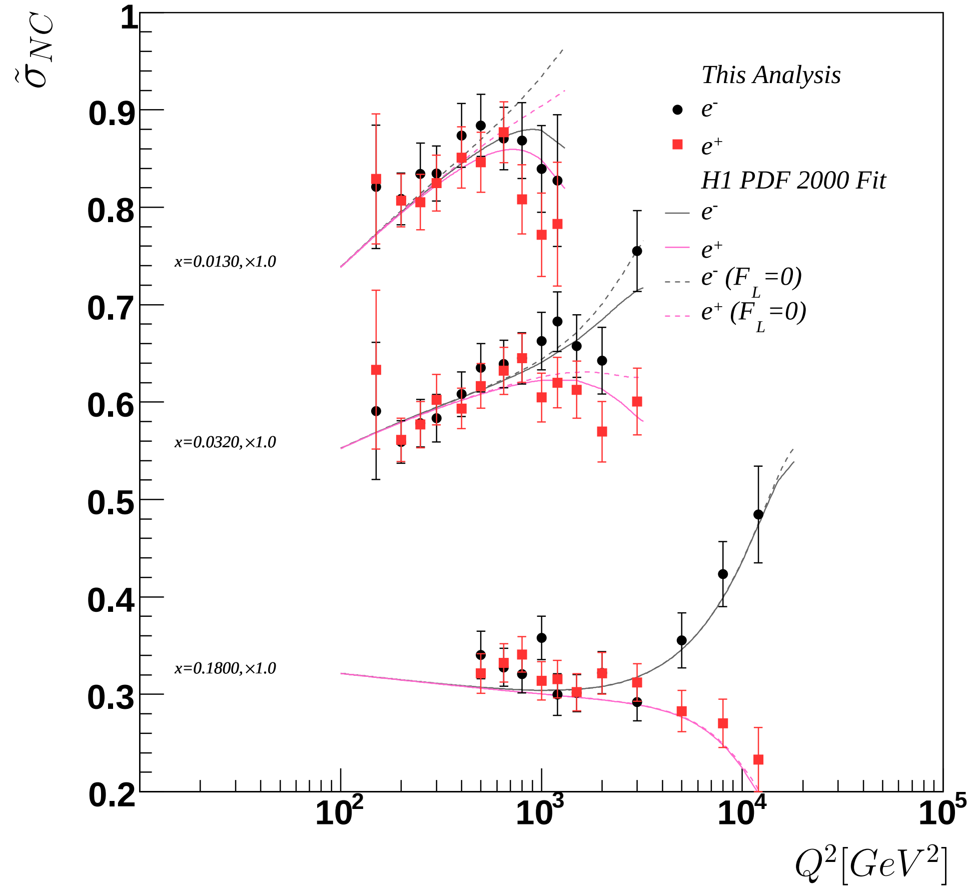

Figure 9.14: *The reduced cross section $\tilde{\sigma}_{NC}$ for fixed x as a function of Q^2 for the e^- and e^+ periods. The error bar includes all sources of error apart from the luminosity measurement. Predictions as determined from the H1 PDF 2000 fit are also indicated. Also shown are the predictions assuming $\tilde{F}_L$=0.*

Electroweak effects at high Q^2 can be seen in figure 9.15 where the reduced cross sections for the e^- and e^+ periods are plotted together with the prediction of the H1 PDF 2000 fit. The presence of the $x\tilde{F}_3$ structure function is evident as it contributes positively to the e^- cross section but negatively to the e^+ cross section (equation 1.4) – the data is well described by the H1 PDF 2000 prediction. The errors indicated are sufficiently small to allow an extraction of $x\tilde{F}_3$ to reasonable accuracy.

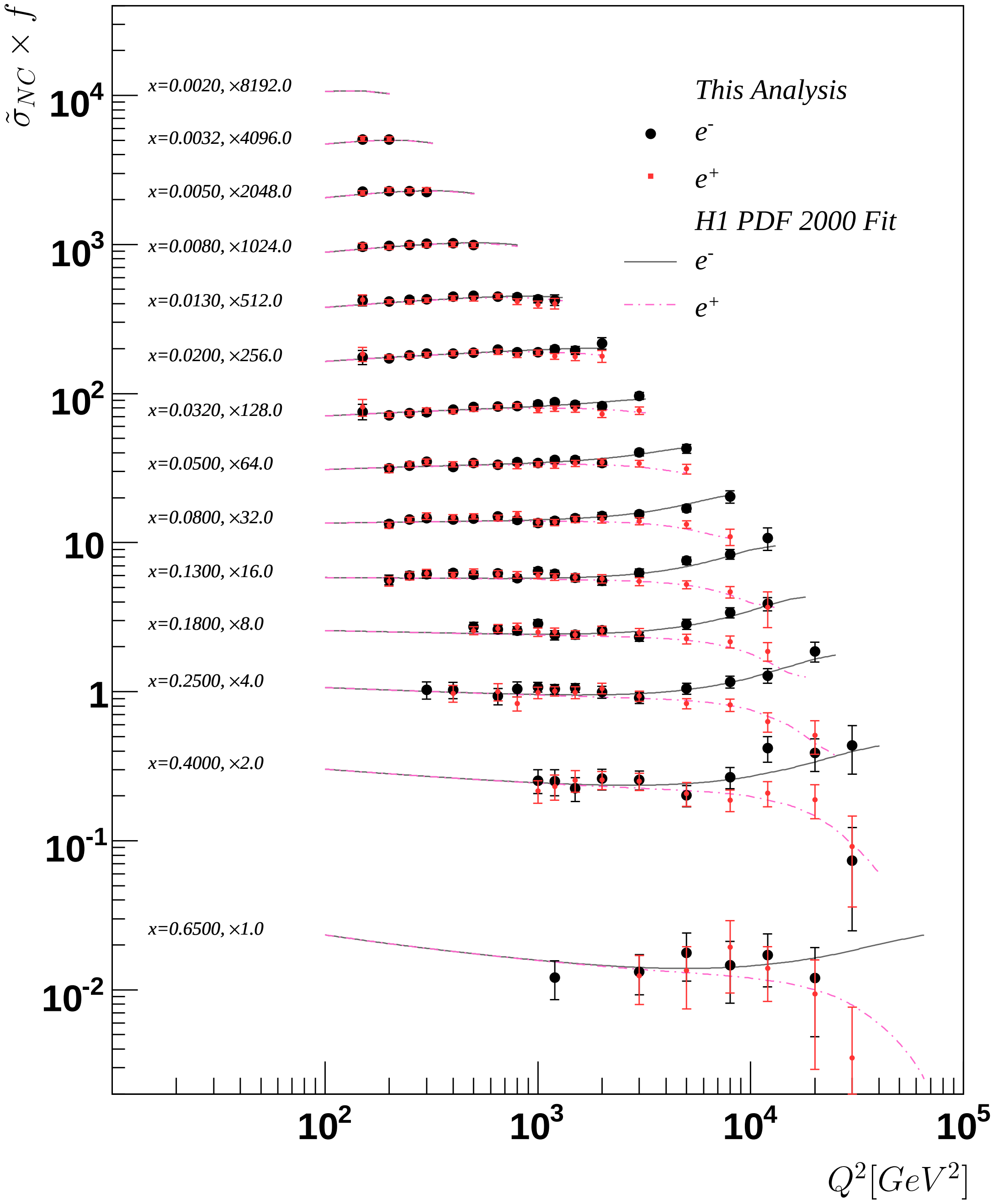

Figure 9.15: *The reduced cross section $\tilde{\sigma}_{NC}$ for fixed x as a function of Q^2 for the e^- and e^+ periods. The mmeasurementsare scaled by a factor f depending on x as indicated. The error bar includes all sources of error apart from the luminosity measurement. Predictions as determined from the H1 PDF 2000 fit are also indicated.*

9.7 High y Reduced Cross Sections $\tilde{\sigma}_{NC}$ and the $\tilde{F_L}$ Proton Structure Function

Finally the reduced cross section for bins corresponding to the high y analysis are shown in figures 9.16(a) and (b) for the e^- and e^+ periods respectively. Predictions as determined from the H1 PDF 2009 and the CTEQ 6m NLO QCD fits (with and without $\tilde{F_L}$ contributions) are indicated – the $\pm 1\sigma$ error bands on the H1 PDF 2009 fit obtained by summing the experimental, model and parameterization uncertainties in quadrature are also shown.

In this region $Q^2 \lesssim 1000$ GeV^2 so that electroweak effects are negligible and $\tilde{\sigma}_{NC} \approx F_2 - (y^2/Y_+)F_L$. The measurements do indeed suggest non-zero values for F_L as the data is well below the $F_L = 0$ prediction.

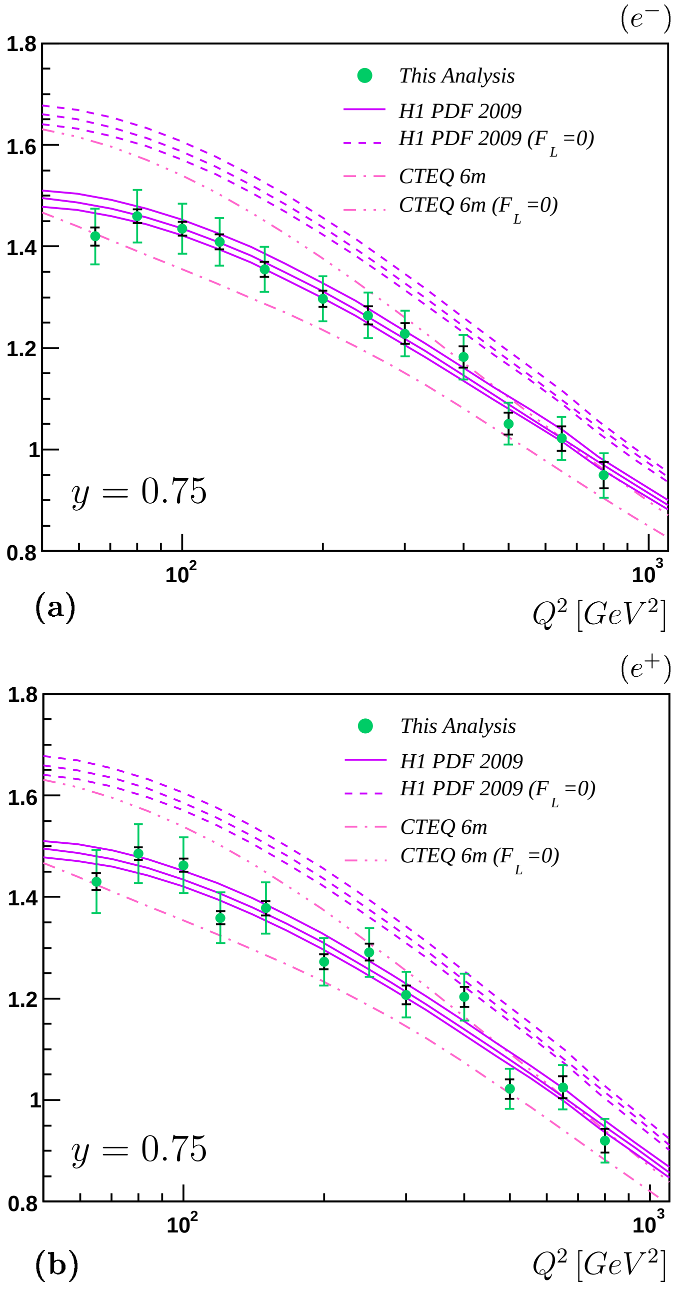

Figure 9.16: *The reduced cross section $\tilde{\sigma}_{NC}$ of the high y analysis for the (a) e^- and (b) e^+ periods. The inner error bar is the uncertainty due to the statistical error in the data while the outer error bar includes all sources of error apart from the luminosity measurement. The measurements are compared to predictions as determined from the H1 PDF 2009 fit as well as the CTEQ 6m fit. Predictions corresponding to $\tilde{F}_L$=0 are also shown. The $\pm 1\sigma$ error bands on the H1 PDF 2009 fit (experimental, model and parameterization added in quadrature) are also indicated.*

Conclusion

Unpolarized neutral current reduced $e^{\pm}p$ cross sections in the four-momentum transfer range $65 \leqslant Q^2 \leqslant 30000$ GeV^2 and $0.00085 \leqslant x \leqslant 0.65$ have been measured using the full H1 data set of the HERA collider in its HERA II phase of running. The cross sections are consistent with previously published H1 results obtained in the HERA I phase of running. There is also reasonably good agreement between the measurement and predictions based on QCD NLO fits using data sets exclusively from the H1 Experiment (H1 PDF 2000 and H1 PDF 2009) as well as the CTEQ 6m global fit.

For the measurements in the kinematic range $Q^2 \leqslant 800$ GeV^2 at $y = 0.75$, the precision obtained from the e^-p data is significantly better than the previous measurement. This improvement is due not only to increased statistics; systematic uncertainties of this measurement are better than the previous by approximately 1-5%. For the e^+p measurement, the uncertainties are similar to the previous measurement. The data suggests non-zero values of the longitudinal structure function F_L.

Outside this kinematic range, by reconstructing the kinematics using a method based on the inelasticity y of the event, the precision at higher y corresponding to larger Q^2 values has been improved. In this kinematic domain the cross section is sensitive to the structure function $x\tilde{F}_3$. These effects have been observed as a difference in the e^-p and e^+p cross sections. The improvement in the precision of the cross section measurements will lead to a more precise measurement of $x\tilde{F}_3$.

$\tilde{F}_2$ scaling violations have also been observed in the region where the $x\tilde{F}_3$ and the longitudinal structure functions are expected to give negligible contributions. The rise of $\tilde{F}_2$ with decreasing x attributable to the increasing density of sea quarks was also observed.

This thesis is a first step in harvesting the wealth of data collected by the H1 Experiment during the HERA II phase of running in determining the structure of the proton. Though the structure functions were not explicitly determined, their effects were observed and improvements in the cross section measurement will translate into a more precise determination of the structure functions.

The cross sections produced represent precise input to QCD analyses, the goal of which is to determine the parton distributions of the proton as well as various Standard Model parameters. This will help to provide the most complete picture we have of the proton.

Appendix

Presented here are the reduced cross section measurements $\tilde{\sigma}_{NC}$ for the e^- (tables 9.1-9.3) and e^+ (tables 9.4-9.6) periods. The relative error on the cross section δ_{tot} together with its statistical (δ_{stat}) and systematic (δ_{sys}) contributions are shown. The statistical contribution comes purely from the data and includes the number of background events in the high y analysis. Statistical errors in the simulation are included in the systematic error δ_{sys}. The relative error due to various sources that contribute to the systematic error are also shown and these include trigger ($\delta^{\epsilon_{trig}}$), electron identification ($\delta^{\epsilon_{id}}$), tracker ($\delta^{\epsilon_{trna}}$ for the nominal analysis and $\delta^{\epsilon_{trhy}}$ and $\delta^{\epsilon_{qid}}$ for the high y analysis) and radiative correction (δ^{rad}). Also given are the relative errors due to the electron energy scale ($\delta^{E'_e}$), electron polar angle measurement (δ^{θ_e}), hadron energy scale (δ^{E_h}) and noise energy scale (δ^{E_n}). Finally the systematic error on the background estimated using Monte Carlo for the nominal analysis is given (δ^{B}) as well as the systematic error due to the uncertainty on the background asymmetry (δ^{κ}) used in the high y analysis. The error due to the luminosity measurement (2.5% and 2.55% for the e^- and e^+ periods respectively) is not included in these tables.

All relative errors given are in percent.

Q^2 [GeV^2]	x	y	$\tilde{\sigma}_{NC}$	δ_{stat}	δ_{sys}	δ_{tot}	$\delta^{\epsilon_{trig}}$	$\delta^{\epsilon_{id}}$	$\delta^{\epsilon_{trna}}$	$\delta^{\epsilon_{trhy}}$	$\delta^{\epsilon_{qid}}$	δ^{rad}	$\delta^{E'_e}$	δ^{θ_e}	δ^{E_h}	δ^{E_n}	δ^{B}	δ^{κ}
65.0	**0.00085**	**0.750**	**1.420**	**1.2**	**3.7**	**3.9**	**1.3**	**1.0**	**-**	**2.0**	**1.0**	**1.0**	**0.7**	**1.8**	**-0.4**	**-0.1**	**-**	**-0.2**
80.0	**0.00105**	**0.750**	**1.460**	**0.9**	**3.4**	**3.6**	**1.0**	**1.0**	**-**	**2.0**	**1.0**	**1.0**	**0.9**	**1.5**	**-0.4**	**-0.2**	**-**	**-0.1**
100.0	**0.00131**	**0.750**	**1.435**	**0.9**	**3.3**	**3.4**	**0.9**	**1.0**	**-**	**2.0**	**1.0**	**1.0**	**0.3**	**1.5**	**-0.4**	**-0.1**	**-**	**-0.1**
120.0	**0.00158**	**0.750**	**1.409**	**1.0**	**3.2**	**3.3**	**0.8**	**1.0**	**-**	**2.0**	**1.0**	**1.0**	**0.3**	**1.2**	**-0.5**	**-0.1**	**-**	**-0.1**
150.0	**0.00197**	**0.750**	**1.355**	**1.1**	**3.1**	**3.3**	**0.8**	**1.0**	**-**	**2.0**	**1.0**	**1.0**	**0.4**	**1.0**	**-0.4**	**-0.1**	**-**	**-0.1**
150.0	0.00320	0.462	1.235	0.8	3.5	3.6	1.1	1.0	2.0	-	-	1.0	1.2	1.5	-0.1	-0.1	-1.1	-
150.0	0.00500	0.295	1.101	0.8	3.4	3.5	1.1	1.0	2.0	-	-	1.0	0.4	1.8	-0.6	-0.4	-0.3	-
150.0	0.00800	0.185	0.940	1.1	4.9	5.1	1.1	1.0	2.0	-	-	1.0	2.6	2.8	1.3	0.3	-0.2	-
150.0	0.01300	0.114	0.821	1.6	7.5	7.7	1.1	1.0	2.0	-	-	1.0	5.7	3.5	1.6	0.6	-0.1	-
150.0	0.02000	0.074	0.685	2.3	10.5	10.8	1.1	1.0	2.0	-	-	1.0	6.2	7.6	2.1	0.7	-0.1	-
150.0	0.03200	0.046	0.591	3.0	11.5	11.9	1.1	1.0	2.0	-	-	1.0	9.1	6.2	0.3	-1.4	-0.1	-
200.0	**0.00263**	**0.750**	**1.297**	**1.3**	**3.2**	**3.4**	**0.8**	**1.0**	**-**	**2.0**	**1.0**	**1.0**	**0.2**	**1.2**	**-0.4**	**-0.2**	**-**	**-0.1**
200.0	0.00320	0.615	1.237	1.2	3.6	3.8	1.1	1.0	2.0	-	-	1.0	0.5	1.7	-0.1	-0.1	-1.4	-
200.0	0.00500	0.394	1.112	0.8	3.6	3.7	1.1	1.0	2.0	-	-	1.0	1.4	1.9	-0.1	-0.1	-0.5	-
200.0	0.00800	0.246	0.956	0.8	3.4	3.5	1.1	1.0	2.0	-	-	1.0	-0.7	1.7	-0.7	-0.6	-0.2	-
200.0	0.01300	0.151	0.808	0.9	3.1	3.3	1.1	1.0	2.0	-	-	1.0	0.2	1.4	-0.2	-0.5	-0.1	-
200.0	0.02000	0.098	0.672	1.0	3.5	3.7	1.1	1.0	2.0	-	-	1.0	1.4	1.5	0.4	-0.5	-0.1	-
200.0	0.03200	0.062	0.559	1.2	3.7	3.9	1.1	1.0	2.0	-	-	1.0	1.4	1.7	0.9	-0.6	-0.0	-
200.0	0.05000	0.039	0.491	1.4	5.2	5.4	1.1	1.0	2.0	-	-	1.0	2.9	2.5	0.1	-2.2	-0.0	-
200.0	0.08000	0.025	0.416	1.5	4.9	5.2	1.1	1.0	2.0	-	-	1.0	3.2	1.9	1.1	-1.1	-0.0	-
200.0	0.13000	0.015	0.352	1.8	7.3	7.6	1.1	1.0	2.0	-	-	1.0	1.4	2.4	3.4	5.1	-0.0	-
250.0	**0.00328**	**0.750**	**1.264**	**1.4**	**3.3**	**3.6**	**0.8**	**1.0**	**-**	**2.0**	**1.0**	**1.0**	**0.5**	**1.2**	**-0.3**	**-0.1**	**-**	**-0.1**
250.0	0.00500	0.492	1.116	1.0	3.4	3.6	1.1	1.0	2.0	-	-	1.0	1.2	1.4	-0.1	-0.1	-1.0	-
250.0	0.00800	0.308	0.972	0.9	3.7	3.8	1.1	1.0	2.0	-	-	1.0	1.7	1.8	0.0	-0.0	-0.3	-
250.0	0.01300	0.189	0.834	1.0	3.6	3.8	1.1	1.0	2.0	-	-	1.0	-1.2	1.7	-0.8	-0.9	-0.1	-
250.0	0.02000	0.123	0.705	1.0	3.5	3.6	1.1	1.0	2.0	-	-	1.0	-1.1	1.6	-0.5	-0.9	-0.1	-
250.0	0.03200	0.077	0.578	1.1	4.1	4.2	1.1	1.0	2.0	-	-	1.0	-2.4	1.6	0.6	-0.6	-0.0	-
250.0	0.05000	0.049	0.514	1.2	4.0	4.2	1.1	1.0	2.0	-	-	1.0	-0.8	1.4	-0.5	-2.4	-0.0	-
250.0	0.08000	0.031	0.445	1.2	4.1	4.3	1.1	1.0	2.0	-	-	1.0	-1.4	1.1	0.6	-2.4	-0.0	-
250.0	0.13000	0.019	0.376	1.3	6.1	6.2	1.1	1.0	2.0	-	-	1.0	-3.4	2.0	2.7	2.5	-0.0	-
300.0	**0.00394**	**0.750**	**1.228**	**1.7**	**3.3**	**3.7**	**0.9**	**1.0**	**-**	**2.0**	**1.0**	**1.0**	**-0.4**	**1.1**	**-0.3**	**-0.1**	**-**	**-0.1**
300.0	0.00500	0.591	1.095	1.7	3.5	3.8	1.1	1.0	2.0	-	-	1.0	1.3	0.8	-0.2	-0.1	-1.4	-
300.0	0.00800	0.369	0.989	1.1	3.4	3.6	1.1	1.0	2.0	-	-	1.0	1.2	1.5	-0.1	-0.1	-0.6	-
300.0	0.01300	0.227	0.835	1.1	3.2	3.4	1.1	1.0	2.0	-	-	1.0	-0.5	1.1	-0.9	-0.6	-0.2	-
300.0	0.02000	0.148	0.723	1.2	3.3	3.5	1.1	1.0	2.0	-	-	1.0	-0.9	1.2	-0.5	-0.9	-0.1	-
300.0	0.03200	0.092	0.583	1.2	4.0	4.2	1.1	1.0	2.0	-	-	1.0	-2.2	1.7	0.1	-0.7	-0.1	-
300.0	0.05000	0.059	0.544	1.4	4.3	4.5	1.1	1.0	2.0	-	-	1.0	-2.1	1.8	-0.3	-1.9	-0.0	-
300.0	0.08000	0.037	0.455	1.4	4.6	4.8	1.1	1.0	2.0	-	-	1.0	-2.0	1.8	0.2	-2.5	-0.0	-
300.0	0.13000	0.023	0.384	1.4	5.6	5.8	1.1	1.0	2.0	-	-	1.0	-3.8	1.9	2.1	1.0	-0.0	-
300.0	0.25000	0.012	0.257	2.2	13.2	13.4	1.1	1.0	2.0	-	-	1.0	-6.9	2.8	4.6	9.4	-0.0	-
400.0	**0.00525**	**0.750**	**1.182**	**1.8**	**3.2**	**3.7**	**0.9**	**1.0**	**-**	**2.0**	**1.0**	**1.0**	**-0.3**	**0.6**	**-0.3**	**-0.1**	**-**	**-0.1**
400.0	0.00800	0.492	0.996	1.4	3.4	3.6	1.1	1.0	2.0	-	-	1.0	0.8	1.5	-0.1	-0.1	-0.9	-
400.0	0.01300	0.303	0.874	1.3	3.5	3.7	1.1	1.0	2.0	-	-	1.0	1.4	1.7	-0.0	-0.0	-0.3	-
400.0	0.02000	0.197	0.722	1.3	3.4	3.7	1.1	1.0	2.0	-	-	1.0	-1.1	1.1	-1.0	-0.9	-0.1	-
400.0	0.03200	0.123	0.608	1.3	3.5	3.8	1.1	1.0	2.0	-	-	1.0	-1.6	1.4	0.1	-0.5	-0.1	-
400.0	0.05000	0.079	0.503	1.6	4.2	4.5	1.1	1.0	2.0	-	-	1.0	-2.6	1.4	0.5	-1.0	-0.0	-
400.0	0.08000	0.049	0.447	1.6	4.0	4.3	1.1	1.0	2.0	-	-	1.0	-1.0	1.3	-0.4	-2.4	-0.0	-
400.0	0.13000	0.030	0.391	1.6	4.4	4.7	1.1	1.0	2.0	-	-	1.0	-2.8	1.3	1.6	0.2	-0.0	-
400.0	0.25000	0.016	0.256	2.4	12.3	12.5	1.1	1.0	2.0	-	-	1.0	-6.8	2.0	5.0	8.2	-0.0	-

Table 9.1: *The reduced cross section* $\tilde{\sigma}_{NC}$ *with its relative error (and contributions) for the* e^-*period. Cross sections from the high* y *analysis are indicated in* ***bold*** *script.*

Q^2 [GeV^2]	x	y	$\tilde{\sigma}_{NC}$	δ_{stat}	δ_{sys}	δ_{tot}	$\delta^{\epsilon_{trig}}$	$\delta^{\epsilon_{id}}$	$\delta^{\epsilon_{trna}}$	$\delta^{\epsilon_{trhy}}$	$\delta^{\epsilon_{qid}}$	δ^{rad}	$\delta^{E'_e}$	δ^{θ_e}	δ^{E_h}	δ^{E_n}	δ^{B}	δ^{κ}
500.0	**0.00656**	**0.750**	**1.051**	**2.0**	**3.3**	**3.9**	**0.9**	**1.0**	-	**2.0**	**1.0**	**1.0**	**0.1**	**0.9**	**-0.4**	**-0.1**	-	**-0.0**
500.0	0.00800	0.615	0.966	2.3	3.4	4.0	1.1	1.0	2.0	-	-	1.0	0.5	1.1	-0.1	-0.1	-1.3	-
500.0	0.01300	0.379	0.884	1.5	3.3	3.6	1.1	1.0	2.0	-	-	1.0	1.0	1.3	-0.1	-0.0	-0.4	-
500.0	0.02000	0.246	0.736	1.6	3.3	3.7	1.1	1.0	2.0	-	-	1.0	-0.8	1.1	-1.1	-0.7	-0.2	-
500.0	0.03200	0.154	0.635	1.5	3.6	3.9	1.1	1.0	2.0	-	-	1.0	-1.6	1.3	-0.6	-0.8	-0.1	-
500.0	0.05000	0.098	0.534	1.7	4.3	4.6	1.1	1.0	2.0	-	-	1.0	-2.9	1.2	0.5	-0.7	-0.0	-
500.0	0.08000	0.062	0.454	1.8	4.0	4.3	1.1	1.0	2.0	-	-	1.0	-0.9	1.0	-0.9	-2.3	-0.0	-
500.0	0.13000	0.038	0.381	2.1	4.8	5.2	1.1	1.0	2.0	-	-	1.0	-3.1	1.8	0.9	-1.1	-0.0	-
500.0	0.18000	0.027	0.340	2.4	6.8	7.2	1.1	1.0	2.0	-	-	1.0	-4.8	1.3	3.0	2.1	-0.0	-
650.0	**0.00853**	**0.750**	**1.022**	**2.3**	**3.4**	**4.1**	**0.9**	**1.0**	-	**2.0**	**1.0**	**1.0**	**-0.2**	**0.6**	**-0.2**	**-0.0**	-	**-0.0**
650.0	0.01300	0.492	0.870	1.9	3.2	3.7	1.1	1.0	2.0	-	-	1.0	0.6	1.1	-0.1	-0.1	-0.8	-
650.0	0.02000	0.320	0.769	1.8	3.4	3.9	1.1	1.0	2.0	-	-	1.0	1.4	1.4	-0.0	-0.0	-0.3	-
650.0	0.03200	0.200	0.639	1.9	3.3	3.8	1.1	1.0	2.0	-	-	1.0	-1.1	1.1	-0.7	-0.6	-0.1	-
650.0	0.05000	0.128	0.520	2.0	3.9	4.3	1.1	1.0	2.0	-	-	1.0	-2.4	0.9	-0.1	-0.6	-0.1	-
650.0	0.08000	0.080	0.467	2.1	4.0	4.6	1.1	1.0	2.0	-	-	1.0	-1.6	1.2	-0.8	-2.0	-0.0	-
650.0	0.13000	0.049	0.388	2.4	4.3	4.9	1.1	1.0	2.0	-	-	1.0	-2.8	0.7	1.0	-0.9	-0.0	-
650.0	0.18000	0.036	0.328	2.8	5.3	6.0	1.1	1.0	2.0	-	-	1.0	-3.8	1.4	1.7	0.4	-0.0	-
650.0	0.25000	0.026	0.234	3.8	12.0	12.5	1.1	1.0	2.0	-	-	1.0	-7.8	1.3	5.6	6.4	-0.0	-
800.0	**0.01050**	**0.750**	**0.949**	**2.7**	**3.7**	**4.6**	**1.0**	**1.0**	-	**2.0**	**1.0**	**1.0**	**0.4**	**0.9**	**-0.4**	**-0.1**	-	**-0.0**
800.0	0.01300	0.606	0.868	3.0	3.3	4.5	1.1	1.0	2.0	-	-	1.0	0.6	1.1	-0.1	-0.1	-1.0	-
800.0	0.02000	0.394	0.740	2.1	3.3	3.9	1.1	1.0	2.0	-	-	1.0	1.0	1.4	-0.0	-0.0	-0.5	-
800.0	0.03200	0.246	0.645	2.2	3.4	4.1	1.1	1.0	2.0	-	-	1.0	-1.1	0.8	-1.1	-0.7	-0.1	-
800.0	0.05000	0.158	0.542	2.2	3.6	4.3	1.1	1.0	2.0	-	-	1.0	-1.8	1.1	-0.3	-0.6	-0.1	-
800.0	0.08000	0.098	0.444	2.6	3.8	4.6	1.1	1.0	2.0	-	-	1.0	-2.0	1.1	-0.2	-1.2	-0.1	-
800.0	0.13000	0.061	0.362	2.9	4.3	5.2	1.1	1.0	2.0	-	-	1.0	-2.6	1.4	0.1	-1.4	-0.0	-
800.0	0.18000	0.044	0.321	3.3	5.1	6.1	1.1	1.0	2.0	-	-	1.0	-3.7	1.1	1.5	-0.3	-0.0	-
800.0	0.25000	0.032	0.261	3.9	10.9	11.6	1.1	1.0	2.0	-	-	1.0	-7.7	1.7	4.8	5.1	-0.0	-
1000.0	0.01300	0.757	0.839	3.2	4.2	5.3	1.1	1.0	2.0	-	-	1.0	0.6	0.7	-0.3	-0.1	-2.8	-
1000.0	0.02000	0.492	0.740	2.5	3.2	4.1	1.1	1.0	2.0	-	-	1.0	0.8	0.9	-0.1	-0.1	-0.9	-
1000.0	0.03200	0.308	0.663	2.4	3.7	4.5	1.1	1.0	2.0	-	-	1.0	1.9	1.5	0.0	0.0	-0.1	-
1000.0	0.05000	0.197	0.535	2.6	3.2	4.1	1.1	1.0	2.0	-	-	1.0	-0.7	0.8	-0.8	-0.7	-0.1	-
1000.0	0.08000	0.123	0.422	2.9	4.0	5.0	1.1	1.0	2.0	-	-	1.0	-2.7	0.5	0.4	-0.5	-0.1	-
1000.0	0.13000	0.076	0.403	3.3	3.9	5.1	1.1	1.0	2.0	-	-	1.0	-1.4	0.9	-0.5	-1.7	-0.0	-
1000.0	0.18000	0.055	0.358	3.5	5.1	6.2	1.1	1.0	2.0	-	-	1.0	-3.5	1.1	1.9	0.4	-0.0	-
1000.0	0.25000	0.039	0.269	4.2	6.4	7.6	1.1	1.0	2.0	-	-	1.0	-4.2	0.5	3.0	2.1	-0.0	-
1000.0	0.40000	0.025	0.127	7.2	16.7	18.2	1.1	1.0	2.0	-	-	1.0	-9.8	1.2	6.4	11.3	-0.0	-
1200.0	0.01300	0.909	0.827	5.8	5.7	8.2	1.1	1.0	2.0	-	-	1.0	-0.8	1.5	-0.3	-0.1	-4.2	-
1200.0	0.02000	0.591	0.776	3.2	3.5	4.7	1.1	1.0	2.0	-	-	1.0	-0.6	1.2	-0.1	-0.0	-1.4	-
1200.0	0.03200	0.369	0.683	2.8	3.5	4.5	1.1	1.0	2.0	-	-	1.0	1.6	0.9	-0.1	-0.0	-0.2	-
1200.0	0.05000	0.236	0.560	2.9	3.4	4.5	1.1	1.0	2.0	-	-	1.0	-1.1	0.9	-0.9	-0.5	-0.1	-
1200.0	0.08000	0.148	0.437	3.2	3.8	5.0	1.1	1.0	2.0	-	-	1.0	-2.2	0.7	-0.0	-0.7	-0.1	-
1200.0	0.13000	0.091	0.387	3.8	3.9	5.4	1.1	1.0	2.0	-	-	1.0	-0.9	0.6	-1.3	-1.6	-0.1	-
1200.0	0.18000	0.066	0.300	4.3	5.7	7.1	1.1	1.0	2.0	-	-	1.0	-4.2	1.1	2.1	-0.4	-0.0	-
1200.0	0.25000	0.047	0.260	4.7	6.1	7.6	1.1	1.0	2.0	-	-	1.0	-4.6	1.1	1.7	1.0	-0.0	-
1200.0	0.40000	0.030	0.125	7.6	18.2	19.7	1.1	1.0	2.0	-	-	1.0	-11.8	0.8	8.9	9.8	-0.0	-
1200.0	0.65000	0.018	0.012	19.3	21.8	29.1	1.1	1.0	2.0	-	-	1.0	-10.0	1.6	6.0	17.1	-0.1	-

Table 9.2: *(...Cont'd) The reduced cross section* $\tilde{\sigma}_{NC}$ *with its relative error (and contributions) for the* e^-*period. Cross sections from the high* y *analysis are indicated in* ***bold*** *script.*

Q^2 [GeV^2]	x	y	$\tilde{\sigma}_{NC}$	δ_{stat}	δ_{sys}	δ_{tot}	$\delta^{\epsilon_{trig}}$	$\delta^{\epsilon_{id}}$	$\delta^{\epsilon_{trna}}$	$\delta^{\epsilon_{trhy}}$	$\delta^{\epsilon_{qid}}$	δ^{rad}	$\delta^{E'_e}$	δ^{θ_e}	δ^{E_h}	δ^{E_n}	δ^{B}	δ^{κ}
1500.0	0.02000	0.738	0.760	4.1	4.4	6.0	1.1	1.0	2.0	-	-	1.0	1.1	0.8	-0.2	-0.1	-2.9	-
1500.0	0.03200	0.462	0.658	3.5	3.4	4.9	1.1	1.0	2.0	-	-	1.0	-1.1	1.0	-0.1	-0.1	-0.3	-
1500.0	0.05000	0.295	0.562	3.5	3.5	5.0	1.1	1.0	2.0	-	-	1.0	-0.8	0.9	-1.3	-0.5	-0.1	-
1500.0	0.08000	0.185	0.454	3.5	3.8	5.1	1.1	1.0	2.0	-	-	1.0	-2.1	0.8	-0.4	-0.3	-0.1	-
1500.0	0.13000	0.114	0.364	4.6	4.0	6.1	1.1	1.0	2.0	-	-	1.0	-2.2	0.7	0.3	-1.0	-0.1	-
1500.0	0.18000	0.082	0.301	4.8	4.1	6.3	1.1	1.0	2.0	-	-	1.0	-2.2	0.7	-0.3	-1.0	-0.0	-
1500.0	0.25000	0.059	0.265	5.2	4.7	6.9	1.1	1.0	2.0	-	-	1.0	-2.6	0.7	1.6	0.6	-0.0	-
1500.0	0.40000	0.037	0.112	8.3	16.3	18.2	1.1	1.0	2.0	-	-	1.0	-11.5	-0.3	7.7	7.5	-0.0	-
2000.0	0.02000	0.985	0.850	6.8	5.5	8.7	1.1	1.0	2.0	-	-	1.0	1.2	1.2	-0.2	-0.0	-3.6	-
2000.0	0.03200	0.615	0.643	4.2	3.3	5.3	1.1	1.0	2.0	-	-	1.0	0.4	0.7	-0.2	-0.1	-0.7	-
2000.0	0.05000	0.394	0.536	4.2	3.3	5.4	1.1	1.0	2.0	-	-	1.0	0.8	0.8	-0.0	0.0	-0.2	-
2000.0	0.08000	0.246	0.472	4.1	3.5	5.4	1.1	1.0	2.0	-	-	1.0	-1.1	0.5	-1.0	-0.5	-0.1	-
2000.0	0.13000	0.151	0.347	5.3	4.5	6.9	1.1	1.0	2.0	-	-	1.0	-3.1	0.3	0.3	-0.4	-0.1	-
2000.0	0.18000	0.109	0.322	5.4	4.0	6.7	1.1	1.0	2.0	-	-	1.0	-1.5	0.8	-0.2	-1.2	-0.0	-
2000.0	0.25000	0.079	0.248	6.0	6.8	9.1	1.1	1.0	2.0	-	-	1.0	-5.3	0.0	2.4	0.5	-0.0	-
2000.0	0.40000	0.049	0.130	8.5	13.5	15.9	1.1	1.0	2.0	-	-	1.0	-9.3	0.7	6.2	6.2	-0.0	-
3000.0	0.03200	0.923	0.755	4.1	3.6	5.5	1.1	1.0	2.0	-	-	1.0	0.4	1.1	-0.2	0.0	-1.3	-
3000.0	0.05000	0.591	0.628	3.4	3.6	4.9	1.1	1.0	2.0	-	-	1.0	1.5	1.1	-0.1	-0.0	-0.4	-
3000.0	0.08000	0.369	0.483	3.8	3.4	5.1	1.1	1.0	2.0	-	-	1.0	1.0	1.1	0.0	-0.0	-0.2	-
3000.0	0.13000	0.227	0.392	4.4	4.0	5.9	1.1	1.0	2.0	-	-	1.0	-2.4	0.1	-0.3	-0.3	-0.1	-
3000.0	0.18000	0.164	0.292	5.3	3.9	6.6	1.1	1.0	2.0	-	-	1.0	-1.4	0.7	-1.0	-1.1	-0.1	-
3000.0	0.25000	0.118	0.228	5.5	6.7	8.7	1.1	1.0	2.0	-	-	1.0	-5.3	-0.4	2.2	0.4	-0.0	-
3000.0	0.40000	0.074	0.128	7.4	12.3	14.3	1.1	1.0	2.0	-	-	1.0	-10.1	-0.5	4.4	3.7	-0.0	-
3000.0	0.65000	0.045	0.013	20.9	21.4	29.9	1.1	1.0	2.0	-	-	1.0	-13.7	1.2	11.3	9.2	-0.1	-
5000.0	0.05000	0.985	0.667	5.6	3.9	6.8	1.1	1.0	2.0	-	-	1.0	-0.9	0.8	-0.2	0.0	-1.5	-
5000.0	0.08000	0.615	0.530	4.1	3.5	5.4	1.1	1.0	2.0	-	-	1.0	1.5	0.7	-0.1	-0.0	-0.5	-
5000.0	0.13000	0.379	0.472	4.5	3.5	5.8	1.1	1.0	2.0	-	-	1.0	1.0	1.0	0.0	0.0	-0.2	-
5000.0	0.18000	0.273	0.356	5.4	5.8	7.9	1.1	1.0	2.0	-	-	1.0	-4.7	-0.3	0.2	0.0	-0.1	-
5000.0	0.25000	0.197	0.262	6.4	5.6	8.5	1.1	1.0	2.0	-	-	1.0	-4.2	0.5	0.4	-0.3	-0.1	-
5000.0	0.40000	0.123	0.101	9.5	12.9	16.1	1.1	1.0	2.0	-	-	1.0	-11.2	-1.5	4.4	1.4	-0.0	-
5000.0	0.65000	0.076	0.018	19.3	29.5	35.3	1.1	1.0	2.0	-	-	1.0	-24.4	-3.7	10.9	9.0	-0.0	-
8000.0	0.08000	0.985	0.637	8.3	4.8	9.6	1.1	1.0	2.0	-	-	1.0	-1.4	0.9	-0.3	-0.1	-1.9	-
8000.0	0.13000	0.606	0.522	6.0	4.1	7.3	1.1	1.0	2.0	-	-	1.0	2.0	0.4	-0.1	-0.1	-0.5	-
8000.0	0.18000	0.438	0.423	6.6	4.3	7.9	1.1	1.0	2.0	-	-	1.0	-1.8	1.1	-0.0	0.0	-0.1	-
8000.0	0.25000	0.315	0.290	7.6	5.1	9.1	1.1	1.0	2.0	-	-	1.0	-3.2	0.5	0.0	0.0	-0.1	-
8000.0	0.40000	0.197	0.133	9.9	12.8	16.2	1.1	1.0	2.0	-	-	1.0	-11.8	-1.1	1.7	-0.4	-0.0	-
8000.0	0.65000	0.121	0.015	23.0	38.2	44.5	1.1	1.0	2.0	-	-	1.0	-34.1	-5.8	12.0	6.6	-0.0	-
12000.0	0.13000	0.909	0.670	15.3	7.8	17.2	1.1	1.0	2.0	-	-	1.0	-3.3	1.4	-0.1	-0.1	-2.5	-
12000.0	0.18000	0.656	0.485	8.8	5.2	10.2	1.1	1.0	2.0	-	-	1.0	-2.9	0.4	-0.0	0.0	-0.5	-
12000.0	0.25000	0.473	0.321	9.5	6.0	11.2	1.1	1.0	2.0	-	-	1.0	-4.0	0.6	0.2	0.0	-0.2	-
12000.0	0.40000	0.295	0.209	10.7	16.3	19.5	1.1	1.0	2.0	-	-	1.0	-15.3	-1.4	0.5	-0.2	-0.1	-
12000.0	0.65000	0.182	0.017	26.8	28.1	38.9	1.1	1.0	2.0	-	-	1.0	-24.6	-6.0	6.4	2.4	-0.1	-
20000.0	0.25000	0.788	0.465	13.8	6.3	15.2	1.1	1.0	2.0	-	-	1.0	-1.2	1.4	0.0	0.0	-0.8	-
20000.0	0.40000	0.492	0.194	15.2	19.3	24.6	1.1	1.0	2.0	-	-	1.0	-18.2	1.4	0.0	0.0	-0.3	-
20000.0	0.65000	0.303	0.012	38.0	46.0	59.6	1.1	1.0	2.0	-	-	1.0	-43.8	-7.7	0.0	0.0	-0.2	-
30000.0	0.40000	0.738	0.218	29.3	20.5	35.8	1.1	1.0	2.0	-	-	1.0	-17.0	-2.5	0.0	0.0	-1.7	-
30000.0	0.65000	0.454	0.074	31.8	58.1	66.2	1.1	1.0	2.0	-	-	1.0	-54.2	4.6	0.0	0.0	-0.1	-

Table 9.3: *(...Cont'd) The reduced cross section $\tilde{\sigma}_{NC}$ with its relative error (and contributions) for the e^-period. Cross sections from the high y analysis are indicated in* ***bold*** *script.*

Q^2 [GeV^2]	x	y	$\tilde{\sigma}_{NC}$	δ_{stat}	δ_{sys}	δ_{tot}	$\delta^{\epsilon_{trig}}$	$\delta^{\epsilon_{id}}$	$\delta^{\epsilon_{trna}}$	$\delta^{\epsilon_{trhy}}$	$\delta^{\epsilon_{qid}}$	δ^{rad}	$\delta^{E'_e}$	δ^{θ_e}	δ^{E_h}	δ^{E_n}	δ^{B}	δ^{κ}
65.0	**0.00085**	**0.750**	**1.431**	**1.2**	**4.2**	**4.3**	**2.1**	**1.0**	**–**	**2.0**	**1.0**	**1.0**	**0.8**	**2.1**	**-0.4**	**-0.1**	**–**	**-0.2**
80.0	**0.00105**	**0.750**	**1.486**	**0.9**	**3.8**	**3.9**	**1.9**	**1.0**	**–**	**2.0**	**1.0**	**1.0**	**0.3**	**1.6**	**-0.4**	**-0.1**	**–**	**-0.1**
100.0	**0.00131**	**0.750**	**1.463**	**0.9**	**3.6**	**3.7**	**1.8**	**1.0**	**–**	**2.0**	**1.0**	**1.0**	**0.6**	**1.4**	**-0.4**	**-0.1**	**–**	**-0.1**
120.0	**0.00158**	**0.750**	**1.359**	**1.0**	**3.5**	**3.7**	**1.7**	**1.0**	**–**	**2.0**	**1.0**	**1.0**	**0.4**	**1.3**	**-0.4**	**-0.2**	**–**	**-0.1**
150.0	**0.00197**	**0.750**	**1.378**	**1.0**	**3.5**	**3.7**	**1.6**	**1.0**	**–**	**2.0**	**1.0**	**1.0**	**-0.6**	**1.2**	**-0.4**	**-0.2**	**–**	**-0.1**
150.0	0.00320	0.462	1.249	0.7	3.6	3.7	1.0	1.0	2.0	–	–	1.0	1.0	1.8	-0.1	-0.1	-1.1	–
150.0	0.00500	0.295	1.081	0.8	3.3	3.4	1.0	1.0	2.0	–	–	1.0	0.5	1.7	-0.4	-0.5	-0.3	–
150.0	0.00800	0.185	0.947	1.0	4.7	4.9	1.0	1.0	2.0	–	–	1.0	2.6	2.5	1.2	0.5	-0.2	–
150.0	0.01300	0.114	0.829	1.6	7.9	8.0	1.0	1.0	2.0	–	–	1.0	6.5	3.2	1.4	0.3	-0.1	–
150.0	0.02000	0.074	0.719	2.2	10.5	10.7	1.0	1.0	2.0	–	–	1.0	6.7	7.1	2.0	1.2	-0.1	–
150.0	0.03200	0.046	0.633	2.8	12.5	12.8	1.0	1.0	2.0	–	–	1.0	9.6	6.9	-0.7	-2.4	-0.1	–
200.0	**0.00263**	**0.750**	**1.272**	**1.2**	**3.5**	**3.7**	**1.5**	**1.0**	**–**	**2.0**	**1.0**	**1.0**	**0.7**	**1.1**	**-0.4**	**-0.2**	**–**	**-0.1**
200.0	0.00320	0.615	1.244	1.1	3.5	3.7	1.0	1.0	2.0	–	–	1.0	0.9	1.3	-0.1	-0.1	-1.4	–
200.0	0.00500	0.394	1.130	0.8	3.6	3.7	1.0	1.0	2.0	–	–	1.0	1.4	1.8	-0.1	-0.1	-0.5	–
200.0	0.00800	0.246	0.935	0.8	3.4	3.5	1.0	1.0	2.0	–	–	1.0	-0.2	1.5	-1.0	-0.8	-0.2	–
200.0	0.01300	0.151	0.807	0.8	3.3	3.4	1.0	1.0	2.0	–	–	1.0	-0.3	1.7	0.1	-0.3	-0.1	–
200.0	0.02000	0.098	0.686	1.0	3.6	3.7	1.0	1.0	2.0	–	–	1.0	1.7	1.4	0.5	-0.4	-0.1	–
200.0	0.03200	0.062	0.561	1.2	3.8	4.0	1.0	1.0	2.0	–	–	1.0	1.8	1.7	0.7	-0.5	-0.0	–
200.0	0.05000	0.039	0.490	1.3	5.9	6.0	1.0	1.0	2.0	–	–	1.0	4.1	2.0	0.1	-2.5	-0.0	–
200.0	0.08000	0.025	0.410	1.4	4.6	4.8	1.0	1.0	2.0	–	–	1.0	2.4	2.2	1.6	-0.2	-0.0	–
200.0	0.13000	0.015	0.344	1.7	7.0	7.2	1.0	1.0	2.0	–	–	1.0	1.8	2.5	3.0	4.7	-0.0	–
250.0	**0.00328**	**0.750**	**1.291**	**1.3**	**3.5**	**3.7**	**1.4**	**1.0**	**–**	**2.0**	**1.0**	**1.0**	**-0.4**	**1.2**	**-0.4**	**-0.1**	**–**	**-0.1**
250.0	0.00500	0.492	1.122	0.9	3.4	3.5	1.0	1.0	2.0	–	–	1.0	1.1	1.4	-0.1	-0.1	-1.0	–
250.0	0.00800	0.308	0.972	0.9	3.7	3.8	1.0	1.0	2.0	–	–	1.0	1.9	1.6	-0.0	-0.0	-0.3	–
250.0	0.01300	0.189	0.805	0.9	3.4	3.5	1.0	1.0	2.0	–	–	1.0	-0.7	1.4	-0.9	-1.0	-0.1	–
250.0	0.02000	0.123	0.701	0.9	3.8	3.9	1.0	1.0	2.0	–	–	1.0	-1.5	2.0	-0.2	-0.6	-0.1	–
250.0	0.03200	0.077	0.577	1.0	4.0	4.1	1.0	1.0	2.0	–	–	1.0	-2.3	1.5	0.3	-0.9	-0.0	–
250.0	0.05000	0.049	0.523	1.1	4.4	4.5	1.0	1.0	2.0	–	–	1.0	-1.3	1.7	-0.4	-2.7	-0.0	–
250.0	0.08000	0.031	0.445	1.1	3.9	4.0	1.0	1.0	2.0	–	–	1.0	-1.3	1.4	0.6	-1.8	-0.0	–
250.0	0.13000	0.019	0.374	1.2	5.9	6.0	1.0	1.0	2.0	–	–	1.0	-3.6	1.7	2.6	2.1	-0.0	–
300.0	**0.00394**	**0.750**	**1.207**	**1.5**	**3.4**	**3.7**	**1.4**	**1.0**	**–**	**2.0**	**1.0**	**1.0**	**0.6**	**0.7**	**-0.3**	**-0.2**	**–**	**-0.1**
300.0	0.00500	0.591	1.129	1.5	3.4	3.7	1.0	1.0	2.0	–	–	1.0	0.3	1.4	-0.2	-0.1	-1.2	–
300.0	0.00800	0.369	0.973	1.0	3.4	3.6	1.0	1.0	2.0	–	–	1.0	1.3	1.6	-0.0	-0.1	-0.6	–
300.0	0.01300	0.227	0.825	1.0	3.3	3.5	1.0	1.0	2.0	–	–	1.0	-0.8	1.3	-0.8	-0.7	-0.2	–
300.0	0.02000	0.148	0.714	1.1	3.6	3.8	1.0	1.0	2.0	–	–	1.0	-1.4	1.7	-0.6	-0.8	-0.1	–
300.0	0.03200	0.092	0.602	1.1	4.2	4.3	1.0	1.0	2.0	–	–	1.0	-2.4	1.9	0.2	-0.7	-0.0	–
300.0	0.05000	0.059	0.544	1.2	4.1	4.3	1.0	1.0	2.0	–	–	1.0	-1.7	1.7	-0.4	-2.0	-0.0	–
300.0	0.08000	0.037	0.470	1.2	4.7	4.8	1.0	1.0	2.0	–	–	1.0	-2.4	2.0	0.4	-2.1	-0.0	–
300.0	0.13000	0.023	0.390	1.3	5.7	5.9	1.0	1.0	2.0	–	–	1.0	-3.9	2.4	1.8	0.9	-0.0	–
400.0	**0.00525**	**0.750**	**1.203**	**1.6**	**3.4**	**3.8**	**1.3**	**1.0**	**–**	**2.0**	**1.0**	**1.0**	**0.4**	**0.9**	**-0.3**	**-0.1**	**–**	**-0.1**
400.0	0.00800	0.492	0.978	1.3	3.3	3.5	1.0	1.0	2.0	–	–	1.0	1.1	1.1	-0.1	-0.1	-0.9	–
400.0	0.01300	0.303	0.851	1.2	3.5	3.7	1.0	1.0	2.0	–	–	1.0	1.4	1.7	-0.0	-0.0	-0.3	–
400.0	0.02000	0.197	0.727	1.2	3.2	3.4	1.0	1.0	2.0	–	–	1.0	-0.7	1.1	-0.8	-0.7	-0.1	–
400.0	0.03200	0.123	0.593	1.3	3.3	3.5	1.0	1.0	2.0	–	–	1.0	-1.2	1.1	-0.2	-0.8	-0.1	–
400.0	0.05000	0.079	0.524	1.4	4.1	4.4	1.0	1.0	2.0	–	–	1.0	-2.6	1.3	0.4	-1.1	-0.0	–
400.0	0.08000	0.049	0.461	1.4	3.9	4.2	1.0	1.0	2.0	–	–	1.0	-1.2	1.2	-0.3	-2.2	-0.0	–
400.0	0.13000	0.030	0.377	1.5	4.1	4.3	1.0	1.0	2.0	–	–	1.0	-2.4	1.1	1.4	0.6	-0.0	–
400.0	0.25000	0.016	0.244	2.2	12.6	12.8	1.0	1.0	2.0	–	–	1.0	-6.9	1.6	5.2	8.5	-0.0	–

Table 9.4: *The reduced cross section* $\tilde{\sigma}_{NC}$ *with its relative error (and contributions) for the* e^+*period. Cross sections from the high* y *analysis are indicated in **bold** script.*

Q^2 [GeV^2]	x	y	$\tilde{\sigma}_{NC}$	δ_{stat}	δ_{sys}	δ_{tot}	$\delta^{\epsilon_{trig}}$	$\delta^{\epsilon_{id}}$	$\delta^{\epsilon_{trna}}$	$\delta^{\epsilon_{trhy}}$	$\delta^{\epsilon_{qid}}$	δ^{rad}	$\delta^{E_e'}$	δ^{θ_e}	δ^{E_h}	δ^{E_n}	δ^{B}	δ^{κ}
500.0	**0.00656**	**0.750**	**1.022**	**1.8**	**3.4**	**3.9**	**1.2**	**1.0**	**-**	**2.0**	**1.0**	**1.0**	**0.2**	**0.5**	**-0.3**	**-0.1**	**-**	**-0.0**
500.0	0.00800	0.615	0.965	2.1	3.4	4.0	1.0	1.0	2.0	-	-	1.0	0.5	1.3	-0.1	-0.1	-1.2	-
500.0	0.01300	0.379	0.846	1.4	3.4	3.7	1.0	1.0	2.0	-	-	1.0	1.1	1.5	-0.0	-0.1	-0.5	-
500.0	0.02000	0.246	0.741	1.5	3.5	3.8	1.0	1.0	2.0	-	-	1.0	-1.2	1.2	-1.1	-0.8	-0.2	-
500.0	0.03200	0.154	0.617	1.4	3.4	3.7	1.0	1.0	2.0	-	-	1.0	-1.2	1.3	-0.7	-0.8	-0.1	-
500.0	0.05000	0.098	0.533	1.6	4.5	4.8	1.0	1.0	2.0	-	-	1.0	-3.2	1.4	0.5	-0.5	-0.0	-
500.0	0.08000	0.062	0.469	1.6	4.0	4.3	1.0	1.0	2.0	-	-	1.0	-1.3	1.2	-0.6	-2.2	-0.0	-
500.0	0.13000	0.038	0.399	1.9	4.2	4.7	1.0	1.0	2.0	-	-	1.0	-2.6	1.1	1.0	-1.1	-0.0	-
500.0	0.18000	0.027	0.321	2.3	5.9	6.3	1.0	1.0	2.0	-	-	1.0	-4.0	1.5	2.4	1.7	-0.0	-
650.0	**0.00853**	**0.750**	**1.025**	**2.1**	**3.7**	**4.3**	**1.1**	**1.0**	**-**	**2.0**	**1.0**	**1.0**	**-0.6**	**1.2**	**-0.5**	**-0.1**	**-**	**-0.0**
650.0	0.01300	0.492	0.877	1.7	3.1	3.6	1.0	1.0	2.0	-	-	1.0	0.6	1.0	-0.1	-0.1	-0.7	-
650.0	0.02000	0.320	0.745	1.7	3.5	3.9	1.0	1.0	2.0	-	-	1.0	1.8	1.2	-0.0	-0.0	-0.3	-
650.0	0.03200	0.200	0.632	1.7	3.4	3.8	1.0	1.0	2.0	-	-	1.0	-1.3	1.2	-0.7	-0.7	-0.1	-
650.0	0.05000	0.128	0.519	1.8	3.7	4.2	1.0	1.0	2.0	-	-	1.0	-2.2	1.0	0.1	-0.5	-0.1	-
650.0	0.08000	0.080	0.459	2.0	3.9	4.4	1.0	1.0	2.0	-	-	1.0	-1.5	1.1	-0.8	-1.9	-0.0	-
650.0	0.13000	0.049	0.384	2.2	5.0	5.5	1.0	1.0	2.0	-	-	1.0	-3.6	1.5	0.9	-1.2	-0.0	-
650.0	0.18000	0.036	0.332	2.6	5.3	5.9	1.0	1.0	2.0	-	-	1.0	-3.8	1.3	1.6	1.0	-0.0	-
650.0	0.25000	0.026	0.251	3.4	12.7	13.2	1.0	1.0	2.0	-	-	1.0	-8.6	1.8	5.5	6.8	-0.0	-
800.0	**0.01050**	**0.750**	**0.920**	**2.5**	**4.0**	**4.7**	**1.1**	**1.0**	**-**	**2.0**	**1.0**	**1.0**	**-0.6**	**1.3**	**-0.5**	**-0.1**	**-**	**-0.0**
800.0	0.01300	0.606	0.808	2.8	3.4	4.4	1.0	1.0	2.0	-	-	1.0	-0.4	1.2	-0.1	-0.1	-1.1	-
800.0	0.02000	0.394	0.706	2.0	3.2	3.8	1.0	1.0	2.0	-	-	1.0	0.9	1.1	-0.0	-0.0	-0.5	-
800.0	0.03200	0.246	0.645	2.0	3.3	3.9	1.0	1.0	2.0	-	-	1.0	-0.8	0.8	-1.1	-0.6	-0.1	-
800.0	0.05000	0.158	0.510	2.1	3.7	4.3	1.0	1.0	2.0	-	-	1.0	-1.9	1.1	-0.5	-0.7	-0.1	-
800.0	0.08000	0.098	0.483	2.3	3.7	4.3	1.0	1.0	2.0	-	-	1.0	-1.9	0.8	-0.3	-1.0	-0.0	-
800.0	0.13000	0.061	0.380	2.6	4.0	4.8	1.0	1.0	2.0	-	-	1.0	-2.0	1.1	0.4	-1.4	-0.0	-
800.0	0.18000	0.044	0.341	2.9	4.5	5.4	1.0	1.0	2.0	-	-	1.0	-2.7	1.1	1.5	-0.6	-0.0	-
800.0	0.25000	0.032	0.208	4.0	9.9	10.6	1.0	1.0	2.0	-	-	1.0	-6.8	0.8	4.3	4.7	-0.0	-
1000.0	0.01300	0.757	0.772	3.1	4.6	5.6	1.0	1.0	2.0	-	-	1.0	0.5	0.9	-0.3	-0.1	-3.4	-
1000.0	0.02000	0.492	0.733	2.3	3.3	4.1	1.0	1.0	2.0	-	-	1.0	0.8	1.2	-0.1	-0.1	-0.9	-
1000.0	0.03200	0.308	0.605	2.3	3.5	4.2	1.0	1.0	2.0	-	-	1.0	1.3	1.5	-0.0	-0.0	-0.1	-
1000.0	0.05000	0.197	0.525	2.4	3.3	4.1	1.0	1.0	2.0	-	-	1.0	-0.6	1.1	-1.0	-0.7	-0.1	-
1000.0	0.08000	0.123	0.427	2.7	4.7	5.4	1.0	1.0	2.0	-	-	1.0	-3.5	1.1	0.4	-0.5	-0.1	-
1000.0	0.13000	0.076	0.376	3.1	3.8	4.9	1.0	1.0	2.0	-	-	1.0	-1.7	1.0	0.1	-1.3	-0.0	-
1000.0	0.18000	0.055	0.314	3.5	5.3	6.3	1.0	1.0	2.0	-	-	1.0	-3.9	0.8	1.4	1.1	-0.0	-
1000.0	0.25000	0.039	0.246	4.1	7.6	8.6	1.0	1.0	2.0	-	-	1.0	-5.3	1.2	3.0	3.0	-0.0	-
1000.0	0.40000	0.025	0.108	7.1	15.7	17.3	1.0	1.0	2.0	-	-	1.0	-9.3	1.5	7.5	9.3	-0.0	-
1200.0	0.01300	0.909	0.783	5.5	5.9	8.1	1.0	1.0	2.0	-	-	1.0	0.6	1.0	-0.4	-0.1	-4.6	-
1200.0	0.02000	0.591	0.694	3.1	3.4	4.6	1.0	1.0	2.0	-	-	1.0	-0.4	0.8	-0.1	-0.1	-1.4	-
1200.0	0.03200	0.369	0.620	2.6	3.2	4.2	1.0	1.0	2.0	-	-	1.0	1.0	0.9	-0.1	-0.1	-0.2	-
1200.0	0.05000	0.236	0.514	2.7	3.3	4.3	1.0	1.0	2.0	-	-	1.0	-0.4	0.6	-1.0	-0.7	-0.1	-
1200.0	0.08000	0.148	0.427	2.9	3.9	4.8	1.0	1.0	2.0	-	-	1.0	-2.4	0.6	0.4	-0.2	-0.1	-
1200.0	0.13000	0.091	0.368	3.5	3.8	5.2	1.0	1.0	2.0	-	-	1.0	-0.6	0.8	-0.9	-1.8	-0.1	-
1200.0	0.18000	0.066	0.316	3.9	4.7	6.1	1.0	1.0	2.0	-	-	1.0	-3.2	0.8	1.0	0.3	-0.0	-
1200.0	0.25000	0.047	0.252	4.3	5.8	7.2	1.0	1.0	2.0	-	-	1.0	-4.0	0.4	2.5	1.0	-0.0	-
1200.0	0.40000	0.030	0.115	7.3	17.7	19.1	1.0	1.0	2.0	-	-	1.0	-11.1	1.0	7.5	10.7	-0.0	-

Table 9.5: *(...Cont'd) The reduced cross section $\tilde{\sigma}_{NC}$ with its relative error (and contributions) for the e^+period. Cross sections from the high y analysis are indicated in **bold** script.*

Q^2 [GeV^2]	x	y	$\tilde{\sigma}_{NC}$	δ_{stat}	δ_{sys}	δ_{tot}	$\delta^{\epsilon_{trig}}$	$\delta^{\epsilon_{id}}$	$\delta^{\epsilon_{trna}}$	$\delta^{\epsilon_{trhy}}$	$\delta^{\epsilon_{qid}}$	δ^{rad}	$\delta^{E'_e}$	δ^{θ_e}	δ^{E_h}	δ^{E_n}	δ^{B}	δ^{κ}
1500.0	0.02000	0.738	0.691	4.1	4.7	6.2	1.0	1.0	2.0	-	-	1.0	0.6	0.8	-0.4	-0.2	-3.3	-
1500.0	0.03200	0.462	0.613	3.4	3.4	4.8	1.0	1.0	2.0	-	-	1.0	-0.3	1.4	-0.2	-0.1	-0.3	-
1500.0	0.05000	0.295	0.530	3.2	3.6	4.8	1.0	1.0	2.0	-	-	1.0	-0.8	0.8	-1.5	-0.6	-0.1	-
1500.0	0.08000	0.185	0.448	3.3	3.4	4.7	1.0	1.0	2.0	-	-	1.0	-1.4	0.5	-0.5	-0.5	-0.1	-
1500.0	0.13000	0.114	0.364	4.1	4.2	5.9	1.0	1.0	2.0	-	-	1.0	-1.8	0.6	-1.1	-1.6	-0.1	-
1500.0	0.18000	0.082	0.302	4.3	4.6	6.3	1.0	1.0	2.0	-	-	1.0	-3.0	0.6	0.7	-0.8	-0.0	-
1500.0	0.25000	0.059	0.248	4.9	8.0	9.3	1.0	1.0	2.0	-	-	1.0	-6.2	1.1	3.2	1.5	-0.0	-
1500.0	0.40000	0.037	0.127	7.5	14.8	16.6	1.0	1.0	2.0	-	-	1.0	-9.6	1.0	6.6	8.1	-0.0	-
2000.0	0.02000	0.985	0.695	7.1	5.9	9.2	1.0	1.0	2.0	-	-	1.0	-1.3	0.3	-0.4	-0.1	-4.2	-
2000.0	0.03200	0.615	0.570	4.2	3.5	5.4	1.0	1.0	2.0	-	-	1.0	0.4	1.1	-0.1	-0.1	-0.9	-
2000.0	0.05000	0.394	0.540	3.8	3.5	5.2	1.0	1.0	2.0	-	-	1.0	1.1	1.1	0.0	-0.0	-0.2	-
2000.0	0.08000	0.246	0.446	3.8	3.9	5.4	1.0	1.0	2.0	-	-	1.0	-2.1	0.8	-0.7	-0.5	-0.1	-
2000.0	0.13000	0.151	0.357	4.7	4.4	6.4	1.0	1.0	2.0	-	-	1.0	-2.6	0.7	0.3	-0.5	-0.1	-
2000.0	0.18000	0.109	0.322	5.0	4.5	6.7	1.0	1.0	2.0	-	-	1.0	-2.7	0.4	-0.4	-0.7	-0.0	-
2000.0	0.25000	0.079	0.263	5.3	6.4	8.3	1.0	1.0	2.0	-	-	1.0	-4.4	0.3	2.9	0.6	-0.0	-
2000.0	0.40000	0.049	0.128	8.0	11.3	13.8	1.0	1.0	2.0	-	-	1.0	-8.0	0.2	4.9	4.5	-0.0	-
3000.0	0.03200	0.923	0.601	4.2	3.8	5.7	1.0	1.0	2.0	-	-	1.0	-0.5	0.8	-0.4	-0.1	-1.7	-
3000.0	0.05000	0.591	0.530	3.4	3.4	4.9	1.0	1.0	2.0	-	-	1.0	-0.9	1.2	-0.1	-0.1	-0.5	-
3000.0	0.08000	0.369	0.435	3.6	4.1	5.4	1.0	1.0	2.0	-	-	1.0	2.4	1.1	-0.0	0.0	-0.2	-
3000.0	0.13000	0.227	0.343	4.4	4.3	6.1	1.0	1.0	2.0	-	-	1.0	-2.4	0.7	-0.7	-1.1	-0.1	-
3000.0	0.18000	0.164	0.312	4.7	3.9	6.1	1.0	1.0	2.0	-	-	1.0	-1.7	0.4	-0.9	0.3	-0.1	-
3000.0	0.25000	0.118	0.233	5.0	6.1	7.9	1.0	1.0	2.0	-	-	1.0	-4.6	0.2	1.9	-0.1	-0.0	-
3000.0	0.40000	0.074	0.125	6.6	11.4	13.2	1.0	1.0	2.0	-	-	1.0	-9.4	-0.2	4.1	3.0	-0.0	-
3000.0	0.65000	0.045	0.012	19.0	30.7	36.1	1.0	1.0	2.0	-	-	1.0	-21.1	-1.2	15.4	14.1	-0.1	-
5000.0	0.05000	0.985	0.487	5.9	4.6	7.4	1.0	1.0	2.0	-	-	1.0	-1.2	0.6	-0.3	-0.1	-2.3	-
5000.0	0.08000	0.615	0.414	4.2	3.8	5.6	1.0	1.0	2.0	-	-	1.0	1.4	1.2	-0.1	-0.0	-0.6	-
5000.0	0.13000	0.379	0.327	5.0	3.5	6.1	1.0	1.0	2.0	-	-	1.0	-0.5	0.7	0.0	0.0	-0.2	-
5000.0	0.18000	0.273	0.283	5.6	5.0	7.5	1.0	1.0	2.0	-	-	1.0	-3.4	-0.5	0.3	0.4	-0.1	-
5000.0	0.25000	0.197	0.208	6.6	4.6	8.0	1.0	1.0	2.0	-	-	1.0	-1.5	0.9	-1.1	-1.6	-0.1	-
5000.0	0.40000	0.123	0.104	8.6	16.0	18.1	1.0	1.0	2.0	-	-	1.0	-14.0	-1.7	5.4	2.7	-0.0	-
5000.0	0.65000	0.076	0.013	23.0	38.1	44.5	1.0	1.0	2.0	-	-	1.0	-33.4	-1.7	11.6	10.7	-0.1	-
8000.0	0.08000	0.985	0.341	10.2	7.6	12.7	1.0	1.0	2.0	-	-	1.0	-4.6	1.0	0.3	0.1	-3.3	-
8000.0	0.13000	0.606	0.291	7.4	4.5	8.7	1.0	1.0	2.0	-	-	1.0	-1.2	1.1	-0.1	-0.1	-0.9	-
8000.0	0.18000	0.438	0.270	7.6	5.2	9.2	1.0	1.0	2.0	-	-	1.0	-2.7	1.5	-0.1	-0.1	-0.2	-
8000.0	0.25000	0.315	0.204	8.2	5.3	9.7	1.0	1.0	2.0	-	-	1.0	-2.9	0.8	0.0	0.0	-0.1	-
8000.0	0.40000	0.197	0.094	10.8	12.3	16.4	1.0	1.0	2.0	-	-	1.0	-11.1	-0.5	-1.0	-0.6	-0.1	-
8000.0	0.65000	0.121	0.019	19.6	46.8	50.7	1.0	1.0	2.0	-	-	1.0	-41.1	-8.4	16.3	8.0	-0.0	-
12000.0	0.13000	0.909	0.230	24.0	11.6	26.7	1.0	1.0	2.0	-	-	1.0	4.3	2.5	-0.5	-0.3	-3.8	-
12000.0	0.18000	0.656	0.233	11.8	7.7	14.1	1.0	1.0	2.0	-	-	1.0	-4.6	1.6	0.0	0.0	-1.3	-
12000.0	0.25000	0.473	0.157	12.6	8.5	15.1	1.0	1.0	2.0	-	-	1.0	-6.3	-0.4	-0.1	0.0	-0.4	-
12000.0	0.40000	0.295	0.104	14.7	12.5	19.3	1.0	1.0	2.0	-	-	1.0	-10.4	-1.0	0.2	-0.2	-0.1	-
12000.0	0.65000	0.182	0.014	27.8	28.9	40.1	1.0	1.0	2.0	-	-	1.0	-25.5	-3.7	4.7	1.7	-0.1	-
20000.0	0.25000	0.788	0.127	22.2	11.9	25.2	1.0	1.0	2.0	-	-	1.0	-6.1	2.2	0.2	0.0	-1.3	-
20000.0	0.40000	0.492	0.095	20.6	15.0	25.5	1.0	1.0	2.0	-	-	1.0	-11.1	-2.1	0.0	0.0	-0.3	-
20000.0	0.65000	0.303	0.009	45.1	52.0	68.8	1.0	1.0	2.0	-	-	1.0	-48.7	-6.2	0.0	0.0	-0.3	-
30000.0	0.40000	0.738	0.046	52.5	30.5	60.7	1.0	1.0	2.0	-	-	1.0	-21.5	4.1	0.5	0.0	-1.5	-
30000.0	0.65000	0.454	0.003	106.1	52.9	118.5	1.0	1.0	2.0	-	-	1.0	-44.0	6.6	0.0	0.0	-1.8	-

Table 9.6: *(...Cont'd) The reduced cross section* $\tilde{\sigma}_{NC}$ *with its relative error (and contributions) for the* e^+*period. Cross sections from the high* y *analysis are indicated in* ***bold*** *script.*

Acknowledgements

H1, a great experiment with wonderful people. I am privileged to be part of it.

My partner in crime – Voica Radescu. It was very fulfilling to have you as my analysis partner for those six months we were pushing for preliminary. I think those were some of the most enriching times for me, filled with laughter, joy, pain, disappointment and whatever else life can throw at you. But in the end we made it, despite me deleting everything!

Many thanks to my Inclusive Group – Vladimir Chekelian, Zhiqing Zhang, Andrei, Biljana, Ringaile – for our weekly video conferences and your comments and criticisms. Thanks for your support. Special thanks to Alexandre Glazov whom I've learnt much from. Thanks for pushing us to get preliminary. I appreciate most of all that I could have called you up and come at a moment's notice to have a discussion. It's good to have a supervisor who still does analysis and in touch with the technical parts of the experiment. Also thanks to Eram Rizvi. Whenever I felt somewhat discouraged I always thought "Call Eram and he'll get you back on your feet." Thanks for your valued input into the analysis.

I wish that Prof. Naroska were here to judge my thesis. I would like to think that I did her proud. Thank you for giving me the opportunity to continue as a PhD student in high energy physics. Thank you for the freedom you gave me that I could do inclusive physics as part of the heavy flavour group. Thanks Prof. Robert Klanner for taking over the responsibility as supervisor. I've come to appreciate your constructive comments as well as your encouraging and down-to-earth nature. I want to say thanks to Benno List for the push that caused me to finish when I did.

I would like to thank the ICSC – World Laboratory for their financial support during the first year of my thesis. In particular Kerstin Borras for her supervision and our discussions during this time.

Many thanks goes to Dave for all his technical help, and for making time when I knew that he did not really have it. Your help was very much appreciated. Thanks also to my referee Paul Laycock. Joachim, thanks for reading my script when it was in its early stages of development. Sorry about that thirty five pages of trigger. Honestly, it's not the part of the analysis I enjoyed the most, it certainly was the most work! Thanks for your valued comments. Thanks Peter and Lea for translating my abstract.

Michael, what's cracking? Thanks for the tea and cappuccino times we had. And for being on the other end of the phone when I had to do all things German. Deniz and Krzysztof (impossible name to spell but thankfully not so impossible to pronounce). I've had many wonderful chats with you guys. Its the stuff that dreams are made of – Polish, Turkish and Trinidadian talking about culture and whatever else that makes the world turn. I hope you make it to the world cup; our chances are slim. Mira, thanks for the tandemning which I still do very much enjoy. Adil Aktas – for the physics and non-physics times. Barbara Warmbein, thanks for your friendship. The Bachs – Christian, Tassi and the kids – thanks for the Sunday "liming" (Trinidadian for "hanging out"). We still have to find 3 kg of goat meat to curry!

My parents – Zainool and Elisha, sorry for being the stubborn and hard-headed teenager that I was. But I don't think I turned out too bad after all. Still working on it though. Sharon, Lystra, Bready, Filly – thanks for brotherly and sisterly love. Alexandra Serna – my adopted sister – never a dull moment chilling with you. Jesus Christ – most importantly, thanks for being there with me in everything. It was my only comfort at times. Thanks.

Bibliography

[1] C. Adloff et al. Measurement and QCD analysis of neutral and charged current cross sections at HERA. *Eur. Phys. J.*, C30:1–32, 2003.

[2] Alexandre Alimovich Glazov. Measurement of the proton structure functions F2(x,Q**2) and F(L)(x,Q**2) with the H1 detector at HERA. DESY-THESIS-1998-005.

[3] Yuri L. Dokshitzer. Calculation of the Structure Functions for Deep Inelastic Scattering and e+ e- Annihilation by Perturbation Theory in Quantum Chromodynamics. *Sov. Phys. JETP*, 46:641–653, 1977.

[4] V. N. Gribov and L. N. Lipatov. Deep inelastic e p scattering in perturbation theory. *Sov. J. Nucl. Phys.*, 15:438–450, 1972.

[5] V. N. Gribov and L. N. Lipatov. e+ e- pair annihilation and deep inelastic e p scattering in perturbation theory. *Sov. J. Nucl. Phys.*, 15:675–684, 1972.

[6] Guido Altarelli and G. Parisi. Asymptotic Freedom in Parton Language. *Nucl. Phys.*, B126:298, 1977.

[7] E. A. Kuraev, L. N. Lipatov, and Victor S. Fadin. Multi - Reggeon Processes in the Yang-Mills Theory. *Sov. Phys. JETP*, 44:443–450, 1976.

[8] I. I. Balitsky and L. N. Lipatov. The Pomeranchuk Singularity in Quantum Chromodynamics. *Sov. J. Nucl. Phys.*, 28:822–829, 1978.

[9] R. Devenish and Amanda Cooper-Sarkar. Deep Inelastic Scattering.

[10] A. Nikiforov. *Measurements of the Neutral Current* $e \pm p$ *Cross Sections Using Longitudinally Polarised Lepton Beams at HERA II.* PhD thesis, Ludwig-Maximilians-Universitaet Muenchen, 2007.

[11] H1 Collaboration. A Precision Measurement of the Inclusive ep Scattering Cross Section at HERA. 2009.

[12] J. Pumplin et al. New generation of parton distributions with uncertainties from global QCD analysis. *JHEP*, 07:012, 2002.

[13] Alan D. Martin, W. James Stirling, and R. G. Roberts. Parton distributions updated. *Phys. Lett.*, B306:145–150, 1993.

[14] A. C. Benvenuti et al. A High Statistics Measurement of the Proton Structure Functions F(2) (x, Q**2) and R from Deep Inelastic Muon Scattering at High Q**2. *Phys. Lett.*, B223:485, 1989.

[15] Ferdinand Willeke. Hera hits new heights. *CERN Courier*, 45:17–19, 2005.

[16] F. D. Aaron et al. Measurement of the Proton Structure Function F_L at Low x. *Phys. Lett.*, B665:139–146, 2008.

[17] D. P. Barber et al. The First achievement of longitudinal spin polarization in a high-energy electron storage ring. *Phys. Lett.*, B343:436–443, 1995.

[18] A. Aktas et al. First measurement of charged current cross sections at HERA with longitudinally polarised positrons. *Phys. Lett.*, B634:173–179, 2006.

[19] H. Oberlack H. Wellisch, J. Kubenka and P. Schacht. Hadronic Calibration of the H1 LAr Calorimeter using Software Weighting Techniques, H1-Internal Note, H1-0294-346. Technical report.

[20] B. Andrieu et al. Beam tests and calibration of the H1 liquid argon calorimeter with electrons. *Nucl. Instrum. Meth.*, A350:57–72, 1994.

[21] B. Andrieu et al. Results from pion calibration runs for the H1 liquid argon calorimeter and comparisons with simulations. *Nucl. Instrum. Meth.*, A336:499–509, 1993.

[22] B. Andrieu et al. Electron / pion separation with the H1 LAr calorimeters. *Nucl. Instrum. Meth.*, A344:492–506, 1994.

[23] B. Andrieu et al. The H1 liquid argon calorimeter system. *Nucl. Instrum. Meth.*, A336:460–498, 1993.

[24] Adrian Perieanu. *The structure of charm jets and the dead cone effect in deep-inelastic scattering at HERA*. PhD thesis. DESY-THESIS-2006-002.

[25] Max Christoph Urban. *The new CIP2k z-Vertex Trigger for the H1 Experiment at HERA*. PhD thesis, Universitaet Zuerich, 2004.

[26] B. List. The H1 central silicon tracker. *Nucl. Instrum. Meth.*, A501:49–53, 2001.

[27] I. Abt et al. The H1 Detector at HERA, H1-Internal Note, H1-01/98-533. Technical report.

[28] Beate Heinemann. *Measurement of Charged Current and Neutral Cross Sections in Positron-Proton Collisions at* $\sqrt{s} \approx 300GeV$. PhD thesis, Universität Hamburg, 1999.

[29] J. K. Kohne et al. Realization of a second level neural network trigger for the H1 experiment at HERA. *Nucl. Instrum. Meth.*, A389:128–133, 1997.

[30] B. Reisert M. zur Nedden and T. Schoerner. H1 Liquid Argon Trigger: Overview, Simulation and Performance, H1-Internal Note, H1-04/01-592. Technical report.

[31] Y. H. Fleming. *The H1 First Level Fast Track Trigger.* PhD thesis, The University of Birmingham, 2003.

[32] C. Wissing et al. The H1 ToF system in 1996 and 1997, H1-Internal Note, H1-01/98-533. Technical report.

[33] I. Abt et al. The H1 detector at HERA. *Nucl. Instrum. Meth.*, A386:310–347, 1997. See: http://www-h1.desy.de/h1/www/h1det/detpaper/contents.html.

[34] G. A. Schuler and H. Spiesberger. DJANGO: The Interface for the event generators HERACLES and LEPTO. In *Hamburg 1991, Proceedings, Physics at HERA, vol. 3* 1419-1432. (see HIGH ENERGY PHYSICS INDEX 30 (1992) No. 12988).

[35] Ingelmann G. Proceedings of the Workshop "Physics at HERA", vol.3 eds. W. Buchmueller, G. Ingelman, DESY (1992) 1366.

[36] A. Kwiatkowski, H. Spiesberger, and H. J. Mohring. HERACLES: AN EVENT GENERATOR FOR e p INTERACTIONS AT HERA ENERGIES INCLUDING RADIATIVE PROCESSES: VERSION 1.0. *Comp. Phys. Commun.*, 69:155–172, 1992.

[37] Leif Lonnblad. ARIADNE version 4: A Program for simulation of QCD cascades implementing the color dipole model. *Comput. Phys. Commun.*, 71:15–31, 1992.

[38] Torbjorn Sjostrand and Mats Bengtsson. The Lund Monte Carlo for Jet Fragmentation and e+ e- Physics. Jetset Version 6.3: An Update. *Comput. Phys. Commun.*, 43:367, 1987.

[39] Torbjorn Sjostrand, Leif Lonnblad, and Stephen Mrenna. PYTHIA 6.2: Physics and manual. 2001.

[40] Berger C. and Kandel P. Prepared for Workshop on Monte Carlo Generators for HERA Physics, Hamburg, Germany, 27-30 Apr. 1998.

[41] Ingelman G. Doyle A. T., Grindhammer G. and editors. Jung H. Lepton Pair Monte Carlo Generators for HERA Physics, 1999. Proceedings of the workshop Monte Carlo Generators for HERA Physics, DESY, Hamburg.

[42] Meyer J. Guide for the H1 simulation program H1SIM, Internal Software-Note, 03-11/89, DESY, 1989. Technical report.

[43] R. Brun, F. Bruyant, M. Maire, A. C. McPherson, and P. Zanarini. GEANT3. CERN-DD/EE/84-1.

[44] https://www-h1.desy.de/icas/oop/finders/efinder/oo LArefinder.html.

[45] Philippe Bruel. *Recherche d´interactions au-delà du Modèle Standard à HERA*. PhD thesis, L´Universite Paris XI Orsay, 1998.

[46] B. Portheault M. Peez and E. Sauvan. An energy flow algorithm for Hadronic Reconstruction in OO: Hadroo2, H1-Internal Note, H1-01/05-616. Technical report.

[47] I. Abt et al. The Tracking, calorimeter and muon detectors of the H1 experiment at HERA . *Nucl. Instrum. Meth.*, A386:348–396, 1997.

[48] A. Nikiforov V. Chekelian and A. Raspereza. High q^2 nc analysis with new vertex treatment procedure. talk given at the high q2 analysis meeting, hamburg, december 2007.

[49] A. Meyer. *Measurement of the Structure Function $F_2(x, Q^2)$ of the Proton at Low Q^2 with the H1 Detector at HERA Using the New Detector Components Spacal and BDC*. PhD thesis, Universität Hamburg, 1997.

[50] A. Dubak. *Measurement of the e+ p neutral current DIS cross section and the F2, F(L), xF3 structure functions in the H1 experiment at HERA*. PhD thesis. MPP-2003-65.

[51] Mira Kraemer. *Measurement of Charm and Beauty Cross Sections in Photoproduction using Events with Muons and Dijets at HERA*. PhD thesis, Universität Hamburg, 2009.

[52] Private correspondence with Sergey Levonian.

[53] A. Mehta. New track based electron finder. talk given at the high q2 analysis meeting, hamburg, october 2003.

[54] Ursula Bassler and Gregorio Bernardi. On the kinematic reconstruction of deep inelastic scattering at HERA: The Sigma method. *Nucl. Instrum. Meth.*, A361:197–208, 1995.

[55] H. Spiesberger. Proceedings of the workshop: Future Physics at HERA, vol. I, eds. G. Ingelman, A. De. Roeck, R. Klancer, DESY (1996) 227.